Fluid-Structure Interaction Under Fast Transient Dynamic Events

by

Alistair Richard Boyd
B. Eng. (Hons)

Thesis submitted for the degree of
Doctor of Philosophy

School of Civil and Environmental Engineering
The University of Edinburgh

1999

To my family

Preface

It is declared that this thesis, and the work contained within, is original research work conducted solely by the author unless otherwise stated. None of the work has been submitted for a higher degree or to any other university or institute.

During the course of the research the following conference papers were produced and are included in Appendix B.

1. Royles, R and Boyd, R., *Influence of high performance computing on analysis and design of underwater structures*, Proc. of 25th AIAS National and International Conference on Material Engineering, Gallipoli/Lecce, volume 1, pages 583-590, 4 – 7 September 1996.

2. Boyd, R. and Royles, R., *Modelling free field UNDEX using LS-DYNA3D*, Proc. of 1st European LS-DYNA Conference, Stratford-Upon-Avon, 18: S2.1-2.11, 20 – 21 March 1997.

3. Boyd, R., Royles, R., El-Deeb, K. M. M. and Haxton, R. S., *Fast dynamic transient loading of underwater structures*, Proc. of 11th Int. Conf. on Experimental Mechanics, Oxford, volume 1, pages 23-28, 24 – 28 August 1998.

A. Richard Boyd

Abstract

Fluid-structure interaction under fast transient dynamic events is complex and can involve both fluid and structural non-linearities. The ability to predict such non-linearities has been limited until now by computing resources. However, recent advancements have made it possible to attempt such predictions with the finite element and boundary element methods.

Underwater explosion (UNDEX) loading resulting from rapid phase transitions (RPTs) is one example of a fast transient dynamic event. The leakage of substances such as liquefied petroleum gas (LPG) or liquefied natural gas (LNG) when stored underwater can cause an RPT. These substances are often stored in a combination of very low temperatures and high pressures with respect to the surrounding fluid (sea water) and their leakage can cause the equivalent of an underwater explosion. Such containers are usually found to be part of a much larger 'storage field' of containers. An RPT occurring in one container would cause underwater explosion loading on neighbouring containers.

By emulating an RPT using explosive charges, experiments were initially designed using theoretical and empirical techniques. The fluid and structural response of a prototype container subject to symmetric and axisymmetric UNDEX loading was then examined experimentally. Theoretical predictions using the finite element hydrocode LS-DYNA and boundary element code USA-DYNA3D were undertaken and compared with experimental observations. Several non-destructive techniques were employed to estimate dynamic collapse buckling criteria from both experimental and theoretical results.

From the experimental work it was concluded that the critical regions of the prototype container were the apex and the base under both forms of loading. The quality of the numerical predictions varied dependent on the form of the loading. In some cases the fluid and structural responses were overpredicted, and in others underpredicted. Within the limitations of these numerical procedures it was possible to predict a

conservative estimate of a critical charge size under axisymmetric UNDEX loading using LS-DYNA. A critical stand off distance was also estimated from experimental results under symmetric UNDEX loading.

The use of numerical approaches to predict fluid-structure interaction was successful for the shock phase of UNDEX loading and both LS-DYNA and USA-DYNA3D have been validated for shock loading. Bubble loading simulations proved unsuccessful. Suggested improvements for future experimental and numerical simulations are proposed to increase the application of, and enhance the reliability of, the techniques used in this work.

Acknowledgements

The author would like to express sincere thanks to the following people for their involvement in the undertaking of this thesis.

- Dr Rodney Royles, my academic supervisor, for his commitment to providing first rate resources, steady supervision and enthusiastic support.
- Dr Khaled El-Deeb, my industrial supervisor, for his invaluable technical advice and teaching, faithful guidance, encouragement, patience and friendship throughout the project.
- Dr R. S. Haxton and the Vulnerability Division at DERA (Rosyth) for their technical and financial support, and the use of computing and experimental facilities throughout the project. Also the expertise and advice of the UNDEX trials laboratory staff during the experimental tests is gratefully acknowledged.
- Dr J. Miles, Mr R. Hollamby and Mr B. Walker from Oasys Limited for their provision of LS-DYNA software and technical support.
- Engineering and Physical Science Research Council (EPSRC) for financial support towards the use of central computing facilities at RAL and for personal maintenance.
- RAL for their generosity in providing the computing resources and support necessary for the project.
- David Anderson, James Jarvis and others of the EUCS team for their willingness and friendliness in overcoming computing problems.

All training and technical advice given by Dr M. Souli (LSTC) is greatly appreciated. Further contributions from Dr W. Mindle (LSTC), Mr T. Littlewood (ETA), Mr M. Nichols (Altair Inc.), Measurements Group (UK) Ltd, CIBA and XYZ Scientific Applications Inc., are also gratefully acknowledged.

Thank you to all my colleagues and friends both within and outwith the department for lasting memories, and their inspiration and motivation during my time here. Special thanks to Anthony Harding and Michael Gordon for your friendship and prayers.

Lastly, I have dedicated this thesis to my family, Mum and Dad in particular. Thank you for your caring advice, encouragement, support and prayers which I have cherished throughout this work.

Heavenly Father, your ways are steadfast and sure, your promises true to the end. Thank you for being there.

> **'The LORD himself goes before you and will be with you; he will never leave you nor forsake you. Do not be afraid; do not be discouraged.'**
>
> ***(Deuteronomy 31:8, NIV)***

Contents

List of Figures

List of Tables

Notation

Definitions of the symbols used in this thesis are listed below. Roman characters are listed first, followed by Greek characters. The symbols are also defined where they first appear in the text. Units used are given in brackets and are assumed throughout unless otherwise stated.

Roman characters

A_f	Cross-sectional area of fluid
$[A_f]$	Diagonal fluid area matrix
C	Damping matrix
D	Detonation velocity (ms^{-1})
E	Young's Modulus / Energy
E_0	Initial total energy per unit mass
E_1	Total energy per unit mass
E_f	Energy flux density (Pa.m)
E_{ke}	Global kinetic energy
E_{vol}	Energy per unit volume
G	Force transformation matrix
I	Impulse per unit area (Pa.s)
M	Structural mass (kg)
M_f	Fluid mass matrix
$P, P(t)$	Pressure (MPa)
P_0	Steady state pressure ($P_a + P_H$)
P_a	Atmospheric pressure
P_c	Cavitation pressure cut off
P_{cd}	Shock tube pressure at contact discontinuity
P_{cj}	Chapman-Jouget pressure
P_{cr}	Critical buckling load
P_{dc}	Non-linear dynamic collapse load
P_{sc}	Non-linear static collapse load
P_I	Incident pressure
P_H	Hydrostatic pressure

P_{max}	Maximum pressure
P_{cmax}	Corrected maximum pressure at shock front
P_r	Radiated pressure
P_R	Reflected pressure
P_S	Scattered pressure
$\dot{P}_S$	Scattered pressure first temporal derivative
$\ddot{P}_S$	Scattered pressure second temporal derivative
P_t	Transmitted pressure
P_T	Total resultant pressure
Q	Chemical energy
R	Stand off distance (m)
SF	Shock factor ($kg^{0.5}m^{-1}$)
$\dot{U}$	Shock wave velocity (ms^{-1})
$\widetilde{V}$	Three dimensional velocity vector
V	Volume (m^3)
V_o	Initial relative volume
W	Charge mass (kg)
a	First order volume correction
c	Speed of sound (ms^{-1})
c_d	Critical damping fraction
$cvtol$	Convergence tolerance
$f(t)$	Force
f_c	Cut off frequency (kHz)
f_d	Applied force vector for the dry-structure
l_e	Shortest element length (mm)
q	Artificial bulk viscosity
$q(t)$	Structural displacement
$\dot{q}(t)$	Structural velocity
$\ddot{q}(t)$	Structural acceleration
t	Time (ms)
t_d	Decay time (ms)
t_r	Rise time (μs)
t_{SF}	Timestep scale factor
t_w	Average shell wall thickness (mm)
$\dot{u}$	Fluid particle velocity
u_{cd}	Shock tube velocity at contact discontinuity
u_d	Detonation particle velocity
u_r	Shock tube rarefaction wave velocity
$\dot{u}_I$	Normal incident velocity
$\dot{u}_S$	Normal scattered velocity
$\ddot{u}_I$	Normal incident acceleration

$\ddot{u}_S$	Normal scattered acceleration
x	Normal structural displacement
$\dot{x}$	Normal structural velocity
$\ddot{x}$	Normal structural acceleration

Greek characters

Δt	Timestep (μs)
ΔR	Displacement range (mm)
ΔV	Volume range (m^3)
Ω_f	Accuracy factor
β	Acoustic element damping ratio
γ	Ratio of specific heats
γ_{cj}	Chapman-Jouget gamma
γ_0	Gruneisen gamma
δ	Deflection
δ_0	Initial deflection or initial geometric imperfection
ε	Material strain
$\dot{\varepsilon}_{kk}$	Strain rate tensor (s^{-1})
η	Damping factor
θ	Decay constant (ms) / circumferential angle (^{o})
μ	Ratio of densities
$\mu\varepsilon$	Microstrain
ν	Poisson's ratio
$\sqrt[3]{\nu}$	Characteristic length
ρ	Density (kgm^{-3})
ρ_0	Initial density (kgm^{-3})
σ	Material stress
σ_d	Prototype material design stress
ϕ	Meridional angle (^{o})
ω_n	Lowest natural frequency ($rads^{-1}$)

Abbreviations

ALE	Arbitrary Lagrangian Eulerian
BE	Boundary element
CAD	Computer aided design
CFD	Computational fluid dynamics
CSD	Computational structural dynamics
DAA	Doubly asymptotic approximation
DERA	Defence Evaluation Research Agency
DOF	Degrees of freedom
ESD	Energy spectral density
ETA	Engineering Technology Associates Inc.
FDM	Fused deposition modelling
FE	Finite element
FSI	Fluid-structure interaction
GRP	Glass reinforced plastic
HIS	Half index shift
HRIT	High resolution interface tracking
LNG	Liquefied natural gas
LPG	Liquefied petroleum gas
LSTC	Livermore Software Technology Corporation
MMALE	Multi-material ALE
MUSCL	Monotone upwind scheme for conservation laws
PG	Pressure gauge
PWA	Plane wave approximation
RAL	Rutherford Appleton Laboratory
RPT	Rapid phase transition
SAVIAC	Shock and Vibration Information and Analysis Centre
SG	Strain gauge
SL	Stereolithography
SLIC	Simple line interface calculation
UNDEX	Underwater explosion
UV	Ultra-violet
VMA	Virtual mass approximation

Chapter 1

Introduction

1.1 Offshore structures

Structures have been utilised for many centuries within the marine environment. Among these uses are methods of transportation, the development of natural resources, entertainment for people, and, more recently, for storage. Storage at sea is often a contentious issue due to the environmental disputes concerning leakage and its impact on the surrounding habitat. A further issue, from an engineering perspective, is the impact a leakage may have on neighbouring structures.

The design of offshore structures is dependent on two main considerations: the activity which the structure is being built for; and the environment into which the structure is being placed. The latter comprises considering whether the structure is to be a surface or a submerged one.

Detailed investigations into the structural response to various loading configurations to which an offshore structure may be subjected are necessary. In the past such investigations have been performed experimentally often incurring huge expenditures. Recent developments in computational capabilities for structural analysis have allowed predictive response studies to be performed numerically using finite element techniques. The use of such techniques for repeatability and behavioural studies would be of valuable benefit to those for whom reliance on experimental work is becoming financially burdensome.

1.1.1 Surface structures

Structures located at the surface are in exposed and often isolated regions depending on their purpose. This location, although easily accessible in calm weather, makes a structure vulnerable and inaccessible in adverse weather conditions. The air-sea interface is an unpredictable and challenging environment for surface structures, whether fixed, tethered or free. Circumstances can be such that operations may have to cease should conditions become too demanding, a costly and often undesirable decision. The extraction and treatment of resources from the ocean using drilling rigs on oil platforms is one example of an isolated surface structure in a demanding environment. Other examples include ships used to transport the resources.

1.1.2 Submerged structures

The submerged environment offers more attractive conditions for structures since they are not exposed to weather conditions as at the surface. Such less demanding conditions allow for transport and storage of resources to be more continuous, so avoiding the cost of production having to temporarily cease. Examples of submerged structures include submarines and underwater storage tanks. Access to the latter for maintenance or loading and unloading can however prove difficult and expensive. Some form of buoyancy is required to alleviate these problems.

1.2 Fluid-structure interaction systems

Fluid-structure interaction (FSI) systems involve a structure interacting dynamically with a volume of fluid after an initial load is applied. Such systems comprise either a structure immersed or partially submerged in fluid, or fluid contained within a structure. Examples of systems where FSI occurs include underwater vessels, pipes used for fluid transport, containment tanks and spillways.

Structures destined for the marine environment must be designed for a variety of loads which will occur throughout their life cycle, i.e., construction, installation, operation and de-commissioning. For fluid-structure interaction to occur forced fluid flow, or structural movement, is required to initiate the system. The initial loading could be of a static or dynamic nature. The resulting fluid and ultimately structural responses are the areas of interest.

1.3 The echinodome

Much work has been done on examining the optimum shape for underwater storage tanks[1]. This work concluded that a spheroidal shell, based on the membrane theory for shells of uniform strength, was an ideal shape for the most efficient use of material. The shell of constant or uniform strength is similar in shape to the profile of a drop of liquid resting on a plane surface. The hydrostatic pressure distribution over the drop shape surface is illustrated in Fig. 1.1. The surface tension forces containing the internal hydrostatic pressure are equal at all points. The pressure head at the apex and material strength parameter (design stress $\times$ thickness) determine the meridional profile of the shell.

The same shape has been adopted by the common sea urchin which supports the suitability of this structural form for underwater applications. These sea animals belong to the phylum echinodermata and hence the generic term for this structure - the *echinodome*[2]. A study of these animals has shown that those living at greater depths tend to be more spherical than those living in shallower waters. However, this tendency results in a reduction in capacity.

The meridional profile corresponding to the head and material strength can be determined from the solution of the differential equations of the drop shaped shell[3]. Initially these equations were solved graphically, and from their solution a prototype shell was designed and built in 1965 using glass-reinforced plastic (GRP). To assist in the designs of such structures a shape prediction program was developed[2–4] which provided a numerical solution to these equations using the explicit modified Euler method, later modified by the present author to the Runge Kutta method to assist in parallelisation of the program[5]. This program assisted in providing the geometrical data for the prototype structure which is employed in the work reported here.

1.4 Applications of the echinodome

Proposals to use the echinodome as an underwater storage tank for various applications have been researched over the years.

The production of oil within the oil industry is an ongoing process. To stop production for a limited time yields unacceptably high costs. The risks and costs associated with a surface storage tanker would be reduced considerably if storage were to be transferred to the submerged environment. A procedure for the design of an echinodome for this purpose was reported earlier[3].

El-Deeb[4] proposed the design of a full scale echinodome to be used for the storage of liquefied natural gas (LNG), based on an earlier proposal[6]. The storage of such a volatile liquid in the underwater environment imposed strict design limits to ensure structural integrity under a variety of accidental loads.

Other applications include the storage and treatment of storm flow from sewage treatment works[7], reducing pollution of the marine environment from such waste.

1.5 Fast transient dynamic events

Structures located within the underwater environment may be subjected to static or dynamic loads. Structural response to such loads will depend on the frequency of the loading pulse. When this frequency is similar to one or more of a structure's natural frequencies the structure will respond very differently compared to the equivalent static load. For slow transient dynamic events the period of the loading pulse is of the order of milliseconds, or seconds, which would cause modes of vibration to be excited resulting in global structural failure. For fast transient dynamic events the frequency of the loading pulse is of the order of microseconds. Such rapid loading can cause localised deformation on a structure. Examples of a range of dynamic events are outlined below.

As mentioned earlier recent developments have been undertaken to examine the possibilities of storing LNG in the underwater environment. Natural gas, cooled to -162^{o}C under atmospheric pressure, condenses and is transformed into LNG. In its liquid form, natural gas is 600 times more compact[8]. Being stored at such low temperatures has the disadvantage of making this product highly volatile due to the much higher temperatures of the surrounding sea water. In the event of leakage of LNG into the sea water, caused by structural failure due to any of the loads mentioned above, the product will become superheated due to the large thermal difference. This will initiate a rapid change of state of LNG from liquid form back to gaseous state. Such a phenomenon is known as a rapid phase transition (RPT).

The rapidity with which this change of state occurs resembles the detonation of an explosive charge underwater. The result is the propagation of the detonation through the LNG medium. Such a process will invariably destroy the structure from which the leakage occurred. The sudden release of energy causes a disturbance transmitting a pressure wave or shock wave which propagates outwards from the originating structure to neighbouring structures. In the context of explosions, this loading is known as underwater explosion (UNDEX) loading. The period of such loading is initially of the order of microseconds increasing to milliseconds as the shock wave propagates outwards.

1.6 Dynamic buckling

Associated with such an RPT event is the risk of both local and global failure. Failure could result from compressive strain levels exceeding the maximum compressive strength of the material, or due to excessive deformation. Failure under excessive deformation is termed buckling, and under dynamic loading conditions it is known as dynamic buckling.

If buckling occurs before material failure the ability of the structure to perform to its original design specification is altered. Certain geometrical configurations cause the structure to stiffen, increasing its ability to endure greater loads. Other configurations reduce the structure's load carrying capability to the point where it is no longer operational.

To improve the design of an underwater storage structure such as the echinodome, it is necessary to establish if dynamic buckling will occur before material failure under fast transient dynamic loadings of the UNDEX type. Furthermore, to establish critical buckling criteria using computational techniques would greatly enhance the design process for structures in terms of both monetary and practical value.

1.7 Scope and objectives of thesis

The advent of computational techniques capable of simulating structural response to fast transient dynamic events makes dynamic buckling studies using non-destructive methods possible. For such techniques to be viable however, they require *verification* against empirical and analytical results, and *validation* against experimental measurements. This terminology will be used throughout the remainder of the thesis.

The work undertaken in this thesis aims to verify and validate two current methods for predicting fluid and structural response to UNDEX loading on the echinodome. The main objectives of the work described in this thesis are as follows.

1. To successfully simulate isolated phenomena pertaining to a free field UNDEX event.
2. To utilise both computational and empirical methods to design experimental UNDEX studies.
3. To successfully perform experimental UNDEX studies on a prototype echinodome without invoking structural damage.

4. To numerically simulate the experimental studies using two computational approaches to predict fluid and structural responses.

5. To assess the reliability of the two computational approaches to undertake dynamic buckling predictions.

6. To establish dynamic buckling criteria for UNDEX loading on the echinodome using non-destructive techniques.

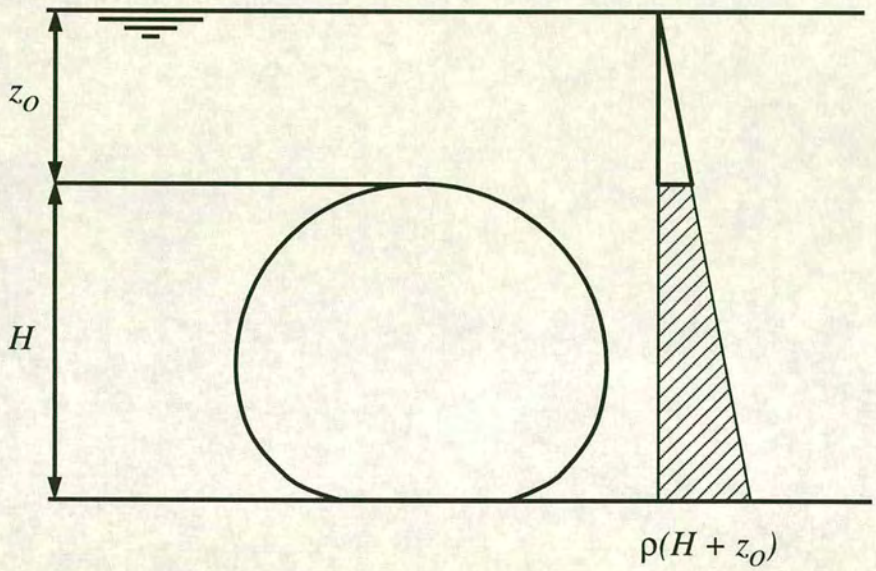

Figure 1.1: Variation of hydrostatic pressure on drop shape

Chapter 2

Background Research Review

2.1 Introduction

The physics of the underwater explosion have been studied extensively and are well understood in the free field environment. When a structure is in the vicinity of such an event the processes involved become problem dependent and often require repeated studies to establish adequate design criteria to ensure structural integrity and gain sufficient understanding of complex structural response to UNDEX loading.

Numerous experimental tests of underwater explosion loading events have been performed and techniques for capturing relevant data are well established. However, reliance on experimental studies is diminishing. The understanding gained from repeated experiments does not justify the ever increasing expense and the availability of data is often restricted to within organisations. From the latter it could be assumed that similar tests are being carried out many times.

Computational techniques are now of sufficient accuracy to cause a shift to reliance on numerical simulation of underwater explosion loading events with the advantages of improved understanding of structural behaviour, repeatability at much reduced cost and the establishment of more precise design criteria. More recent use of generic structures has permitted results to be published and techniques compared.

A background to previous work performed on the echinodome shell introduced in chapter 1 is accompanied by a detailed description of the underwater explosion and common structural response characteristics. A brief review of experimental studies and suitable numerical approaches for simulating underwater explosion events precedes an introduction to the software used in this work.

2.2 Previous work on echinodome

A prototype echinodome structure has been used for many years to investigate the response of such a structure to various loading configurations. Using experimental and theoretical membrane and finite element (FE) techniques Sofoluwe[1] initially examined the shell's response to hydrostatic pressure, discovering that at nine times the design head the stress in the membrane of the structure was well below that of the design stress. Llambias[3] then investigated the structural response to axisymmetric and symmetric point loads, performed linear and non-linear buckling analyses[9–11] and examined the vibration of the structure using a free vibration analysis. Experimental and FE techniques employed in this research led to the linear elastic static design and analysis of a full scale structure for storing oil.

The most recent work by El-Deeb[4] examined the prototype's response to accidental dynamic loading caused by impact and explosion, and established a full scale design procedure under consideration of such loads. Experimental investigations of static and dynamic point loads compared well with theoretical analyses[12]. It was concluded that a step loading with zero ramping time was the most severe dynamic loading to which the echinodome could be subjected. A theoretical dynamic buckling analysis under this form of loading concluded that the dynamic collapse buckling load was more critical than its static correspondent.

Experimental investigations subjecting the prototype echinodome to explosive loading were also undertaken[4,13,14]. These tests were designed to minimise structural damage whilst producing measurable strains. Cylindrical charge masses of 1g and 4g were placed 5.0m away from the maximum diameter of the shell and the strain response recorded. Insufficient experimental data were available to predict critical charge sizes or stand off distances using non-destructive techniques. An assessment of the shell after the experiments had been conducted concluded that no damage had occurred, however, analysis of the results indicated that the base was a critical region under explosive loading. Comparisons were made against a numerical model using a boundary element (BE) approach. The technique was found to be insufficiently developed at the time to permit accurate predictions of structural response to explosive loads and so ascertain critical charge sizes or stand off distances using numerical techniques. However, the results of the FE work carried out did assist in proposals for the design and construction of a full scale structure for storing LNG.

2.3 Characteristics of an UNDEX event

An explosion is a chemical reaction in an unstable compound, either solid or liquid, which converts the original material into a gas at very high temperatures and pressures. In air this process and resulting phenomena occur with extreme rapidity being completed in a few milliseconds. Underwater they may take up to several seconds to dissipate. Both explosions in air and underwater involve a great deal of heat and energy release. The underwater explosion process and resulting phenomena are illustrated in Fig. 2.1 and described in more detail below[15].

2.3.1 Detonation

The chemical reaction converting the original explosive material into the compressed gaseous products is initiated by mechanical impact or thermal radiation onto especially sensitive material which in turn initiates a reaction in the main body of the explosive. This is known as detonation. The position at which this is initiated is known as the detonation point. Once initiated, a detonation wave propagates through the explosive material at very high speed. The narrow region separating exploded material from unexploded material is known as the reaction zone and is characterised by a steep shock front, comprising an almost instantaneous rise in pressure and velocity. The propagation speed of the detonation wave is characteristic of each explosive material but is of the order of several thousand metres/sec, e.g. EDC-1 has a detonation velocity[16,17] of 8716ms^{-1}.

2.3.2 Shock wave

The result of the detonation process is a disturbance of the surrounding water. This takes the form of a steep fronted compression wave, or shock wave, propagating radially outwards from the point of detonation, separating the undisturbed water from the disturbed water. The arrival of the shock front is signified by an almost instantaneous rise in pressure in the undisturbed water. Spherical divergence of the shock wave leads to the reduction in the peak pressure at the shock front. The decay behind the shock front resembles that of an exponentially decaying function. The decay rate, i.e., the time for the peak pressure to reduce by $\frac{1}{e}$, is represented by the decay constant. As distance from the charge increases the rate of pressure decay is observed to decrease. The rise time, peak pressures and decay rates will vary depending on the type of explosive material used, the shape of explosive material, e.g. spherical or cylindrical, and distance

from the explosive source. The peak pressure is one indicator of the severity of an explosion, however, because it is a dynamic loading the impulse or energy contained within the shock wave is generally regarded as more representative of its capability to cause structural damage. Later in time the impulse becomes negligible and much of the energy dissipates into heat.

The speed of the shock wave decreases rapidly from the detonation velocity close to the detonation point, to the speed of sound in water at some distance from the charge. The acoustic speed of the wave in water typically ranges from $1400 - 1500 \text{ms}^{-1}$ depending on density, salinity and temperature of the water.

2.3.3 Afterflow

Following the passage of the shock wave the water behind the shock front has an outward velocity, known as afterflow or surge, which continues as long as there is pressure in excess of the prevailing hydrostatic pressure. For charges close to a structure this can contribute significant loading.

2.3.4 Gas bubble

The afterflow conditions resulting from the emission of the shock wave are now combined with the energy remaining in the gaseous explosive products to assist in the expansion of the gases. The pressure within the explosive products is still much higher than the surrounding hydrostatic pressure. The outward velocity of the water surrounding the explosive products combined with the pressure differential permits expansion of the gases into a spherical bubble. The pressure inside the bubble decreases until the pressure differential is reversed, i.e. the pressure inside falls below the equilibrium value outside (atmospheric + hydrostatic pressure). Expansion continues due to the inertia of the afterflow.

At the point where the outward flow stops the bubble is said to have reached its maximum radius. Since the hydrostatic pressure outside the bubble is now greater than the pressure inside, the bubble begins to contract at an increasing rate due to the inertia of the now inward flowing water. Contraction continues, compressing the gases inside the bubble, until maximum compressibility, i.e. minimum bubble radius, is reached. At this point the gases enter a second expansion cycle and a second pressure peak is observed. If assumed to be incompressible the pressure in the water surrounding the bubble is proportional to the square of the rate of bubble expansion or contraction.

This rate would be expected to be greatest at the point of minimum volume when the gases are under maximum compression.

Assuming free field conditions, one expansion and contraction cycle constitutes what is known as a bubble period and is proportional to the cube root of the internal energy and the inverse five-sixths power of pressure[15].

2.3.5 Secondary pulses

Multiple expansion and contraction cycles, or bubble pulses, can occur as illustrated in Fig. 2.2. These pressure pulses are caused by a build up of pressure as the bubble contracts and subsequent release of pressure as the bubble expands. The peak pressure observed is approximately 10-20% of the peak shock wave pressure, however the energy is estimated to be approximately equal to that of one decay constant after the initial peak pressure. Usually only the first pressure pulse is considered significant since a considerable amount of energy is lost in each pulse due to the rapidity of the event itself causing turbulence, and also due to vertical motion of buoyancy, resulting in successively weaker pulses and shorter pulse duration.

The number of pulses is dependent on energy losses through dissipation of heat, gravity and interaction with boundary surfaces. The buoyancy of the bubble causes it to rise to the surface whilst oscillating, however the proximity of rigid or near rigid surfaces will attract it and inhibit its free field motion. Using high speed photography it is possible to capture the motion of the gas bubble. In doing so, estimates of the bubble radius, boundary velocities and buoyancy effects have been studied in detail[18].

2.3.6 Surface effects

Water is a finite medium in which boundaries exist in the form of the free surface (air-water interface), side and bottom surfaces, and obstructions. The subsequent phenomena relating to an UNDEX event are a consequence of the interaction of the shock wave and bubble pulse with a boundary.

The most visible dramatic features of an UNDEX event occur at the free surface, the nature of which reduces as the depth of the explosive charge increases, becoming undetectable for deep charges, or as the mass of the charge is reduced.

Spray dome

The reflection of the shock wave off the surface results in a whitish mound of broken water being thrown up known as a 'spray dome'. Its growth is dependent on the incident pressure, being largest directly above the charge, and cavitation effects which are discussed in the section following. Pressure equilibrium at the free surface means the water particles exhibit only a vertical component of velocity equal to twice the velocity of the incident wave (see cavitation section). When the opposing forces of gravity and atmospheric pressure have reduced the velocity to zero the spray dome sinks back into the water. The spray dome can have steep sides depending on the velocity imparted on the water directly above the charge.

Plume

As well as the shock wave producing surface effects, a shallow charge will cause the gas bubble to break the surface in the form of venting. This venting gives rise to plumes of water and explosive products varying in height, velocity and direction depending on charge depth and bubble state (minimum or maximum radius). For shallow charges it is likely that the bubble will vent the surface during its expansion state when its global upward velocity is relatively slow, due to drag forces, hence the plume will also have a small upward velocity and the venting is radial. If the bubble is near the point of minimum radius its upward velocity is greater and so the resulting velocity of the water will be greater causing a more vertical plume.

Cavitation

Equilibrium conditions at the free surface require that, whilst the velocity of the water particles at the surface is twice the normal component of the velocity of the incident wave, the net pressure at the surface must be zero. This is satisfied by a reflected wave of negative pressure (a rarefaction wave) resulting from the air-water interface's inability to sustain compression. The resultant pressure is a superposition of the rarefaction wave onto the original, now decaying, shock wave. It is possible that the absolute pressure in the water could fall to a value equal to or lower than vapour pressure, if the pressure of the rarefaction wave was significantly greater than that of the shock wave. Under these circumstances tensile forces are applied to the water. But water is incapable of withstanding significant tensile forces and, consequently separation of the water particles occurs and the water vaporises. This form of vaporisation due to an UNDEX event is known as bulk cavitation.

2.3.7 Fluid-structure interaction

Free field UNDEX phenomena do not vary much between explosive materials. However, when the motions of the fluid and the structure must be treated as a single system, much of the resulting responses become case-dependent. These responses are mainly a function of structural inertia, the distance between the charge and the structure, i.e. the stand off distance, R, and the distance to boundaries and neighbouring structures. Several phenomena common to most cases concern the nature of shock wave propagation once it reaches the structure, the structural motion due to the impingement of the shock wave and the fluid response to structural motion.

Reflected pressure

When the shock wave impinges a rigid boundary the ability of that boundary to sustain compression will primarily influence resultant pressures in the water. For a infinitely rigid fixed plate the net fluid particle velocity becomes zero, since there is no movement of the plate, and the reflected pressure is a compression wave of the same magnitude as the incident pressure wave. Consequently the resultant pressure, comprising the incident and reflected pressures, is twice the incident.

Such boundaries are idealistic to gain a simplified understanding of fluid motion and associated pressure. The presence of a real deformable structure obstructing the path of a shock wave introduces energy absorption and movement of the structural boundary which adds further complications to the fluid motion. The interaction of the fluid and structure becomes the main element of interest.

Scattered pressure

The scattered pressure in the fluid just above the structural boundary is a combination of the reflected pressure, i.e., that which would occur if the structure were a perfectly rigid boundary, and pressures resulting from movement of the structural boundary.

The impingement of the shock wave and subsequent vibration of a deformable structure can generate pressure waves known as radiation pressures. The rigidity and extent of the structural boundary, and the medium behind the structural boundary, will affect the magnitude of these pressures. For a perfectly rigid structure the radiated pressure will be equal to zero, increasing as rigidity decreases. Depending on the contents of a structure a shock wave could also be partially transmitted into the medium inside the structure. Since water is more capable of sustaining a compression wave than air it is

clear that the transmitted pressure in a water backed structure would be greater than for a structure backed with air. The deformation of a water backed structure would be less due to the presence of the water behind the structure resulting in lower radiated pressures.

Thus the total resultant pressure, P_T, in the fluid at the structural boundary is seen to be composed mainly of incident and scattered pressures. Transmitted pressures could also add to the total pressure such that,

$$P_T = P_I + P_S + P_a + P_H + P_t \tag{2.1}$$

where,

P_I = incident pressure generated by explosive charge;
P_S = scattered pressure $\Rightarrow$ reflected (P_R) and radiated (P_r) pressures;
P_a = atmospheric pressure;
P_H = hydrostatic pressure; and
P_t = transmitted pressure.

Diffraction

The extent to which a structure affects the propagation of a shock wave depends on its geometry. In order for the shock wave to continue past the structure it must propagate around it, and in doing so, the portion of the shock wave close to the surface of the structure trails behind the rest causing the shock front to alter its shape. This process is known as diffraction and affects velocity and pressure.

Cavitation

When a structure is impinged by a shock wave it acquires a velocity corresponding to its inertia and rigidity. This sudden acceleration can cause the structure to separate from the surrounding fluid, particularly when the structure is thin. This form of separation is known as local, or hull, cavitation. The pressures behind the shock front then transmit further velocity to the separated fluid which buffets the structural boundary again.

2.4 Development of UNDEX research

The development of studies into fluid and structural responses to fast transient dynamic events, such as an UNDEX event, span most of this century. Much work has been done using experimental techniques to aid the design of structures. The construction of new more complex structures during the Second World War, for which there was no experimental data, motivated the subsequent rapid development of empirical and analytical techniques to reduce the cost and timescale for design, and exploit the use of rapidly growing computing facilities.

2.4.1 Experimental techniques

UNDEX experiments were initially focused on obtaining data to characterise loading from different explosive materials. Numerous studies were performed in the free field environment to collect data relating to shock and bubble loading at various distances from explosive charges, and to observe how bubble behaviour was influenced by charge depth[19].

Full scale and large model testing were often used to measure the physical processes involved in an UNDEX event and were relied heavily upon as the understanding of the physics involved was limited. The ultimate purpose of any experimental UNDEX test is to understand structural failure modes, and their cause, to assist in structural design. Testing full scale structures to failure imposes obvious limitations and associated costs, but even scale models tested to failure can only be used once and the amount of data that can be collected from a model is limited by the instrumentation capabilities.

Access to any available test data was restricted usually to defence organisations, who were the main benefactors of such research. Any data that could be obtained was not transferable between different types of structure. Today full scale tests are rarely performed due to the enormous costs involved. The Italian Navy, in collaboration with the US Navy, published some results of an investigation into shock response and whipping of a decommissioned frigate[20], mainly in an attempt to develop a numerical solution to predicting the phenomenon for future designs.

The demand for improved analytical solutions and more widely available data encouraged experimental investigation of more generic problems, based on simplified idealised geometry of real life structures, in an attempt to compile benchmarks against which the capabilities of analytical approaches could be evaluated and validated. The purpose of scale models was to attempt to isolate behaviour of different parts of

a structure subject to UNDEX. The structural response of submerged flat circular plates, and submerged cylindrical and spherical shells were studied extensively[21,22]. The more complex problem of bubble migration towards structural boundaries and eventual collapse, causing jetting, have also been reported[19].

Experimental work must still be relied on to provide realistic results. Techniques for exciting certain physical behaviour are improving as this research continues, along with the complexity of instrumentation gauges and data acquisition.

2.4.2 Empirical and analytical techniques

Much of the free field experimental work led to the formation of empirical relationships for characterising shock waves generated by various commonly used explosive materials. From these equations UNDEX loading could be quantified and used in conjunction with well known analytical methods for predicting fluid and structural response to such loads.

Numerical approaches for UNDEX phenomena stemmed from the basic laws of mechanics and thermodynamics and from these, pressure-volume relationships suitable for the treatment of problems involving detonation and shock phenomena were developed. These relationships form equations of state for explosives and fluids which relate pressure, volume, density and velocity. They describe the conditions within and behind the detonation and shock fronts, and wave propagation of the incident, reflected, transmitted and radiated waves.

Simplification of the loading to that of plane transverse shock waves applied to the generic structures above permitted the use of analytical methods such as separation of variables, wave front and ray tracing, Laplace transform solutions and the method of characteristics to provide exact closed form solutions.

2.4.3 Computational techniques

Recent developments in the programming of analytical solutions to the physics of fluid and structural behaviour has permitted the study of UNDEX phenomena using computational techniques. These provide a cheaper method for the design and testing of marine structures subject to such loading. With recent advancements in graphical representation of data, visualisation of predicted fluid and structural responses to UNDEX can also assist in improving the understanding of FSI.

Existing finite element, boundary element and finite difference methods provided a

suitable platform on which to implement these analytical solutions into computational models. Special purpose computational fluid dynamics (CFD) and computational structural dynamics (CSD) codes existed which allowed a discretised model of a problem to be constructed and an approximate solution found. As codes matured, more accurate solution techniques were developed approaching those of the exact solutions.

Although reliance has shifted from the early experimental techniques to these alternative analytical and computational approaches they should not be viewed as replacements of the experimental method. Numerical techniques offer several advantages but only after validation against reliable experimental data. Often it is necessary to repeat experiments to increase the reliability of results, or make slight alterations to an experiment to gain understanding of structural behaviour, or even extrapolate results to obtain failure criteria. The reproduction of responses under laboratory conditions is both time-consuming and difficult. However, once a numerical approach has been validated, such repetition of experimental simulations is unnecessary. Numerical techniques also provide a method of determining failure loads non-destructively and quantifying a more detailed structural response than is possible with experimental techniques.

2.5 Empirical approach to UNDEX

2.5.1 Detonation

A detonation wave differs from a shock wave in that it is self-sustaining and will not dissipate provided energy is supplied. Chemical energy from the transformed explosive material builds up a stable propagation rate through the explosive at a material velocity determined by the internal conditions just behind the detonation front. The velocity is assumed equal to the Chapman-Jouget condition[15],

$$D = c_d + \dot{u}_d \tag{2.2}$$

where,

D = detonation velocity;
c_d = velocity of small amplitude waves in detonation products; and
$\dot{u}_d$ = detonation particle velocity.

For a detonation wave to exist $D > c_d + \dot{u}_d$. The stable propagation rate signifies a stable pressure build up in the material, known as the Chapman-Jouget pressure, P_{cj}.

2.5.2 Shock wave propagation

Empirical equations based on observations from numerous experiments were first produced to mathematically represent shock wave characteristics for particular explosive materials and the propagation of shock waves through water. The shock wave propagation theory and the principle of similarity were utilised to produce equations to predict shock and bubble related loading parameters.

The shock wave propagation theory, first developed by Kirkwood and Bethe[15], predicted that the pressure-time curve for high explosives decayed exponentially with time according to Eqn 2.3.

$$P(t) = P_{max} e^{-\frac{t_r - t}{\theta}} \tag{2.3}$$

where,

t_r = rise time, ms;
t = time, ms;
P_{max} = peak pressure in the shock front, MPa; and
θ = decay constant, ms.

This approximation was found to be good for pressures up to one third of the peak value and for stand off distances of between 10 and 100 times the charge radius[15]. The ability of a shock wave to inflict damage on a structure can be measured by the duration of the applied pressure, i.e., the impulse, or the energy flux density, the transport of energy across a unit area radiated from the source.

The area under the pressure-time curve gives the impulse loading from the shock wave. Pressure behind the shock front continues to decay exponentially for some considerable time due to the existence of pressures resulting from the disturbance of the fluid and the motions of the gas sphere. Consequently an upper limit for integrating under the pressure-time curve is nominally defined[15] as 6.7θ, as shown in Fig. 2.3. The impulse per unit area is then given by,

$$I = \int_0^{6.7\theta} [P(t) - P_H]dt \tag{2.4}$$

with units $Pa.s$. Energy, or work done, is described as a force acting over a given distance. The total work done on a volume of fluid is given by,

$$E = \int_0^{6.7\theta} [P(t) - P_H]A_f \dot{u}dt \tag{2.5}$$

where,

A_f = cross sectional area of fluid, m^2; and
$\dot{u}$ = fluid particle velocity, ms^{-1}.

Assuming that the fluid is an elastic medium, the transmission of the shock wave may be described by an equation analogous to the transmission of a stress wave through a solid elastic medium in which the stress, σ, is given by[16]

$$\sigma = \rho c\dot{u} \tag{2.6}$$

where,

ρ = density of water, kgm^{-3}; and
c = speed of sound in fluid ($\approx 1500ms^{-1}$ in water).

This gives a relationship between fluid particle velocity and pressure in the form of

$$P(t) = \rho c\dot{u} \tag{2.7}$$

Rearranging Eqn 2.7 and substituting for u into Eqn 2.5 gives the energy flux density, E_f, as

$$E_f = \frac{1}{\rho c}\int_0^{6.7\theta} [P(t) - P_H]^2 dt \tag{2.8}$$

with units $Pa.m$. Usually P_H is negligible compared to the incident pressure.

To describe the conditions at the shock front, Rankine-Hugoniot jump conditions, valid for both planar and spherical waves, were derived from conservation of mass, momentum and energy to relate conditions ahead of and behind the shock front[15]. From Fig. 2.4,

Mass

$$\rho(\dot{U} - \dot{u}) = \rho_0(\dot{U} - \dot{u_0}) \tag{2.9}$$

Momentum

$$P - P_0 = \rho_0 \dot{U}(\dot{u} - \dot{u_0}) \tag{2.10}$$

Energy per unit mass

$$E_1 - E_0 = \frac{P - P_0}{2} \frac{\rho - \rho_0}{\rho_0 \rho} \tag{2.11}$$

where,

$\dot{U}$ = shock wave velocity, ms^{-1};
$\dot{u_0}$ = particle velocity prior to arrival of shock wave, ms^{-1};
$\dot{u}$ = particle velocity after arrival of shock wave;
ρ_0 = density prior to arrival of shock wave, kgm^{-3};
ρ = density after arrival of shock wave;
E_0 = energy prior to arrival of shock wave, $N.m.kg^{-1}$;
E_1 = energy after arrival of shock wave;
P_0 = pressure prior to arrival of shock wave, MPa; and
P = pressure after arrival of shock wave.

2.5.3 Power laws

From early experimental measurements shock wave characteristics were seen to behave according to the principle of similarity. This principle states that, all other parameters being equal, if the linear dimensions of a spherical charge, stand off distances and measurement times are altered by some factor, λ, then the shock wave characteristics will be the same at the corresponding distances and times.

If sufficient experimental data were available shock wave parameters could be related to charge mass and stand off distance using power laws (Eqns 2.12–2.15). These could be produced by power curve fits to the data according to the appropriate equation. Such

equations were based on artificial detonation conditions (assuming 100% detonation) and have been shown to overpredict shock wave characteristics by 15-20%[15]. The power laws take the following form.

Peak pressure

$$P_{max} = k\left(\frac{W^{\frac{1}{3}}}{R}\right)^{a} \tag{2.12}$$

Impulse per unit area

$$I = lW^{\frac{1}{3}}\left(\frac{W^{\frac{1}{3}}}{R}\right)^{b} \tag{2.13}$$

Energy per unit volume

$$E_{vol} = mW^{\frac{1}{3}}\left(\frac{W^{\frac{1}{3}}}{R}\right)^{c} \tag{2.14}$$

Decay constant

$$\theta = nW^{\frac{1}{3}}\left(\frac{W^{\frac{1}{3}}}{R}\right)^{d} \tag{2.15}$$

where the variables a, b, c, d and k, l, m, n, are explosive related constants derived from the similarity curves, W is the mass of explosive, in kg, and R is the stand off distance, in m. There are limitations to the use of these power laws. They are not applicable to problems involving non-scalable variables, e.g. viscosity, and do not take into account chemical changes in explosive materials.

The shock factor is also used as a crude approximation of the severity of shock loading induced by a conventional explosive charge. It is a generic parameter, independent of explosive material, relating charge mass and stand off distance and considers only the primary loading relating to an UNDEX event[15]. The shock factor, SF ($\mathrm{kg}^{0.5}\mathrm{m}^{-1}$) is given by,

$$SF = \frac{\sqrt{W}}{R} \tag{2.16}$$

Using the above equations a conservative estimate of the loading generated in an UNDEX event can be quickly obtained. They are often used in the design of experimental studies involving large charge sizes.

2.6 Analytical approach to UNDEX

2.6.1 Fluid dynamics

Numerical solutions of the kinematic deformation of continuous media are available in two forms: Eulerian and Lagrangian, usually referring to the solution of fluid and structural deformation respectively.

CFD codes provide a way of solving the above jump conditions with a set of differential equations established through the application of the principles of conservation of mass, momentum and energy[23] as summarised below.

Conservation of mass – the continuity equation satisfies mass transfer. For variable mass density,

$$\frac{\partial \rho}{\partial t} + \nabla \cdot (\rho \widetilde{V}) = 0 \tag{2.17}$$

where,

$\widetilde{V}$ = velocity vector $(\dot{u}i + \dot{v}j + \dot{w}k)$; and
$\nabla \cdot (\widetilde{V})$ = spatial variation of velocity $\left(\frac{\partial \dot{u}}{\partial x} + \frac{\partial \dot{v}}{\partial y} + \frac{\partial \dot{w}}{\partial z}\right)$.

Conservation of momentum – the Eulerian form of the Navier-Stokes equation assumes zero viscosity and satisfies momentum transfer,

$$\frac{D(\rho \widetilde{V})}{Dt} = -\nabla P \tag{2.18}$$

where,

$\frac{D()}{Dt}$ = total derivative; and
∇P = pressure differential $\left(\frac{\partial P}{\partial x}i + \frac{\partial P}{\partial y}j + \frac{\partial P}{\partial z}k\right)$.

from which the wave equation is derived,

$$\frac{1}{c^2}\frac{\partial^2 P}{\partial t^2} = \nabla^2 P \tag{2.19}$$

D'Alembert's solution to Eqn 2.19 approximates the incident and scattered pressures resulting from a propagating wave[23].

Conservation of energy – the net work done by pressure is equal to the increase in kinetic and potential energy per unit mass giving,

$$\rho \frac{dE_1}{dt} = \frac{P}{\rho} \frac{d\rho}{dt} \tag{2.20}$$

From these the changes in internal energy per unit mass, i.e., thermal and chemical energy, can be related to pressure and density using Eqn 2.20 to give,

$$\frac{dP}{d\rho} = \frac{\frac{P}{\rho^2} - \frac{\partial E}{\partial \rho}}{\frac{\partial E}{\partial P}} \tag{2.21}$$

The fundamental equations on which CFD codes are built are the approximate solutions to these equations for ideal incompressible fluids, assuming negligible changes in density, salinity and temperature. Usually an Eulerian approach is adopted for the solution to problems involving fluid flow. They are often used in conjunction with equations of state to incorporate compressibility.

2.6.2 Structural dynamics

CSD codes provide approximate solutions to structural dynamics. Structural response to a dynamic force can be defined in terms of mass, acceleration and displacement using,

$$M\ddot{x}(t) + C\dot{x}(t) + Kx(t) = f(t) \tag{2.22}$$

where M and C are the mass and damping matrices respectively, K represents the stiffness matrix, $f(t)$ represents the external forces, x is the displacement vector (temporal derivatives indicated by dots) and t is time. These are often combined with equations relating to constitutive behaviour for stress-strain relationships, virtual work for conservation of energy, and damping. Many analytical benchmark problems relating to UNDEX loading are reported elsewhere[19].

2.7 Finite element approach to UNDEX

Although CFD and CSD codes are capable of performing the task for which they were written, they often require expansion for application to other areas. Out of expansion of these codes developed more general purpose codes combining features from both CFD and CSD with existing finite element codes, producing codes capable of simulating wave propagation in multi-material, compressible, transient, continuum mechanics and elastic/plastic behaviour. Such codes are known as hydrocodes[24]. In using hydrocodes to model fast transient dynamic events, in particular, the sequence of events in an underwater explosion, it is necessary to appreciate the limitations of the methodologies used and possible sources of error prior to verifying and validating the code's capabilities. It is assumed that the reader is familiar with the finite element (FE) method in engineering. A discussion of the mathematical formulations of FE is outside the interest of this work, however related texts can be found elsewhere[25,26]. A brief introduction to six forms of hydrocode currently available is given below. A more detailed overview of hydrocodes has been reported elsewhere[27,28].

2.7.1 Lagrangian

Node positions are fixed to the material and elements deform as the material moves. In so doing there is the ability to keep an accurate history of events. Boundary conditions are easily defined and material interfaces are easy to determine. However, mesh distortion limits the code's practical use for fluid flow and large distortion problems, e.g., bubble pulses. Published work utilising this approach is reported elsewhere[19].

2.7.2 Free Lagrange Method (FLM)

The accuracy of the Lagrangian technique has been implemented into codes which allow the connectivity of the mesh to alter with movement of the material. Element connectivity is redefined throughout the calculation allowing large distortion problems to be solved using Lagrangian methods.

2.7.3 Smoothed Particle Hydrodynamics (SPH)

SPH is a meshless Lagrangian technique benefiting from the accuracy associated with Lagrangian tracking methods but not suffering from the large distortion problems. Individual particles have associated material properties and thicknesses and movement

is arbitrary, i.e. non-physical. Particles are not rigidly connected as in FE codes. SPH codes are often coupled to fully Lagrangian finite element codes to take advantage of the well established Lagrangian shell formulations. This method is attractive for fluid-structure interaction problems such as UNDEX using Lagrangian particles for fluid and charge, and Lagrangian shells for structural elements. More detailed descriptions of this approach can be found elsewhere[29].

2.7.4 Eulerian

Node positions are fixed in space and material is permitted to flow through elements quantifying mass, energy, pressure, momentum and velocity, as it flows. Very capable of solving large distortion problems in continuum dynamics. Recent development of multi-material Eulerian hydrocodes (more than one material per element) improved its capabilities, particularly in modelling UNDEX phenomena as mixing of materials overcame material boundary interface problems at early time in the analysis. However at later times the boundary interfaces are known to suffer from diffusion, where the analysis is no longer able to track the material boundary accurately. This presents problems when modelling bubble behaviour and collapse. Difficulties also occur when modelling dynamic response of thin plate structures due to smearing of solid properties when mixed with fluid cells[30]. This smearing also causes loss of data relating to mass and momentum transfer thereby reducing the accuracy of the solution. Examples of the Eulerian approach used for UNDEX simulations have been published[31].

2.7.5 Coupled Eulerian-Lagrangian (CEL)

CEL is a combination of the Eulerian method for modelling fluid behaviour and the Lagrangian method for modelling structural response with information being passed between the two using a coupling module. Interface elements coincident with the structure determine the volume of fluid in a cell. Since structures are not commonly flat small volumes often get created which require 'blending' with neighbouring cells to avoid severe time step reductions. Difficulties arise in complex structural geometry where fluid is seen by both sides of a structural element. This non-physical condition of two separated fluid regions within one Eulerian cell makes application of this code limited, however, codes incorporating this approach have been used for FSI problems[32–35].

2.7.6 Arbitrary Lagrangian-Eulerian (ALE)

The Eulerian mesh principle applied to a Lagrangian mesh. Each timestep, Lagrangian motion of the mesh is followed by a remap, or advection step, in which the spatial mesh is either rezoned to its original shape, smoothed to a more advantageous shape or not smoothed at all. This way the mesh is neither restricted to following material motion nor remaining fixed in space. This control on arbitrary mesh distortion within Eulerian and Lagrangian formulations renders this as the ALE formulation. No separate coupling module is required and the rezoning step is computationally inexpensive compared to the cost of transporting material and history variables. The complex structural geometry mentioned in CEL is also difficult to model with this technology. A more detailed description of this approach can be found elsewhere[28,36]. Examples of ALE hydrocodes used for UNDEX simulations are widely available[19,37,38].

2.8 Boundary element approach to UNDEX

The applicability of hydrocode approaches to UNDEX-FSI problems is overshadowed by the inherent cost, particularly of three dimensional models. Alternative approaches based on approximate integral solutions of wet surface response variables have been developed.

Analytical solutions were initially solved using approximate methods such as the plane wave and virtual mass approximations (PWA & VMA) based on Kirchoff's retarded potential formulation. Both of these approaches were combined[39–41] to form doubly asymptotic approximations (DAA). The approach was incorporated into first order (DAA_1) and second order (DAA_2) accurate boundary elements which represent the acoustic medium surrounding a structure as a membrane covering the wet surface. The principal advantage of the DAA approach over the hydrocode approach is that it simulates the fluid-structure interaction in terms of wet surface response variables only, eliminating the need for fluid volume elements around the outside of the structure. The DAA elements serve two purposes in controlling the pressure at the boundary: to conserve fluid mass flow at the mesh boundary and to simulate a non-reflecting boundary, preventing reflections interfering with structural response.

DAAs are so named due to being asymptotically exact for both high and low frequency, i.e. early and late time fluid responses and, DAA_2 in particular, transitions smoothly through the intermediate frequency range. Differential equations calculate the scattered pressures resulting from the structural response to an incident pressure wave assuming

irrotational flow in an infinite, inviscid and incompressible fluid. The force on a structure, $f(t)$ (Eqn 2.22), excited by an acoustic wave is given by,

$$f(t) = -G[A_f](P_I + P_S) + f_d \tag{2.23}$$

where,

P_I, P_S = incident and scattered pressure vectors,
$[A_f]$ = diagonal matrix containing areas of elements representing the wet surface,
$[G]$ = transformation matrix relating fluid and structural forces,
f_d = applied force vector for the dry structure.

The scattered pressures are calculated from the DAA equations which include the plane wave approximation for high frequency responses, and the virtual mass approximation for low frequency responses. In basic form (DAA_1) relates the scattered pressure to the scattered acceleration.

$$M_f \dot{P}_S + \rho c[A_f]P_S = \rho c M_f \ddot{u}_S \tag{2.24}$$

where,

M_f = fluid mass matrix;
$\dot{P}_S$ = first temporal derivative of scattered pressure;
ρ = density of fluid; and
$\ddot{u}_S$ = normal scattered acceleration vector.

Eqn 2.24 approaches exactness for early- and late-time responses but gives a poor prediction for the intermediate frequency range. Also DAA_1 is only first order accurate. Under excitation by an acoustic wave the scattered displacement, u_S is related to the structural response by the assumption that the unknown normal scattered velocity vectors are assumed equal to the known normal structural velocity vectors at the wet surface of the structure. From this assumption the compatibility relation between the structural response and fluid response is given as,

$$G^T \dot{x} = \dot{u}_I + \dot{u}_S \tag{2.25}$$

where,

G^T = transpose of transformation matrix linking fluid and structural forces;
$\dot{u}_I$ = normal incident velocity vector;
$\dot{x}$ = normal structural velocity vector on wet surface of structure; and
Ω_f = accuracy factor[42], s^{-1}.

The more advanced second order accurate DAA_2 is written as,

$$M_f\ddot{P}_S + \rho c[A_f]\dot{P}_S + \rho c\Omega_f[A_f]P_S = \rho c M_f[(G^T\ddot{x} - \ddot{u}_I) + \Omega_f(G^T\dot{x} - \dot{u}_I)] \qquad (2.26)$$

where,

$\ddot{P}_S$ = second temporal derivative of scattered pressure; and
$\ddot{u}_I$ = normal incident acceleration vector, ms^{-2}.

Eqns 2.23 is solved in combination with either Eqn 2.24 or Eqn 2.26 in the time domain to mathematically describe fluid-structure interaction. For an infinite fluid domain the fluid response is assumed linear and the boundary elements are coincident with the structure controlling the total pressure at the boundary. This technique will be referred to as DAA for the remainder of the thesis. These boundary elements are single degrees of freedom pressure elements. Their low cost is counteracted by the associated costs of forming the fluid matrices.

DAAs are known to experience problems solving concave bodies involving high frequency response, and since they only account for acoustic wave propagation they are not appropriate for close stand off distances. Recent enhancements to the DAA approach include modelling non-linear fluid effects such as cavitation using acoustic elements, bubble loading, taking account of fluid displacements, and internal fluid volumes[43]. Further literature and applications of the DAA approach can be found elsewhere[44–49].

Limitations on computing resources eventually placed restrictions on the range of problems that could be analysed. But the more recent advent of high performance computers has increased the applicability of FE and BE methods to more complex fluid and structural related problems. A compilation of computer software available for shock and vibration analysis is available from SAVIAC[50]. Also a good FE and BE bibliographical database has been constructed for a variety of problems involving FSI by Mackerle[51].

2.9 Analysis software

The analysis packages used throughout this work are LS-DYNA and USA-DYNA3D. Brief descriptions of the features of LS-DYNA and USA-DYNA3D used in this project for UNDEX-FSI are discussed below.

Both the FE and BE methods are available for modelling UNDEX phenomena within LS-DYNA and USA-DYNA3D respectively. LS-DYNA provides the ALE formulation and USA-DYNA3D provides the DAA boundary element technique. For a mathematical description of these techniques user[52] and theory[53] manuals should be consulted.

2.9.1 LS-DYNA

LS-DYNA is a general purpose, non-linear, explicit three dimensional finite element analysis code for predicting large deformation response of elastic and inelastic solids and structures. It is under continuous development at Livermore Software Technology Corporation (LSTC) and supported, amongst others, by Ove Arup & Partners (OASYS Ltd). Based on the original DYNA3D program written for contact-impact simulations, the range of applications has grown steadily as the employment of advanced algorithms, material descriptions and element formulations expanded its numerical proficiency and capabilities. More recently the implementation of hydrocode methodology extended its application to the fields of continuum mechanics, e.g. soil-structure and fluid-structure interaction problems.

ALE formulation

Within LS-DYNA the Eulerian formulation has been implemented to assist in problems involving fluid flow. For problems involving fluid-structure interaction the Eulerian and Lagrangian formulations are combined with coupling techniques to provide an ALE formulation. The range of problems that can be solved with ALE formulations is related to the number of materials permitted per element and the accuracy of the algorithms used for smoothing the mesh and transporting the material through the mesh. Two ALE formulations are currently available within LS-DYNA.

1. **Single material ALE (SALE)** – one material per element forces material boundaries between two advecting materials to be modelled as Lagrangian preventing flow across material interfaces, e.g. bubble expansion into surrounding

fluid. This formulation will ultimately cause mesh breakdown if the bubble is allowed to collapse in on itself since Lagrangian interface elements are not capable of collapse.

2. **Multi-material ALE (MMALE)** – at the time of writing three materials are permitted per element. This formulation overcomes the inherent problem within SALE. The material interfaces are modelled as Eulerian boundaries and hence the mesh is permitted to remain fixed in space making the numerical study of such problems as bubble collapse more feasible.

Coupling techniques

When two media such as fluid and a structure are interacting they transfer loads between each other. If these two media are described by Eulerian and Lagrangian formulations respectively, then interaction requires the use of coupling techniques. Two coupling techniques are available in LS-DYNA.

1. **general coupling** – the structure can be positioned in the fluid without the need to align nodes. The coupling surface is found automatically using a search algorithm over a designated area (bucket search). Using this technique no distortion of the Eulerian mesh takes place. Searching for the coupling surface contributes significantly to computational cost.

2. **ALE coupling** – fluid and structural nodes are coincident hence the material boundary of the fluid next to the structure is purely Lagrangian and nodes at this interface move at all times according to Lagrangian motion. This imposes restrictions on the form of the fluid mesh making it more complex to construct than in the general coupling technique.

ALE smoothing

Using the ALE coupling method it is clear that for problems undergoing severe deformation, or failure, the layer of elements at the fluid-structure interface will become distorted. A distorted mesh will cause the timestep to diminish and the calculation may even terminate should the Eulerian mesh become tangled. Under these circumstances, in order for the calculation to continue, smoothing is applied to spread the deformation throughout the Eulerian mesh corresponding to the amount of Lagrangian deformation. This smoothing may also be termed as a relaxation of the Eulerian mesh.

A global form of smoothing is available in LS-DYNA which keeps nodes in a straight line between two other nodes. More complex local relaxation techniques have been implemented to assist in the simulation of large deformation problems. These are discussed elsewhere[53]. Although representing only a small part of an entire ALE timestep, these smoothing adjustments can be restricted to specific regions of the mesh to reduce the time spent smoothing. Much more time is spent on transporting material through the mesh.

Advection

Several advection schemes exist for the transport of materials defined with a material model and equation of state. The cost of an advection step is associated with the transport of element centred variables, such as density, internal energy, shock viscosity and history variables requested from each element, and node centred velocities, transported and combined with the element centred density in order to conserve momentum. All these variables are transported using flux, mass or volume. Compared to a Lagrangian timestep, an advection step is usually two to five times more expensive.

The algorithms for advecting flux, mass or volume, seek to conserve mass, momentum and energy while maintaining monotonicity, stability and numerical accuracy. In three dimensions the advection is performed isotropically with transport occurring through each coincident face but not diagonally. Separate algorithms have been implemented for momentum transport since this is dependent on the velocities which are node centred variables rather than element centred. Consequently there are four combinations of advection algorithms available in LS-DYNA which vary in cost effectiveness and accuracy.

1. **Donor cell** – a first order accurate Godunov method assuming distribution of variables is constant over an element face. Both element centred and node-centred variables are advected. Very cost effective but generates dispersion errors.

2. **Van Leer & half index shift (HIS)** – a second order accurate Godunov method assuming a linear distribution of variables over an element face. Van Leer's monotone upwind scheme for conservation laws (MUSCL) algorithm is used to transport element centred variables and Benson's HIS algorithm is a modified first order staggered mesh algorithm for momentum transport[54].

3. **Van Leer** – second order accurate version of (2) but without separate momentum transport algorithm.

4. **Donor cell & HIS** – as (1) with separate momentum transport.

Treatment of shock waves

In reality the thickness of the shock front depends on the shock strength, approaching zero for strong shocks and infinity for weak shocks. In fluids it is nominally of the order of 10^{-4}-10^{-5}mm[27]. The finite element method is limited in analysing particular shock front characteristics as resolving this thickness with sufficiently small element sizes would prove computationally very expensive. Hence a technique of thickening the shock front was devised based on the discovery that quantities, such as pressure and density, within the shock front are found to vary smoothly when viscosity is taken into account. Artificial bulk viscosity was introduced to smear the shock front over several elements hence allowing the propagation of the shock front to be tracked using finite element methods at a cheaper cost[28]. Within LS-DYNA the term was added to the conservation of momentum and energy equations. It includes both a quadratic term and a linear term to dampen numerical oscillations occurring once the shock front has passed. For three dimensional simulations the artificial bulk viscosity, q, is given as,

$$q = \begin{cases} 0 & \text{if } \dot{\varepsilon}_{kk} \geq 0 \\ \rho \sqrt[3]{V} \left(C_0 \sqrt[3]{V} \dot{\varepsilon}_{kk}^2 - C_1 c \dot{\varepsilon}_{kk} \right) & \text{if } \dot{\varepsilon}_{kk} < 0 \end{cases} \tag{2.27}$$

where,

C_0 & C_1 = dimensionless constants;
$\dot{\varepsilon}_{kk}$ = strain rate tensor, s^{-1}; and
V = volume, m^3.

One limitation associated with artificial bulk viscosity occurs when the aspect ratio of elements, i.e., ratio of linear dimensions, is poor (> 5). The use of the characteristic length for such elements can result in anomalous values for q and numerical instability. Also the choice of values for the constants C_0 and C_1 control the number of elements over which the shock front is smeared and the degree of oscillations behind the front. The default values of 1.5 and 0.06 were used throughout this work.

Element library

A large range of shell elements are available with varying degrees of complexity and cost effectiveness. Hexahedral solid elements are used for modelling fluid domains in three dimensions. Eulerian elements are used mainly for fluid flow although Lagrangian acoustic elements are also available for acoustic propagation problems. For a more detailed list of the element library the reader is referred to the input manual[55].

Boundaries

Advection seeks to conserve mass, momentum and energy in the transport of variables through a finite element mesh. However at mesh boundaries there is nowhere to transport the variables to. Consequently the boundary conditions declared determine what happens numerically to the variables being transported. Three types of boundaries can be defined within LS-DYNA for ALE or Eulerian meshes.

An Euler boundary condition option is available in the ALE control card input which controls velocity conditions at Eulerian and ALE mesh boundaries. The slip condition applies to problems where the normal velocity of the material at the boundary is zero, e.g., a rigid boundary. The stick condition forces the material velocities at a boundary to be zero in all directions. These boundary segments ensure conservation of mass throughout the mesh.

The non-reflecting boundary option is used at the exterior of a semi-infinite domain, such as fluid, to prevent numerical reflections generated at the boundary from interfering with results. LS-DYNA computes an impedance matching function at each boundary segment based on the assumption of linear material behaviour. Should any non-linear behaviour be significant to a model, e.g., cavitation, it must be contained within the model. Mass flow is not conserved with this boundary option, hence, any reversal of material flow, such as during bubble contraction, cannot be simulated with this option.

Nodal point constraints can be assigned at the nodes of Eulerian elements to control the flow of material through the element. Each node can have up to six degrees of freedom (DOF): x, y and z translation, and rotation about the x, y and z axes. The constraint of any of these degrees of freedom will stop flow occurring in the DOF direction. For example, to model a reflecting boundary using nodal point constraints, all six DOF would be constrained, or, to model symmetry in the x, y plane, a node would be constrained from translation in the z direction and from rotation about the

x and y axes.

Timestep control

The timestep in LS-DYNA is controlled either automatically (explicit time integration scheme) or by specifying a timestep-time curve. Automatic timestep control calculates the largest timestep which will not invoke numerical instability, is governed by the shortest element dimension, ignoring shell thicknesses and beam elements, and is updated every timestep. Hence if deformation of an element occurs during an analysis, such that the element lengths increase or decrease, the timestep will increase or decrease as a result. The timestep is estimated using the Courant condition.

$$\Delta t = t_{SF}\frac{l_e}{c} \tag{2.28}$$

where,

l_e = shortest element length, mm;
c = speed of sound, $\sqrt{\frac{E}{\rho}}$, ms^{-1}; and
t_{SF} = scale factor.

Other governing lengths can be used instead, e.g., volume to area ratio. From Eqn 2.28 several factors are seen to influence the size of the timestep, namely the scale factor and the density of material used in the model. The value of t_{SF} defaults to a maximum of 0.9, but a lower value will reduce the automatically calculated timestep. For shock wave problems a value of 0.67 is recommended to make the analysis more stable. A value of 0.7 was used throughout this work. The higher the material density in a model, the higher the sound speed and hence the element lengths for materials of high density should be as large as possible to avoid its degree of control on the timestep calculation. In an UNDEX simulation the structural material ultimately controls the timestep as usually it has the highest density. Initially the charge has the highest density, however this rapidly reduces after detonation due to formation of the gaseous products.

The cost of the ALE timestep is governed by further parameters. It depends on the element formulations and material models used. Using hexahedron elements designates four boundary nodes for every element onto a Lagrange boundary and eight nodes per element for every interior element. The degree of motion of the four Lagrange nodes determines the degree of smoothing of the interior nodes. The tasks involved in an ALE timestep can be summarised as follows.

1. Perform a Lagrange timestep (mesh moves with material).
2. On Eulerian regions restore mesh to original co-ordinates.
3. On ALE regions perform an advection step
   (a) move boundary nodes (purely Lagrangian),
   (b) move interior nodes (specified regions whose boundaries are Lagrangian)
   (c) transport element-centred variables, and
   (d) transport momentum and update velocity.

Ultimately the cost of a simulation is dependent on the computing resources available. Unless otherwise stated, all CPU times reported in this work are based on models executed on a 180MHz SGI Origin 200 machine with an R10000 processor, 512Mb RAM, 32Kb primary cache and 1Mb secondary cache.

Material models

A constitutive equation relates stress in a material with the degree of distortion (strain) required to produce this stress (including strain rate effects, material hardening, thermal softening, etc.). Numerous material models are available in LS-DYNA which account for linear and non-linear material behaviour[55].

Materials such as explosives and fluids are represented as material models combined with equations of state which relate volume (or density) and internal energy (or temperature) with pressure. The increase in internal energy of the products must be the sum of the chemical energy Q released by the reaction and the work done by the pressure at the detonation front. A knowledge of the energy per unit mass, E, the energy release, Q, and the equation of state provides sufficient information to solve the detonation front equation.

2.9.2 Underwater Shock Analysis (USA)

The boundary element method applied to UNDEX is an alternative approach to the FSI analysis capabilities of LS-DYNA, and is accommodated by the coupling of the USA code[21]. USA calculates the transient linear response of a submerged structure and surrounding fluid to a spherical shock wave using the DAA approach. The coupling to LS-DYNA permitted non-linear structural behaviour capabilities to replace the linear restrictions of the USA code[56]. The USA code has been successfully validated

against several fluid and structural non-linear problems involving the response of submerged imperfect cylindrical shells[57], inelastic infinite cylindrical shells subject to step exponential plane waves and fluid cavitation, and also the interaction of two submerged shells[58]. The DAA approach has also been used to design low and high severity UNDEX experiments against flat plates[59].

The DAA_1 and DAA_2 techniques are both available for infinite fluid domains (DAA) in which the fluid is treated as linear. However, this formulation limits the cavitation representation to wet surfaces of structures. The complexity of simulating cavitation and shock wave diffraction occurring close to structures has been simplified by linking the acoustic element available in LS-DYNA. The DAA_1 equations were modified to act as a radiating boundary which was combined with the use of the acoustic elements to represent a semi-infinite region of fluid surrounding the structure[60], thus providing a bilinear fluid modelling capability. The acoustic elements allow the development of separation and subsequent closure phenomena that can occur between fluid and structure. They are single degrees of freedom solid elements and consequently are inexpensive. The DAA boundary elements are placed at the outer limits of the semi-infinite acoustic domain. This technique will be referred to as DAA-MAT90 for the remainder of the thesis.

This boundary element approach has the distinct advantage that the explosion source and, in simplified cases, the fluid domain, do not have to be modelled. An arbitrary pressure loading profile, representative of shock and/or bubble loading is used to apply the free field load. When calculating pressures at various points on a structure, the DAA technique uses direct line of sight from the position of the charge to the position where pressure is being applied. The DAA-MAT90 technique accounts for diffraction around a structure using the acoustic elements to allow tracking of the shock wave, a more qualitative representation of the loading at a point on a structure.

2.10 Pre- and post-processing software

For some analysis codes the finite element models are processed by external programs known as a pre-processors and post-processors. Several programs were utilised in this work to assist in the construction of suitable finite element models for analysis with LS-DYNA and USA-DYNA3D and to ensure adequate visualisation and understanding of the results. All pre- and post-processing was performed using a 150MHz SGI Indigo Extreme with an R4400 processor and 320Mb RAM.

2.10.1 HyperMesh

HyperMesh[61] is an interactive pre- and post-processor developed at Altair Engineering Inc. Geometric models or previously generated finite element models can be imported from concurrent engineering applications and external analysis codes, and meshed or processed accordingly.

For pre-processing a HyperMesh database is created comprising component collectors for different regions of a model into which geometry, materials, elements, loads and boundary constraints are assigned. Structured meshes comprising shell and solid elements can be automatically generated from surface geometry. Automatic mesh generation is currently only available for tetra solid elements. Hexahedral solid elements are constructed using appropriate node configurations or the extrusion of shell elements to another surface.

The post-processing capabilities offered by HyperMesh were rejected in favour of the facilities that come with LS-DYNA. The results from an LS-DYNA analysis require translation before being processed by HyperMesh which proved to be time consuming and required substantial storage space on top of the analysis results. The post-processing applications with LS-DYNA results are described in more detail below.

2.10.2 TrueGrid

TrueGrid[62] is an interactive general purpose pre-processor developed at XYZ Scientific Applications Inc. A geometric model can be tessellated into a multiple block structured mesh or grid. The mesh can comprise hexahedral brick or quadrilateral shell elements.

A predefined regular block of elements divided into one or more regions is manipulated to roughly fit the geometry of the model. The projection method is then used which allows faces, edges and nodes of a mesh to be directly moulded around surfaces, and edges and nodes of a mesh to be fitted along curves. The curves and surfaces can be created within TrueGrid or imported from a CAD/CAM system via an IGES file. Support is also included for various element types including beams, springs and lumped masses. Prescribed boundary conditions and constraints can also be applied to specific regions of the mesh.

This tool is ideal for the fast generation of a regular solid mesh around a structure, such as is required in fluid-structure interaction problems.

2.10.3 LS-TAURUS/Oasys D3PLOT and THIS

The results from an analysis performed using LS-DYNA or USA-DYNA3D can include both ASCII data and binary output if requested. To access this information LS-TAURUS and the OASYS post-processing suite were utilised. These were provided by LSTC and OASYS Limited respectively[63,64].

These post-processors offer capabilities for visualising results as continuous contour, line contour or vector plots on the finite element model or the viewing of $x - y$ data and subsequent output to file. From the binary output it is also possible to generate animated sequences which greatly improve the understanding of dynamic responses.

Figures representing individual frames of animations have been included in the presentation of results. However, movie sequences have been saved and can be obtained from the author on request.

2.11 Concluding remarks

In recent years the development of UNDEX research has moved away from expensive experimental testing and become more reliant on numerical techniques. Continued development and improvement of these numerical approaches to such a complex problem is being actively encouraged and supported due to the financial benefits and the possible improvements to structural designs.

Nonetheless predictions of structural response must be substantiated experimentally and empirically prior to numerical approaches being utilised in the design of structures subject to UNDEX loads. This verification procedure is a vital part of the development process of codes like LS-DYNA and USA-DYNA3D.

In the design of an echinodome for storing LNG it is necessary to consider the event of rupture and subsequent UNDEX loading to which neighbouring echinodomes may be subjected. As results from previous numerical approaches were unsatisfactory, alternative approaches were sought. The multi-material ALE and DAA approaches available in USA-DYNA3D are thought to offer an improved representation of the physics involved in such an event.

The remainder of this thesis is devoted to an examination of the ability of LS-DYNA and USA-DYNA3D to model UNDEX loading on the echinodome and predict both the fluid and structural response satisfactorily. Subsequently, the use of such techniques to predict dynamic buckling criteria will be assessed.

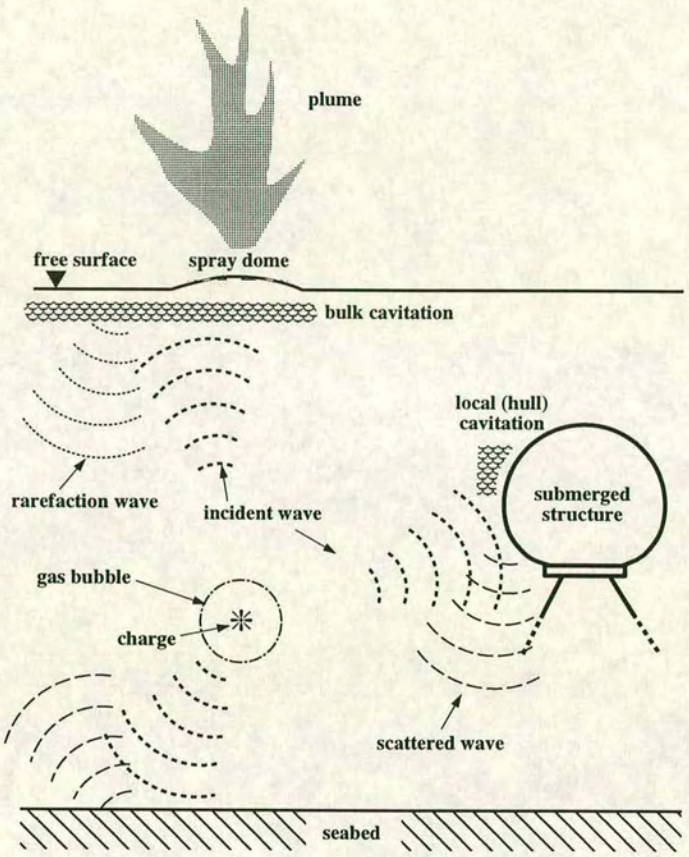

Figure 2.1: UNDEX phenomena in the vicinity of a structure

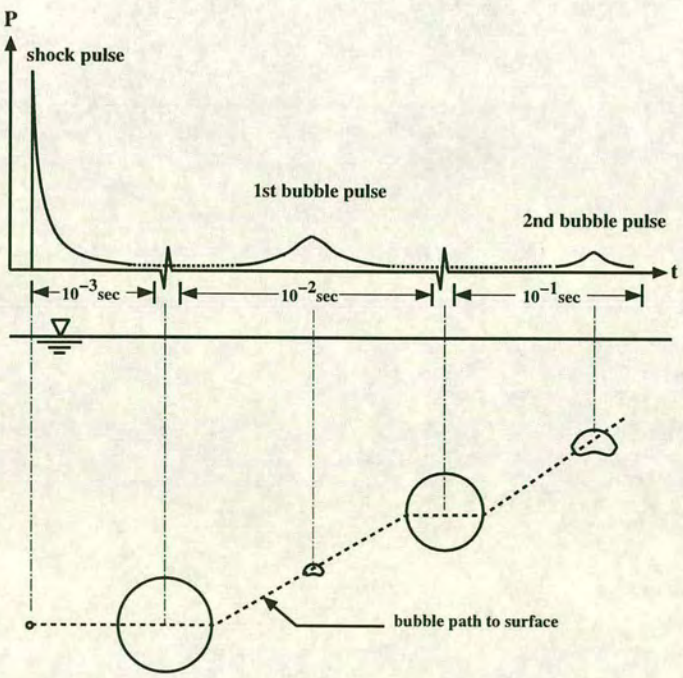

Figure 2.2: Sketch of typical free field pressure-time history and bubble pulses[16]

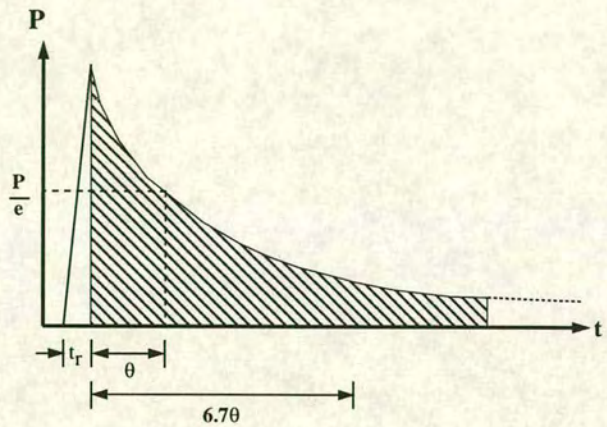

Figure 2.3: Area integrated under pressure-time curve for shock impulse

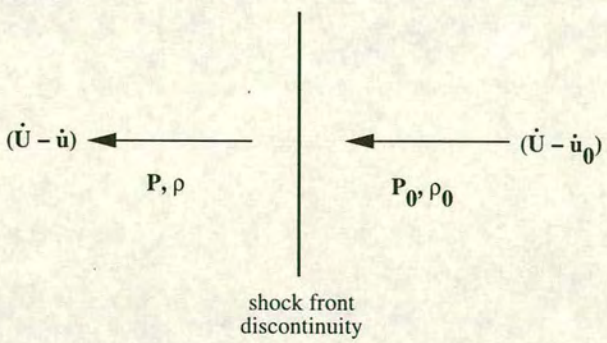

Figure 2.4: Conditions at shock front

Chapter 3

Numerical simulation of free field UNDEX and static structural response

3.1 Introduction

The preceding chapter introduced the sequence of events characteristic of an underwater explosion. Background to numerical methods used to simulate such events was given and the hydrocode LS-DYNA and BE code USA-DYNA3D were introduced as being the software used in this work to model UNDEX loading.

In a complex submerged structural system the prediction of fluid and structural responses to an UNDEX event requires confidence in the hydrocode to accurately represent the physics of such events. The physics taking place can be characterised into isolated processes, according to which stage of the event is under consideration. Several such studies have been performed using earlier versions of LS-DYNA, and other hydrocodes, with moderate degrees of success. These studies were limited very often to the numerical techniques available at the time. Recent advancements in hydrocode methodology and more realistic mathematical descriptions have extended the capabilities of hydrocodes to more complex problems.

The objective of this chapter is to use LS-DYNA to successfully model each of the processes involved in a free field UNDEX event prior to simulating the more complex UNDEX-FSI problem in the following chapter. The simulations examine detonation, shock wave propagation, free field fluid response and bubble behaviour. Alongside

this, validation of a suitable discretisation for modelling the prototype echinodome is pursued using results from earlier static loading analyses.

The aim of these preliminary simulations is to assess LS-DYNA's dynamic analysis capabilities, and limitations, for modelling fluid and structural behaviour, and assess necessary considerations in constructing suitable finite element models for future UNDEX-FSI problems.

3.2 Isolation of UNDEX phenomena

Using benchmark example problems[65] the fundamental processes of an underwater explosion, namely detonation and shock wave propagation, were initially modelled as isolated phenomena. These models provided an early assessment of LS-DYNA's ability to model such physical phenomena using the Eulerian approach and gave confidence in constructing a free field UNDEX model.

3.2.1 Steady state detonation

The purpose of this model was to simulate the detonation of solid explosive material, the propagation of a plane wave igniting the material and examination of conditions after ignition of all the material. Conditions within the explosive are known from theoretical predictions of pressures and experimental observations permitting a comparison with a numerical model. It is important for this process to be modelled accurately, since the pressure in the fluid at the shock wave front is a direct consequence of the detonation process.

A quasi-one dimensional mesh of 200 solid single material Eulerian elements was used to represent a slab of explosive, 0.01×0.01×0.5m, shown in Fig. 3.1 entailing an element thickness of 0.0025m.

The explosive material used in this analysis was EDC-1. The explosive material was modelled using the material card *MAT_HIGH_EXPLOSIVE_BURN[55] in conjunction with the Jones-Wilkins-Lee (JWL) equation of state (Eqn 3.1)[55]. This equation of state relates the pressure in the exploded part of the explosive material to the specific internal energy per unit volume using the exponential relationship given in Eqn 3.1.

$$P = A\left((1-\frac{\omega}{R_1V})e^{-R_1V} + B(1-\frac{\omega}{R_2V})e^{-R_2V}\right) + \frac{\omega E_1}{V} \tag{3.1}$$

Symbol	Property	EDC-1 value
ρ_o	density	1795 kgm^{-3}
D	detonation velocity	8716 ms^{-1}
P_{cj}	Chapman-Jouget	34.25×10^9 Pa
A	material constant	9.036×10^{11} Pa
B	"	9.033×10^9 Pa
R_1	"	4.647
R_2	"	0.8717
ω	"	0.275
E_0	initial internal energy	1.050×10^{10} Jkg^{-1}
V_0	initial relative volume	1.0

Table 3.1: Properties and JWL constants of explosive material EDC-1[17]

where $E_1 = \frac{E_o}{\rho}$ and V represents the volume of exploded material. The remaining material properties and JWL constants for Eqn 3.1 are presented in table 3.1. The gaseous products were assumed to behave as a γ-law gas for which the theoretical Chapman-Jouget pressure, P_{cj} is given by,

$$P_{cj} = 2(\gamma_{cj} - 1)E_o \tag{3.2}$$

where γ_{cj} is the Chapman-Jouget gamma. This gives a theoretical value for P_{cj} of 37.4×10^9Pa, which compares well with the experimentally established value[17] of 34.25×10^9MPa. The experimental P_{cj} was used in this model.

The ignition point is the centre of the left face of the mesh, as shown in Fig. 3.1, and the ignition time is $t = 0$. Upon ignition, the lighting time is computed for each element by dividing the distance from the detonation point to the centre of the element by the detonation velocity[53]. A 'programmed + burn' algorithm is used in LS-DYNA to model the propagation of the detonation wave through the explosive material. 'Burn fractions' multiply the pressure given by the equation of state to control the release of chemical energy over the lighting time for each element as the detonation front propagates. Once the detonation wave has propagated through the entire volume of explosive material the pressure and energy associated with the detonated products is known.

A 'no flow' boundary was declared perpendicular to all sides of the mesh and a 'flow' boundary declared longitudinally along the slab length. These boundary conditions and the one dimensional nature of the mesh ensured plane wave propagation throughout

the analysis.

The duration of the analysis was 60μs, the time required for the detonation wave to travel the length of slab at the detonation velocity (given in table 3.1). Output was requested every microsecond.

Results

The propagation of the detonation wave is illustrated in Fig. 3.2. The detonation front is well defined and the wave is observed to propagate the entire length of the slab. When the finite element mesh is overlaid, the detonation front is noticeably smeared over several elements.

Fig. 3.3 shows the peak pressure profiles behind the detonation front at various distances along the slab length compared with the theoretical and experimental Chapman-Jouget pressures. The code requires about 70 elements to build up the majority of the pressure in the detonation front at which time the pressure is equal to 90% of the experimental P_{cj}. As the detonation wave continues to propagate through the explosive material the rate of pressure increase reduces, converging to a final value of 31.57×10^9Pa, 92% of the experimental P_{cj}. Adiabatic conditions behind the detonation front are illustrated by the exponential decay to a pressure of 9.33×10^9Pa, representing the internal pressure of the explosive gases.

The underestimate of the predicted P_{cj} is attributed to two factors. Firstly, the Eulerian elements used were first order accurate. This explains the smearing of the detonation front observed which results in a reduction in peak pressure. Secondly, the JWL equation of state parameters are valid only for large charges[66]. The overall simulation of detonation is in good agreement with both experiment and theory.

3.2.2 Shock wave propagation

Shock tubes are used to observe the propagation of shock waves through gaseous mixtures in a similar manner to shock waves propagating through the water due to detonation of an explosive. An accurate trace of the velocities and peak pressures involved in this propagation process is necessary since, in the context of UNDEX, it is the shock wave which provides the initial loading on a structure and its magnitude is of considerable importance. The propagating wave in this model is simplified to a plane wave.

Quantity	High pressure gas	Low pressure gas
density, ρ	1.0 kgm^{-3}	0.125 kgm^{-3}
initial velocity, u_o	0	0
specific internal energy, E_o	2.5 Jkg^{-1}	0.25 Jkg^{-1}
pressure, P	1.0 Pa	0.1 Pa

Table 3.2: Initial conditions of shock tube gases

A shock tube comprises a rigid cylinder consisting of two gases separated by a gastight diaphragm. The shock tube is initialised by applying a pressure difference across the diaphragm. In this initial state there is a single discontinuity between the gases, as illustrated in Fig. 3.4. The high and low pressure regions either side of the diaphragm are referred to as the compression and expansion chambers respectively. When the diaphragm is ruptured the pressure in the shock tube equalises by means of a shock wave propagating into the expansion chamber and a rarefaction wave propagating into the compression chamber. In the region between the shock wave front and the rarefaction wave front the velocity and pressure are constant and a contact discontinuity resides at the original diaphragm location[67].

The following model examines the movement of a shock wave and a rarefaction wave along the length of a shock tube and compares velocity and pressure peak values against analytical values. The purpose of the model is to demonstrate low velocity shock wave propagation.

A shock tube 1.0m in length and 0.1m in diameter was represented by 6400 solid multi-material Eulerian brick elements Fig. 3.5. The two regions in the shock tube are filled with gases whose initial conditions are given in table 3.2. The gases were modelled using *MAT_NULL[55] in conjunction with the γ-law form of the linear polynomial equation of state[55],

$$P = (\gamma - 1)\frac{\rho}{\rho_o}E_1 \tag{3.3}$$

where,

γ = ratio of specific heats ($\gamma = 1.4$);
E = internal energy;
ρ_o = initial density; and
ρ = density after $t = 0$.

The gases are initialised at $t = 0$ and the boundary between them is a single discontinuity. At $t > 0$ the high pressure gas has a rarefaction front with velocity u_r moving into the compression chamber, and the low pressure gas has a shock front with velocity u_s moving into the expansion chamber.

All elements were declared with 'flow' conditions along the longitudinal axis of the shock tube only. Both ends of the mesh were declared with 'no flow' boundary conditions. The termination time for the analysis was 338ms.

Results

Fig. 3.6 shows the propagation of the shock and rarefaction waves along the length of the shock tube with the wave fronts clearly defined.

Examination of the pressure and velocity profiles along the shock tube reveals that the pressure and velocity are observed to rise more sharply within the shock wave front than within the rarefaction wave front. Pressure and velocity peak values along the length of the shock tube, presented in Figs 3.7 (a) and (b) correspond well with theoretical predictions for the times shown.

The numerically predicted peak value for the pressure at the point of contact discontinuity, P_{cd}, of 0.32Pa, compares reasonably well to the analytical value of 0.303Pa.[68–70] Similarly, the numerical peak value for the velocity at the point of contact discontinuity, u_{cd}, of 0.95ms^{-1} compares well with the analytical value[68–70] of 0.927ms^{-1}. The plateaux behind the peak values of pressure and velocity are closer to the analytical values.

Uncharacteristic overshoots and undershoots are observed in these plateaux which may be attributed to the advection scheme's difficulty in resolving a sharp change in solution between the region of contact discontinuity and either in front of or behind the region. However, the mean of these oscillations compares well with analytical results indicating accurate tracking of low velocity shock wave propagation.

3.3 Free field UNDEX

Early assessments of the predictive ability of the single material ALE technology implemented in LS-DYNA for free field UNDEX were undertaken with limited success[71,72]. These investigations involved the use of solid Lagrangian elements for the charge material, solid single material Eulerian elements for the fluid material beyond the maximum radius of the bubble and solid single material ALE elements for the fluid within the bubble expansion region. Encouraging predictions were reported to within 10% of experimental measurements. However such technology has been superseded with multi-material Eulerian elements and it is the capability of these elements that is being examined here.

From the previous two simulations confidence in LS-DYNA's ability to model detonation and shock wave propagation using Eulerian elements permitted the development of a free field UNDEX model. Theoretical pressure profiles at various stand off distances, obtained from peak pressures and decay rates measured experimentally[73] using 2kg of EDC-1, were available for comparison and assisted in the validation of the multi-material capabilities of LS-DYNA.

In constructing a suitable numerical model the first consideration is the charge shape since this will determine the geometric form of the charge and fluid meshes. The basic form of charge shapes are line, cylindrical or spherical. The above simulation of detonation (see section 3.2.1) was performed using a line charge. At distances close to the detonation of a line charge a conical shock wave will be produced. Experimentally this has been observed to produce an unequal pressure distribution around the charge after detonation. However, for line charges at depths greater than 100.0m this conical shock wave becomes spherical in nature, due to hydrostatic conditions, at large distances from the detonation point (greater than 10 $\times$ longest charge dimension).

Whilst obtaining a spherical shock wave is desirable for the purposes of generating equal load distribution, accurate prediction of the peak pressure is primarily the objective of these models.

3.3.1 Cube model

A spherical shock wave profile can be produced at distances close to the detonation point using a cylindrical charge whose height and diameter are equal, or a spherical charge.

In order to simplify the pre-processing of a 3-D model of a 2kg cylindrical charge, a cubic

charge was initially adopted because of its symmetrical form and simple connection to any fluid around it. Fig. 3.8 illustrates the mesh adopted to represent the free field model. The charge domain (height = 64.21mm) is shown in red, the fluid domain in blue.

In using such a charge shape symmetry was exploited, since theoretically, there should be an equal pressure distribution in all directions after detonation. This reduced both the amount of charge and fluid that needed to be modelled and consequently reduced the computation time required to run the model. Only one eighth of the cubic charge was modelled with a detonation point declared as a single point source at the centre of the charge, i.e., the corner of the mesh. The JWL equation of state combined with the *MAT_HIGH_EXPLOSIVE_BURN material model were used to represent the charge. After detonation, at time $t = 0$, the detonation wave was assumed to propagate equally in the x, y and z directions out to the perimeter of the charge. Hence symmetrical boundary conditions were declared on the three planes of symmetry, restricting flow perpendicular to the boundary, using single point constraints. These symmetry planes extended out into the fluid domain to a distance of 0.75m from the centre of the charge. This distance was limited due to the number of elements involved.

The water was modelled as suggested in the training manual[74] using the *MAT_NULL[55] material combined with the Gruneisen equation of state, Eqn 3.4[55], which defines pressure as,

$$P = \frac{\rho_o c^2 \mu \left[1 + \left(1 - \frac{\gamma_o}{2}\right)\mu - \frac{a}{2}\mu^2\right]}{\left[1 - (S_1 - 1)\mu - S_2 \frac{\mu^2}{\mu+1} - S_3 \frac{\mu^3}{\mu+1}\right]^2} + (\gamma_o + a\mu)E_1 \tag{3.4}$$

The properties and material constants for the water are listed in table 3.3. A total of 132621 solid multi-material Eulerian elements were used in the model, 125 to represent the explosive material and 132526 for the fluid domain. Using these elements permitted the explosive material to mix with the fluid material without the mesh boundary at the exterior of the charge deforming. Initially the default advection scheme (van Leer & HIS) was used. Gravity was not accounted for in this model using the standard density-depth curve approach because of the assumed symmetry conditions. However, an initial internal energy, equivalent to the hydrostatic pressure at the charge depth, was applied to the fluid material.

On the exterior boundary of the fluid a non-reflecting boundary was declared to represent an infinite fluid domain and preventing artificial stress wave reflections from

Symbol	Property	Water value
ρ_o	density	1000 kgm^{-3}
c	speed of sound	1484 ms^{-1}
S_1	material constant	1.979
S_2	"	0.0
S_3	"	0.0
γ_o	"	0.11
a	"	3.0
E_o	initial internal energy	3.072×10^5 Jkg^{-1}
V_o	initial relative volume	1.0

Table 3.3: Properties and Gruneisen constants of water[37]

coming back off the boundary and distorting the free field pressure-time responses. The model was run up to 1.0ms and output was requested every 100μs for binary output and every 1μs for ASCII output.

Results of cube model

The results, illustrated in Fig. 3.9, are compared with the profile fitted to experimental data. They indicate that the peak pressures at 0.25m and 0.5m are within $\pm 10\%$ of the experimental values. The oscillations in the decay of the predicted pressure profiles are uncharacteristic. Similar disturbances were also observed in the detonation example in section 3.2.1. These oscillations are numerically generated and are often termed overshoots and undershoots. They are caused by the advection scheme's attempt to simulate the instantaneous jump conditions at the shock front. The quadratic and linear bulk viscosity damping factors were included in the model by default to minimise the effect of these oscillations on the pressure profile.

The shock wave initially propagates in the same profile as the charge shape. At later time it quickly adopts a spherical form as propagation proceeds further into the fluid. Overall the predicted free field pressure-time history is in good agreement with the experimental results. The CPU time for this model was 0.716 hours.

3.3.2 Wedge model

In an attempt to improve on the results of the cube model a cylindrical charge shape was adopted with height/diameter ratio equal to one. One benefit of using cylindrical geometry for the charge is the saving on CPU time through exploiting the symmetry of the cylinder along the longitudinal axis. This was done using a 5^o wedge as illustrated in Fig. 3.10. The wedge, or penta, element is not included in the LS-DYNA element library. Instead LS-DYNA treats this element as a hexahedral element with one face collapsed. The wedge was orientated such that the longitudinal axis of the cylinder was coincident with the y-axis.

Detonation was declared to occur at a single point source, as used in the cubic model, with detonation occurring at time $t = 0$. Symmetry conditions were declared to restrict flow perpendicular to the 0^o and 5^o planes, permitting flow along the planes. Flow was also permitted along collapsed edge of the wedge. A non-reflecting boundary at the exterior of the fluid domain ensured no reflections interfered with the free field pressure-time histories.

38150 solid multi-material Eulerian elements were used in the model, with 30 elements representing the 2kg charge (radius = 64.21mm). Gravity was not included in the model. The fluid domain extended out to 2.0m from the centre of the charge. The same analysis time and output frequencies were used as for the cube model.

Results of wedge model

Contour plots from the wedge model are presented in Fig. 3.11. Three difficulties in using wedge elements for UNDEX simulations were highlighted by this model.

LS-DYNA interprets the collapsed face of the hexahedral elements as a face with a very small length and subsequently the timestep is controlled by these elements. Rather than the wedge model saving on CPU time the resulting timestep was of the order of 0.1μs. (compared to 3.7μs for the cube model). The resulting solution time (8.7 hours) was considered unreasonable for such a simple problem.

Although the model produces a spherical shock wave the pressure distribution along the wave front is not uniform. The density of the elements is the same in both the x and y directions however, from the shock wave contour plot (see Fig. 3.11(a)), higher pressures are evident along the collapsed edge.

The expansion of the bubble into the fluid also indicates an anomaly along the collapsed

edge making the bubble boundary non-spherical. Fig. 3.11(b) indicates that the material along the collapsed edge is advecting with a slower velocity than the rest of the explosive gases. In LS-DYNA the velocities are calculated at the nodes. The collapsed face of the solid elements may be causing the velocities to be calculated incorrectly.

From the above findings it was concluded that the wedge element could not be used with confidence for free field UNDEX simulations. Consultations with the authors of the code confirmed this error[75]. Consequently the predicted pressure-time responses were discarded.

3.3.3 Sphere model

As a second attempt to improve on the cube model a spherical charge shape was adopted. As with the cube model one eighth symmetry was exploited, a detonation point was declared at the centre of the charge and the same three symmetry planes and non-reflecting boundary at the exterior of the 2.0m fluid domain were declared. Again, gravity was not included in the model. To avoid using wedge elements as the first elements from the centre of the charge, the butterfly mesh approach[62] for meshing a cylinder with solid elements was adapted for a spherical charge mesh of radius 64.21mm.

Two charge meshes were constructed with appropriate adjoining fluid meshes: a coarse mesh, shown in Fig. 3.12 comprising a total of 8289 solid multi-material Eulerian elements, of which 189 elements were reserved for the explosive material; and a fine mesh (not shown) comprising 10935 elements, of which 1431 were reserved for the charge. Biasing of the elements in the fluid domain was used to reduce the total number of elements in the models, with element size increasing towards the outer fluid boundary. This pre-processing utility generates non-uniform mesh spacing and is explained in more detail in chapter 4. The analysis time and output frequencies used in the cube model were also adopted here.

Results of sphere model

Fig. 3.13 indicates the predicted pressure peaks from the sphere models compare well with those measured experimentally. The pressure-time histories in general exhibit the characteristic sharp rise followed by a smooth exponential decay, although the predicted decay rate is noticeably more rapid for both meshes than the fitted profile decay rate at 0.25m stand off. Although both meshes overpredicted the peak pressure magnitude at all stand off distances except 1.2m, the coarser mesh is closest to the experimental value at the closest stand off (within 8%). The results are presented in

Stand off (m)	Experimental peak pressure (MPa)	Numerical peak pressure (MPa)	
		Fine	coarse
0.25	635.6	706.3	674.1
0.50	195.1	273.8	228.1
0.76	109.6	154.5	128.8
1.20	64.1	44.2	41.3

Table 3.4: Comparison of experimental[73] and predicted pressure peaks for 2kg EDC-1 sphere model

table 3.4. The predicted peak pressures and decay rates are both observed to decrease with increasing stand off distance, confirming well known experimentally observed characteristics, however, the accuracy is also seen to reduce.

The pressure-time histories at greater stand off distances are shown to indicate the smearing effect arising from the advection scheme causing the pressure to increase much less sharply when the shock wave arrives. This smearing effect is clearly observed in the pressure contour plots tracking the propagation of the shock wave through the mesh (see Fig. 3.14). The shock front is almost five elements thick, each element being 6mm in the direction of propagation.

The sphericity of the shock wave from the sphere model is well represented from early time after detonation since the charge itself is spherical. The regularity and size of the element spacing, relative to the charge, in the direction of propagation, most likely contributed towards the successful prediction of the variation of pressure with time.

All four advection schemes available in LS-DYNA were assessed on the coarser sphere model for accuracy and cost. These results are presented in table 3.5. It is evident that advection scheme four (donor cell & HIS) is the most accurate, producing a predicted peak pressure to within 5% of the experimentally measured value. Advection scheme one is computationally cheaper than scheme four, however, is less accurate. The default scheme (van Leer & HIS) is observed to be computationally the most expensive.

Despite the sphere model producing good agreement with experimental pressure-time histories for a propagating shock wave, this form of mesh is not suitable for applying pressure loading in a fluid-structure interaction simulation. A typical structural model comprises a large number of shell elements encompassed by many fluid elements in the direction of the propagating shock wave. However, the element dimensions

Advection scheme	Peak pressure (MPa)	Time per zone cycle (μs)	Solution time (s)
Donor cell	686.0	38.917	183.0
van Leer + HIS	674.1	79.919	374.0
van Leer	712.2	56.302	267.0
Donor cell + HIS	662.3	42.665	199.0

Table 3.5: Comparison of free field UNDEX solutions for various advection schemes (stand off = 0.25m)

perpendicular to the direction of shock wave propagation increase linearly with distance from the charge. Consequently, at large distances from the charge, there may be only one or two elements perpendicular to a structure, through which the pressure from the shock wave may be applied which would result in inaccurate loading. As a general rule, to ensure accurate loading of a structure, the mesh density ratio of fluid to structural elements, in the region where the load is being applied, should be approximately equal to one.

3.4 Units

Examination of previous numerical studies on free field UNDEX[73] and collaboration with the authors of the code led to the discovery that the code had been written for use with imperial units. When using different units different answers were obtained for calculation of pressure in the free field sphere model.

Fig. 3.16 illustrates the difference ($< 10\%$) in predicted results using metres, kilograms, seconds compared with centimetres, grams, microseconds for the sphere model. The experimental value obtained for the peak pressure at 0.25m is plotted in Fig. 3.16 to indicate that the latter units result in an answer closer to the experimental values. This suggests that the non-standard units produce a more accurate answer for this case. The small element sizes generate microsecond orders of magnitude for the timestep. Hence using microseconds for the units of time in these analyses will render less floating point errors because timestep values will be closer to unity.

This does not indicate any limitation of the code but merely highlights the effect units can have in simulating UNDEX analyses. The remainder of the simulations in this work will use the units of centimetres, grams, microseconds, and contour plots of pressure and density results will be illustrated in accordance with these units. However, the

presentation of numerical input within the thesis will remain in SI units.

3.5 UNDEX bubble

A further extension of the free field UNDEX simulations is to assess the feasibility of using LS-DYNA to predict the bubble pulse characteristics, namely maximum bubble radius and the time to first minimum bubble radius (bubble period). The first bubble pulse is of most interest, as the damage due to this phenomena can exceed that due to the primary shock wave. The loading from subsequent bubble pulses is significantly less due to energy dissipation.

The sphere model utilised for the prediction of peak pressure and decay values for 2kg of EDC-1 was shown to simulate the spherical expansion of explosive gases of a lower density than the material in its initial state. Earlier investigations assessing the performance of newly implemented ALE capabilities for LS-DYNA[71,76] also included an UNDEX bubble analysis. The problem involved a TNT charge of mass 1298.0kg. The resulting bubble radius-time curve offered convincing proof of bubble expansion and contraction, however, the results were not validated against experiment.

The bubble simulations performed in this work were validated against a series of experimental studies conducted on TNT charges at various depths[37]. Bubble characteristics for the following spherical charges at respective depths were examined: 25.7g at 1.5m, 227g at 152.4m, 300g at 91.4m and 300g at 172.8m. The purpose of the simulations was to examine the relationship between charge size and depth, and bubble characteristics.

The 300g at 172.8m experiment was initially chosen for simulation, as the shortest period was recorded for this experiment and consequently it is likely to take the least amount of CPU time. Also the larger radius of the 300g charge (35.29mm) permits large element sizes to be used for modelling the charge which would assist in increasing the timestep reducing the CPU time further.

3.5.1 Sphere model

Geometric modifications were made to the sphere mesh used in the free field UNDEX analysis for comparison of numerically predicted bubble pulse parameters with experimentally recorded and empirically predicted values obtained for the above TNT charge. The JWL equation of state was used for the TNT material and the Gruneisen

Symbol	Property	TNT value
ρ_o	density	1630 kgm^{-3}
D	detonation velocity	6930 ms^{-1}
P_{cj}	Chapman-Jouget	29.0 $\times 10^9$ Pa
A	material constant	3.712 $\times 10^{11}$ Pa
B	"	0.0321 $\times 10^{11}$ Pa
R_1	"	4.15
R_2	"	0.95
ω	"	0.3
E_o	initial internal energy	2631.9 Jkg^{-1}
V_o	initial relative volume	0.0

Table 3.6: Properties and JWL constants of explosive material TNT[66]

equation of state was used to model the water. The JWL constants for TNT are listed in table 3.6.

Although deep charges are known to undergo little vertical migration due to gravity[15], it does impose an initial pressure on the sea water equal to standard atmospheric and hydrostatic pressure at a depth of 172.8m. Due to the symmetry of this model gravity could not be modelled hence an initial specific internal energy of 3750.4Jkg^{-1} was applied to the fluid.

The simulation analysis time was set at 50.0ms, based on the bubble period measured experimentally (17.8ms) and an empirical relationship prediction (17.5ms). This length of analysis time presents a problem for the non-reflecting boundary segments used in the free field UNDEX sphere model. Mass flow is permitted out of the boundary segments, beyond the extent of the fluid, but any reversal of flow is not simulated. Consequently, the fluid mass within the mesh will reduce as material flow reaches this boundary. During the propagation of the shock wave fluid mass flow does occur, hence this boundary is correct for predicting pressure-time data. However, for the prediction of the bubble pulse the afterflow and reverse flow of the fluid are vital for accurately predicting the characteristics associated with expansion and collapse of the bubble.

This imposed a costly increase in computation. As a result of this limitation the exterior of the fluid domain was moved to 100.0m from the charge. The larger extent of fluid ensures that no fluid mass will flow out of the mesh during the time required for at least one bubble pulse. The number of elements used to discretise such a large volume of fluid were kept to a minimum using biasing techniques. A total of 16254 solid multi-material

Eulerian elements were used in the model, with 108 elements representing the 300g charge. The pressure-time history was recorded at the expected position of maximum bubble radius (0.387m).

Results of sphere model

A plot of the predicted pressure-time history for 300g TNT charge is shown in Fig. 3.17. Two bubble pulses are predicted each indicating approximately the same period. The first prominently occurs at 18.3ms, whereas the second is less clear, but exhibits a peak pressure at approximately 36.0ms. The maximum radius of the bubble was 0.356m which compares to an experimental value of 0.387m.

As expected the arrival of the shock wave is characterised by the sharp rise in pressure. However the peak pressure at 0.387m of 91.0MPa did not compare closely with the empirical value for TNT of 120.0MPa at this stand off distance.

Although the predicted period and maximum bubble radius are within 10% of experimental values the pressure-time history suffers excessively from noise. This numerical distortion presents problems when ascertaining other bubble related characteristics for assessing the severity of bubble loading, such as peak pressure, impulse and energy. The peak pressure for the bubble is not clearly defined and the area under the pressure-time curve is difficult to evaluate. These results do not give confidence in LS-DYNA's ability to predict pressure-time histories or bubble characteristics for smaller charge sizes using the sphere model.

3.5.2 Quasi-1D model

In an attempt to improve on the results of the sphere model, a second model was constructed, based on earlier work for the validation of the hydrocode MSC/DYTRAN[37].

A quasi-one dimensional model of 300g TNT and surrounding fluid was constructed of the form illustrated in Fig. 3.18. To maintain spherical symmetry a diverging pyramid shaped region of fluid was used to account for the increasing volume of fluid with distance away from the centre of the charge.

'No flow' boundary conditions were declared perpendicular to all sides of the mesh. The use of a five noded element, which is not a standard finite element shape, at the centre of the charge was avoided by creating a small hole. This hole reduces the radius of the charge by 8.75% which in turn reduces the energy of the explosive material

by approximately 5%, an acceptable amount for this problem. The four nodes at the centre of the charge were constrained from translation and rotation. To prevent any reflections from the exterior boundary of the fluid domain the fluid was modelled out to a distance of 100.0m.

Non-rectangular solid multi-material Eulerian elements, whose top and bottom were parallel, whose lower face was parallel to the x-axis and whose upper face had a slope of $\tan^{-1}5^{o}$, were used for both the charge and the fluid. The JWL and Gruneisen equations of state were used for the charge and fluid respectively, with the same constants as in the sphere model.

A total of 4259 elements were used to model the fluid with biasing towards the charge, and 7 elements were used to model the charge. A close up of the finite element mesh for the charge is shown in Fig. 3.18. Gravity was not accounted for in this model, however, as in the one eighth sphere model a specific internal energy of 3750.4Jkg^{-1} was applied to the material. Pressure at the expected position of maximum bubble radius was requested.

Results of quasi 1D model

The quasi-1D model was unsuccessful in predicting bubble behaviour. The results of the model, presented in Figs 3.19 and 3.20, clearly indicate a loss of tracking material behaviour when the bubble reaches its first collapsed state. The characteristic rise and fall in pressure as the bubble collapses and expands again are not clearly defined as expected.

The density contour plots in Fig. 3.20 illustrate the initial expansion and contraction of the bubble. The bubble appears to reach minimum radius at approximately 14.0ms, after which no expansion is evident.

Encouragingly the peak pressure at the stand off distance was predicted to within 5% of the empirical value, 120.0MPa. For comparison purposes, the same model was run on the MSC/DYTRAN code[73]. The predicted pressure-time history is much improved. The period of the bubble pulse is within 10% of empirical and experimental values.

3.6 Structural analysis

Having investigated the simulation of a free field UNDEX event and associated fluid response, modelling of geometric and material behaviour associated with the prototype

echinodome is the final stage of LS-DYNA's preliminary assessment. The behaviour of the shell under static loading in air is well understood having been examined thoroughly in previous work[1,3,4]. The static load case is therefore considered in the following sections to establish a suitable form of discretisation to simulate geometrical and material behaviour under static loading.

3.7 Simulation of structural response to static loading

Static load problems must be solved dynamically with LS-DYNA due to the transient nature of the code. This implies that any static load must be applied over time, i.e., it becomes a quasi-static load. Two methods are available to solve for quasi-static loading: dynamic relaxation, or slow transient analysis. Both methods solve for the steady state solution of the transient response of structures allowing both linear and non-linear quasi-static systems to be solved.

3.7.1 Slow transient analysis

A transient solution to a static load case involves the solution of the equations of motion governing structural dynamics mentioned in chapter 2 (Eqn 2.22).

The transient solution oscillates about the equivalent result that a static code would converge on. Simulating a quasi-static load requires the step function to be ramped over a short period of time, thereby making it a dynamic load. If the load is applied too suddenly the amplitude of the oscillations in the transient solution are too large to accurately determine the static equivalent.

Several ramping times were adopted for this analysis: 10ms, 50ms and 100ms, to examine the effect of the ramping time on the accuracy of the solution.

3.7.2 Dynamic relaxation

Dynamic relaxation (DR) is an explicit iterative method. The procedure involves the inclusion of a damping term to the structural equation of motion (Eqn 2.22) forcing convergence to the static solution in a minimum time. The solution is usually the lowest deformation mode[52].

To obtain convergence in a minimum time an optimum or critical damping factor must be chosen which is most suitably estimated using the lowest natural frequency of a

structure[52]. The damping factor multiplies all the nodal velocities at each timestep to reduce the oscillations. This can be either calculated automatically or input manually. The damping factor, η, is given by,

$$\eta = 1 - 2c_d\omega_n\Delta t \tag{3.5}$$

where c_d is the desired fraction of critical damping, ω_n is the lowest natural frequency of oscillation (rads^{-1}) and Δt is the timestep. The damping is applied to the velocity, v, at each time step according to

$$v^{n+\frac{1}{2}} = \eta v^{n-\frac{1}{2}} + a^n\Delta t \tag{3.6}$$

where,

a^n = acceleration at the nth timestep, ms^{-2}.

The convergence criterion is based on the global kinetic energy and is assumed if

$$E_{ke} = cvtol E_{ke_{max}} \tag{3.7}$$

where *cvtol* is the convergence tolerance (default = 0.001), i.e. when the kinetic energy in the transient system has decayed to 0.001 of the maximum kinetic energy during the analysis. Further information on dynamic relaxation can be found elsewhere[77,78].

The manual input option was chosen for this work. The lowest natural frequency of the prototype echinodome underwater is not known. However, in air it was calculated to be 60Hz[79]. Assuming $\Delta t = 1\mu$s, η is calculated to be equal to 0.999.

3.8 The prototype shell

The structure to be used in this work is the same prototype shell as that used in previous experiments (see Fig. 3.21). The shell profile is illustrated in Fig. 3.22. These dimensions are unique for an apex design head, z_o = 1.525m, a uniform design stress, σ_d = 0.446MPa, and an average shell wall thickness, t_w = 3.8mm, the average of variations

found when measured using an ultrasonic thickness tester[3]. The shell is constructed using two halves bonded together with araldite along a meridional seam. Each half is made from an epoxy matrix GRP material with a glass fraction of 0.26, the fibres being arranged in a randomly chopped strand mat fabric. Material control tests[1] determined the following material properties:

$$\begin{aligned} \text{Young's modulus (E)} &= 8800\text{MPa} \\ \text{Poisson's ratio } (\nu) &= 0.36 \\ \text{Ultimate tensile strength} &= 55.4\text{MPa} \\ \text{Mass density } (\rho) &= 1100\text{kgm}^{-3} \end{aligned}$$

When bonded the shell encloses a volume of 0.2152m^3. Also bonded to the bottom of the shell using the same araldite is a square tufnol base, $0.2\text{m} \times 0.2\text{m} \times 0.02\text{m}$, for the purpose of fixing eye-hooks to assist the tethering of the shell. The tufnol base has the following properties:

$$\begin{aligned} \text{Young's modulus (E)} &= 13200\text{MPa} \\ \text{Poisson's ratio } (\nu) &= 0.284 \\ \text{Mass density } (\rho) &= 1360\text{kgm}^{-3} \end{aligned}$$

3.8.1 Structure idealisation

The axisymmetric nature of the structure combined with the symmetric form of the load permitted a half symmetry model of the structure to be constructed. Using the shape prediction program[2] in modified form[4,5] to provide the meridional profile, a geometric representation of half the idealised shell was generated. From this geometry three finite element meshes were constructed comprising different levels of refinement to examine convergence on the static solution.

The coarsest level of discretisation consisted of 896 four noded Belytschko-Lin-Tsay shell elements, the default shell element formulation in LS-DYNA[53]. This mesh was refined twice more by a factor of two (approx.) to produce two finer meshes (2124 and 4248 elements) of the same element formulation. All three meshes are presented in Fig. 3.23.

The numerical model of the shell accounted for imperfections in the wall thickness using the thicknesses averaged every tenth percentile, as measured in earlier work. Previous experimental observations[3] indicated shell thickness varied down the meridian and around the parallel circles. Only the meridional imperfections were considered in this model. These were represented as circumferential bands of the appropriate

thickness every 10% down the meridian. Also the prototype shell was assumed to be monolithic. In reality a bonded seam exists dividing the shell symmetrically. An examination of the influence of this seam on the structural response to static loads revealed its significance to be negligible[4] and hence it was not included in the simulation. Out of plane translational and rotational constraints were applied to the symmetry edge.

The tufnol base was incorporated into the circular flat base of the shell permitting the use of only one layer of shell elements in this region. The strength of the GRP base was combined with the strength of the bonded tufnol to approximate an equivalent base thickness (19.0mm) with tufnol properties. It was considered unnecessary to model the effect of the tufnol base using separate shell elements since the base of the shell was declared as constrained against rotation and translation in accordance with the experimental conditions.

Control tests performed previously[4] on the GRP indicated the stress-strain relationship for the material was linear until failure and consequently, a linear elastic material model (*MAT_ELASTIC[55]) was assumed sufficient to represent the GRP with the properties presented earlier. Previous investigations also concluded that geometric non-linearity was negligible under a 300N static load[4]. Hence this loading was applied to the shell at $\phi = 60^o$, $\theta = 0^o$ from the apex (where ϕ and θ are the meridional and circumferential angles respectively) in the form of a ramped point load as shown in Figs 3.24 and 3.25 respectively.

Both the slow transient and dynamic relaxation solution approaches were applied to the static load case on the three discretisations for the prototype echinodome. An extensive shell element library exists with LS-DYNA with varying degrees of numerical accuracy and computational efficiency. The default Belytschko-Lin-Tsay shell is described as being computationally the most efficient shell formulation, using five through-the-thickness integration points. It also accounts for rotations and velocity-strain formulations and has built-in hourglass control. However, several other four noded shell element formulations were tested from this library in an attempt to determine the most accurate formulation for predicting displacement under quasi-static loading.

3.8.2 Results of structural analysis

Application of the ramped quasi-static load using the concentrated point load approach causes the finite element mesh to develop a zig-zag appearance, as shown in Fig. 3.26(a).

This 'hourglass deformation' is known to occur when a load is concentrated at a single node and the element has too few integration points. Hourglassing is a non-physical zero energy deformation mode with no stiffness associated with it.

Suggested solutions to this problem[52] are to use the stiffness method of hourglass control, to use the fully integrated shell element formulation, or to spread the load over several nodes. Using the stiffness hourglass control has been found to overstiffen results and the fully integrated shell element is known to be more expensive than the default shell formulation. In the experiment the load applicator had a base area of approximately $100mm^2$. Consequently it was decided to apply the same 300N load as a pressure load at the same position. In so doing, the deformation of the mesh, as illustrated in Fig. 3.26(b), is observed to contain no hourglassing.

Using this pressure load the numerical simulations were performed at various ramping times for both approaches in an attempt to determine the optimum ramping time, i.e., a ramping time that would give acceptable results in a reasonable timescale.

Displacement results from the three transient simulations are presented in Fig. 3.27. They indicate that a 10ms. ramping time generates such large oscillations in structural response that the static equivalent result is difficult to evaluate accurately. Loads applied at this rate are usually viewed as impact loads by structures such as the prototype echinodome, from which the predicted transient displacement is expected. At 50ms ramping time, the oscillations in the structure have reduced sufficiently to easily determine the static result. Only a slight improvement is observed at 100ms ramping time. The CPU time for the 100ms. simulation was 8051s which, in view of the negligible improvement in displacement oscillations over the 50ms simulation, was considered too long for this simple quasi-static load case. The CPU time for the 50ms simulation was 4817s. Hence, the 50ms ramping time was concluded to be the optimum ramping time for the slow transient approach.

The CPU times for the dynamic relaxation simulation are not comparable. The 50ms ramping time required 34171s of CPU time for the solution to converge to 0.001 tolerance. Reducing the ramping time to 10ms decreased the solution time to 7129s The ramping time was reduced further to 1ms in an attempt to reduce the solution time. However, the displacement solution was found to contain a spike prior to converging indicating that the load was being applied too suddenly. Moreover, the converged solution for this ramping time was lower than all previous simulations. The displacements resulting from the dynamic relaxation simulations are illustrated in Fig. 3.28.

In view of the computational cost of dynamic relaxation it was concluded that, for

quasi-static loading, the slow transient approach was more suitable for obtaining results within a reasonable timescale. Moreover, from Fig. 3.29, it is clear that the mean displacement from the slow transient approach was closer to the experimental value than the converged solution of the dynamic relaxation approach. Hence, the ramped pressure load was applied, using the slow transient approach, to the three discretisations mentioned earlier, in order to ascertain the optimum discretisation for structural response.

The experimentally measured global displacement at the load point was 0.66mm. All three meshes underpredicted the displacement at the load point. Fig. 3.29 shows the displacement predicted by each of the three meshes vary by approximately 0.05mm. The coarsest level of discretisation predicted a displacement of 0.54mm. Increasing the mesh size from 896 elements to 2124 elements improved the value to 0.57mm. However further convergence on displacement by the finest discretisation (0.59mm) did not justify the increase in computational cost (14090s), three times more expensive than the 2124 element mesh (4306s). The simulated behavioural response is the same for all three meshes, consisting of rotation about the base. The predicted deformed shape, shown in Fig. 3.30(a), compares well with that observed. Fig. 3.30(b) clearly illustrates that as well as the load point experiencing significant principal stresses, the base region experiences tensile and compressive stresses to a moderate degree. Previous work also indicated these regions to be most critical.

Improvement on the accuracy of the displacement given by the slow transient solution for the 2124 element mesh was then sought by utilising different shell element formulations. The displacements predicted by these simulations are presented in Fig. 3.31. The solution times for each shell formulation are listed in table 3.7. It is clearly evident that the shell formulation computing a displacement closest to the experimental value is the default shell. Moreover, the default shell also resolves the problem in the shortest CPU time (4306s). The Hughes-Liu, Belytschko-Leviathan and Belytschko-Wong-Chiang shell formulations produce displacements closest to the default shell, although the Belytschko-Leviathan and Belytschko-Wong-Chiang require, on average, 50% more CPU time. The selectively reduced (S/R) Hughes-Liu and co-rotational Hughes-Liu elements took almost 1200% and 2400% respectively more CPU time than the default shell.

The underprediction of the displacement at the load point may be attributed to a combined effect of the assumptions made regarding the model. Firstly, neglecting the seam in the numerical model may have made the model globally stiffer than in reality. The higher frequency of the predicted response, 70Hz, compared to the measured value of 60Hz, confirms this. Consequently, the predicted global displacement would be less

Shell formulation	Solution time (s)	Time per zone cycle (μs)
Hughes-Liu	13166	33.891
Belytschko-Lin-Tsay (default)	4306	11.081
S/R Hughes-Liu	106301	273.661
S/R co-rotational Hughes-Liu	54863	141.239
Belytschko-Leviathan	6857	17.648
Belytschko-Wong-Chiang	6010	15.468
Fast (co-rotational) Hughes-Liu	9109	23.446
Fully integrated shell	16189	41.674

Table 3.7: Comparison of computational cost of various shell formulations for transient response to quasi-static loading

than that measured experimentally. Secondly, no circumferential imperfections were included in the model, so any contribution these may have made to the experimental displacement is not taken into account. Thirdly, the elastic material model used to represent the GRP is most likely too simple for accurate behavioural response. The behaviour of the epoxy resin and glass fibres near the load point may be more complex, particularly given the age of the shell and the different environments in which it has been residing over the years. Any changes to material properties due to these factors could lead to errors in material data. Finally, previous work[3,4] revealed that fully constrained boundary conditions at the base were an inaccurate representation for the prototype model because of the araldite bonding used to fix the shell base to the experimental apparatus. This bonding does not provide fully rigid conditions. Earlier FE analyses relaxed the stiffness of the boundary conditions to compensate for this weakness. Doing the same here would undoubtedly increase the displacement of the numerical model.

Despite underpredicting the displacement by $\approx 15\%$, the result from the 2124 element mesh is considered adequate given that LS-DYNA is an explicit transient analysis code. The accuracy of the solution must be balanced against the computational cost of obtaining the solution. The dynamic relaxation solution for the 10ms ramping time, performed on the 2124 element mesh, is shown to justify the rejection of this approach for this particular problem. Aside from the increased cost, the displacement predicted by dynamic relaxation is lower than that predicted by the 896 element mesh. A finer mesh or tighter convergence may improve the dynamic relaxation solution but at extra computational cost. The simulation of a static load on the mesh using an implicit static code (ABAQUS[80]) is estimated to take approximately 15s of CPU time.

3.9 Conclusions

LS-DYNA is concluded to be successful in the modelling of isolated detonation and shock wave propagation phenomena. It is in good agreement both quantitatively, and qualitatively, with theoretical and experimental observations. Validation of the free field fluid response to the detonation of 2kg EDC-1 has also indicated good comparison against experiment up to 1.2m stand off distance.

At the time of writing, LS-DYNA is not capable of satisfactorily simulating UNDEX related bubble phenomena. The results indicate a distorted pressure-time history and loss of numerical tracking of the charge material boundary after one expansion and contraction cycle.

A suitable finite element model of the prototype echinodome has been constructed and transient response to quasi-static point loading validated. The model is symmetrical about the plane perpendicular to the seam and comprises 2124 four noded Belytschko-Lin-Tsay shell elements. Variations in thickness down the meridian and the tufnol base are accounted for.

In addition several issues regarding the construction of suitable finite element meshes for propagation of detonation and shock waves, and the use of explicit transient codes for static loading have been highlighted.

1. A significant number of elements representing the charge, and the quality of the charge mesh in the direction of propagation, are required to ensure the pressure in the exploded charge material reaches Chapman-Jouget values signifying complete detonation.

2. A fine mesh of similar geometric form to the shock wave front, within the region tracking the shock wave, is required if the pressure at the shock front is to be accurately modelled for a considerable stand off distance.

3. The collapsed hexahedral element used in LS-DYNA to generate a wedge element could not be used, at the time of writing, for UNDEX studies involving shock wave propagation or bubble behaviour.

4. Smearing of the shock wave is unavoidable as it is a feature of the advection scheme. As a general rule, the Eulerian elements should maintain the same thickness throughout the region of interest and should not exceed the largest charge element length.

5. For problems involving small magnitudes of timestep (microseconds) the efficiency of LS-DYNA's performance can be improved by using non-standard units of the same order.

6. The slow transient approach to solving the quasi-static point load case considered is computationally more efficient, and numerically more accurate, than the dynamic relaxation approach.

7. The Belytschko-Lin-Tsay shell element is concluded to be computationally the most efficient element, providing sufficient numerical accuracy in a reasonable timescale and should be used for simulating structural response to quasi-static loading.

The analyses presented above provide sufficient confidence in LS-DYNA's ability to be utilised for modelling UNDEX loading problems. The free field sphere model can be used to verify free field pressure predictions from any model constructed for FSI simulations.

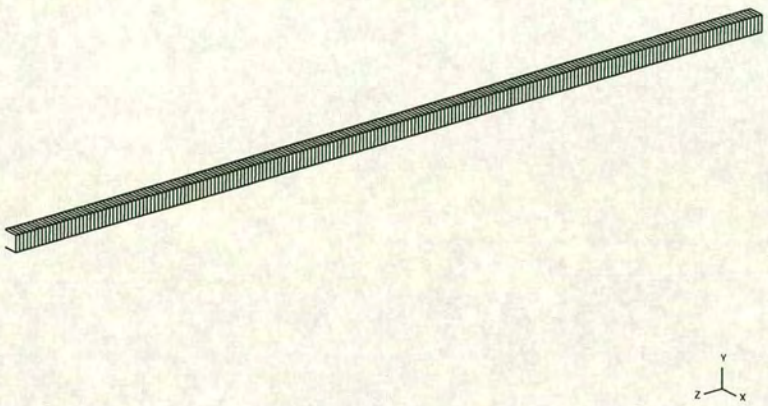

(a) Finite element mesh

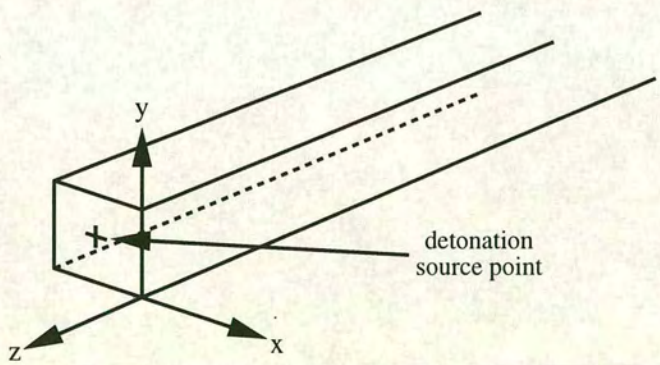

(b) Ignition point

Figure 3.1: EDC-1 explosive slab (0.01m $\times$ 0.01m $\times$ 0.5m)

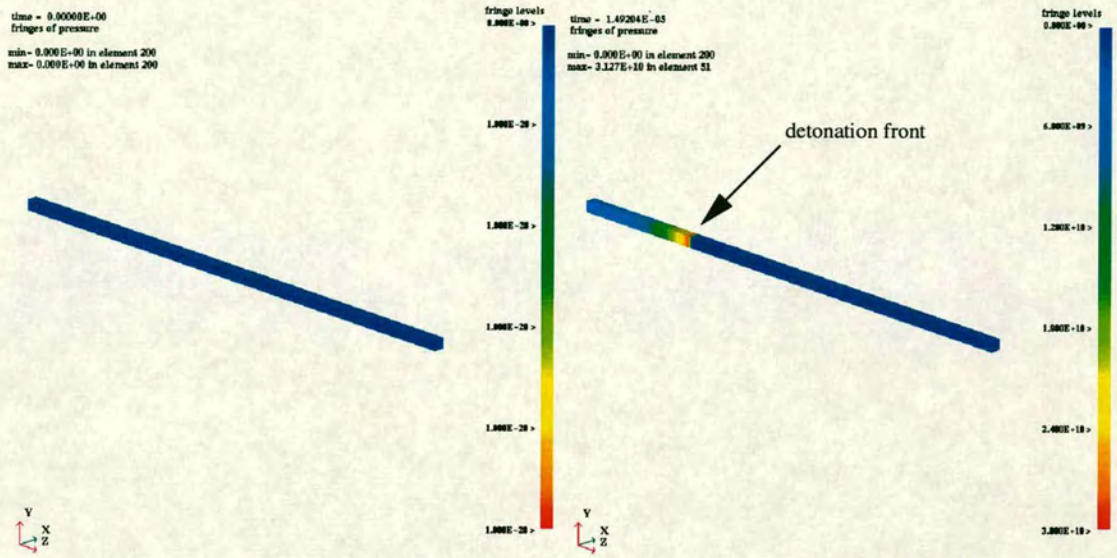

(a) t = 0.0μs

(b) t = 15.0μs

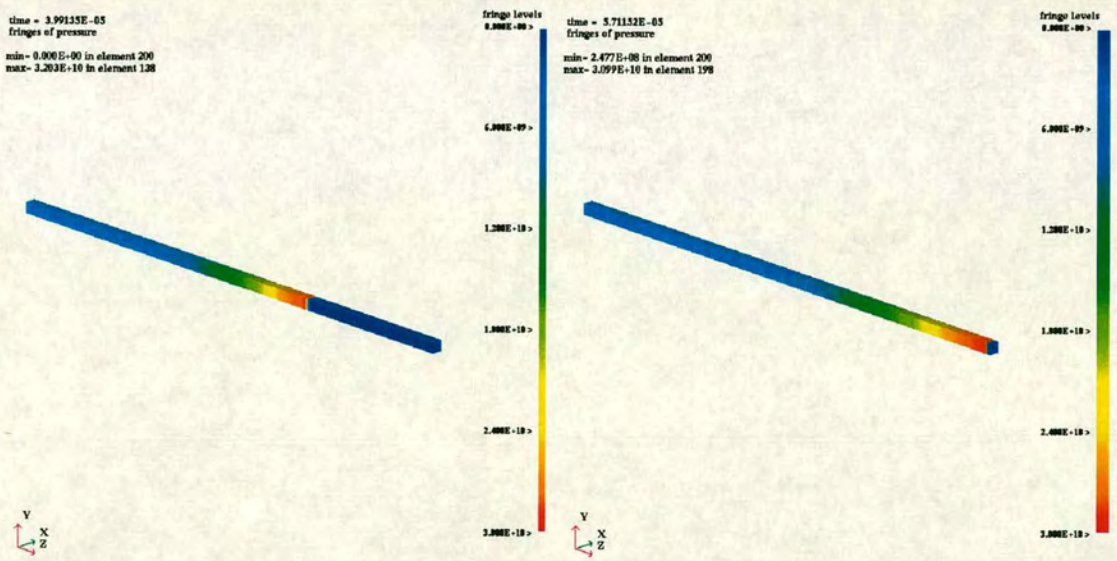

(c) t = 40.0μs

(d) t = 57.0μs

Figure 3.2: Propagation of detonation wave along EDC-1 explosive slab (pressure units = Pa)

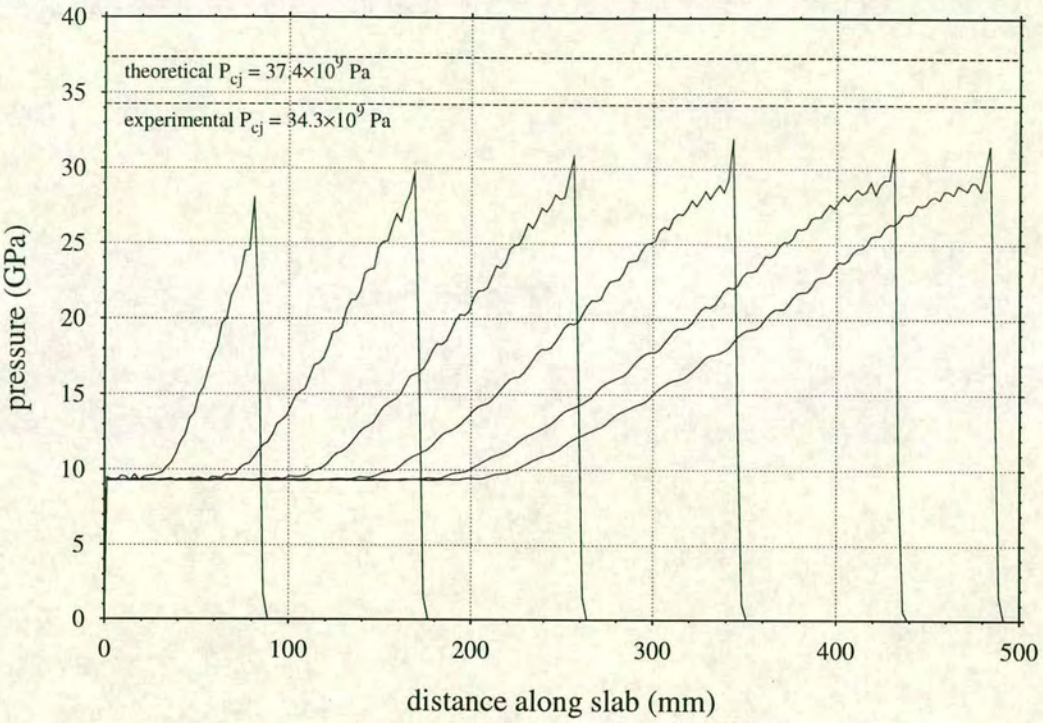

Figure 3.3: Peak pressure profiles along EDC-1 slab

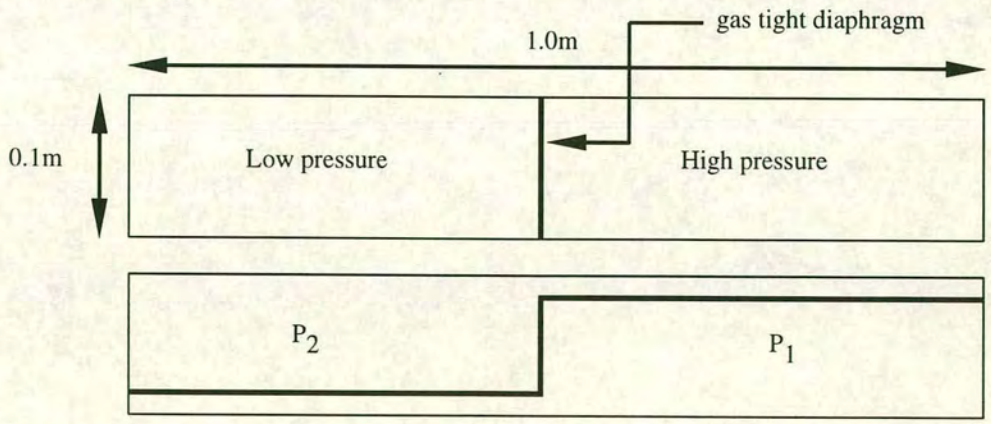

Figure 3.4: Shock tube setup and initial pressure distribution

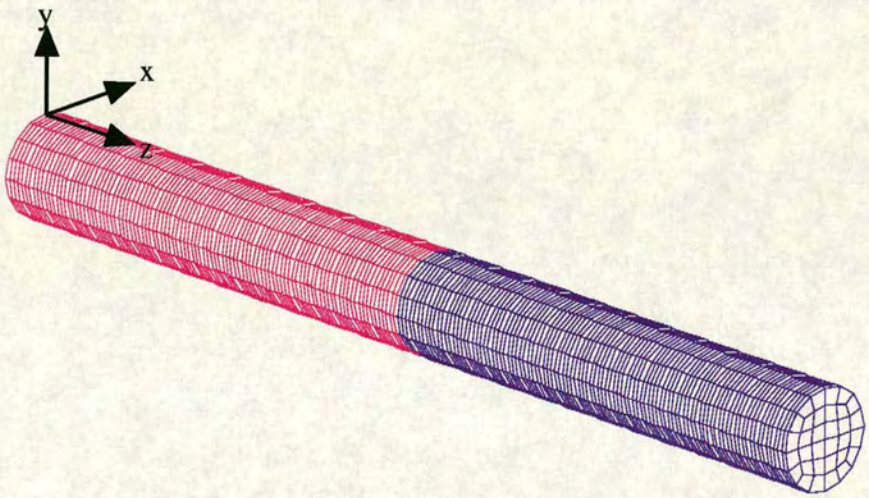

Figure 3.5: Finite element mesh of shock tube (diameter = 0.1m, length=1.0m)

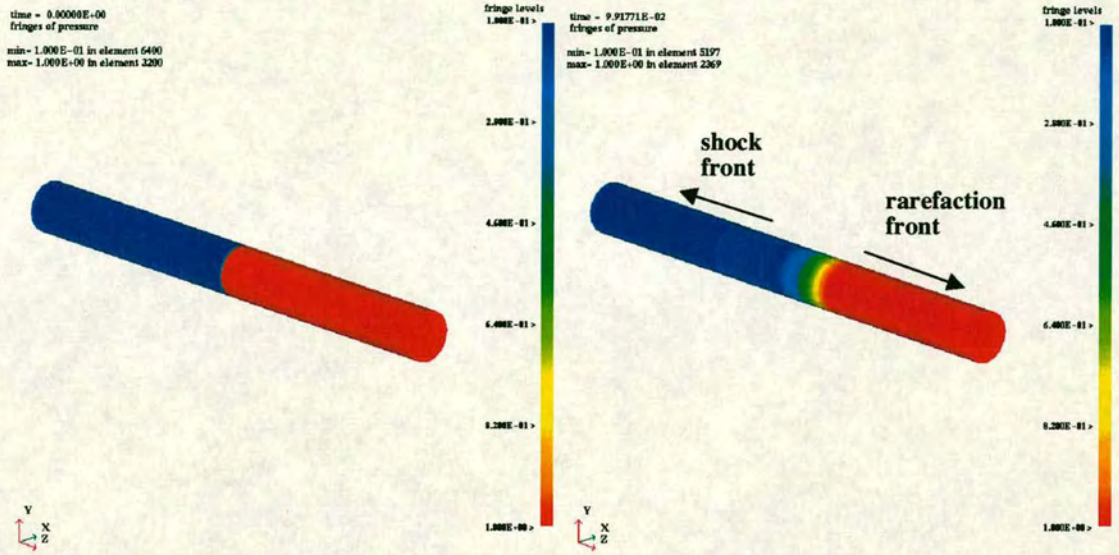

(a) t = 0.0ms

(b) t = 100.0ms

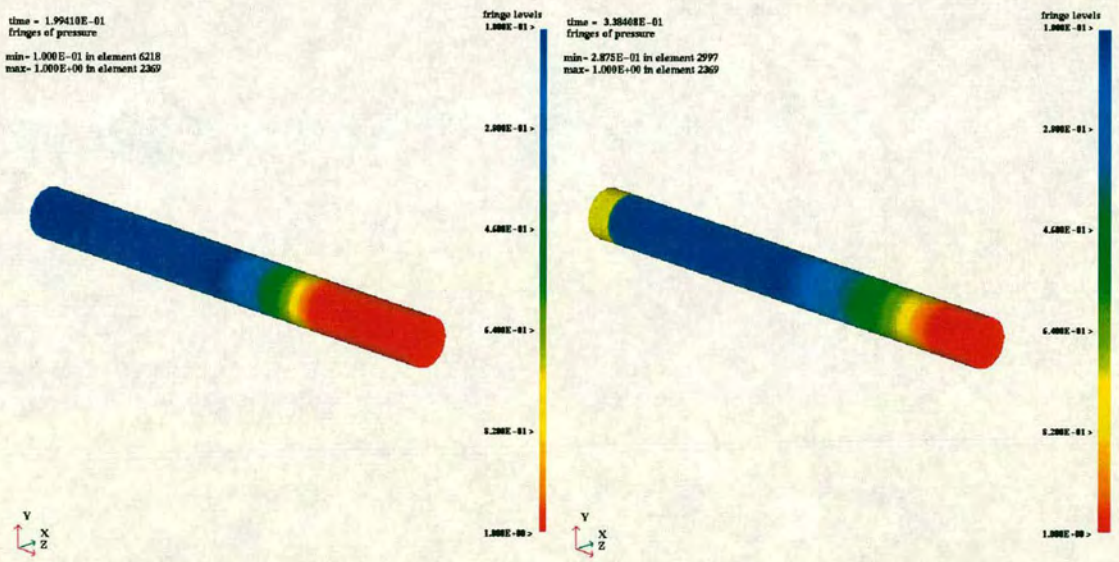

(c) t = 200.0ms

(d) t = 338.0ms

Figure 3.6: Propagation of shock and rarefaction waves along shock tube (pressure units = Pa)

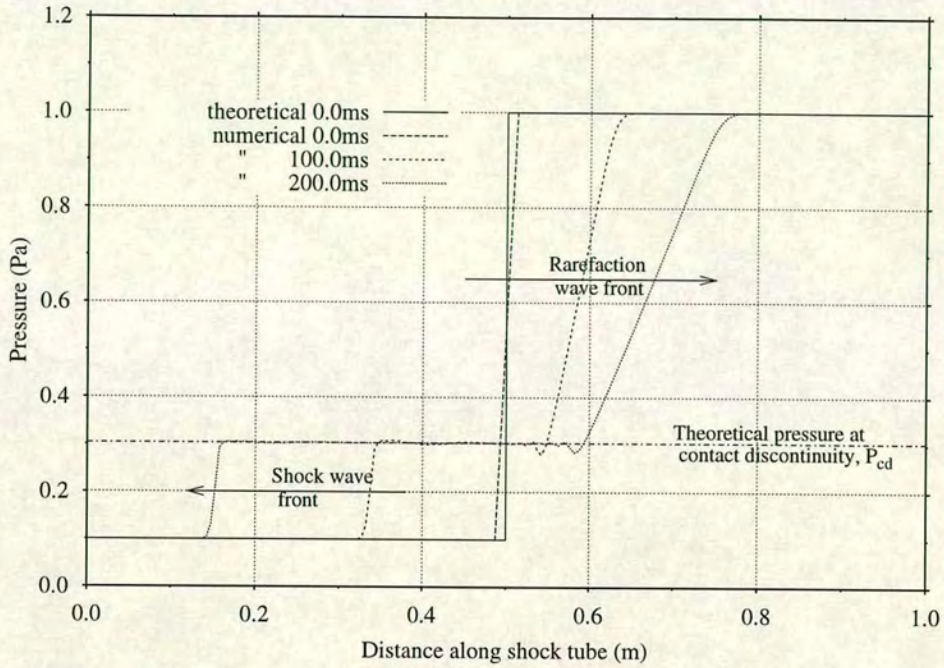

(a) Pressure

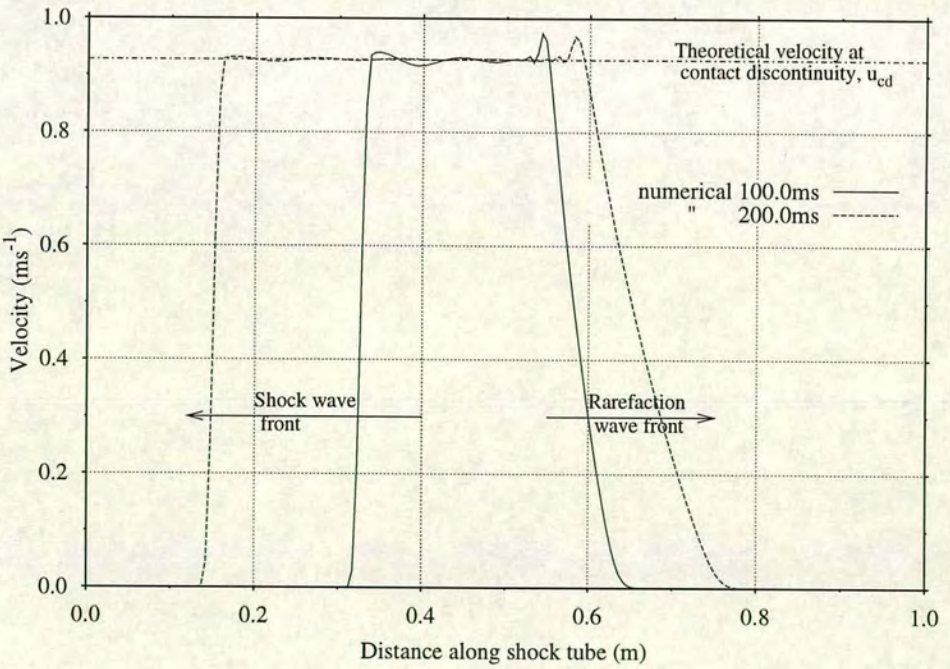

(b) Velocity

Figure 3.7: Pressure and velocity profiles along a shock tube

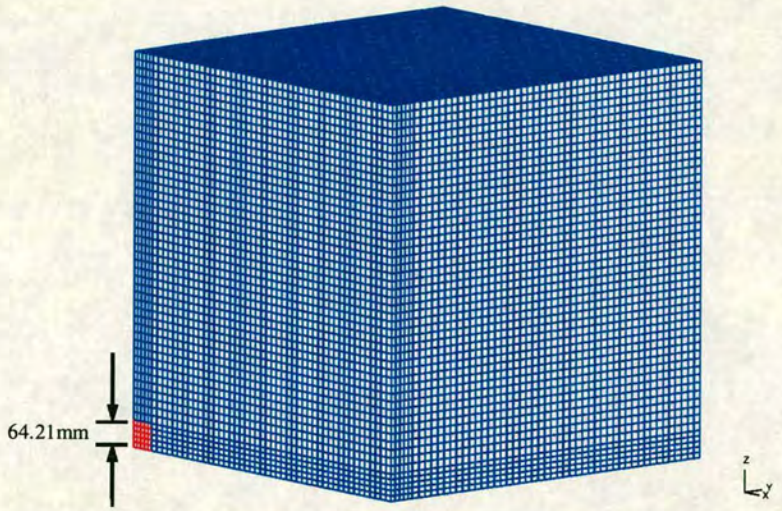

Figure 3.8: Finite element mesh of 2kg EDC-1 cube model, 0.75m × 0.75m × 0.75m (charge in red, fluid in blue)

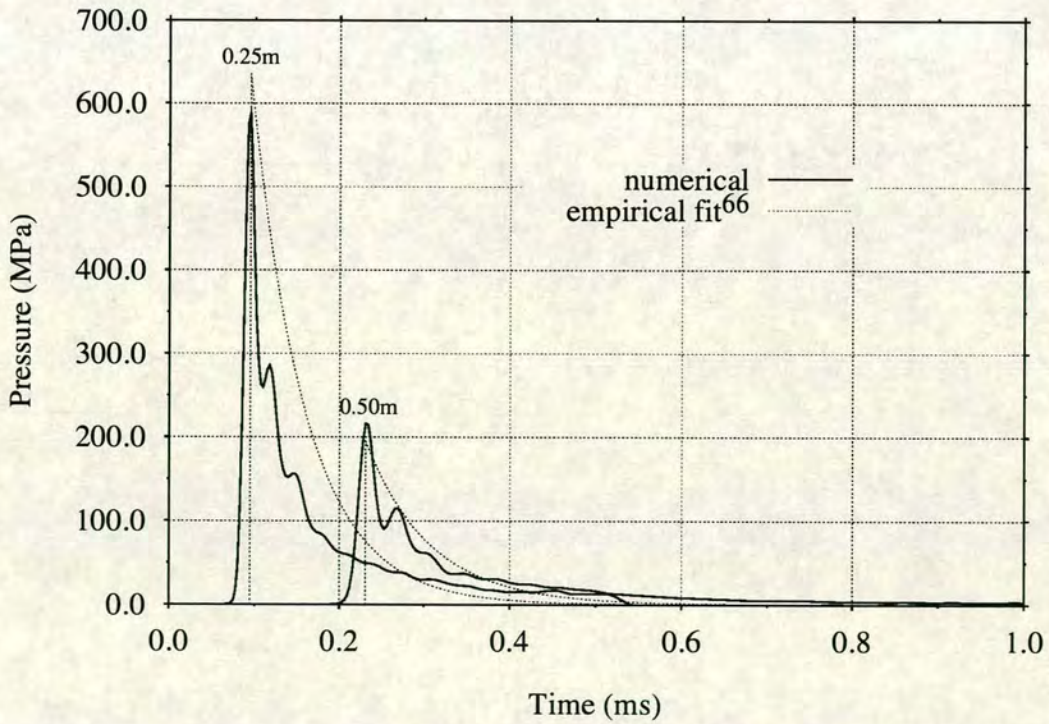

Figure 3.9: Free field fluid response for 2kg EDC-1 cube model

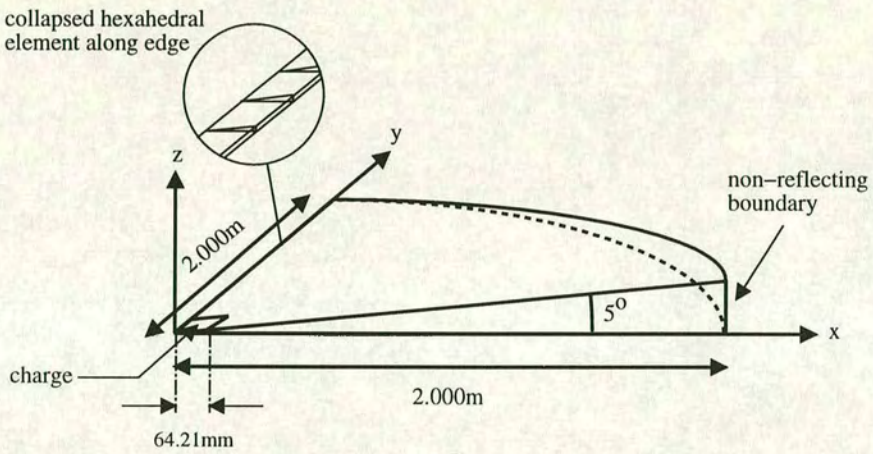

Figure 3.10: Sketch of 2kg EDC-1 wedge model

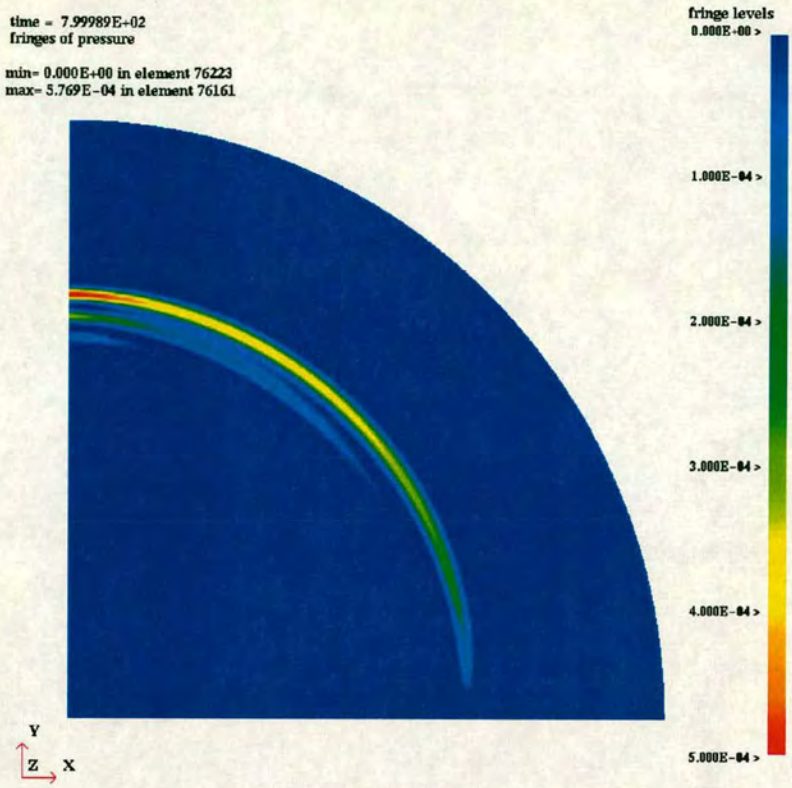

(a) Shock wave

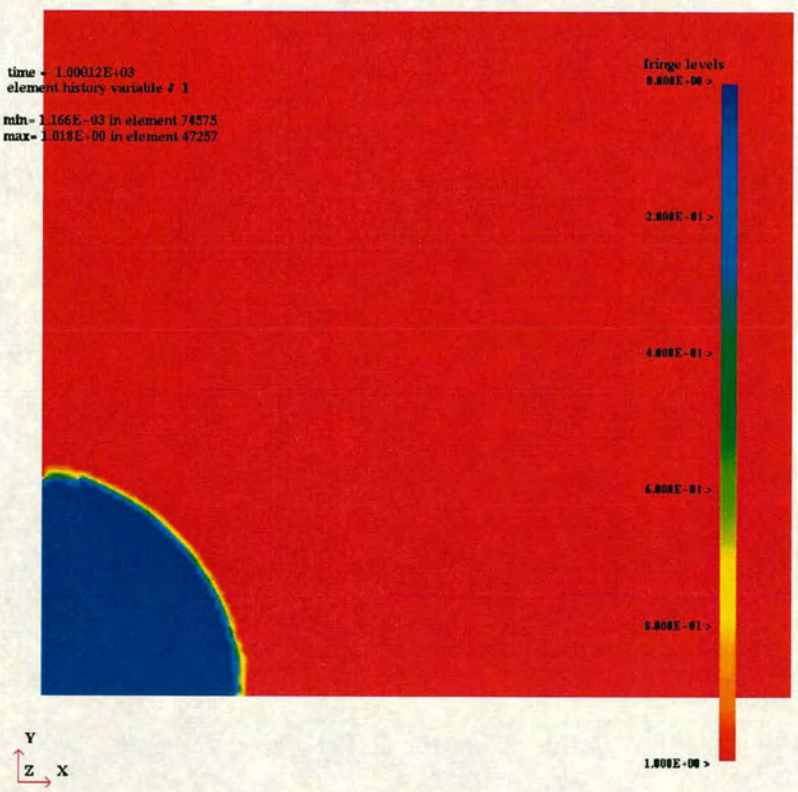

(b) Bubble

Figure 3.11: Free field fluid response for 2kg EDC-1 wedge model

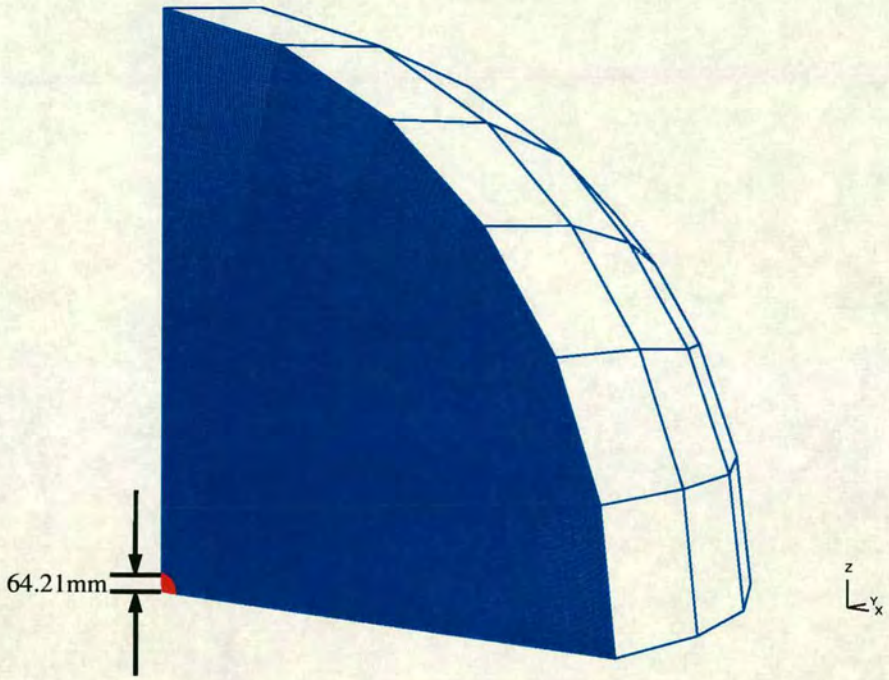

Figure 3.12: Finite element mesh of 2kg EDC-1 sphere model (8289 elements)

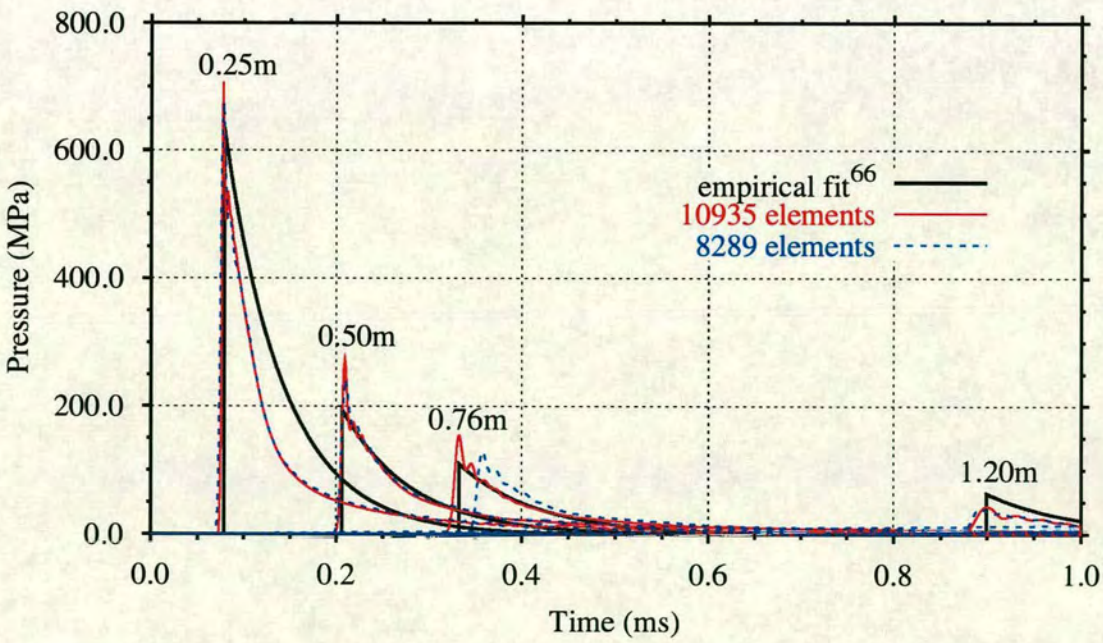

Figure 3.13: Free field fluid response for 2kg EDC-1 sphere model

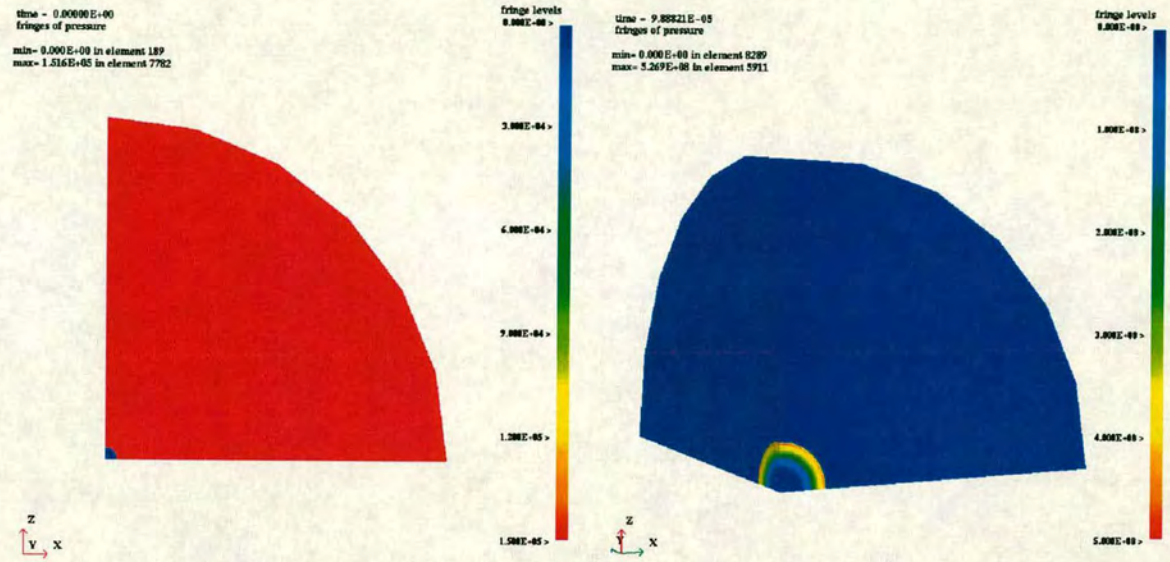

(a) t = 0.0ms

(b) t = 0.1ms

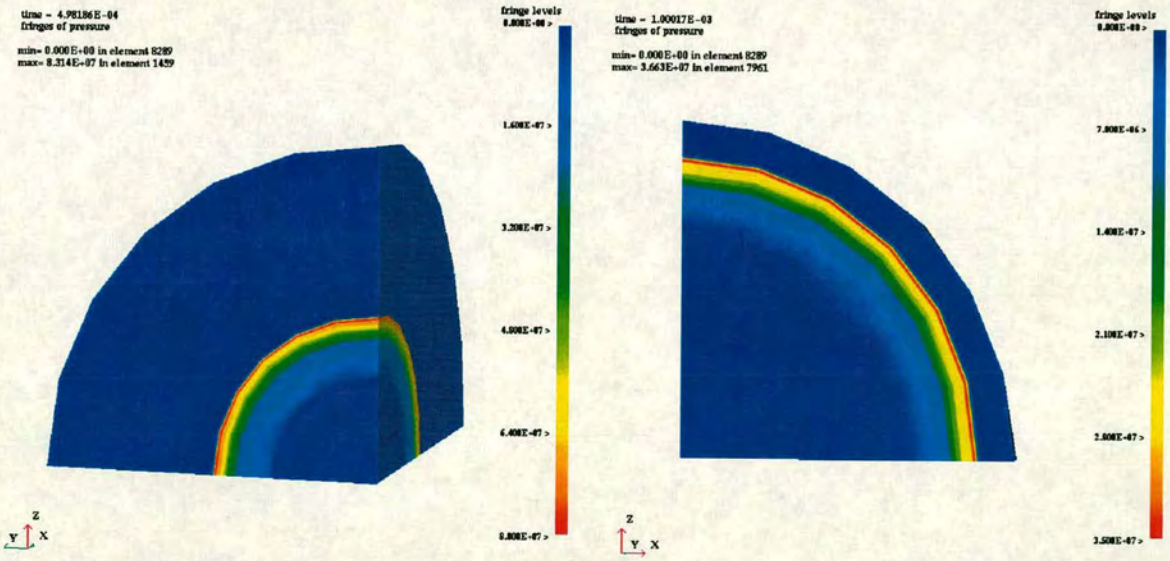

(c) = 0.5ms

(d) t = 1.0ms

Figure 3.14: Propagation of shock wave for 2kg EDC-1 sphere model (pressure units = Pa)

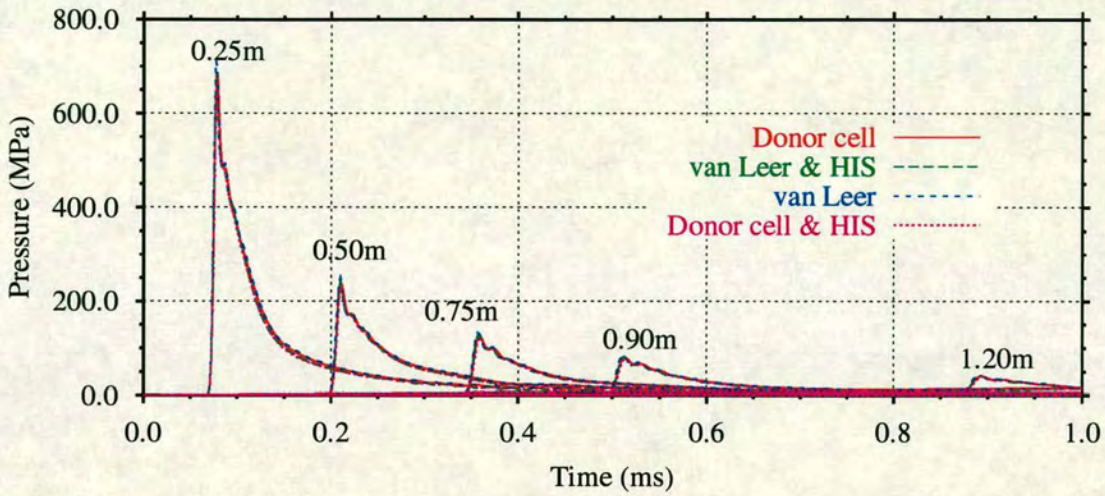

Figure 3.15: Effect of advection schemes on predicted fluid response

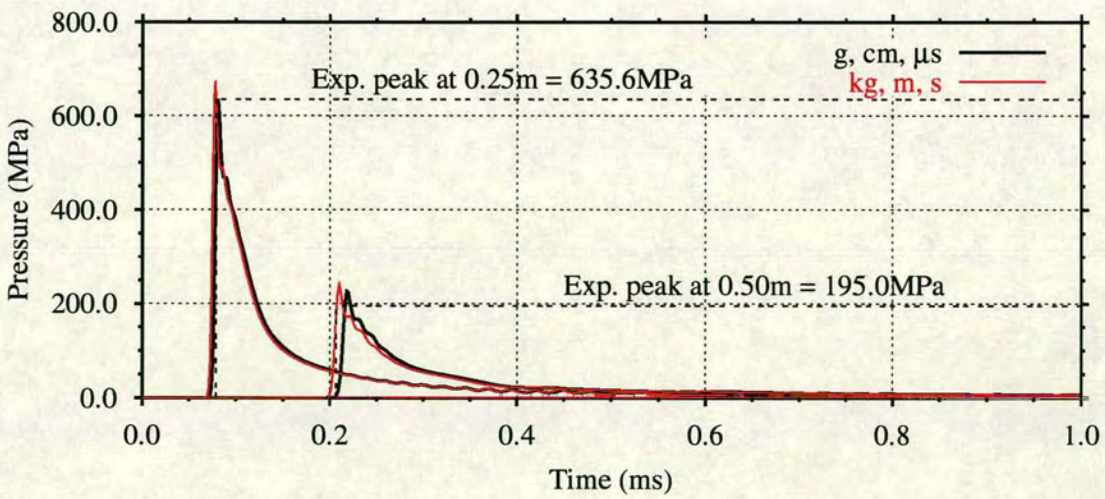

Figure 3.16: Effect of units on predicted fluid response

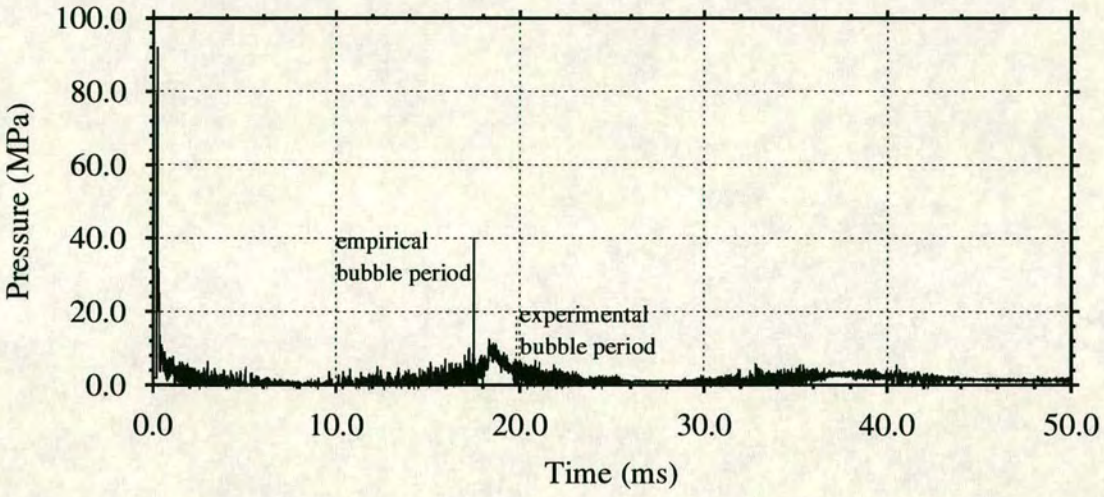

Figure 3.17: Free field bubble response for sphere model at 0.387m from charge

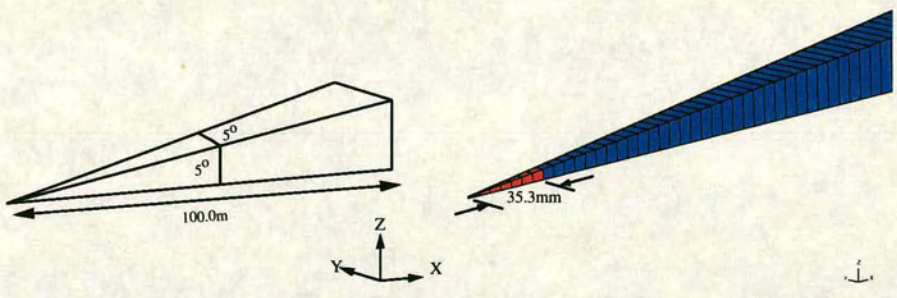

(a) Extent of fluid

(b) Finite element mesh (zoom on charge)

Figure 3.18: Quasi-1D UNDEX bubble model

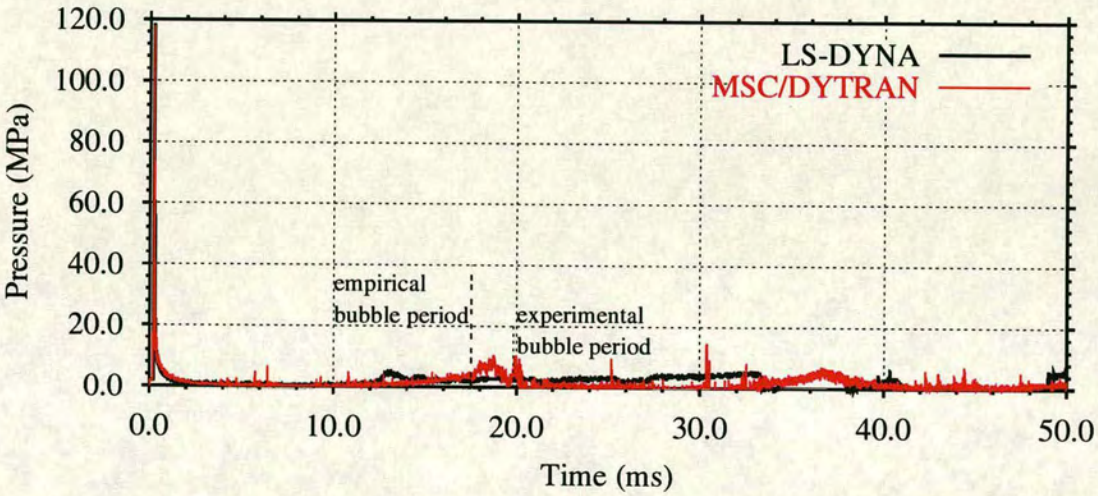

Figure 3.19: Free field bubble response for quasi-1D model at 0.387m from charge

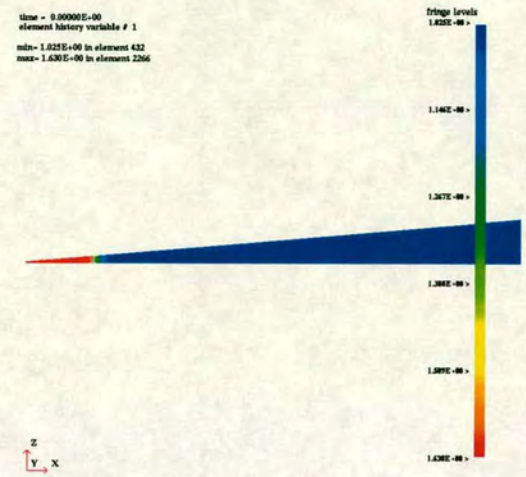

(a) t = 0.0ms

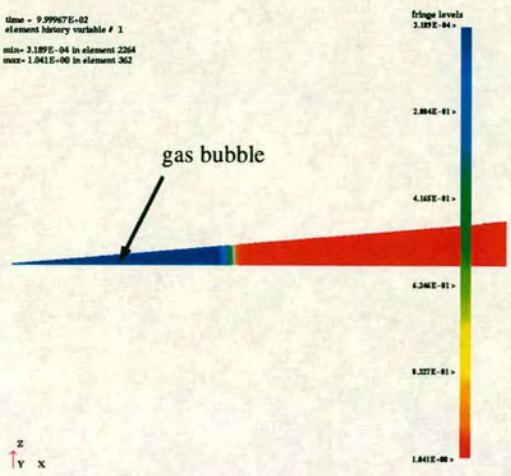

(b) t = 1.0ms

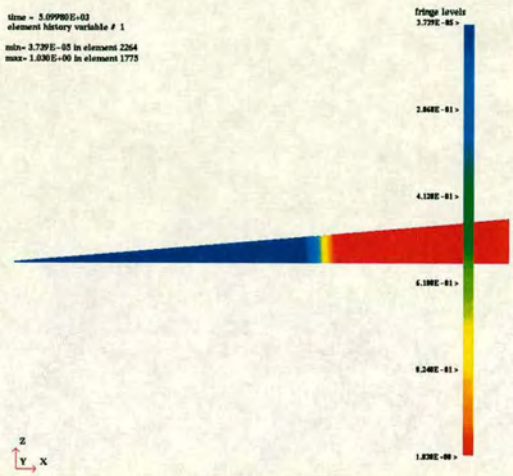

(c) t = 5.0ms

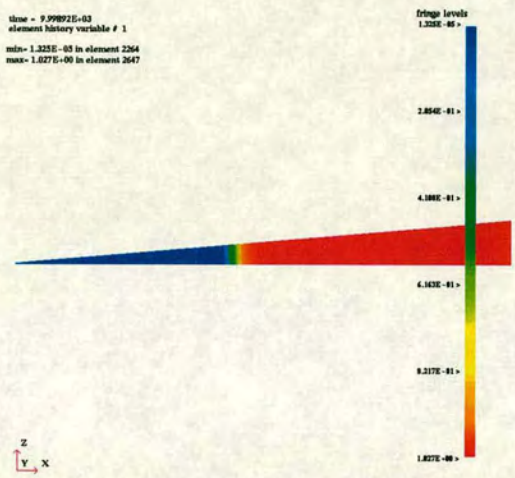

(d) t = 10.0ms

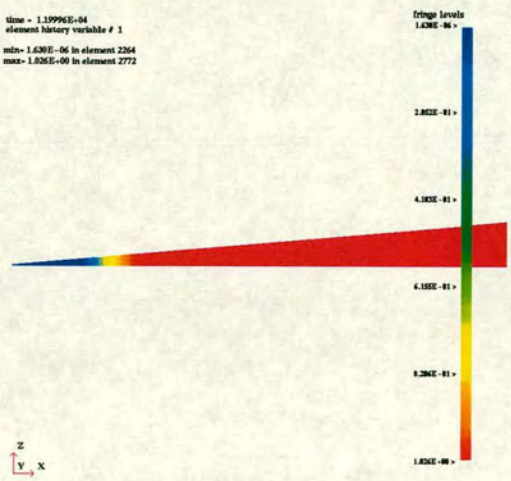

(e) t = 12.5ms

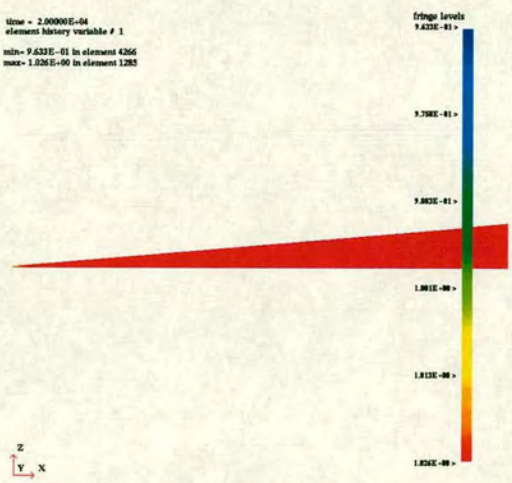

(f) t = 20.0ms

Figure 3.20: Expansion and contraction of UNDEX bubble for quasi-1D model (density units = $\text{kgm}^{-3} \times 10^{-3}$)

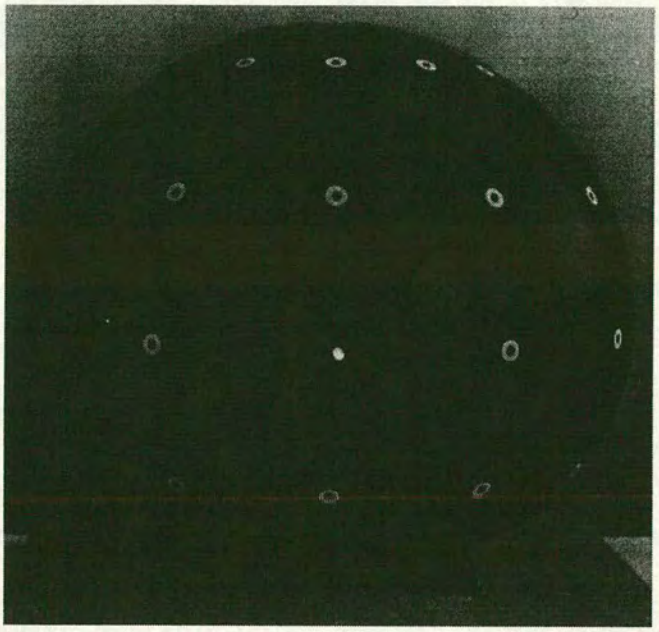

Figure 3.21: Prototype echinodome shell

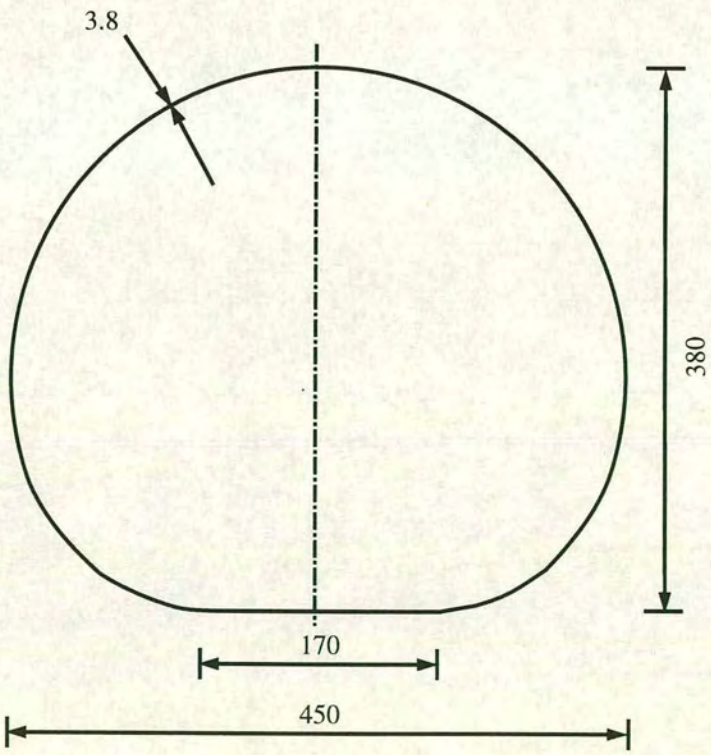

(dimensons in mm)

Figure 3.22: Prototype shell dimensions

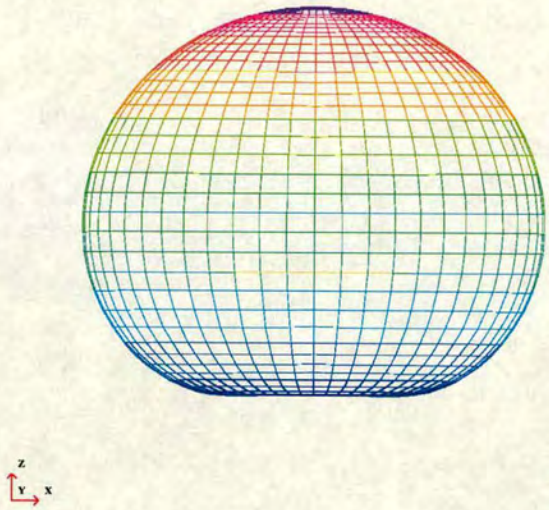

(a) 896 elements

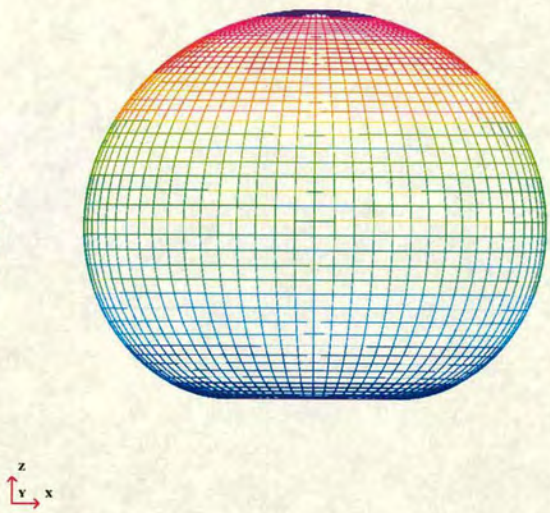

(b) 2124 elements

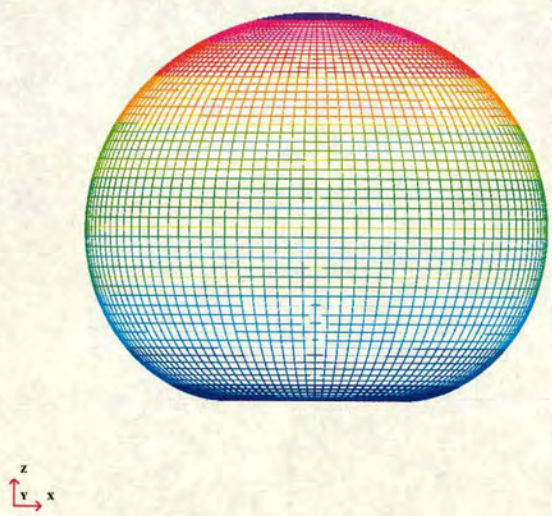

(c) 4248 elements

Figure 3.23: Finite element meshes of prototype echinodome shell

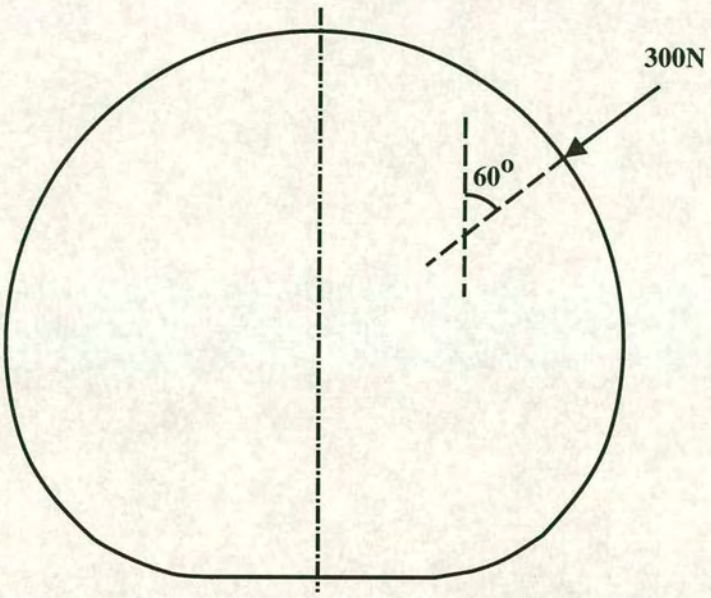

Figure 3.24: Load application point on echinodome shell

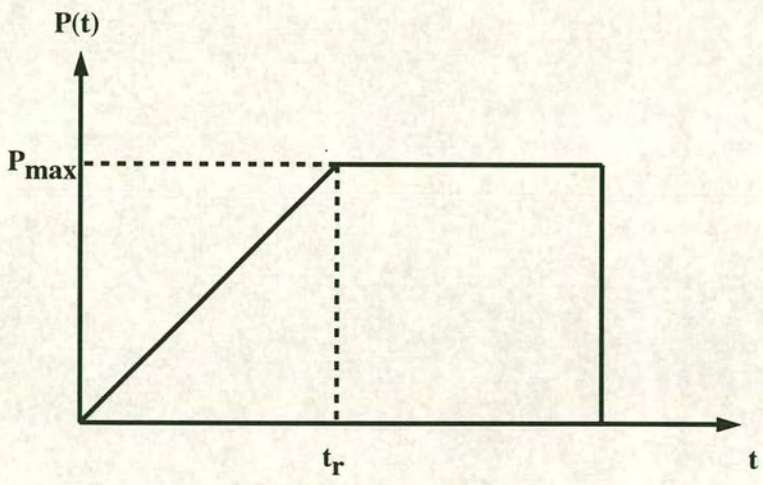

Figure 3.25: Variation of load with time

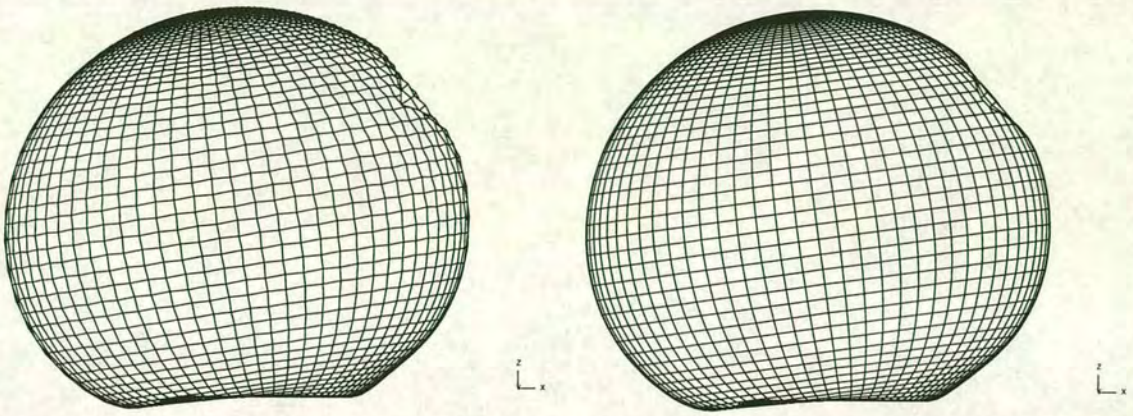

(a) Hourglassed mesh (concentrated ramped point load)

(b) Smooth mesh (ramped pressure load)

Figure 3.26: Deformations due to 300N load (disp. $\times$ 100)

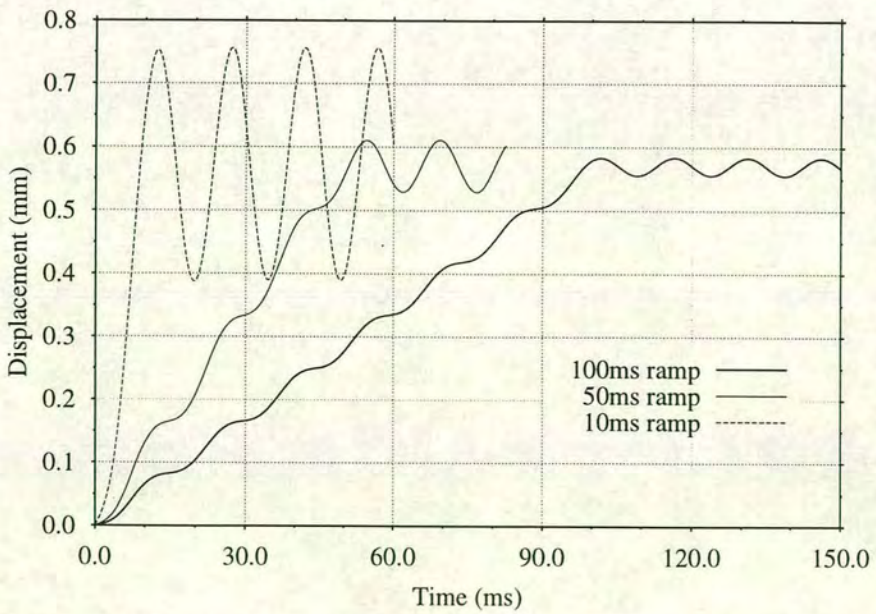

Figure 3.27: Slow transient displacement due to ramped 300N pressure load

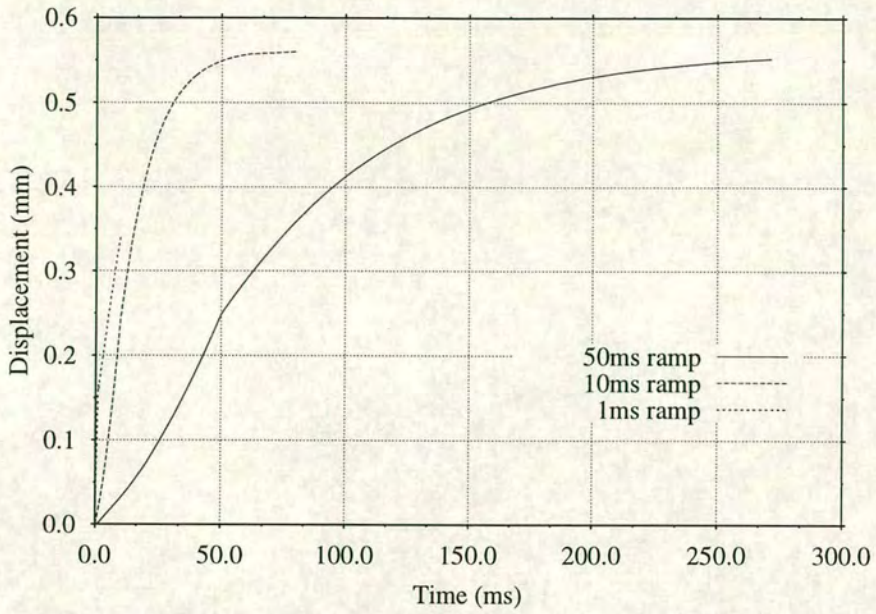

Figure 3.28: Dynamic relaxation displacement due to ramped 300N pressure load

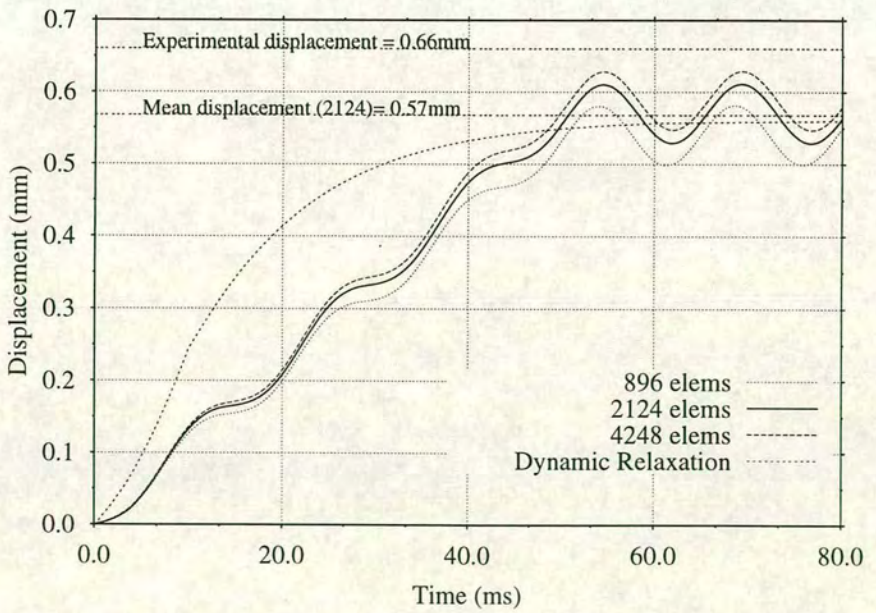

Figure 3.29: Displacements of various discretisations at load point due to ramped 300N pressure load

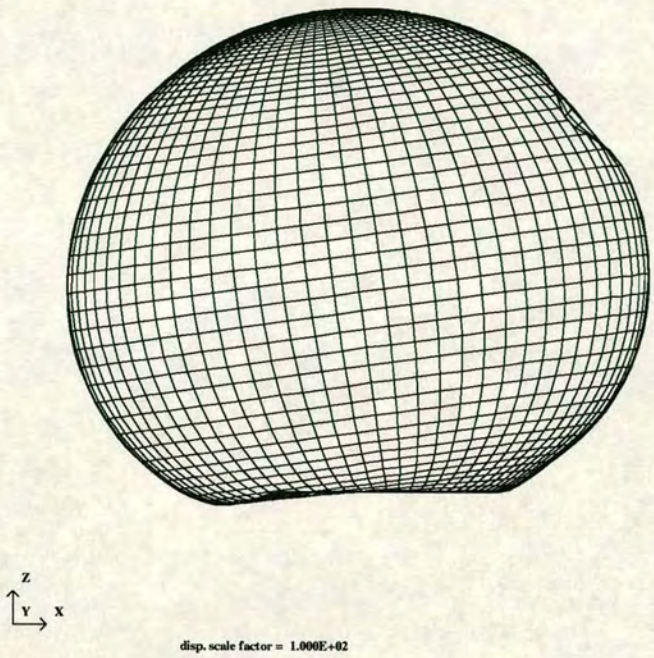

(a) Final deformed shape

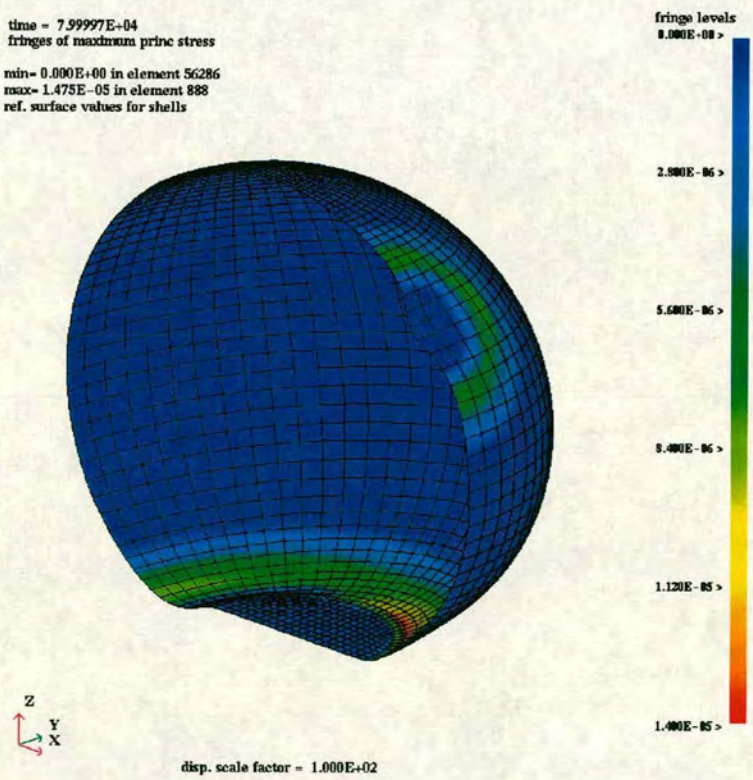

(b) Maximum principal stresses

Figure 3.30: Simulation results due to ramped 300N pressure load on prototype echinodome (disp. $\times$ 100)

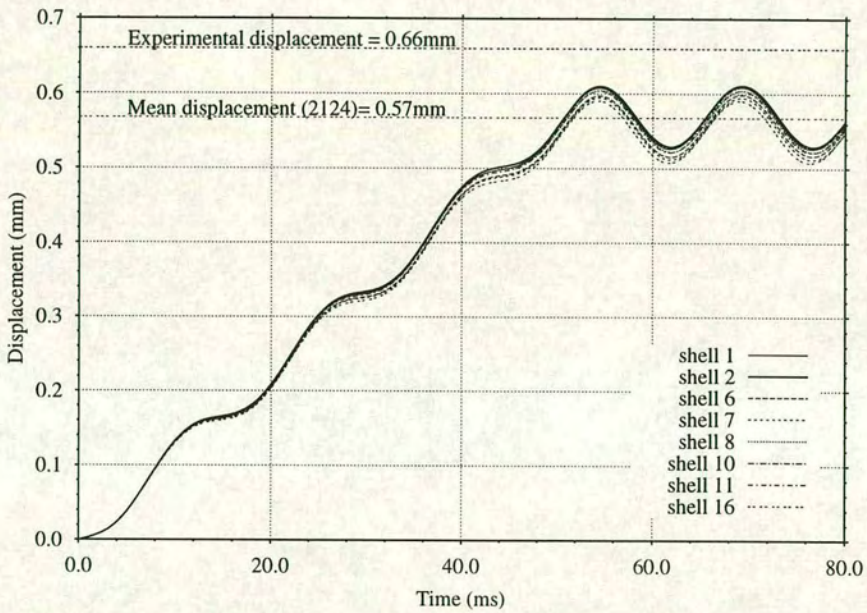

Figure 3.31: Displacements of various shell formulations at load point due to ramped 300N pressure load

Chapter 4

Verification of numerical simulation of UNDEX loading

4.1 Introduction

The foundations for utilising LS-DYNA to simulate UNDEX loading have been established in the previous chapter. LS-DYNA's ability to model detonation, shock wave propagation and free field fluid response using the multi-material Eulerian capabilities were successfully validated against theoretical and experimental results. The simulation of the bubble pulse, however, was considered inadequate to be endorsed for bubble pulse loading problems. A finite element mesh of the prototype echinodome was validated for transient response to linear quasi-static loading. The model was simplified through appropriate geometric and material descriptions, and an optimum discretisation was obtained.

An assessment of fluid and structural response predictions to UNDEX loading prior to performing experiments would assist in their design such that measurable results could be produced whilst minimising the damage to the prototype. Also, it is important to know the limitations of a model for the purposes of designing experiments which could be simulated.

Fluid-structure interaction under shock loading is modelled using two techniques available, MMALE and DAA. The construction of suitable finite element models, incorporating known experimental factors and the prototype echinodome, is pursued. One UNDEX load case is simulated and some verification of fluid response predictions is made against empirical results. The predicted structural response is also examined to assist in configuring the experiments such that no material failure will be caused by

the pressure loading.

4.2 Effect of experimental setup on numerical model

In using a numerical model to design experiments it is good practice to carefully examine both procedures to ensure resources are not wasted. The form of a numerical model is determined by the reality which it represents. Vice versa, the reality which is being represented should be constrained to the limitations of the numerical model. To perform experiments which cannot be modelled fails to meet the objectives of a simulation. Similarly, to develop a detailed numerical model of an experiment, in its entirety, is time consuming to construct and requires an inordinate number of calculations to obtain the desired results. Both lead to an inefficient use of resources which is unnecessarily expensive.

The following sections provide details of those aspects of the experimental and numerical simulations which influence the form of the numerical model and details procedures aimed at constructing an accurate model whilst minimising the cost of computation.

4.3 Experimental simulation setup

The experiments are to be designed to consider two directions of UNDEX loading on the shell, axisymmetric and symmetric. Axisymmetric loading is to be applied by placing an explosive charge above the apex of the shell, symmetric loading is to be applied using a charge placed off to the side of the shell, at the same depth as the shell's maximum diameter. Several load cases are to be examined for the symmetric direction, but only one for the axisymmetric direction. The hydrostatic conditions for which the shell was designed, combined with these two directions of loading, control where the charge and shell are to be positioned in the test tank.

4.3.1 Test tank

The test tank in which the experiments are to be carried out has dimensions 12.190m $\times$ 6.090m and a water depth of 3.500m, as illustrated in Fig. 4.1. The tank walls and floor are constructed from reinforced concrete and lined with thick steel plates. A wooden platform and movable walkway also form part of the tank.

4.3.2 Position of prototype shell

As Fig. 4.1 indicates, the shell is to be positioned in the tank at a depth of 1.525m, the head of water for which it was designed, 2.800m from the back of the tank (the back being defined as that part of the tank covered by the platform) and 3.045m from the side of the tank (along the longitudinal centreline). The seam of the shell is to lie perpendicular to the longitudinal centreline of the tank. The maximum stand off distance for the symmetric load case, 5.0m, determines its location from the front of the tank. This position allows sufficient time for measurements to elapse between the initial impingement of the shock wave on the shell, and any additional loading from reflections off boundaries and bubble behaviour. The shell is to be empty throughout the duration of the experiments and, consequently, the positive buoyant forces on the structure were resisted by four ropes used to tether the shell to the floor of the tank.

4.3.3 Instrumentation

Pressure and strain gauge rosettes are to be used to record fluid and structural responses to the various load cases. The position of these gauges has been carefully considered to minimise the quantity of data acquired, but obtain sufficient information to observe the sequence of events and validate the computed fluid and structural responses of a numerical model.

Fig. 4.2 details the rectangular strain gauge rosette positions (one gauge aligned with the meridian, oblique at 45^o and circumferential at 90^o) for the prototype shell at $\phi = 0^o$, 30^o, 60^o, 90^o, 120^o and 150^o on the meridian closest to the charge in the symmetric load cases ($\theta = 0^o$). The parallel circle, at $\phi = 90^o$, contains strain gauge rosettes on meridians $\theta = 0^o$, 30^o, 60^o, 120^o, 150^o, 180^o and 270^o. Previous dynamic loading studies[4] indicated weaknesses in the prototype near the base of the shell, which denoted the need for several strain gauges in this region. Strain gauge rosettes left over from previous experiments on the interior surface at $\phi = 150^o$, on the 0^o and 180^o meridians, were utilised, and external gauges were placed at the same locations. It was decided to ignore shear and normal strain responses from the shell strain levels in these two directions as they were expected to be negligible compared with strains in the circumferential, meridional and oblique directions. Consequently, all strain gauge rosettes are to record three strain results at every location.

Pressure gauges are to be located on the shell at $\phi = 0^o$, 45^o, 90^o and 135^o on the $\theta = 0^o$ meridian, and at $\theta = 90^o$, 180^o and 270^o on the maximum diameter.

In order to avoid repeating the instrumentation procedure after a load case is complete it is a requirement that one instrumentation configuration obtains sufficient information concerning the load distribution and structural response for both the axisymmetric and symmetric load cases. This requirement is satisfied by placement of the gauges at the positions indicated and determined mainly by the arrival of the shock wave at the shell.

Several aspects of the fluid response are of interest, namely the sphericity of the shock wave, the free field pressure at the stand off distance, i.e. the load as seen by the nearest point on the shell to the charge, and the fluid response at the shell. The setup shown in Fig. 4.3 illustrates the relevant positions of the pressure gauges in the fluid as being at 1.0m, 2.0m, 3.0m, 4.0m and 5.0m from the charge. This was for the 5.0m symmetric load case only. For the remaining symmetric load cases PGs 8 and 9 are to be used to obtain free field data at 1.0m stand off distance and a third gauge is to be placed on the rod (shown in Fig. 4.3) at a distance equivalent to the minimum stand off between the charge and the prototype shell. For the axisymmetric load case PGs 8 and 9 will be used at a 1.0m stand off distance and the third gauge is to be located 0.075m below the free surface (0.45m stand off), directly above the charge, to record bulk cavitation.

4.3.4 Charge

The charge location is governed by the position of the shell in the tank and varies according to the stand off distance and the loading direction. For all symmetric load cases the depth of the charge is to be 1.728m, the same depth as the maximum diameter of the shell. However, the stand off distance varies for each individual load case in the range 2.0 – 5.0m at 1.0m intervals, as shown in Fig. 4.3.

Fig. 4.1 shows the axisymmetric load case with the charge location fixed at 1.0m above the structure. This ensures that if the gas bubble radius expanded to more than 0.525m then it would be forced to vent, and so eliminate bubble loading on the structure. At that radius there is a risk that the bubble pulse might invoke geometric or material non-linearities on the prototype shell.

The charge used is to be made from EDC-1 material, cylindrical in form and held in place by a metal frame supported on the traversing walkway in each load case. The simulation of the load case with the closest stand off distance, and hence most severe loading on the shell, will provide sufficient information, regarding shell integrity, for the design of all the load cases. The axisymmetric load case is noted to have the closest stand off distance. Results from experiments performed previously combined

with numerical results from this work provided guidance to an initial estimate for a suitable charge mass that produces measurable strains on the prototype but does not invoke material or geometric non-linearity.

4.4 Numerical simulation setup

It could be concluded from the above discussion that only the axisymmetric load case required modelling to provide sufficient data for the choice of a suitable charge mass for all load cases, since it is likely to induce the severest loading. The influence of the experimental setup on the construction of suitable numerical model is now considered.

4.4.1 Fluid and test tank

A numerical model of the entire test tank is complicated to construct and expensive to analyse. Closer examination of the nature of the structure and applied loading reveals that axisymmetry could be exploited. Reductions to the extent of the fluid region, using symmetry planes, would reduce the pre-processing time and computational cost of the numerical model considerably. For the axisymmetric load case a quarter model was initially used. The vertical symmetry planes act in the same manner as reflecting boundaries where fluid is assumed not to flow normal to the boundary, only along it.

Gravity could also be included to model the hydrostatic pressure on the shell. The structure being positioned at a depth of 1.525m would undergo the application of hydrostatic pressure prior to the arrival of the shock wave, of approximately 15.0kN at the apex. The initial stress due to hydrostatic pressure was found earlier to invoke negligible stresses on the shell[4]. The atmospheric pressure was considered to add negligible pressure to the existing hydrostatic pressure and hence was ignored.

In order to avoid modelling the materials used in the walls and floor of the tank they will be assumed perfectly rigid acting as reflective boundaries. The platform and walkway, although used in the experiment, do not perform any function other than for positioning instruments and charges and therefore were not required to be modelled.

4.4.2 Prototype shell

A similar structural mesh to that concluded from the analysis in chapter 3 will be adopted, with axisymmetric conditions declared according to the fluid mesh chosen. The number of elements discretising the numerical model of the shell was reduced to

1062 elements. Geometric and material non-linearities were not expected to occur from this load case, hence the same elastic material model could be utilised. The shell is to be modelled as empty, or air backed.

4.4.3 Position of prototype shell

To ensure experiment-model continuity, the shell was positioned relative to the free surface and the side walls, as according to the experimental setup. The influence of the rope on the shell's behaviour was found to be negligible from strain measurements recorded in previous experiments[4]. The ropes constituted a neutrally buoyant state for the shell as the buoyancy force on the structure is balanced by the force on the ropes, and is approximately equal to 450N. Neglecting the buoyancy forces in the numerical model, which are negligible compared to the forces applied under shock loading, will ensure the structure is in a neutrally buoyant state. Hence it was not necessary to model the rope tethers.

4.4.4 Instrumentation

The position of the gauges on the prototype and within the fluid determine from which shell and brick elements output should be requested to predict the structural and fluid responses discussed above. Shell normals point into the fluid defining the upper surface of the shell as the outer surface on which the strain gauge rosettes will be bonded. Exploiting axisymmetry has the benefit of reducing the numerical output.

4.4.5 Charge

A cylindrical shape with a height to diameter ratio equal to unity was adopted which approximated a spherical shape and hence a spherical shock wave was expected to propagate from it. It was located at the stand off distance, 1.0m above the apex of the shell, and orientated such that its longitudinal axis lay on the same line as the axis of symmetry of the prototype shell. The frame used to locate the charge had no influence on the loading of the structure and hence did not require modelling.

A model of a cylindrical 10g charge of EDC-1 properties was initially used to provide the loading. This decision was based on an estimate from strains measured from previous experiments, combined with knowledge of the ultimate strength of the material. From the ultimate tensile strength of the material a static material failure strain was calculated to be -6295$\mu\varepsilon$. Despite the possibility of a reduction in impact

strength due to heating effects[81], the failure strain under dynamic, compressive, loading would attain higher strain levels than this value, hence this was regarded as a conservative datum when designing the experiment. Details of the calculation used to estimate this charge size are given in appendix A.

4.5 Numerical simulation of UNDEX loading

To determine the most efficient discretisation for an UNDEX loading simulation, a similar procedure to that used for the free field UNDEX and structural response simulations in chapter 3 was adopted. Construction of suitable numerical models for both the MMALE and DAA approaches is discussed in the following sections and the predicted results presented thereafter.

4.5.1 MMALE analysis

Despite attempting to reduce the size of the model by exploiting axisymmetry, the charge size forced a costly reduction on the element size.

It was concluded in chapter 3 that, to accurately simulate the detonation of a charge and subsequent fluid pressure, a significant number of elements are required for the charge, and the surrounding fluid elements should be of the same order of size in the direction of propagation. The radius of the cylindrical 10g charge is 7.63mm. A material in LS-DYNA is required to be initialised by element rather than by geometry. To accurately model such a small charge, and the fluid region of interest, i.e., the 1.0m of fluid between the charge and the structure, would result in a large number of small elements. The small element lengths would control the timestep for the entire analysis due to the explicit time integration scheme used in LS-DYNA.

To keep the number of elements in the mesh to a minimum, transitioning and biasing techniques were adopted in mesh construction.

- **transitioning** – three elements converge into one element through the use of a transition zone comprising irregular elements (see Fig. 4.4(a)),
- **biasing** – element intervals are of a non-uniform size, increasing with distance from the region of interest (Fig. 4.4(b)).

Maintaining mesh quality is important in constructing a finite element model for preserving accuracy, particularly in tracking shock waves through a fluid. The quality

of the mesh can be measured using the aspect ratio and the physical regularity observed by eye. As discovered in chapter 3, smearing of the shock front could occur even in a regular mesh with a good aspect ratio (< 5), reducing the pressure at the wave front which would reduce the loading applied on a structure. As is evident from Fig. 4.4(a) transitioning preserves a good aspect ratio in x, y and z directions, but introduces irregular elements in the transition zone. Biasing maintains regularity in a mesh only in the diagonal direction and the increasing aspect ratio in the x, y and z directions reduces mesh quality rapidly.

4.5.1.1 Quarter symmetry model

To form a quarter symmetry model the region cut by the meridional planes, $\theta = 0^o$ and 90^o on the structure, were declared as symmetry planes (see Fig. 4.2). The fluid immediately surrounding the structure extended to the bottom of the tank, the free surface and out to the tank walls. A total of 506634 multi-material Eulerian brick elements were used to model this fluid region, and 200 to represent the charge. This included transitioning and biasing to reduce the number of elements away from the region of interest.

The estimated solution time for this model on a 300MHz DEC-Alpha 8400, based on a timestep calculated using the smallest element length and density associated with the shell model, was approximately thirty days. Dynamic buckling predictions are intended to be made using the MMALE technique, and an adequate dynamic buckling study would require approximately 8-10 runs. Such a study, with CPU times of this magnitude, was impractical in the time available. Hence an alternative form of model was sought.

4.5.1.2 Pseudo-wedge axisymmetry model

The large number of complex computations associated with the MMALE method could be reduced in several ways. The most obvious way was to make further reductions in the number of elements discretising the fluid region.

Collaborations with DERA[73] led to the development of a quasi-three dimensional wedge model using TrueGrid[62]. The wedge was moulded from a regular block using one element in the circumferential direction to subtend an angle of 22.5^o about the axis of symmetry, as illustrated in Fig. 4.5. This resulted in reducing the propagation of the shock wave to two dimensions.

In chapter 3 it was concluded that the collapsed brick wedge element could not be used for UNDEX studies. In an attempt to overcome this restriction, a small hole was incorporated through the axis of symmetry of the model, thus permitting a brick element to be used without collapsing one face, forming a pseudo-wedge model. The radius of the hole was fixed at 20% of the charge radius. The hole, combined with the angle of the pseudo-wedge, would result in an energy loss in the detonated explosive of $\approx 4\%$, a negligible reduction in the UNDEX loading on the shell.

The pseudo-wedge model was initially constructed as a radial wedge mesh of 37320 multi-material Eulerian brick elements, 18 of which defined the charge. A radial mesh was chosen, based on the quality of results from the sphere free field model in chapter 3. A mesh with similar geometry to that of the shock wave was found to maintain the shock wave's sphericity, and improved the tracking of pressure at the wave front. The geometry and discretisation of the shell had to be modified to a similar form as the fluid. The general coupling technique was used to simplify the incorporation of the shell model into the fluid and to exploit the adaptivity feature available for Lagrangian elements, to refine the structural mesh so as to improve the accuracy of the predicted response. The shell elements were approximately the same size as the fluid elements.

As the element size increased radially outwards using such a mesh, as discussed in chapter 3 regarding the free field UNDEX sphere model, transitioning was necessary to reduce the size of the fluid elements to approximately those of the shell. This ensured the shock loading would be applied to the majority of the shell elements. Accurate tracking of the shock wave beyond the structure, as far as the fluid mesh boundary, was not practical with this form of mesh. Hence transitioning was used to increase the element size again. The fluid mesh boundary was placed 4.0m away to avoid reflections interfering with the structural response.

4.5.1.3 MMALE problem issues

Coupling – upon initialising the model, investigation of the output revealed that the elements inside the coupling surface were not being declared as void using the *INITIAL_VOID card, at time $t = 0$. As a result the structure was being initialised by LS-DYNA as water backed. This is evident from the density contour plot shown in Fig. 4.7(a). As the shock wave was reflected off the structure a pressure wave was evident on the inside of the coupling surface from a contour plot of the pressure (see Fig. 4.7(b)) which, for a water backed structure, would occur in reality, but for this study the prototype shell is air backed. The only alternative was to use the ALE coupling method. This restriction on the fluid mesh impelled an alternative model for

the prototype shell to be constructed, the number of shell elements being governed by the number of fluid elements next to the structure. This restriction placed a further obstacle on the use of the adaptivity feature. A refinement of the Lagrangian structural mesh would require a corresponding refinement of the Eulerian mesh. The adaptivity feature has not been extended to the Eulerian formulation at the time of writing.

Free surface – bulk cavitation occurs if the negative pressure of the rarefaction wave is of greater magnitude than the decaying pressure of the incident shock wave. To accurately represent a rarefaction wave from the free surface, the correct boundary conditions must be assigned to the model. The particle velocity at the free surface is known to be twice the normal component of the incident wave[15], hence flow normal to the boundary must be permitted.

Air was initially included in the radial model in an attempt to represent the free surface. The initialisation of materials by element rather than by geometry presented a difficulty for the free surface in that, because specific elements had to be assigned with air, a smooth interface could not be defined. An alternative rectangular pseudo-wedge was then adopted to create a level interface with 0.20m of elements above the free surface assigned with material properties for air. The elements discretising the air were later omitted when it was discovered that the multi-material feature only permitted two materials in a mesh in any one run, not three. Several alternative representations of the free surface were examined,

- solid Lagrangian elements representing air;
- the stick and slip Euler boundary conditions discussed in chapter 2; and
- single point constraints (SPCs) on the nodes at the free surface.

The solid Lagrangian elements caused severe deformation of the Eulerian mesh when the shock wave reached the free surface. The nodes shared between the Eulerian and Lagrangian elements at the free surface interface behave with Lagrangian motion and hence move with the material, which is moving with a velocity of several thousand metres per second at this point. Of the two Euler boundary options, neither was considered an accurate representation of the free surface as normal velocity is set to zero at the boundary by both options.

The most accurate boundary conditions achieved from the above study was for SPCs to be applied to the nodes at the free surface, restricting material to move in the z direction only. This forced the material velocity to double in the vertical direction and

reduce to zero in the horizontal direction, thus allowing cavitation to form at the free surface.

Transitioning and biasing – transitioning and biasing techniques were again used in the rectangular pseudo-wedge mesh to increase the element size after 0.70m from the charge resulting in a fluid mesh consisting of 35902 multi-material Eulerian brick elements. However, the unexpected problem of reflections, illustrated in Fig. 4.8(a), was encountered from the transition elements and also from biased regions where the increase in element size was sudden (not shown). Fig. 4.8(b) clearly shows a sharp rise in pressure 30.0mm before the transition zone shortly after the arrival of the shock wave. Furthermore, the pressure 30.0mm after the transition zone was indicating a peak pressure at the shock front 35% less than at 30.0mm before. Previous analytical and experimental observations[15] showed a rapid reduction in shock front peak pressure with distance, close to the charge (< 25 charge radii), however, at larger distances from the charge the reduction in peak pressure became progressively lower. The transition zone in the rectangular wedge mesh was located at 91 charge radii implying that the difference in pressure before and after the zone should have been small. That a reduction of 35% was predicted can only be explained by the irregular elements of the transition zone obstructing the advection of the flow and causing the pressure after the zone to be reduced due to reflections.

The fact that the transition and biasing regions were not of the same spherical form as the propagating shock wave was thought to be the cause of the reflections, as none was apparent in the pressure contours of the radial pseudo-wedge mesh. However, examination of the peak pressure before and after the transition zone revealed a drop in pressure of 70-80%. In both the radial and rectangular pseudo-wedge meshes the irregular element shape and different dimensions at the transition zone corresponded to an interruption in the regular advection of material through the zone, introducing a hidden boundary from which the reflections were seen to propagate. These reflections would eventually interfere with the expansion of the explosive gases. This discovery highlights the numerical sensitivity of these pre-processing techniques, and their application to finite element simulations, particularly in modelling fluid transport, requires caution.

As a consequence of these numerical boundaries the transition zones were removed from the rectangular pseudo-wedge mesh and the biasing altered to entail a more gradual increase in element size, This had the repercussion of increasing the number of elements in the mesh. A good aspect ratio was conserved in the fluid region surrounding the charge and the structure to maintain mesh quality so as to track the shock wave

accurately from the charge to the structure.

In an attempt to reduce the number of fluid elements the total depth of water modelled was reduced from the 3.5m depth of a full test tank to 2.910m, i.e. 0.59m from bottom of the tank, and a rigid boundary was placed 4.0m away from the axis of rotation. These boundaries at the bottom surface and side walls of the tank are sufficiently far away that reflections from them will not interfere with the shock loading on the structure.

4.5.1.4 Summary details of numerical model

The final mesh was constructed in TrueGrid using twenty six parts in total. The fluid elements were divided into separate blocks primarily to ease construction of the mesh. However, the separate parts also served to minimise the number of elements requiring ALE smoothing constraints. ALE smoothing was permitted in each region of fluid which had nodes coincident to the Lagrangian elements of the shell model. Rigid boundaries were declared 4.0m from the axis of rotation and 2.910m below the free surface. Flow normal to the free surface was permitted using SPCs.

All elements were moulded to surfaces to create a 22.5^o pseudo-wedge model with a hole incorporated at the axis of symmetry. The fluid region was meshed with a total of 81628 multi-material Eulerian brick elements, and the *MAT_NULL material card combined with the Gruneisen equation of state (Eqn 3.4). Hydrostatic pressure was included in the model in the form of a density vs depth curve[55]. Atmospheric pressure was assumed to equal zero. Some biasing was applied to the fluid elements in regions where accuracy was not important, i.e. towards the rigid boundaries. The beginning of this biasing can be observed in Fig. 4.6(a). Pressure cut off in the fluid was declared as zero[23] initially.

The 10g charge was meshed using 10 multi-material Eulerian brick elements, and the *MAT_HIGH_EXPLOSIVE_BURN material card combined with the JWL equation of state (Eqn 3.1). The JWL constants for EDC-1 are given in table 3.1.

As mentioned earlier the number of elements representing the prototype shell was governed by the number of fluid elements next to the shell (see Fig. 4.6(b)). Using the ALE coupling technique, 93 Belytschko-Lin-Tsay Lagrangian shell elements were tied to the fluid elements. The original material properties used in chapter 3 were retained in this new model.

Fluid and structural responses for the first 5.0ms were of interest, enough time for the shock wave to completely engulf the structure, but insufficient time to allow interference

by boundary reflections. The findings from chapter 3 concluded the donor cell & HIS advection scheme to be the most computationally efficient for a free field UNDEX problem. However, this may not necessarily be the case for UNDEX problems involving FSI, therefore all four schemes were tested again. Strain and pressure gauge output was requested every microsecond for all positions modelled, and binary plot data every 100μs. The solution time of this model was estimated to be approximately thirty hours.

4.5.2 DAA analysis

Application of the DAA technique to the axisymmetric load case proved to have much fewer problems associated with it than the MMALE technique. This was mainly due to the exclusion of the fluid geometry, meaning that fewer elements were required. Hence concerns over solution times were minimal. The absence of the charge geometry also eliminated any restrictions on the element sizes and mesh geometry.

Two models were developed for the DAA-MAT90 and DAA techniques based on the half symmetry shell prototype model developed in chapter 3. The model could have been reduced by exploiting the same axisymmetry as in the MMALE method. However, since the execution time involved in the DAA technique is much less (see section 6.5) it was concluded unnecessary. A half model aids the visualisation and understanding of the structural deformation. Structural motion normal to the symmetry plane was constrained.

DAA – the DAA boundary elements were placed next to the wet surface of the structure, positioned so that the nodes of the structural and DAA boundary elements coincided creating a total of 2124 DAA boundary elements. The positive normal of the shell elements and boundary elements was orientated away from the structure, i.e., into the fluid domain. The second order accurate form of DAA elements, DAA_2, was used for the calculation of fluid pressures at the shell. The mesh is illustrated in Fig. 4.9.

DAA-MAT90 – in order to validate the DAA-MAT90 approach initially a benchmark problem of similar geometry to the echinodome was used[73]. A layer of 0.25m of solid acoustic elements was included around the model to represent the fluid domain. The extent of the fluid domain was determined by estimating the size of the non-linear cavitation region and the prevention of reflections from the numerical boundary interfering with the shell response. The nodes of the acoustic elements were aligned such that they coincided with the nodes of the shell model. The DAA boundary elements were repositioned at the exterior of the fluid domain, with the

element normals pointing away from the fluid, functioning as a radiating boundary creating a semi-infinite fluid domain around the shell model.

To test for convergence a model comprising a 0.50m acoustic layer was also constructed. A comparison of the fluid response at the shell surface, revealed that predicted peak total pressures were closer to experimental values using the 0.25m layer. However, a comparison of the strain response at $\phi = 30^o$ from the apex, indicated the opposite to be true for the predicted peak strains. This contradiction was attributed to the more dense acoustic element spacing in the 0.25m layer. Consequently, the density of the element spacing in the 0.50m layer was increased. This 0.50m acoustic domain was then used as the DAA-MAT90 model.

The final fluid domain adopted comprised 93456 acoustic elements with material definition *MAT_ACOUSTIC[55]. Damping and cavitation options are available with this material definition. Numerical damping is a feature of the acoustic elements which incorporates the damping effect of the surrounding fluid on the shell. The damping is controlled by a damping ratio, β, lying within the range 0.0 – 1.0. A value of 0.1 was initially chosen. The cavitation option was activated to capture any cavitation. The same symmetry conditions as the structure were applied to the fluid domain. Only the first order accurate form of DAA elements, DAA_1, was available for use in conjunction with the DAA-MAT90 technique. The mesh is illustrated in Fig. 4.10.

The pressure loading input for the 10g charge of EDC-1, at a stand off distance of 1.0m above the structure, was described initially using a theoretical peak pressure and decay rate calculated from empirical equations[73]. These were given as $P_{max} = 9.300$MPa and $\theta = 29.5\mu$s. The equations used were derived from many experiments performed using large charge sizes. The above values were assumed to be higher than would be expected of a 10g EDC-1 charge, but are commonly used at the design stage of experimental tests.

Reflections can be accounted for in the DAA technique using imaging techniques[56]. However, since reflections were not expected to interfere with structural response in the analysis time being examined here (5.0ms), such features were not utilised.

4.6 Numerical simulation results

The results obtained from the MMALE and DAA axisymmetric models discussed in the previous section can be subdivided into three sections: free field fluid response; fluid response at the shell; and shell response. All data is analysed as direct output

Advection scheme	Free field peak pressure (MPa)	Peak strain at apex ($\mu\varepsilon$)	Time per zone cycle (μs)	Solution time (s)
Donor cell	5.083	-4709	49.551	59775
van Leer + HIS	4.861	-4959	88.503	106716
van Leer	5.136	-4451	64.712	78047
Donor cell + HIS	4.770	-4568	54.519	65758

Table 4.1: Comparison of UNDEX-FSI solutions for various advection schemes

from the simulations.

Prior to presenting the results of the MMALE simulations it is appropriate at this point to discuss the differences in the advection schemes for UNDEX simulations involving FSI. Figs 4.11(a) and (b) and Fig. 4.12 show the free field pressure at 1.0m stand off, and, total pressure and strain levels recorded at the apex and base regions (known critical locations on the shell). Table 4.1 lists the solution times for each advection scheme.

Compared to the default scheme (van Leer & HIS) the free field pressure is predicted to be approximately 5% greater using the van Leer scheme, and the peak total pressure is concurrently predicted to be approximately 30% higher at the apex (see Fig. 4.11(b)), The strain levels on the other hand, are 10% higher at the apex using the default scheme. Negligible difference is noticed at the base.

The van Leer advection scheme is second order accurate, i.e. the quadratic terms of the velocities are calculated, compared to the first order accuracy of the default scheme. It was recommended by the authors of the code to use the default scheme rather than the van Leer scheme. However, as is evident from table 4.1, the default scheme takes 35% longer to solve. Comparison with experimental data would be required to validate the various schemes. However, for the remaining simulations in this chapter, the van Leer scheme is adopted on the basis of the cheaper computational cost and associated higher degree of accuracy, although no validation can be made at this stage.

4.6.1 Free field fluid response

Hydrostatic pressure

Accurate representation of the hydrostatic pressure ensures the initial pressure conditions are included for bubble motion. Fig. 4.13 shows a contour plot of the hydrostatic pressure at time $t = 0$ for the MMALE model. The pressure in the fluid is seen to increase linearly with depth, as expected, from 0 at the free surface (assuming atmospheric pressure $P_a = 0$) to a maximum pressure of 28.5kPa at the bottom of the tank corresponding to 2.910m. At the apex of the structure the pressure is 14.9kPa corresponding to a head of 1.525m, i.e., the design head of the prototype shell.

In the DAA-MAT90 technique the shock wave is initialised at time $t = 0$ and the pressure in the acoustic elements is set relative to the pressure in the shock wave. Although input explicitly, the hydrostatic pressure is not observed in the contour plot, however, it is observed in the pressure records (see section 4.6.2). This hydrostatic pressure is not applied to the charge in the MMALE analysis.

Shock wave propagation

A spherical shock wave was observed to propagate through the fluid from the detonated cylindrical charge (10g EDC-1) as expected, in both techniques. Fig. 4.14(a) shows the shock wave in the MMALE mesh several microseconds after the detonation wave reached the perimeter of the charge material. Pressures at 0.25m radius above ($\phi = 0^o$), to the side ($\phi = 90^o$) and below ($\phi = 180^o$) the charge were recorded (see Fig. 4.14(b)). The arrival time of the shock wave at this distance is observed to be approximately 0.15ms at all three locations. The highest peak pressure recorded was 45.9MPa at 0.25m above the charge, the lowest was 36.8MPa to the side of the charge. A variation in peak pressures might have been expected from a cylindrical charge had the height to diameter ratio been greater or less than one. However, in this simulation the height to diameter ratio is equal to one. Hence, the 25% variation between the pressures at $\phi = 90^o$ and the other two locations are most likely due to numerical loss of pressure caused by deterioration of mesh quality away from the charge in the $\phi = 90^o$ direction.

Free field pressure

Fig. 4.15(a) shows the shock wave initialised in the DAA-MAT90 mesh at time $t = 0$, one element away from structure. The pressure-time curve, applying the UNDEX

loading to the structure, is illustrated in Fig. 4.11(a). On the same graph, this is compared with the numerical pressure-time curve predicted by the four advection schemes at 1.0m from the charge, which represents the transient load the structure in the MMALE analysis is subjected to, and the pressure-time curve obtained from a one eighth sphere free field model. The numerically estimated peak pressure of 4.860MPa is much lower than the empirical value of 9.300MPa and the pressure-time history is disappointing. The empirical peak pressure value is not considered to provide an accurate verification of the numerical prediction for reasons explained earlier (see section 4.5.2). The one eighth sphere free field mesh from chapter 3, for 2kg EDC-1, serves as a more appropriate verification. For 10g EDC-1 a peak pressure of 6.046MPa at 1.0m stand off is predicted by this model.

It is worth noting that in the MMALE analyses, the mesh approaching the apex of the structure is of a higher quality than the mesh approaching the measurement point at 1.0m. Consequently, the load on the structure is expected to be higher than that predicted. Several oscillations of decreasing magnitude are observed in the decay part of all the 1.0m pressure-time curves calculated from the MMALE analyses. Although pressure oscillations in the tail of the shock wave have been recorded in previous experimental work[15] such disturbances of this magnitude are uncharacteristic and are considered numerical rather than physical. Similar oscillations were observed and explained in the one eighth sphere free field model in chapter 3.

Free surface cavitation

Usually where rarefaction waves occur cavitation is common. Water under normal conditions can withstand several MPa in tension[15] beyond which the water density falls close to zero and the tensile force of the rarefaction wave causes the water particles to separate and a cavitation region is formed.

By declaring a pressure cut off of zero[23], negative pressures would not be resolved in the MMALE model. A pressure cut off of -0.1MPa was also used, however, apart from a minimum value of -0.1MPa rather than zero, no difference was observed in the peak pressure results. A cavitating region could be considered as a region of very low density. A density contour plot (see Fig. 4.16(a)) indicates that at time $t = 5.0$ms a significant cavitating region has formed next to the free surface. This suggests rarefaction waves are being modelled at the free surface and causing the water in this region to undergo significant tensile forces. At the shell a similar phenomenon is noticed at the apex and the base (see Fig. 4.16(b)). Under the impingement of the shock wave the shell surface is accelerated downwards and the sudden movement would cause separation between

the water and the shell membrane. Cavitation is also observed to be occurring at the base. Such a phenomenon has been observed elsewhere[73]. As the shell membrane oscillates at high frequencies, separation occurs in the fluid next to the shell surface.

Gas bubble

In Fig. 4.16(a) a gas bubble is observed to expand radially outwards from the centre of the charge. By this time the density of the gases within the bubble would have reduced considerably from the initial density of the charge (1795kgm^{-3}) to values one order of magnitude lower.

Further study of the bubble loading caused by expansion and contraction cycles is estimated to require approximately 600hrs on the currently available computing resources. Due to time constraints such a study was not pursued in this work. For the purpose of designing the experiment the bubble pulse loading was not considered as crucial as the shock pulse loading since any damage to the prototype shell was expected to be initiated by the shock pulse.

4.6.2 Fluid response at shell

Pressure

Total pressure-time histories one element away from the shell for $\phi = 0^o$, 45^o, 90^o and 135^o are illustrated in Fig. 4.17 and 4.18 for MMALE and DAA-MAT90 meshes. The record does not resemble that of the free field pressure-time history. Instead an initial peak is accompanied by multiple pressure peaks of varying amplitude.

The total pressure is calculated to be lower than that recorded at the free field position. By definition the total pressure should be greater than the free field pressure since it comprises both the incident and scattered pressures. The DAA-MAT90 analysis pressure-time history predicts that the total pressure is higher than the incident pressure for the same position. The shell model used in the MMALE analysis has fewer elements, and is perhaps too simplified, to obtain the accurate effect of its response on the fluid. Also the acoustic element formulation does not calculate pressure in the same way as the pressure volume relationship used for the Eulerian element.

Negative pressures are not observed in the MMALE pressure records due to the zero pressure cut off. However, times of zero pressure could represent cavitation. In the same way the DAA pressure records also indicate cavitation occurring at several positions

on the shell in support of the density contour plot of Fig. 4.16(b).

The pressure at $\phi = 90^o$ and 135^o are of noticeably longer duration than at $\phi = 0^o$ or 45^o. An applied dynamic load of longer duration is more characteristic of a quasi-static load. The peak magnitudes are significantly lower than those of the shorter duration impulses nearer the apex.

Multiple peaks are observed in the fluid response at the apex in the MMALE analysis. This erratic response is possibly a result of the oscillating nature of the applied loading as discussed earlier. The load at the apex consisted of several impulses of decreasing magnitude mixed with concurrent reflected pressures. The applied loading in the DAA-MAT90 analysis does not include these disturbances, however similar multiple peaks are evident.

Reflections

The prototype was modelled as an air backed structure and from the lower total pressure anomaly in the MMALE analysis no reflected pressure contours were expected from the MMALE analysis. As is clear from Fig. 4.19(a) this is observed to be the case. However, reflected pressure contours were observed 0.5ms after the shock wave impinged the structure (not illustrated). The pressure contours were not spherical, as expected, and were considered to be radiated rather than reflected pressure.

It is postulated that this late occurrence and form of reflections is a combination of the low severity of the shock loading, the low rigidity of the GRP material, and absorption of the incident pressure by an elastically deforming GRP laminate. Consequently, the reflection is composed mainly of radiated pressure which is delayed in arriving by a time equivalent to the time the shell takes to respond to the impingement of the shock wave.

The analysis was repeated replacing the GRP material with 15.0mm steel. The resulting pressure contours indicate an immediate reflection (see Fig. 4.19(b)), supporting the above hypothesis.

Axisymmetry of loading

Fig. 4.20 presents pressure and strain time histories for two positions on the maximum diameter ($\phi = 0^o$ and 90^o) from the DAA-MAT90 analysis. The axisymmetric nature of the loading and the structural response is clearly indicated. This check for axisymmetry

was not possible with the MMALE approach due to the nature of the model, however, the boundary conditions assumed axisymmetry.

4.6.3 Shell response

From each of the three techniques used for the axisymmetric load case, output was requested from six shells corresponding to the experimental strain gauge positions on the $\theta = 0^o$ meridian of the prototype shell (see Fig. 4.2). At each of these positions strains in accordance with the circumferential and meridional directions, i.e. around the parallel circle and down the meridian, were extracted from the results. As expected the shear and normal strain levels were found to be less than circumferential and meridional strain levels and are not included in the results analysis.

Figs 4.21 – 4.24 depict the circumferential and meridional strain response respectively for the six positions of interest. From observation of these records it is noticeable, particularly for the meridional direction, that both DAA results suffer from numerical noise whereas the MMALE results are comparatively noise free. This may be attributed to the second order accuracy of the advection scheme used to apply the load to the prototype compared with the first order accurate acoustic elements used in the DAA analyses.

Initial peaks are followed by a dampened response at positions $\phi = 0^o$, 30^o, 60^o and 90^o both circumferentially and meridionally. At positions $\phi = 120^o$ and 150^o, the initial peaks are followed by a dampened response only in the meridional direction. Circumferentially the initial peaks are accompanied by responses of similar magnitude, or greater, for the remainder of the analyses. This shell membrane response might be produced by the oscillations of the membrane above these positions or could be caused by the stiffer tufnol base vibrating at a higher frequency than the GRP membrane.

A large variation in the initial peak strain magnitudes predicted for each position is clearly evident. MMALE and DAA-MAT90 techniques predict a higher initial peak than the DAA technique and compare well for almost all positions.

Closer examination of the initial peak strains recorded reveals that, for each position, all records exhibit an initial strain rise at times corresponding to the arrival time of the shock wave, as predicted by the pressure-time histories. These times are compared in table 4.2. Some irregularity is observed between strain positions $\phi = 90^o$ and 120^o.

The highest initial peak strains predicted by all three techniques are noticeably at $\phi = 0^o$ and 150^o. These are summarised in table 4.3. Previous static and dynamic load

Position ϕ		Arrival time (ms)	
Pressure	**Strain**	**Pressure**	**Strain**
0^o	0^o	0.620	0.632
—	30^o	—	0.644
45^o	—	0.662	—
—	60^o	—	0.705
90^o	90^o	0.749	0.798
—	120^o	—	0.784
135^o	—	0.801	—
—	150^o	—	0.803

Table 4.2: Comparison of shock wave arrival and strain rise times along the meridian $\theta = 0^o$

The highest initial peak strains predicted by all three techniques are noticeably at $\phi = 0^o$ and 150^o. These are summarised in table 4.3. Previous static and dynamic load case studies have revealed these two regions of the prototype shell to be critical under loading.

It is also worth noting that each DAA technique predicts approximately the same level of strain response in both directions at the apex, which was expected from all three techniques under axisymmetric loading since the apex is essentially a single point without a definitive circumferential and meridional direction. A shell element at the apex would inevitably predict a small variation in strain due to its finite size. However, the MMALE method predicted an unexpectedly large variation of 47% which was indicative of inaccuracies in the pseudo-wedge model. The response of the apex element in the DAA analyses might be influenced by the shell elements surrounding it but this would not occur in the MMALE model. At 150^o there was less variation between the three techniques.

From all positions the highest predicted peak strain was almost 80% of the static material failure strain (-6295$\mu\varepsilon$). For the purpose of using the above results to choose a suitable charge size for the experimental work the predicted strains are not trustworthy without validation at this stage. Hence these levels are considered in danger of invoking material non-linearity either on a microscopic or macroscopic scale.

Position ϕ, θ	Circum. strain ($\times 10^6$)			Merid. strain ($\times 10^6$)		
	MMALE	DAA-MAT90	DAA	MMALE	DAA-MAT90	DAA
0^o, 0^o	-2521	-3877	-2438	-4766	-3722	-2289
30^o, 0^o	-2610	-2849	-1470	-2306	-2836	-1316
60^o, 0^o	-1713	-1651	-886	-1828	-2134	-1334
90^o, 0^o	-988	-914	-733	-2066	-2330	-1168
120^o, 0^o	-1513	-1625	-996	-2622	-2995	-1392
150^o, 0^o	-1796	-1932	-887	-3282	-3470	-1615

Table 4.3: Comparison of MMALE and DAA predicted initial peak strains along the meridian $\theta = 0^o$

Frequency response

The time considered in these analyses is insufficient to gain information about the frequency response of the shell when subject to a 10g charge. The analyses would need to be run up to 50ms in order to obtain an accurate representation of the frequency response requiring an inordinate number of CPU hours. Moreover additional computational features such as bubble loading and afterflow on the shell would be necessary.

4.7 Conclusions

Based on the observed predicted responses it was decided to reduce the charge size in the experimental axisymmetric load case in order to avoid any risk of damage to the structure. Using the shock factor relationship ($\frac{\sqrt{W}}{R}$) the effect of altering the charge mass and/or stand off distance can be quickly estimated. The shock factor for 10g EDC-1 at 1.0m stand off is $0.1\text{kg}^{0.5}\text{m}^{-1}$. Decreasing the charge size to 5g reduces the shock factor to $0.071\text{kg}^{0.5}\text{m}^{-1}$. This will have the effect of reducing the load levels and hence the peak strain responses particularly at the apex to $\approx -3500\mu\varepsilon$, whilst producing measurable strains at all other positions of interest.

For the symmetric load case the severity of the shock loading from a 10g charge is, at most, $0.05\text{kg}^{0.5}\text{m}^{-1}$ for the 2.0m stand off, and at least, $0.02\text{kg}^{0.5}\text{m}^{-1}$ for the 5.0m stand off. This reduction in load by factors of between two and five will inevitably reduce strain levels to between $\approx -2500\mu\varepsilon$ and $\approx -1000\mu\varepsilon$. This gives strain levels under

the severest symmetric load case well within the breaking strain of the GRP material, whilst under the least severe load the strain levels should be measurable above any signal noise levels.

Several additional observations have been made regarding mesh construction and UNDEX simulations using LS-DYNA and USA-DYNA3D.

1. For axisymmetric loading the problem was reduced to a quasi-three dimensional pseudo-wedge model substantially reducing the cost of the analysis. In doing so, the problems of the collapsed brick wedge element discovered in chapter 3 were overcome by incorporating a small hole along the axis of symmetry.

2. The general coupling approach did not initialise the interior elements of the coupling surface correctly, restricting FSI problems to using ALE coupling.

3. The multi-material element only permitted two materials to mix. This limited accurate representation of the free surface.

4. Transitioning and biasing techniques should be used with caution for problems involving shock waves. In regions where accuracy is required it is recommended that they be avoided due to numerical reflections.

Despite these modelling restrictions the effectiveness of investigating UNDEX loading using LS-DYNA and USA-DYNA3D combined with experimental predictions has been illustrated. The ability of using numerical simulations to examine the physics of an UNDEX event more closely has also been demonstrated.

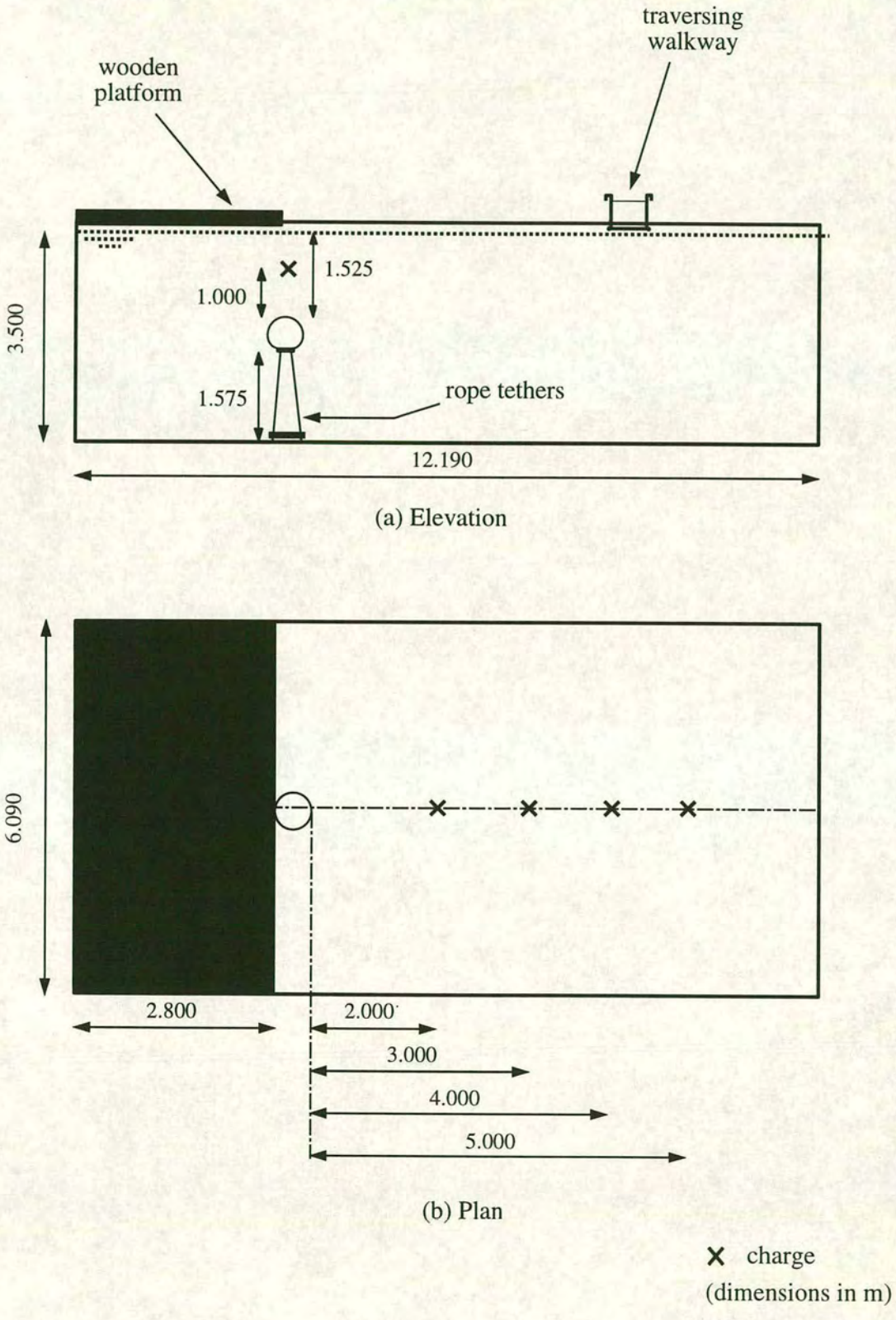

Figure 4.1: Test tank geometry and shell location

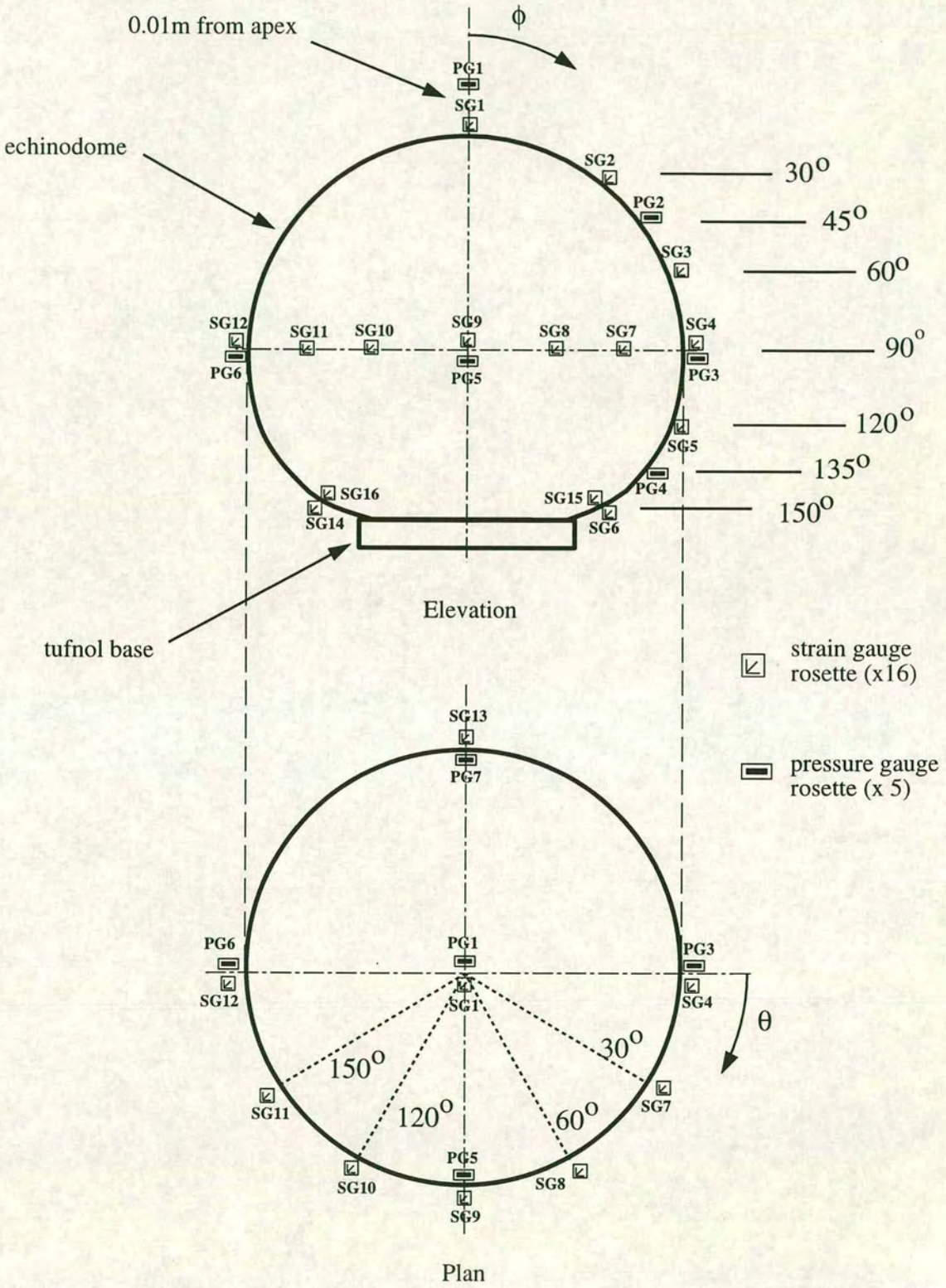

Figure 4.2: Prototype shell instrumentation

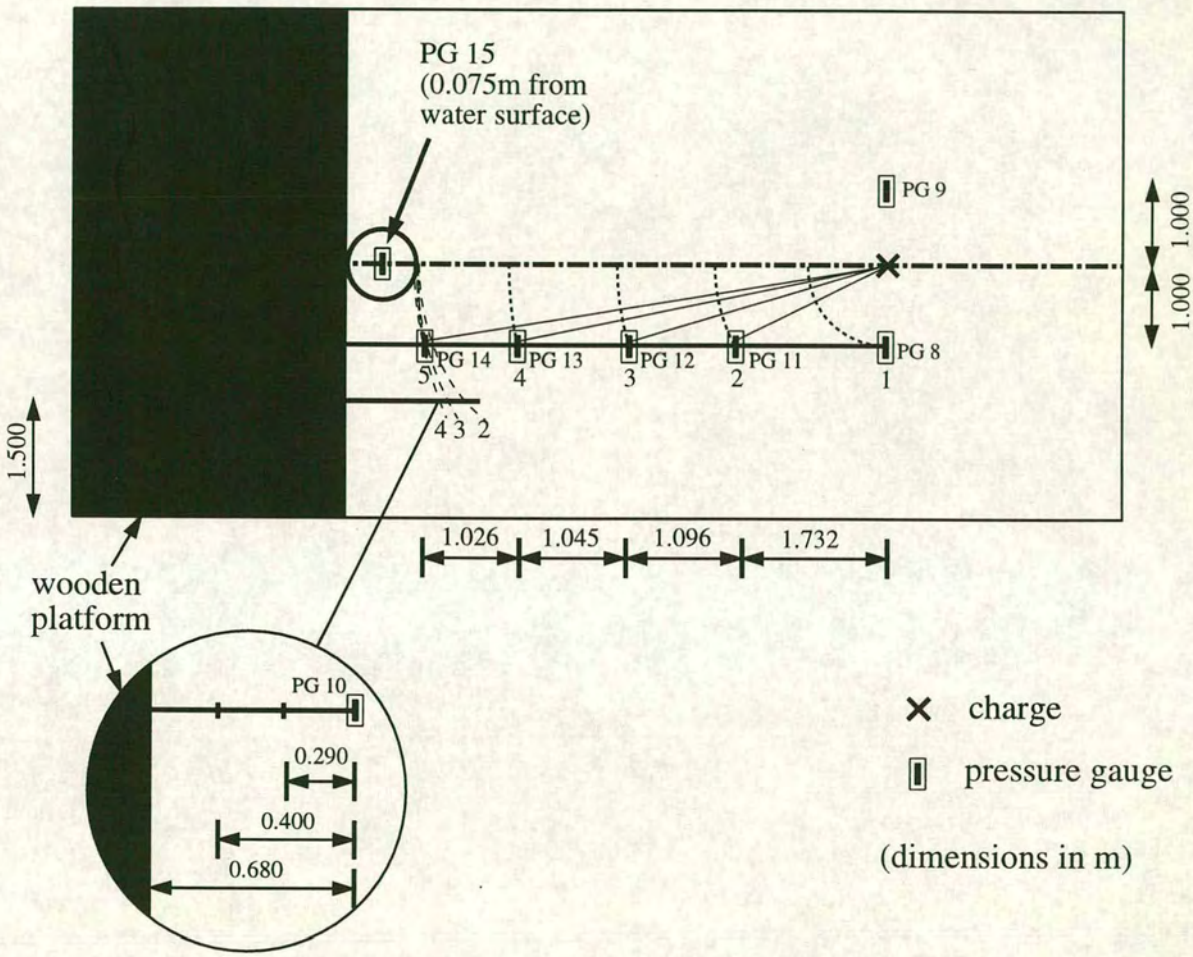

Figure 4.3: Free field instrumentation

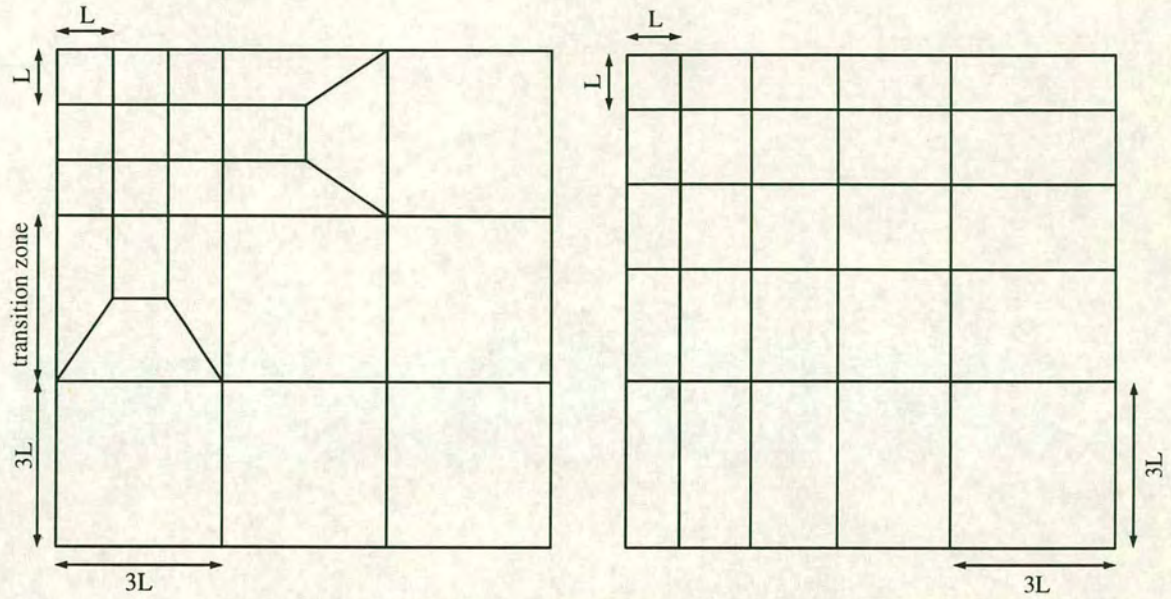

(a) Transitioning (b) Biasing

Figure 4.4: Modelling techniques to increase element size

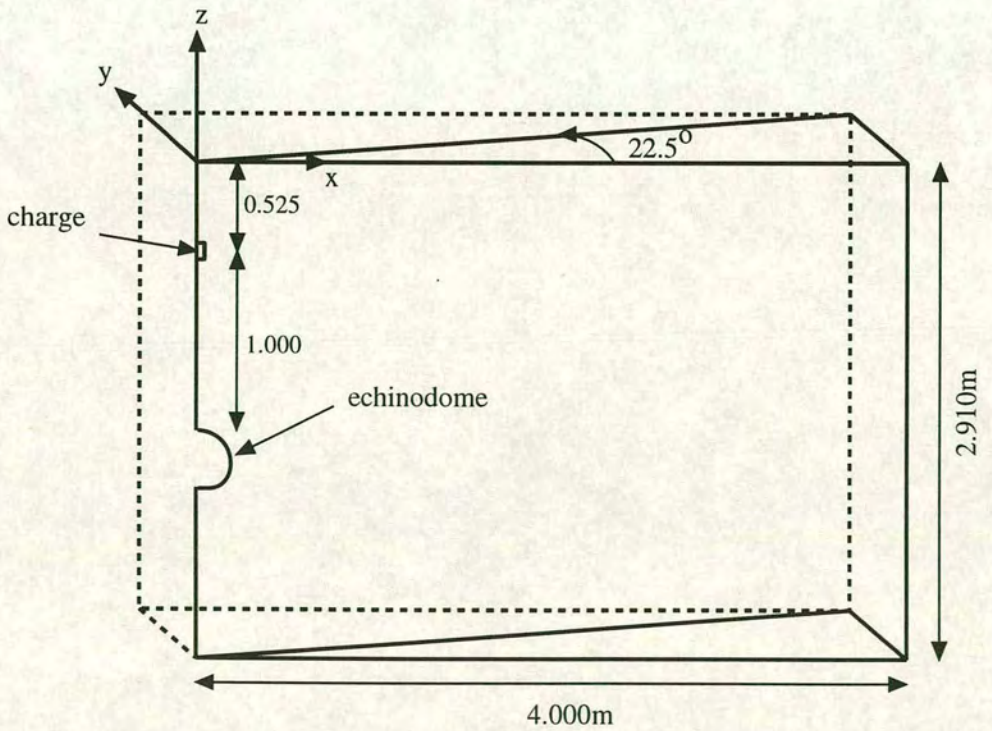

Figure 4.5: Sketch of pseudo-wedge model

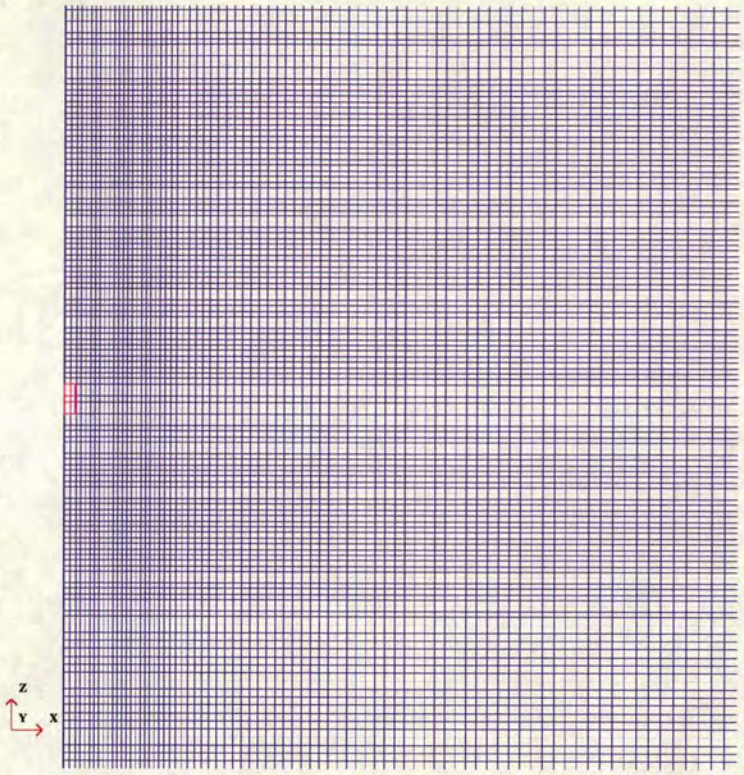

(a) Zoom on charge

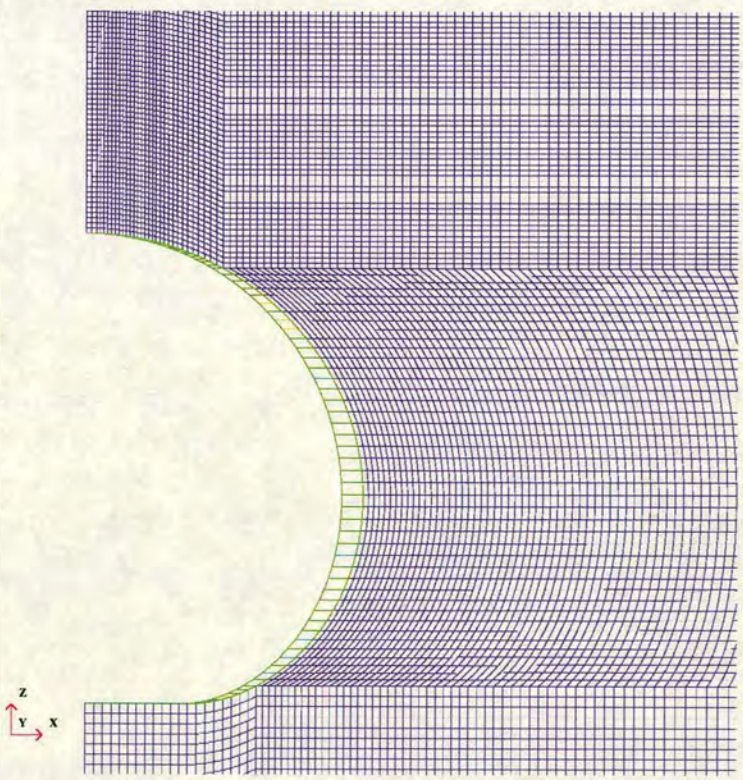

(b) Zoom on structure

Figure 4.6: Finite element mesh for MMALE pseudo-wedge model

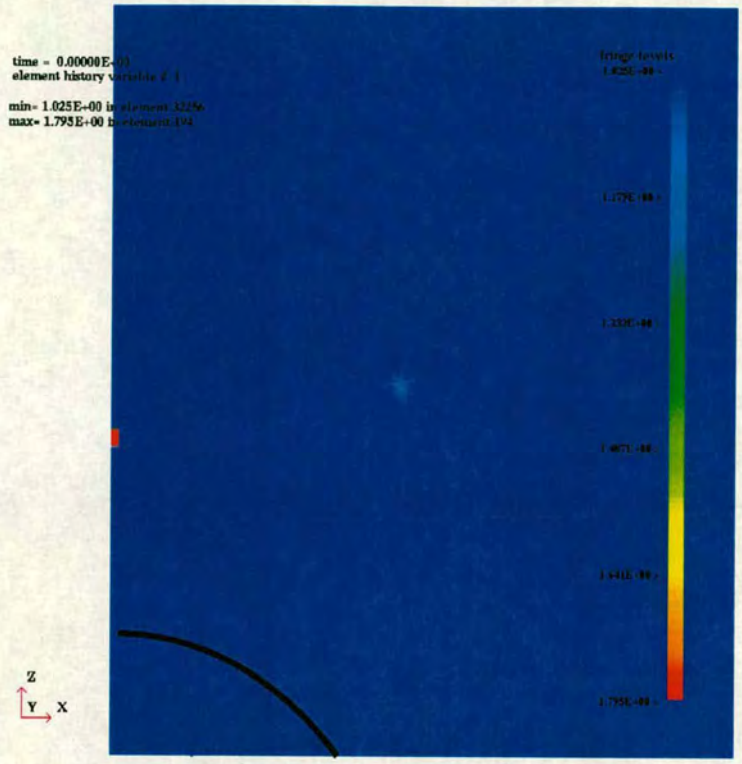

(a) Density contours (density units = $\text{kgm}^{-3} \times 10^{-3}$)

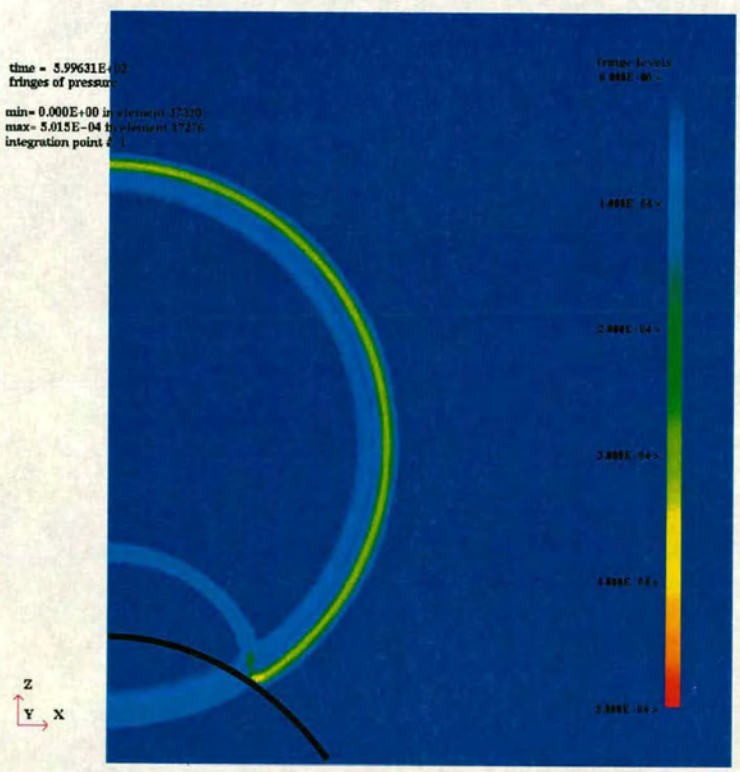

(b) Pressure contours (pressure units = Pa $\times 10^{-11}$)

Figure 4.7: Contour plots from general coupled mesh (structure emphasised)

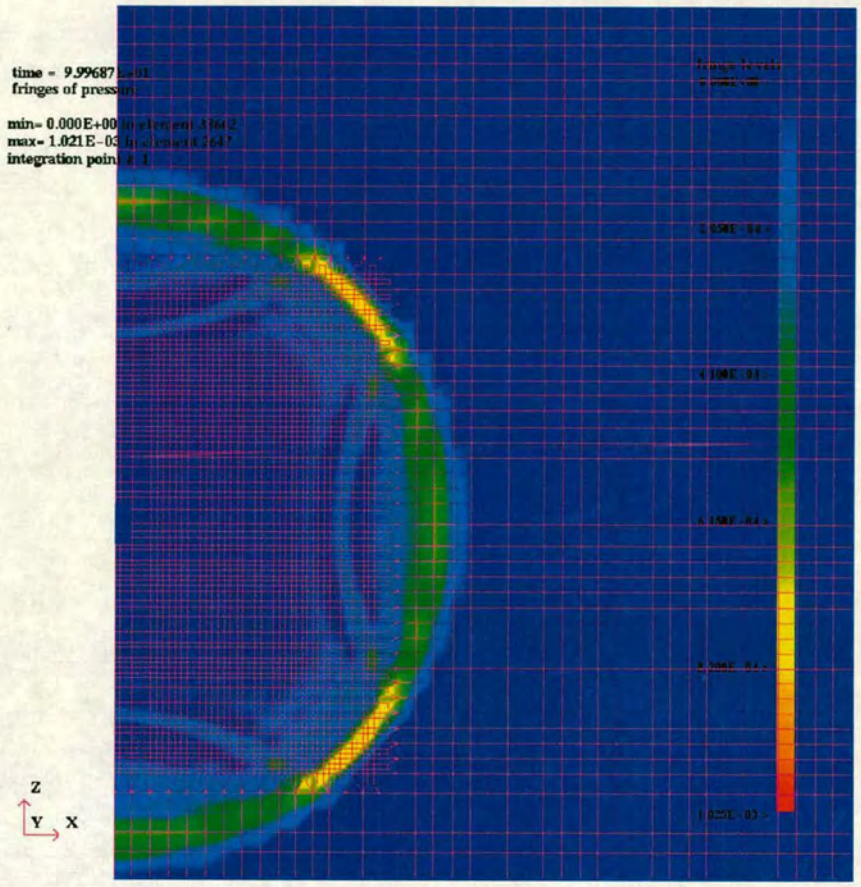

(a) Pressure contours (pressure units = Pa $\times 10^{-11}$)

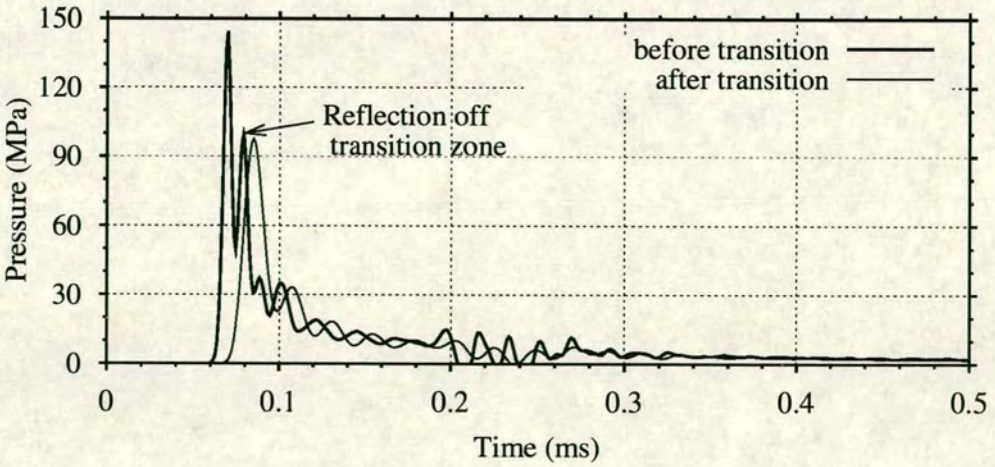

(b) Pressure-time curve

Figure 4.8: Reflection problems in transition zones

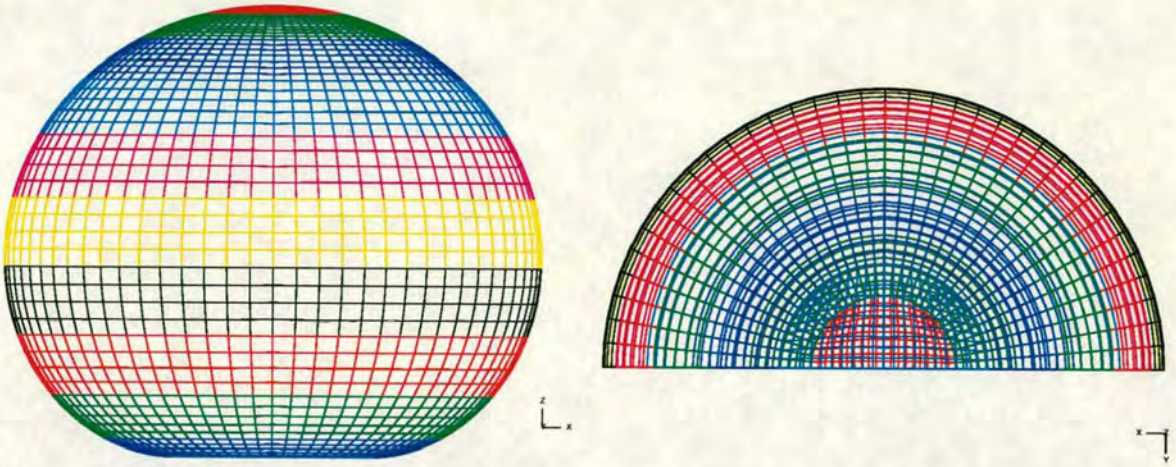

(a) Elevation

(b) Plan

Figure 4.9: Finite element mesh for DAA infinite fluid domain

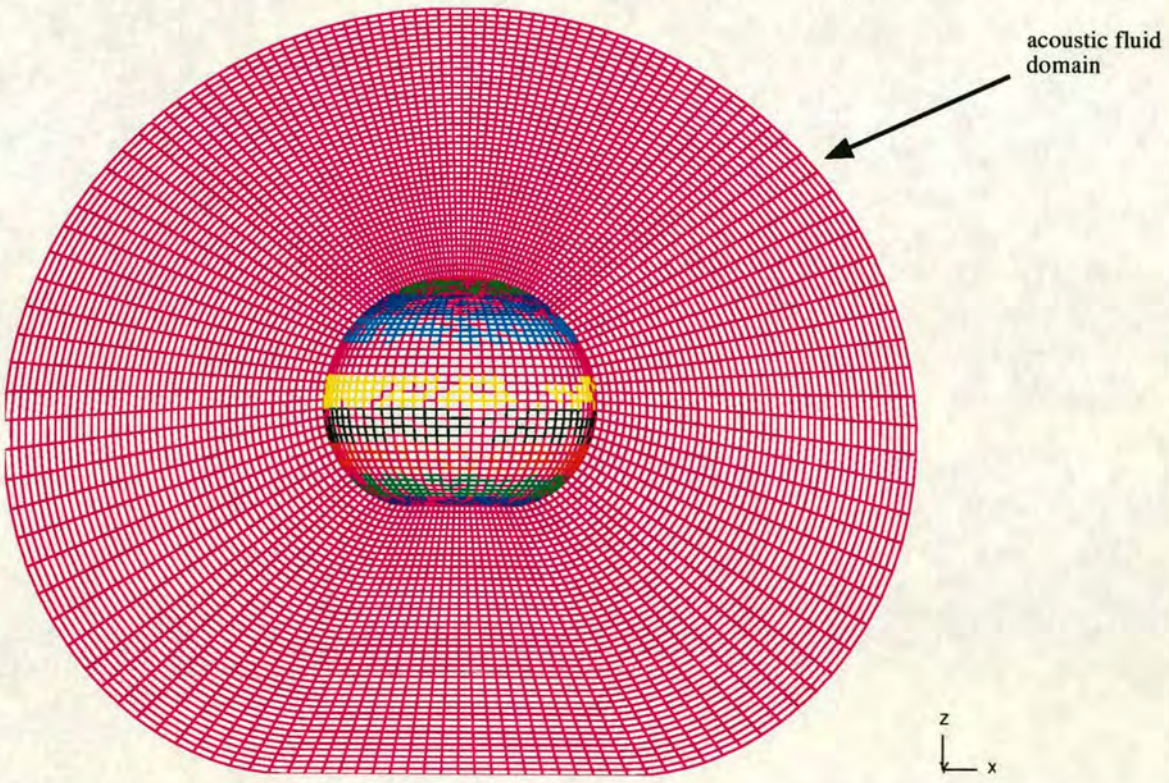

Figure 4.10: Finite element mesh for DAA semi-infinite fluid domain (radial thickness = 0.50m)

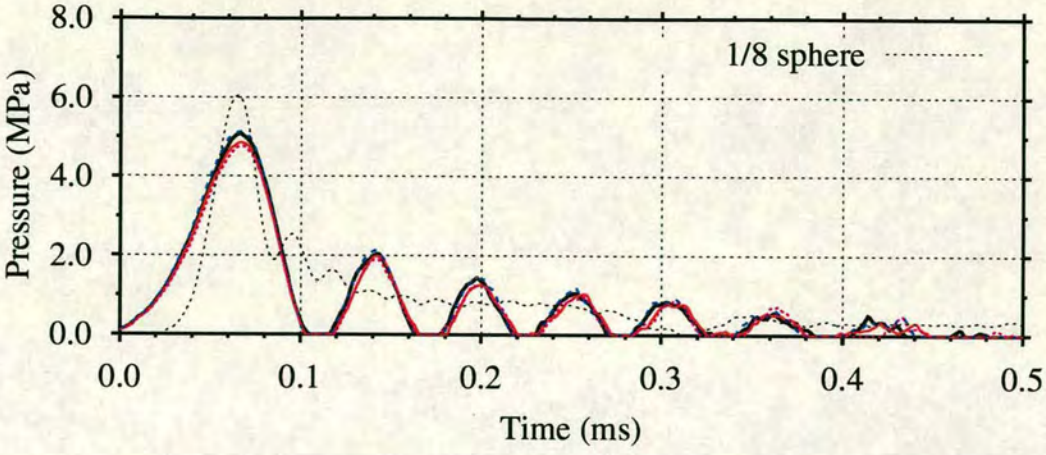

(a) Free field pressure at 1.0m from 10g EDC-1

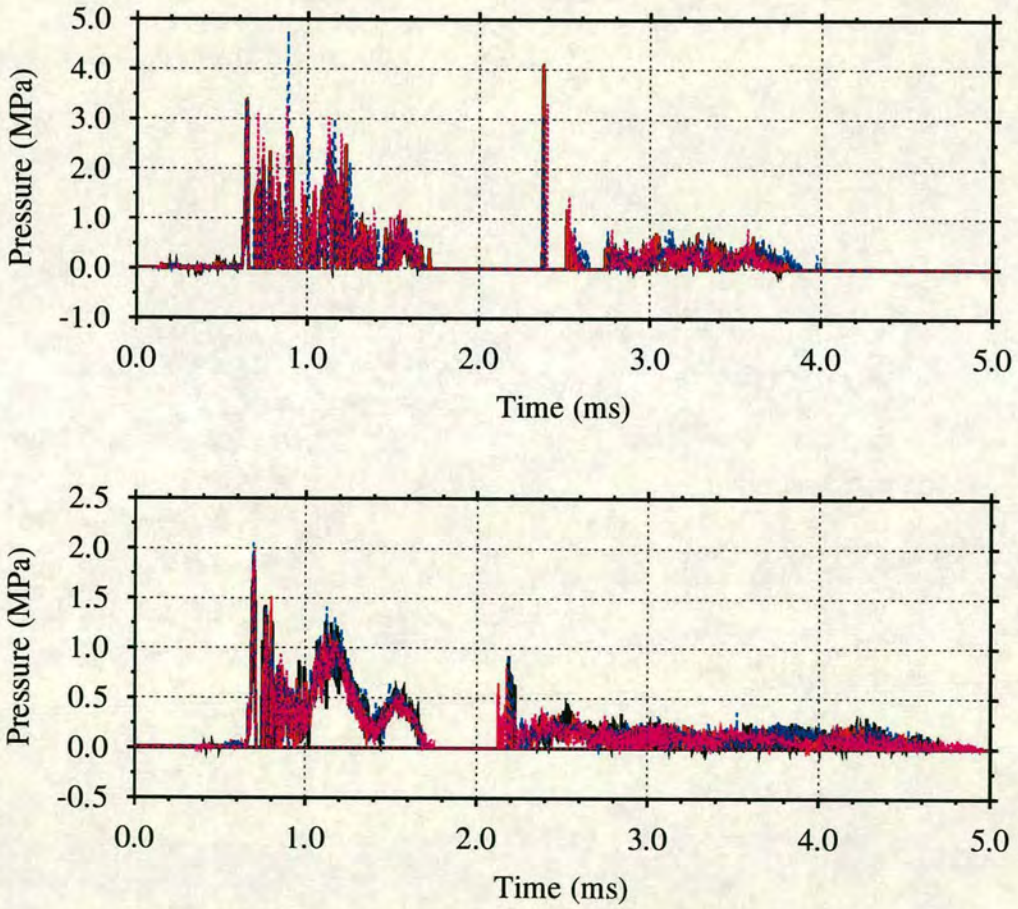

(b) Total pressure at $\phi = 0^o$ and $135^o, \theta = 0^O$

Figure 4.11: Comparison of pressures predicted by advection schemes 1 – 4

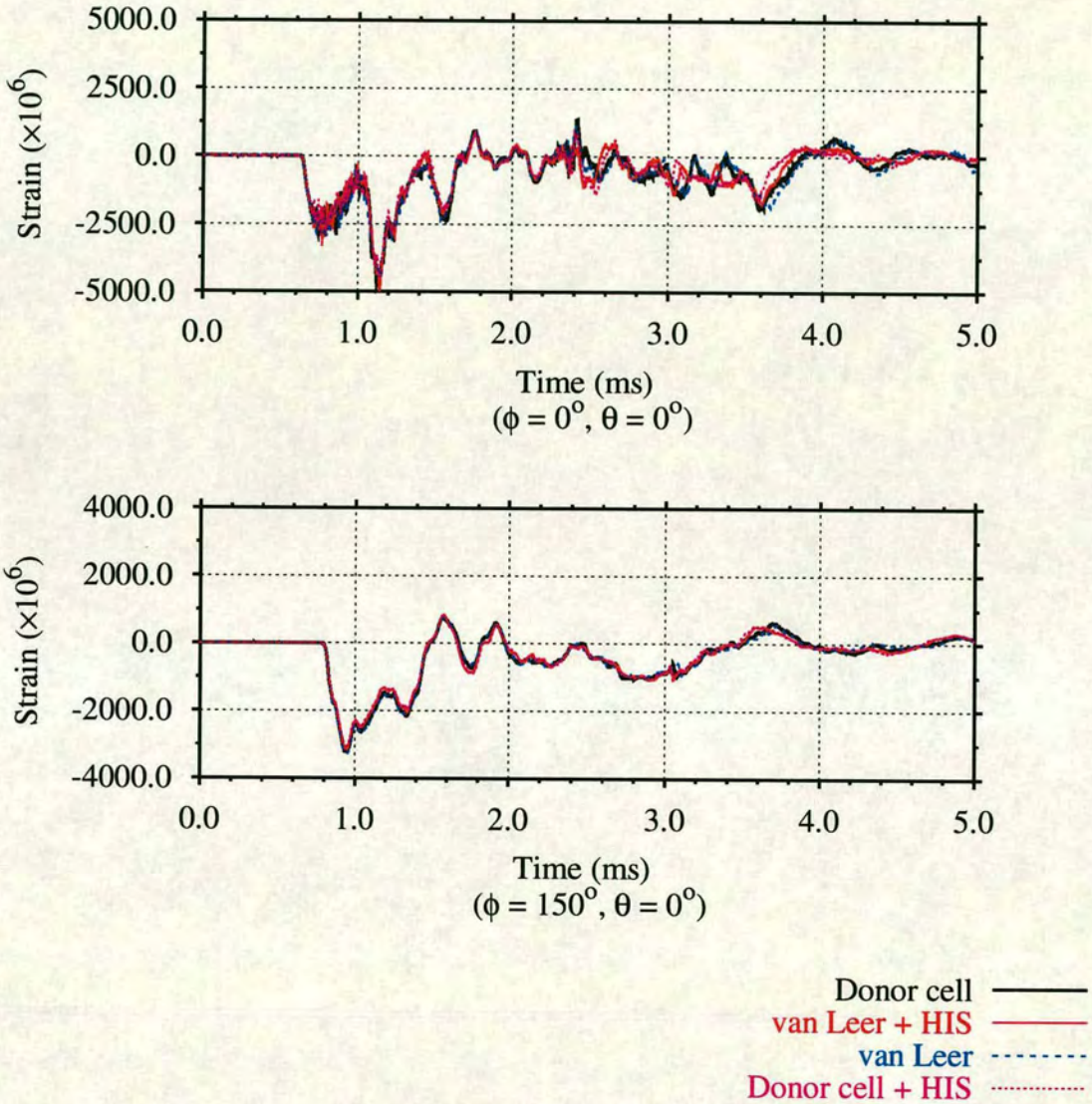

Figure 4.12: Comparison of meridional strains predicted by advection schemes 1 – 4

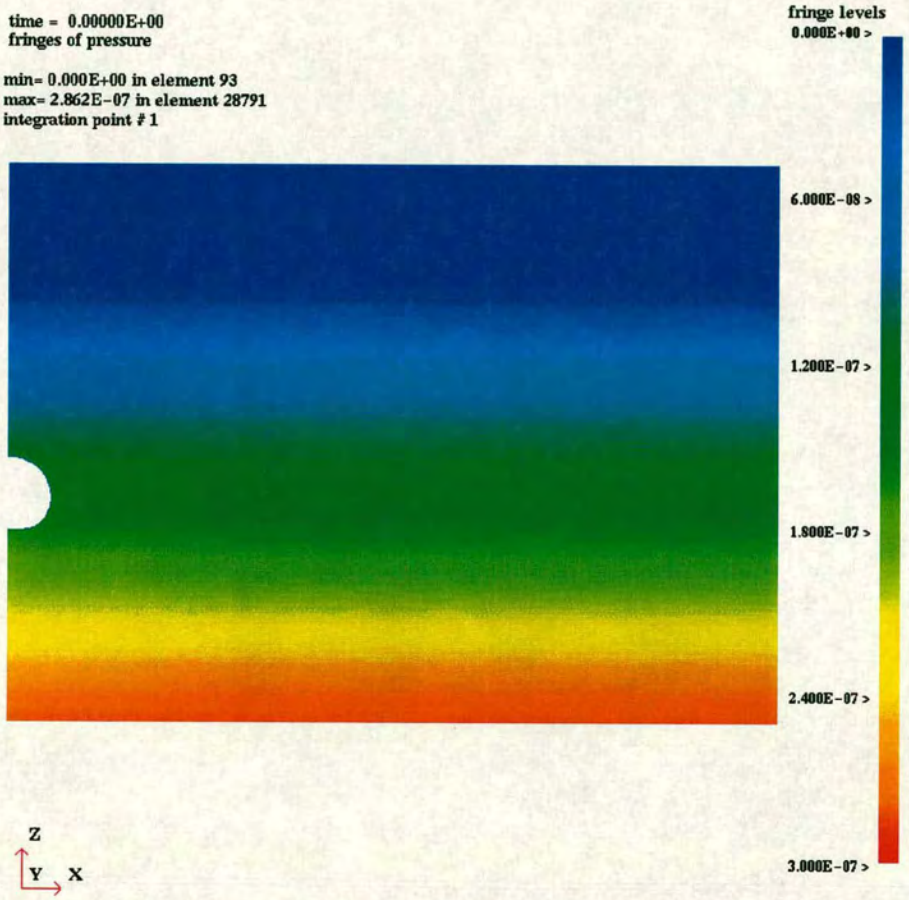

Figure 4.13: Pressure contour plot of hydrostatic pressure (pressure units = Pa $\times 10^{-11}$; $t = 0$)

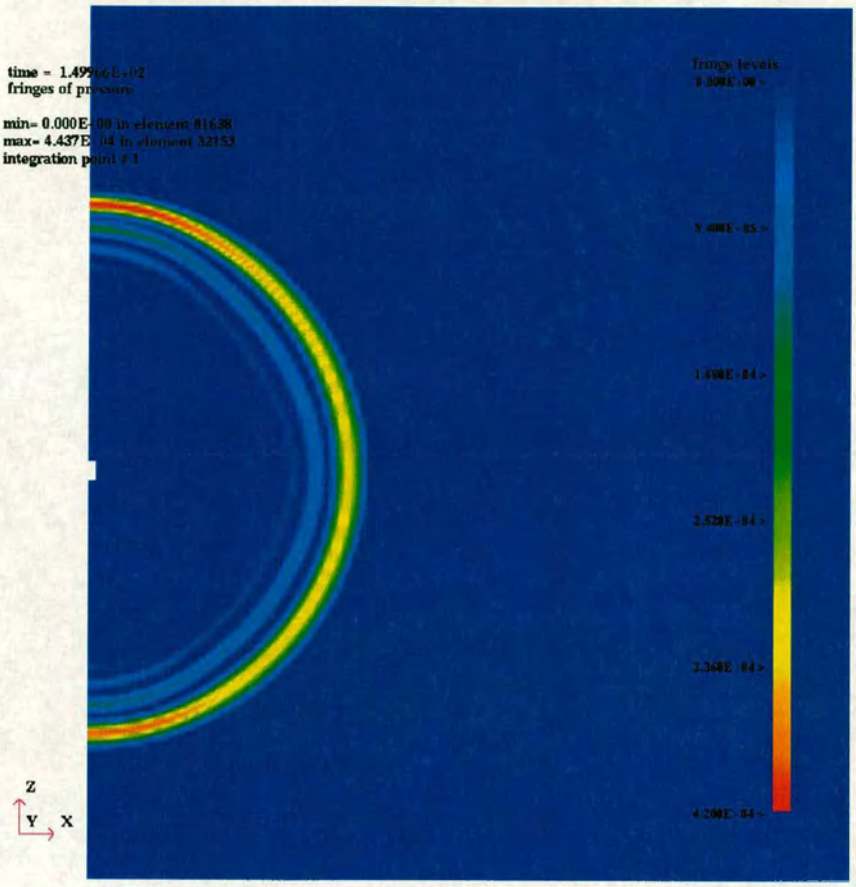

(a) Pressure contours (pressure units = Pa $\times 10^{-11}$; $t = 150.0\mu$s)

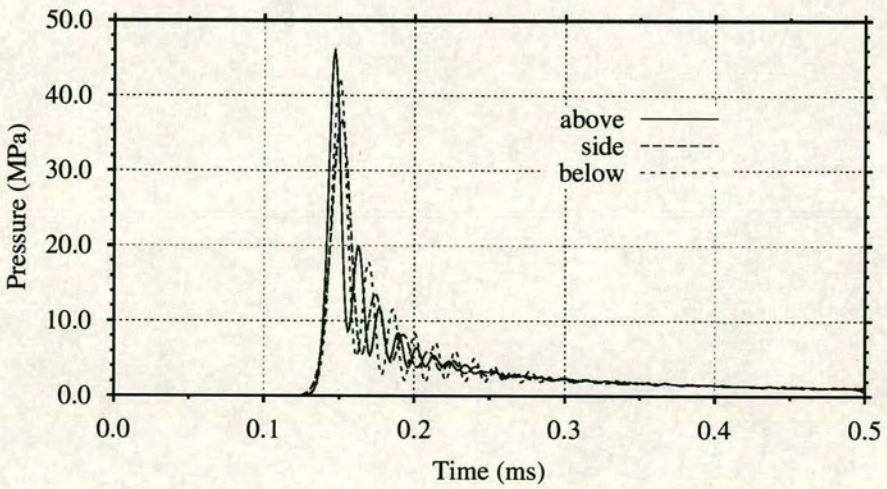

(b) Pressure-time curve at 0.25m from 10g EDC-1

Figure 4.14: MMALE predicted pressure at shock front

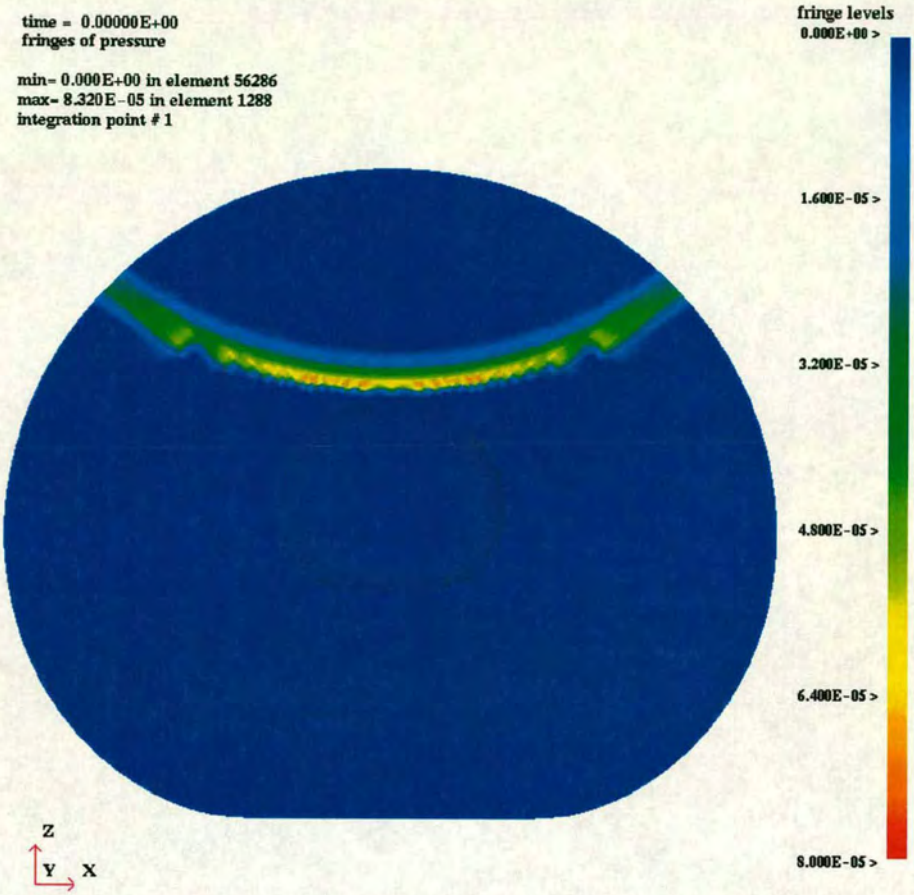

(a) Pressure contours (pressure units = Pa $\times 10^{-11}$; $t = 0$)

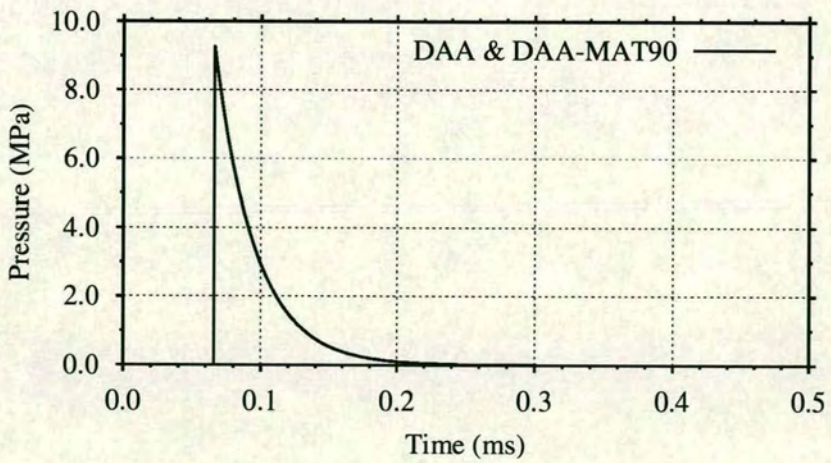

(b) Pressure-time curve at 1.0m from 10g EDC-1

Figure 4.15: Theoretical pressure at shock front for DAA analyses

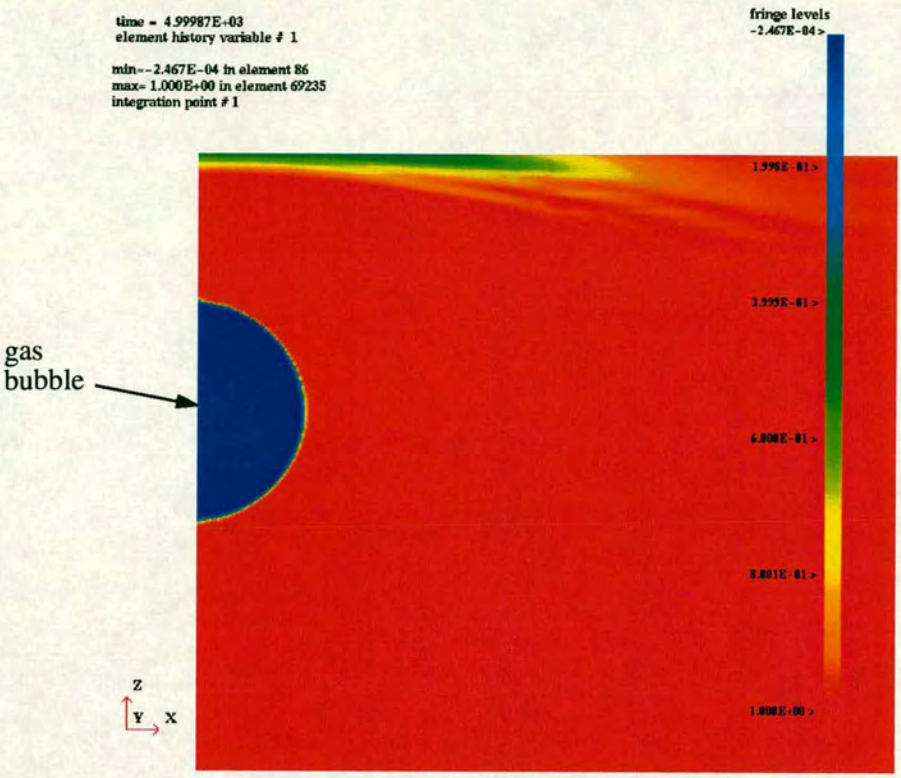

(a) Free surface cavitation and bubble expansion

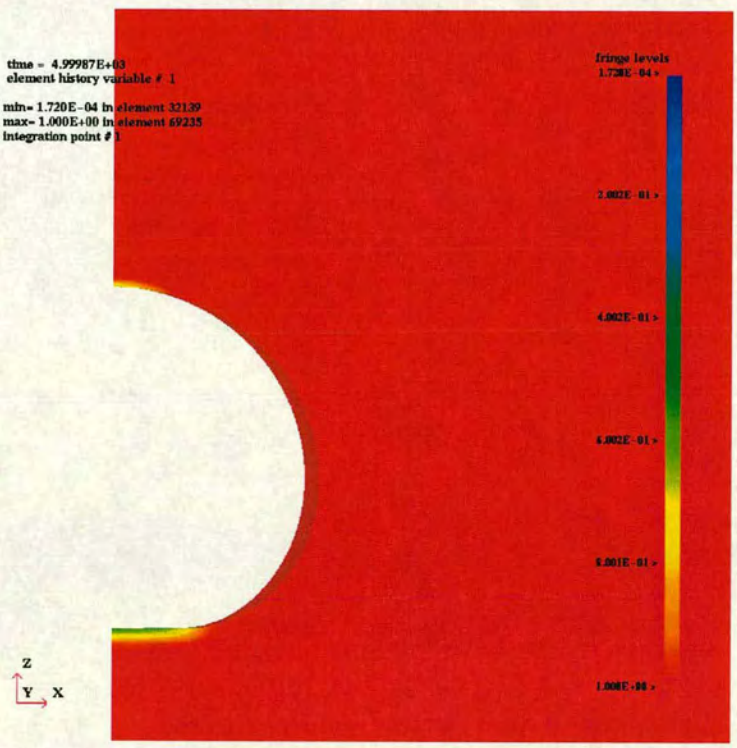

(b) Shell surface cavitation

Figure 4.16: Density contour plot of MMALE mesh (density units = $\text{kgm}^{-3} \times 10^{-3}$; $t = 5.0\text{ms}$)

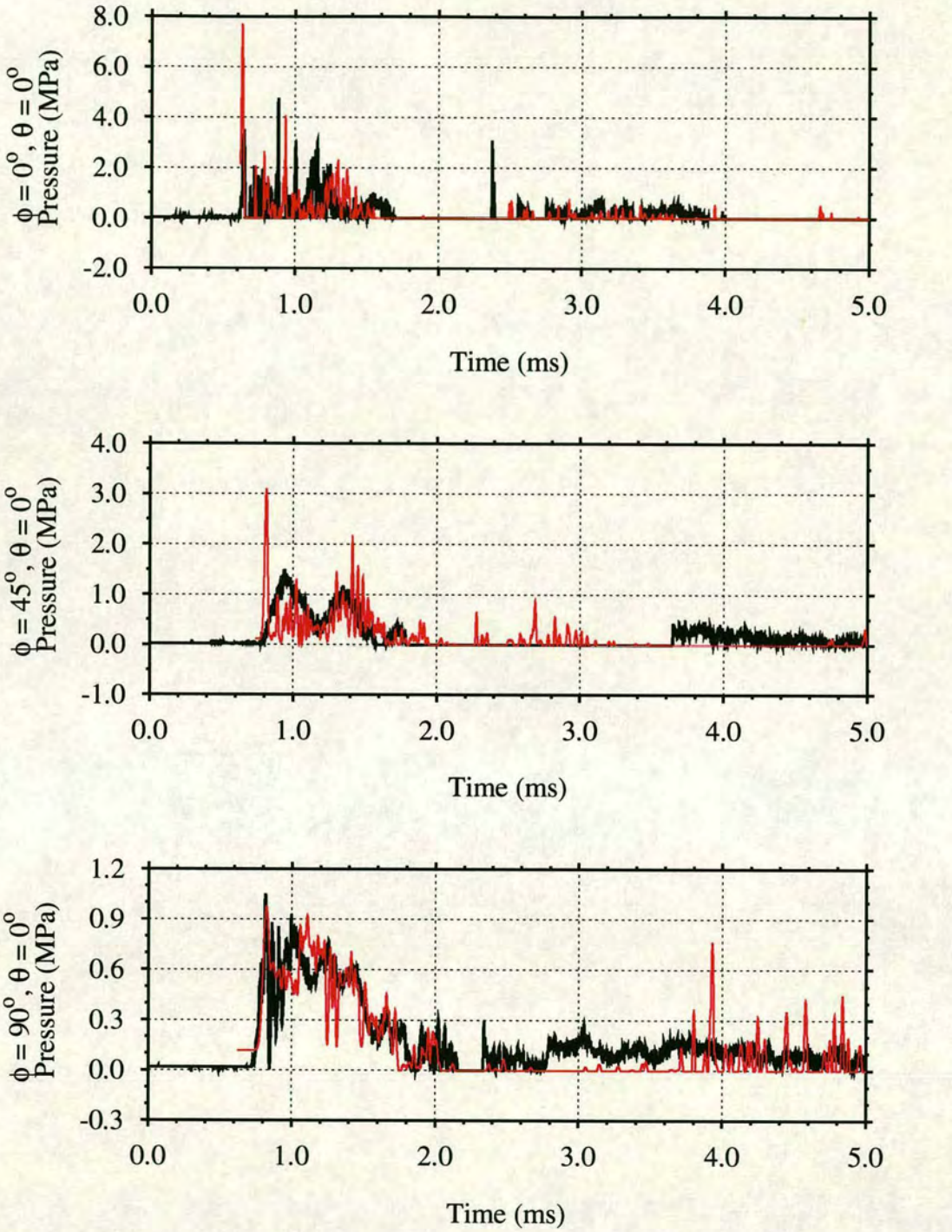

Figure 4.17: Comparison of predicted total pressures ($\phi = 0^o$ - 90^o, $\theta = 0^o$)

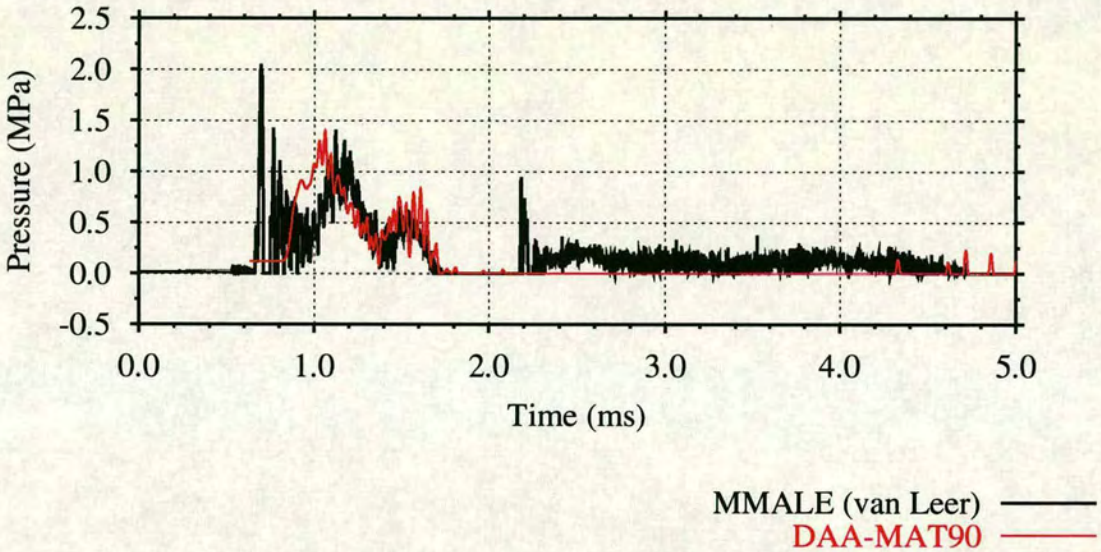

Figure 4.18: Comparison of predicted total pressure ($\phi = 135^o$, $\theta = 0^o$)

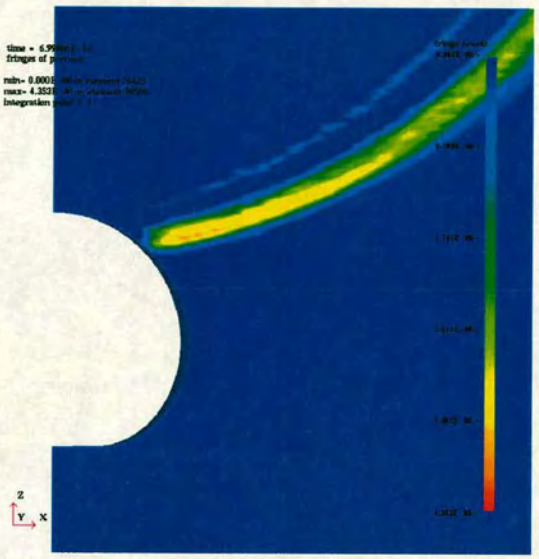

(a) GRP - no reflection ($t = 0.7$ms)

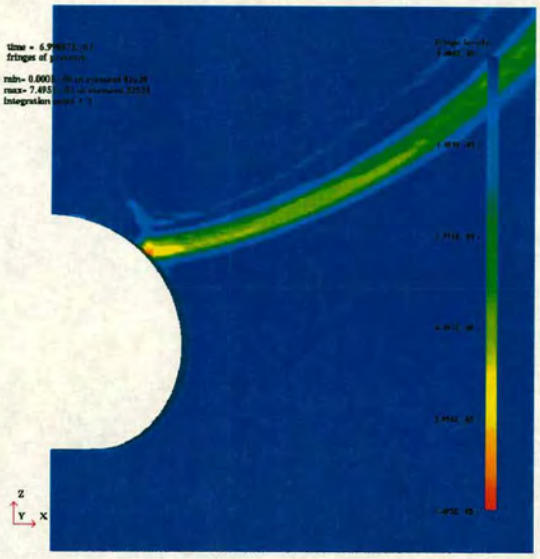

(b) Steel - reflection ($t = 0.7$ms)

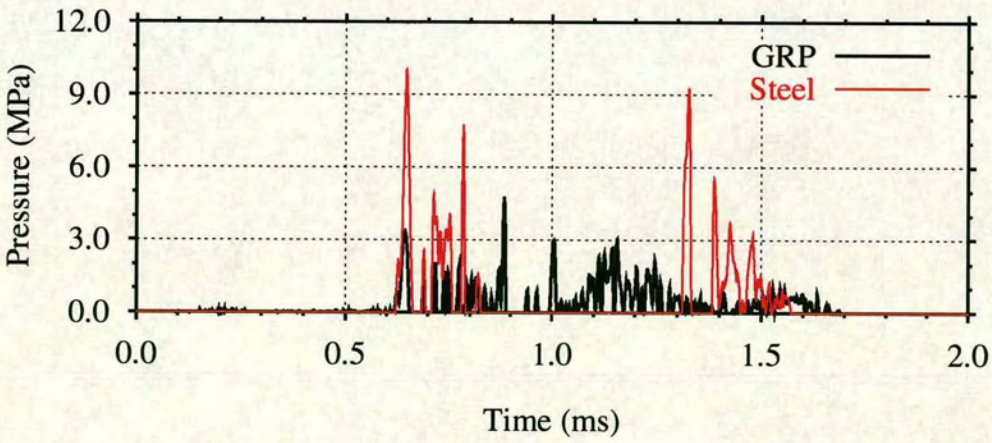

(c) Pressure-time history at apex ($\phi = 0^o, \theta = 0^o$)

Figure 4.19: Variation in reflections off GRP and steel in MMALE analysis (pressure units = Pa $\times 10^{-11}$)

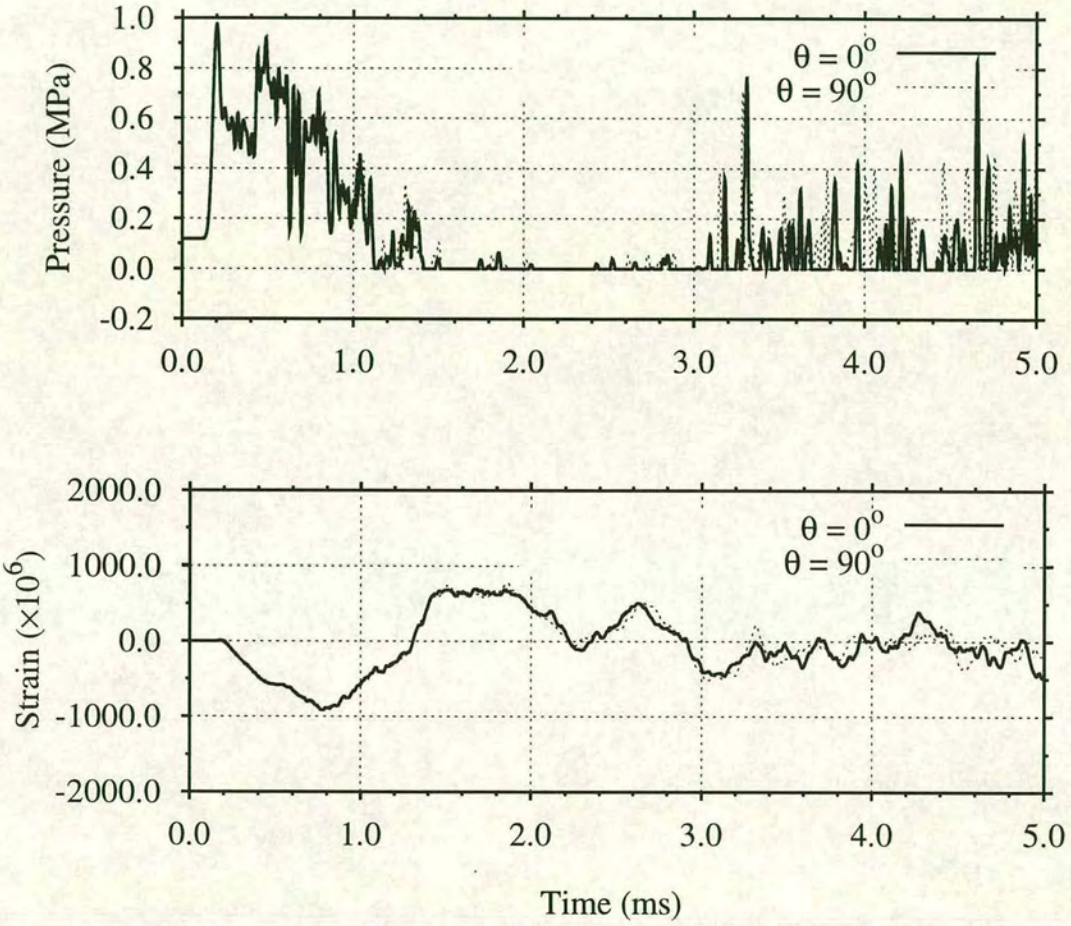

Figure 4.20: Axisymmetry of loading from strains and pressures predicted by DAA-MAT90 at $\phi = 90^o$

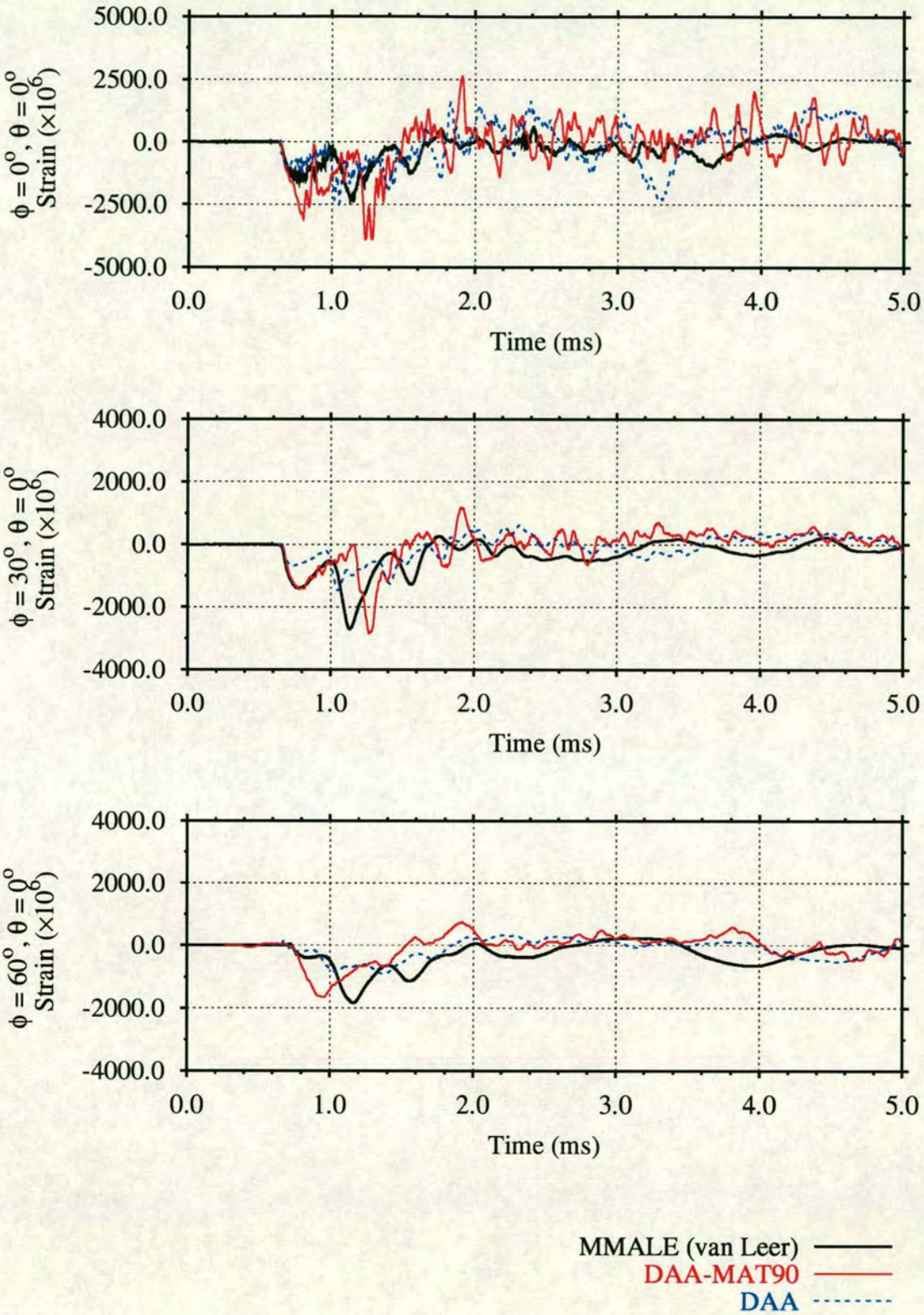

Figure 4.21: Comparison of predicted circumferential strains ($\phi = 0^o$ - 60^o, $\theta = 0^o$)

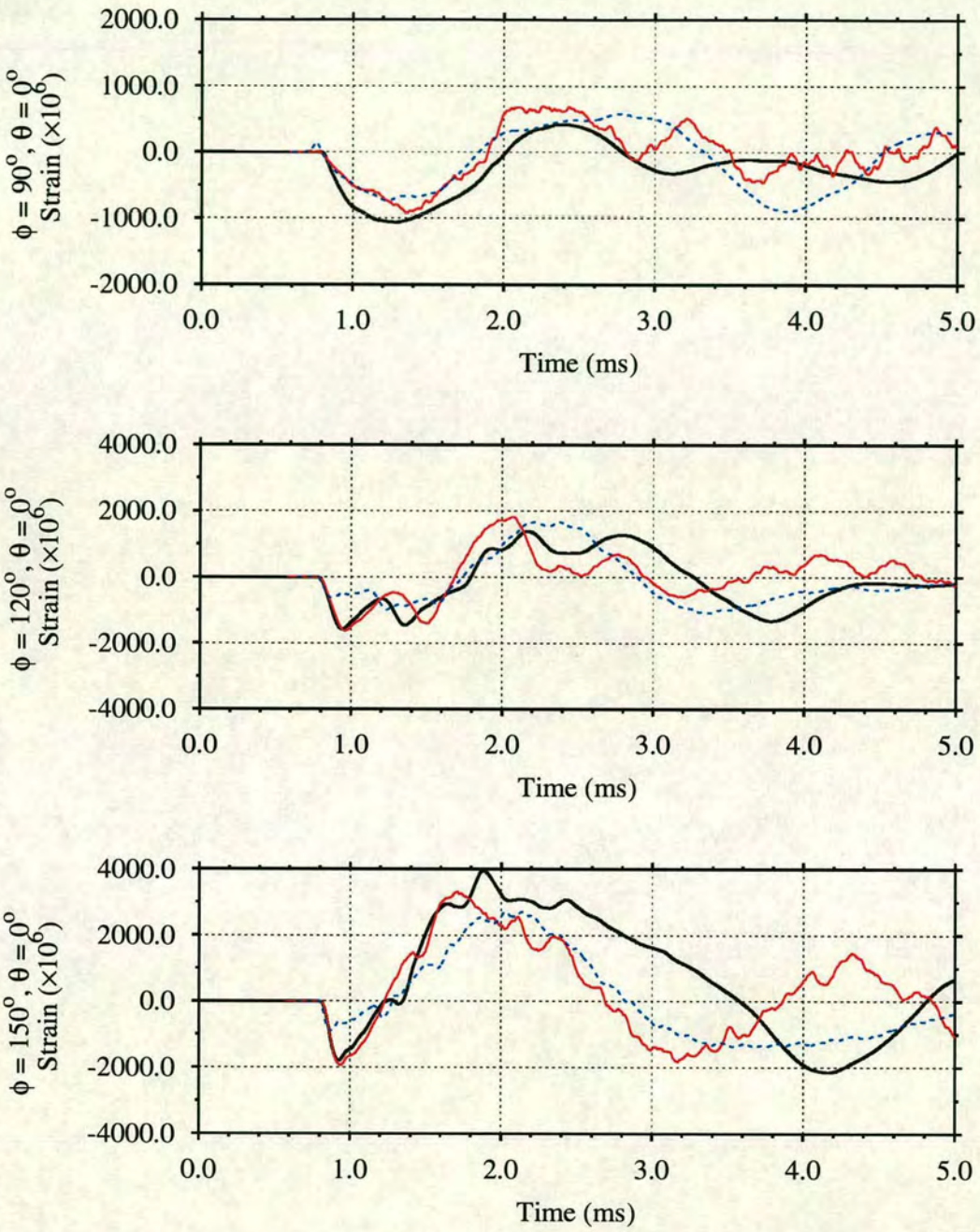

Figure 4.22: Comparison of predicted circumferential strains (ϕ = 90° - 150°, θ = 0°)

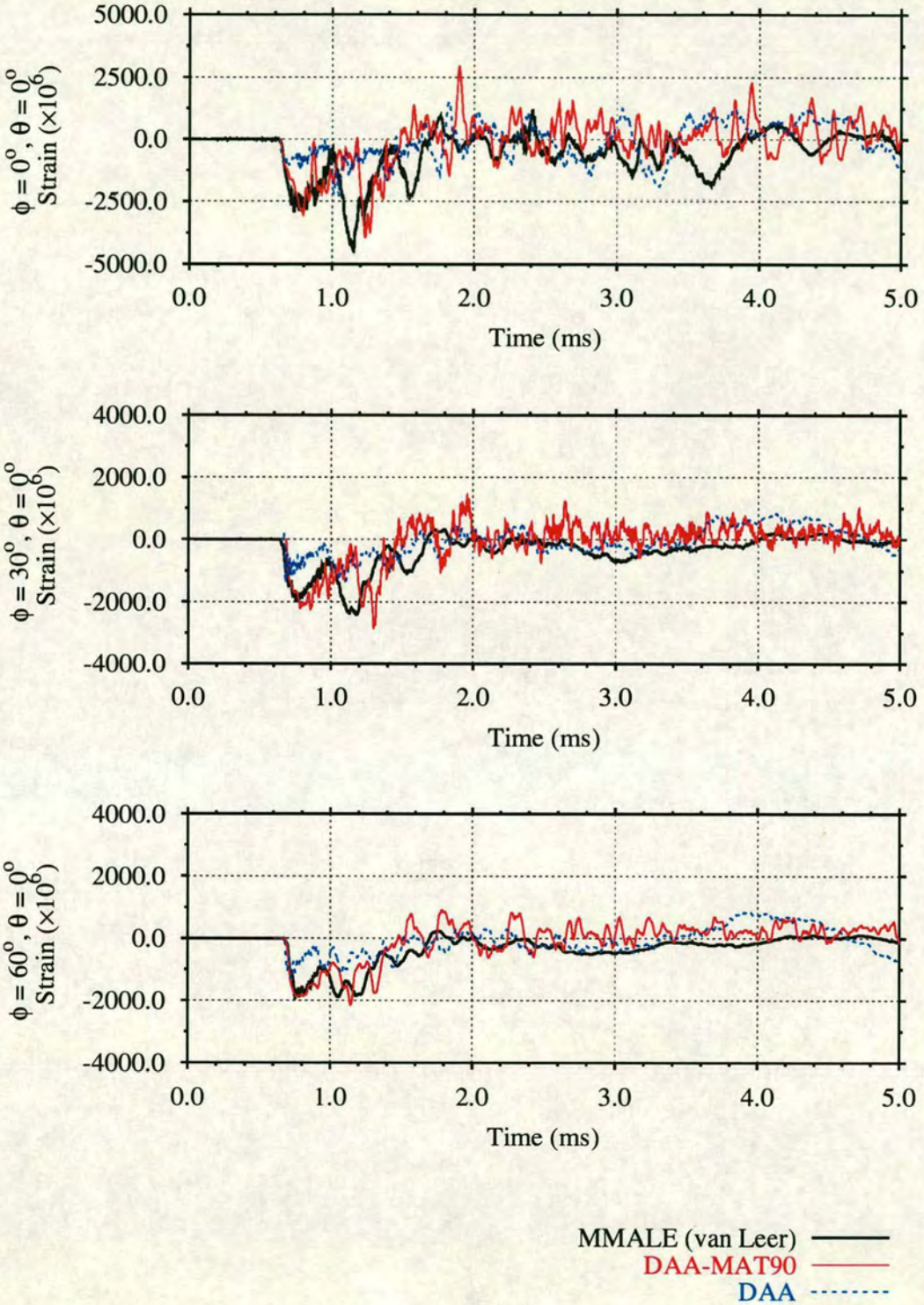

Figure 4.23: Comparison of predicted meridional strains ($\phi = 0^o$ - 60^o, $\theta = 0^o$)

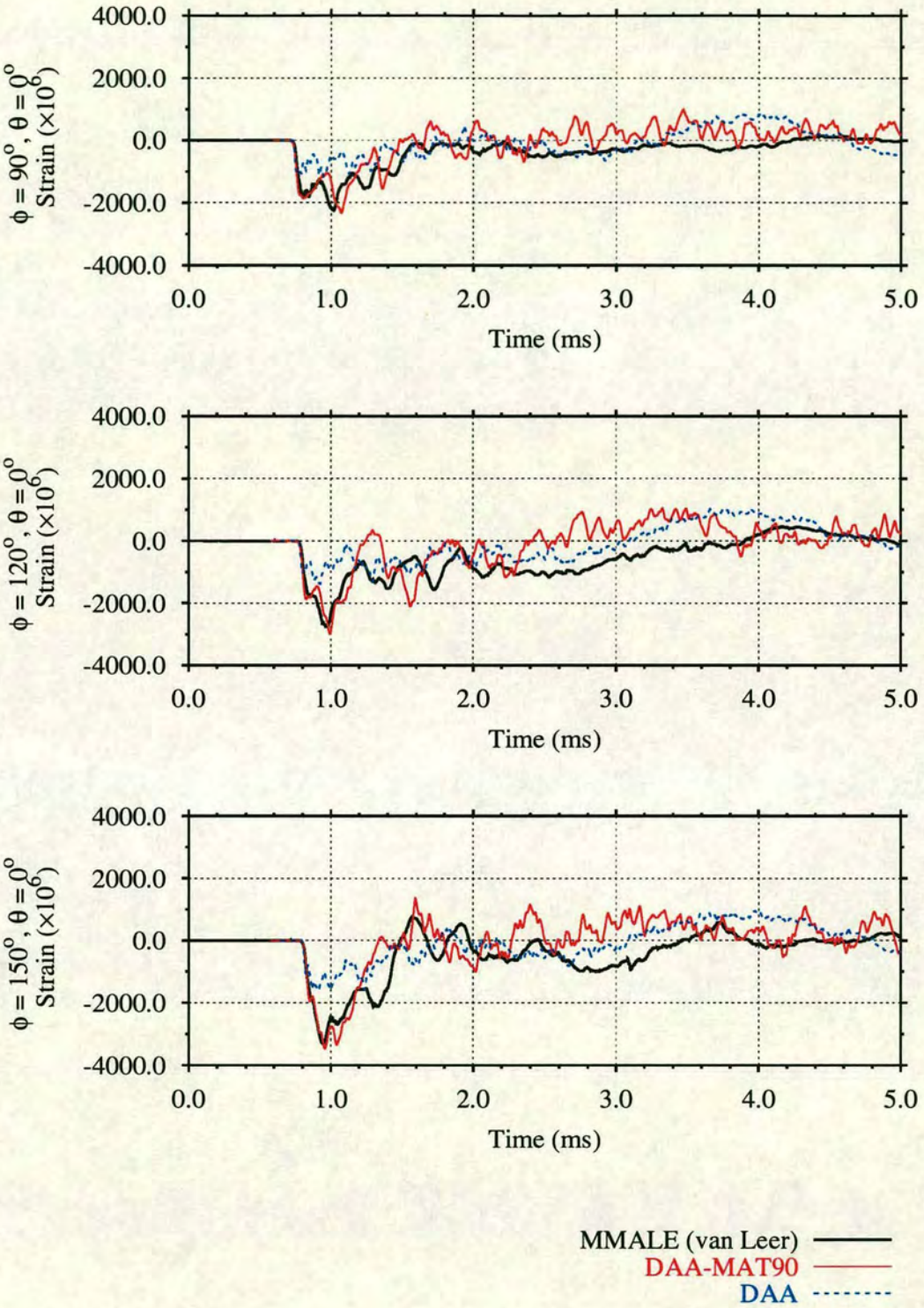

Figure 4.24: Comparison of predicted meridional strains (ϕ = 90° - 150°, $\theta = 0°$)

Chapter 5

Experimental simulation of UNDEX loading

5.1 Introduction

Preliminary numerical simulations described in chapter 4 assisted in the design of experimental tests to be performed on the prototype echinodome. It was concluded that the initial choice of charge for the axisymmetric load case, 10g EDC-1, was in danger of producing strain levels close to the estimated maximum strain the shell material is capable of sustaining. Consequently, the charge size was reduced to 5g for the axisymmetric load case. The 10g charge was considered to be sufficient for the symmetric load cases, due to the greater stand off distances involved.

The numerical simulations of both chapters 3 and 4 have been shown to be capable of modelling the majority of the physics involved in an UNDEX event. The next stage in the validation of LS-DYNA and USA-DYNA3D for the simulation of fluid-structure interaction is to gather reliable experimental data.

Additional information regarding the axisymmetric and symmetric load cases, outlined in the previous chapter, is discussed here. The experiments were performed, and results processed, at DERA (Rosyth). Analysing experimental data provided both a quantitative and qualitative assessment of the response of the prototype shell to UNDEX loading.

5.2 Experimental details

Much of the details concerning the experimental setup for the symmetric and axisymmetric load cases have already been discussed in chapter 4. The simulation of the sequence of events over the first 5.0ms of an UNDEX loading problem, i.e., detonation, shock wave propagation, and structural response, were encouraging. Bubble loading was not addressed in chapter 4 based on the problem of interface tracking between the explosive gases and the fluid encountered in chapter 3.

There are experimental techniques available to remove bubble loading from an UNDEX test, however, no such techniques were incorporated in these experiments as a full understanding of all phenomena pertaining to UNDEX loading was desired. No alterations had to be made to the experimental setup as a result of the numerical modelling. However, some adjustments to gauges locations and order of tests were made and are explained below.

5.2.1 Position of prototype shell

The shell was positioned in the test tank as illustrated in Fig. 4.1 using the method outlined in section 4.3.2. This location was maintained for all load cases.

5.2.2 Instrumentation

All rectangular strain gauge rosettes were bonded to the outer surface of the prototype shell according to Fig. 4.2. The gauges to be located on the seam were offset by 10mm to ensure the measured response was that of the GRP material and not of the seam. The strain gauge rosette at $\phi = 0^o, \theta = 0^o$ however, could not be neatly bonded 10mm from the seam, due to the nonhomogeneous shell surface. Consequently this offset was increased to 15mm from the meridian. In the rectangular strain gauge rosette nominal orientations were upwards along the meridian, oblique at 45^o and circumferential at 90^o clockwise.

Due to a shortage of free field pressure gauges, PGs 5 and 7, on the shell, were relocated as free field gauges for use in the first load case (5.0m symmetric) and renumbered as PGs 13 and 14 respectively. For this load case, pressure gauges were required at stand off distances 1.0m, 2.0m, 3.0m, 4.0m and 5.0m according to the setup shown in chapter 4 (Fig. 4.3). For the 2.0m, 3.0m and 4.0m symmetric load cases, gauges were located 1.0m either side of the charge and one free field gauge located at a distance from

the charge equivalent to the stand off distance. The free field gauge locations for the axisymmetric load case remained unchanged at 1.0m either side of the charge. A third gauge (PG 15) was located 0.450m above the charge to capture any bulk cavitation.

The free field gauges were suspended from steel bars at the charge depth for each load case. All pressure gauges located at the shell were taped to the outer surface.

Throughout the experiments all pressure and strain data were digitally recorded on a PC in voltage units for each gauge. The recording frequencies were 100kHz for strain gauges and 1MHz for pressure gauges. The pressure gauges recorded the difference in ambient pressure, i.e., hydrostatic pressure is not included in the pressure gauge results. All gauges were checked for malfunction prior to performing the experiment and were concluded to be fully functional.

5.2.3 Charge

The cylindrical charges to be used in the experiment were orientated such that the longitudinal axis was perpendicular to the seam of the shell in all load cases. A 5g EDC-1 charge was used for the axisymmetric load case and 10g EDC-1 charges for all symmetric load cases.

For large charge sizes the detonator is placed within the explosive material. However, the charge masses in these experiments are so small that, to do so, would have added significant mass to the charges. Moreover, the detonator generates a pressure pulse of its own which, combined with the pressure pulse of the explosive material, would have altered the free field data and, ultimately, increased the loading on the shell. Consequently, the explosive charge was detonated using a remote technique[73].

The order of the experiments were planned to be executed from least severe to most severe, as a precaution against carrying out experiments on a damaged shell. The risk of damage to the shell is highest in the axisymmetric load case and consequently this load case was executed last.

5.3 Processing of experimental results

Using the relevant calibration constants the measured data was scaled to the corresponding pressure and strain units.

Approximately 250ms of pre-trigger was recorded for each gauge. All time domain

signals were shifted backwards to remove the pre-trigger to within 3.0ms of when the closest gauge started to record the arrival of the shock wave, ensuring that the subsequent arrival times at the other gauges remained unaffected by the adjustment. The free field pressure records from the 5.0m symmetric load case were found to be incomplete. Hence no data was available beyond 42ms. Consequently no bubble information could be discerned from the free field data for this load case.

As with the numerical results discussed in chapter 4, the experimental results for each load case will be presented in the order of free field fluid response, fluid response at the shell and the shell response. All analysis was conducted using unfiltered data unless otherwise indicated.

5.4 Results of symmetric loading

5.4.1 Free field fluid response

Pressure

All free field data recorded during the symmetric load cases was observed to exhibit the characteristic rise to peak pressure followed by an exponential decay. A typical response at 1.0m stand off is depicted in Figs 5.1(a) and (b), as taken from PGs 8 and 9. A sharp rise in pressure indicated the arrival of the shock wave at each pressure gauge which was immediately followed by a rapid decay to approximately 25% of the peak value in 50μs. A secondary peak pressure, 30% of the first, is observed prior to a further gradual decay to pressure values under 10% of the initial peak. These disturbances behind the shock front are commonly generated from cylindrical charges[15], however, in this case it could correspond to the detonator pulse. The irregularity in the decay from the initial peak pressure makes it difficult to evaluate a single decay constant from this data, however, a fitted theoretical profile to the experimental data gives an estimated value of 49ms (see section 5.6).

The arrival times of the shock wave at PGs 8 and 9 (1.0m either side of charge) were found to differ by 15μs suggesting either the shock wave is not conforming to the sphericity expected from the charge or the pressure gauges were misplaced by a distance of 20mm (assuming $c = 1500\text{ms}^{-1}$). Experimental error is the most probable cause for this difference considering the scale of the experiment.

The variation in incident peak pressures for 1.0 – 5.0m stand off distances is illustrated in Fig. 5.2. The averages of these peak pressures are listed in table 5.1. It is clear

Stand off (m)	Ave. incident pressure, P_I (MPa)	Incident pressure, P_I (MPa)	Total pressure, P_T (MPa)
1.0	5.020	—	—
2.0	1.793	1.862	1.693
3.0	1.382	1.415	1.376
4.0	0.871	0.957	1.025
5.0	0.811	0.811	0.733

Table 5.1: Free field and total peak pressures at the stand off position under symmetric loading from 10g EDC-1 for various stand off distances

that the reduction in peak pressure becomes progressively less with increasing distance from the charge, as observed by Cole[15]. A standard deviation for the 1.0m stand off of 0.69 is observed. The large spread of readings may be due to problems relating to the remote detonation technique or degradation of PGs 8 and 9 used for the 1.0m stand off positions either side of the charge. Whilst observing each load case at the time of testing, a difference in severity of each detonation was perceived. Examination of the test tank after each load case revealed fragments of unexploded charge material on the floor of the tank. Complete detonation of such small charge sizes could not be guaranteed with the remote detonation technique and, consequently, a variation in peak pressures can result. Alternatively, after each load case, the quality of the measurements made by PGs 8 and 9 could have deteriorated.

It is clear the average peak pressure decreases with distance from the charge. However, it is also worth noting that the difference between each consecutive average pressure value reduces with distance, indicating the decay constant is also decreasing with distance, as expected.

Bubble pulses

Some time after the shock wave has passed the pressure in a typical free field record is observed to increase again as illustrated in Fig. 5.1(a). This increase is more gradual than that of the shock wave pressure and is followed by a gradual decrease. This pressure pulse is characteristic of the first bubble pulse. The maximum pressure of 0.69MPa indicates when the bubble is at minimum radius. Hence, the bubble period, i.e. the time between the shock peak pressure and the bubble peak pressure, is 54ms.

Gauge no.	Peak pressure (MPa)		Impulse, I (Pa.s)		Energy, E_f (Pa.m)	
	Shock	Bubble	Shock	Bubble	Shock	Bubble
8	4.297	0.668	335.18	449.87	147.99	47.70
9	4.083	0.651	330.25	539.81	141.81	46.74

Table 5.2: Comparison of shock wave and first bubble pulse characteristics at 1.0m stand off from 10g EDC-1

Table 5.2 compares parameters relating to the shock and first bubble pulses at 1.0m stand off from the 10g EDC-1 charge. Only one record was available for the 2.0m stand off, insufficient to obtain reliable bubble pulse parameters. Second and third bubble pulses, much weaker than the first, were detected at 97ms and 130ms. The first bubble pressure-time history was integrated over the time equivalent to $t_{pmax} - t_{\frac{pmax}{100}}$ (where P_{max} is the maximum bubble pressure), rather than 6.7θ, to obtain the impulse and energy content for the bubble. The time corresponding to 6.7θ is only valid for the impulse due to the shock wave. The longer duration bubble pulse requires a longer integration time.

Table 5.2 registers the pressure loading from the bubble as approximately 15% that of the shock wave, but the impulse per unit area of the bubble is 1.5 times the impulse of the shock wave. The longer duration of the bubble pulse produces a more critical impulse loading. The radiated bubble energy is observed to be of the order of one third of the radiated shock energy. For close stand off distances (< 1.0m) the bubble could be responsible for supplementary damage. In such cases, it is important that bubble loading be included in the design loads.

Reflections

Positive pressure peaks corresponding to reflections off the walls of the tank are evident later in time from the 1.0m stand off free field pressure-time records (see Fig. 5.1(b)). The peak pressures caused by the reflected shock waves are observed to be approximately 20-25% of the incident shock wave, reductions resulting from the longer distance travelled and some absorption of the pressure by the wall material. Despite reductions in magnitude it is clear how reflections, along with bubble loading, could also be responsible for supplementary damage.

5.4.2 Fluid response at shell

Total pressure

All pressure-time histories of the fluid response exhibit similar qualitative characteristics. Typical pressure-time histories at the shell are depicted in Figs 5.3 – 5.4 for the 2.0m stand off load case. As Fig. 5.4(a) illustrates, the total pressure at the nearest approach to the charge (stand off point) rises rapidly to a sharp peak with the arrival of the shock wave and is followed by a rapid decay to negative pressure values, possibly indicating separation of the shell from the water, i.e., cavitation. At later times the pressure is observed to rise sharply again indicating the arrival of reflections at the shell. The same characteristics are recorded at $\pm 45^o$ from the stand off point (Fig. 5.3(b) and 5.4(b)). Towards the apex of the shell the initial peak loading is considerably lower and no immediate cavitation is indicated. For all pressure records a sustained period of negative pressure is recorded later in time. It is not certain, at the time of writing, if negative pressures can be quantified accurately by the tourmaline pressure gauges used in the experiment, however, it is clearly indicated that local cavitation is occurring at various positions around the shell. An uncharacteristic negative pressure peak, greater than the total pressure peak, was observed in the 5.0m load case, at the apex. This is thought to be due to signal noise.

The total pressure in the vicinity of the shell is composed of incident and scattered pressure. The magnitude of the total pressure, at the stand off point in particular, is therefore expected to be greater than the incident pressure, as observed by Cole[15] and Mouritz[82], for air backed plates. However, as table 5.1 indicates, only for the 4.0m load case is the total pressure at the stand off point on the shell observed to be approximately 7% greater than the incident pressure. For the 2.0m, 3.0m and 5.0m load cases, the total pressures are observed to be less. The definition of reflected pressure is the pressure assuming a perfectly rigid structure, i.e., twice the incident pressure. Since the prototype shell is not perfectly rigid, the initial radiated pressure, i.e. that due to the deformation of the shell, must be negative. For the scattered pressure to be less than the incident pressure suggests that the initial radiated pressure is significantly negative. The prototype echinodome is a thin shell structure and consequently has a high degree of flexibility accounting for high levels of radiated pressure. It is possible that some of the energy of the shock wave may have been absorbed by the GRP material and rigid body motion. It is also worth mentioning that the magnitude of the total pressure was expected to be greatest at the stand off point which was true in all cases except the 2.0m load case. As the results clearly show, PG 2 ($\phi = 45^o, \theta = 0^o$) recorded the highest total pressure.

On the shadow side of the shell, at PG 6, the rise in pressure is noticeably less sharp, indicating the shock front has thickened whilst diffracting around the shell. Moreover, the pressure pulse is of considerably longer duration than at any other position. At other positions, after the initial rise and decay, a lower sustained pressure is also observed for approximately 1.0ms. These longer duration impulses are attributed to a combination of the shock wave decay pressure, scattered pressure and pressures imparted to the water due to rigid body motion. Such a loading is likely to be perceived by the shell as a short duration static load, but is of significantly less magnitude to be of importance under 10g EDC-1. However, their consideration in design under higher UNDEX loads could be necessary as they might invoke more damage to the shell than shorter duration impulses. Long periods of negative pressure were recorded for this position suggesting that cavitation is also occurring at the shadow side of the shell. This has been observed previously[73] and is attributed to the inward motion of this region of the shell upon impact of the shock wave at the near side.

Secondary sharp peaks produced from reflections off the floor of the tank are observed after the initial peak. These peaks are as high as 80% of the initial peak at some gauges in the 4.0m load case. In the other load cases they are of the order of 30-40% of the initial peak. The pressure recorded in the 4.0m load case suggests that a greater percentage of the charge may have detonated generating larger incident pressures and consequently larger reflected pressures.

Symmetry of loading

It was discovered upon assembling the results that the gauges relocated from the shell to the free field for the first load case were incorrectly chosen. The remaining gauges on the shell (PGs 3 and 6) were located at $\phi = 90^o$ on the $\theta = 0^o$ and 180^o meridians. To acquire data relating to the symmetry of the loading the gauges would have needed to have been located at $\phi = 90^o$ on the $\theta = 90^o$ and 270^o meridians. An alternative way of assessing the symmetry of the loading is to analyse the symmetry of the shell response which will be discussed in the following section.

5.4.3 Shell response

Primary peak strains

The majority of strain records, for all the symmetric load cases, exhibit a general trend similar to that shown in Fig. 5.5 over the first 50.0ms. An initial compressive peak

strain is followed by an oscillating decaying response indicating the damping influence of the impedance of the surrounding water's inertia.

The material stress wave generated by the impingement of the shock wave, and resistance to rigid body motion provided by the surrounding water, will result in a squashing of the shell and account for the initial compressive peak strain response observed at all strain gauge rosettes on the shell. Initially, as the shock wave engulfs the near side of the shell, this region will compress. Meanwhile the impingement of the shock wave will cause a stress wave to travel through the material at a higher velocity than the shock wave propagation velocity (speed of sound in GRP material $\approx$ 2200m^{-1}). Consequently, a rise in compressive strain is recorded prior to the arrival of the shock wave for positions on the shadow side of the shell. The impingement of the shock wave will also cause deformation of the shell as it attempts to push the shell away from the charge. The reaction pressures of the water on the shadow side will compress the shadow side of the shell inwardly. As the shock wave continues to propagate over and around the shell onto the shadow side the compression will increase. This is indicated by similar levels of strain on the shadow side.

Typical initial peak strains for the most severe load case are summarised in table 5.3. The entire strain response for the stand off position is depicted in Fig. 5.5. Strain records for other positions are examined in more detail when compared to numerical predictions in chapter 6.

Data was found to be corrupted at several gauges (SGs 13, 15 and 16). Strain responses revealed offsets leading to uncharacteristically high strain levels in certain directions which most likely were caused by gauge loosening. The two internal gauges fitted close to the base recorded almost double the strain levels of the external surface. The nature of the record suggested that the gauges had malfunctioned and hence these results were not considered as part of the shell response.

Unexpectedly, the highest initial peak strain response was recorded at the apex rather than at the maximum diameter for all symmetric load cases. The second highest circumferential peak strain was recorded at the base on the near side of the shell. The presence of the seam and imperfections of fit between the two halves of the shell could have generated higher strain levels in the circumferential direction at the apex which might not otherwise have occurred had the shell been monolithic. Previous dynamic loading studies concluded that the base region ought to be considered critical in design[3,4]. Significant levels of compressive and tensile strain are also recorded close to the base on the $\theta = 180^{o}$ meridian. Any flexure in these regions is attributed to a combination of the squashing effect mentioned above, and the influence of the tufnol

Position	Initial peak strain ($\times 10^6$)			Max. principal	Principal
ϕ, θ	Circum.	Merid.	Oblique	strain ($\times 10^6$)	angle
$0^o, 0^o$	-1921	-1357	-1701	-1928	6.2^o
$30^o, 0^o$	-935	-1405	-1067	-1427	11.8^o
$60^o, 0^o$	-570	-784	-537	-853	26.3^o
$90^o, 0^o$	-881	-905	-737	-1049	42.8^o
$90^o, 180^o$	-839	-925	-766	-1006	34.8^o
$120^o, 0^o$	-864	-921	-682	-1105	41.1^o
$150^o, 0^o$	-1433	-1373	-677	-2130	-43.8^o
$150^o, 180^o$	-1621	-1126	-1076	-1760	-25.1^o

Table 5.3: Initial peak strains, maximum prinicpal strains and principal angles under symmetric loading from 10g EDC-1 at 2.0m stand off

base. The shell gradually flattens, levelling out at the tufnol base plate. The stiffer base would exhibit higher modal frequencies than the rest of the shell. The transfer of these vibrations into the local weaker GRP laminate could amplify the bending in this region of the shell. Comparing the strain records at the apex and base it is evident that the strain response has a higher frequency at the base than at the apex. This is significant to any future design of an echinodome since the base region is were temporary or permanent attachments might be connected, and, in the case of a storage tank for storm flow[7], a base will be required to contain zeolite chemicals for treatment of the contents of the tank. It is therefore vital to consider the stiffness and mass effects of connections on the membrane under symmetric UNDEX loading.

An examination of the trends in the directions of peak strains gives a clearer understanding of the global response along the $\theta = 0^o$ meridian. Higher strains were recorded in the meridional direction at $\phi = 30^o - 120^o$ and in the circumferential direction at the apex and near the base. The circumferential radius of curvature of the laminate is greater than the meridional around the maximum diameter region. The smaller radius to thickness ratio meridionally implies the laminate should be stiffer meridionally and the higher strains recorded for this direction confirm this to be the case. Towards the apex and base flexibility in the circumferential direction is more prominent. The radii of curvature are equal near to the apex. Consequently, the same levels of strain were expected. The difference could be due to the mismatch of the seam at this position. At the base a larger difference is recorded on the shadow side than the near side. These differences might be caused by effects from the tufnol base

and/or variations in material thickness.

The maximum principal compressive strains induced by the symmetric UNDEX loading are observed to increase from the loading point towards the apex and base. The highest maximum principal strains occur on the near side at the base and at the apex. Interestingly, the principal strains on the shadow side at the base are almost 20% less than those on the near side. From the principal angles it is clear that the direction in which the principal strains are occurring increases from approximately 6^o at the apex to almost 45^o on the near side at the base. Whilst the strain levels under this particular load case are not in danger of exceeding the critical strain of the shell laminate, under higher symmetric UNDEX loading it could be necessary to alter the configuration of any reinforcement bars for different regions of a concrete shell. For the region $\phi = 0^o - 60^o$ the original recommendation[4] of bars positioned at 0^o and 90^o is sufficient, however, for the region $\phi = 60^o$ to the base extra bars positioned at 45^o would be needed to strengthen a full scale shell in this direction.

Secondary peak strains

The significance of the bubble pulse mentioned earlier is clearly evident from Fig. 5.5. The energy contained within the bubble pulse generates strain rates, and peak strains, of the same order of magnitude and, in some instances, higher. The consideration of the bubble pulse loading in the design of an echinodome is clearly important, particularly if weakening has resulted from the shock pulse loading, as the bubble may induce permanent damage.

At no position did the initial or secondary peak strains exceed the static material failure strain of the GRP (-6295$\mu\varepsilon$) under symmetric loading conditions. The highest strain recorded, in the apex region, came to within 32% of the ultimate. Fig. 5.7 shows a linear relationship exists between peak structural response to shock loading and load confirming that non-linearities were not invoked at the critical regions.

Symmetry of response

SGs 9 and 13 recorded a variance in the symmetry of the shell's response for the oblique direction (45^o), as illustrated in Fig. 5.6. The peak strain response at SG 13 is almost double that of SG 9. Without having pressure-time histories for these locations it is difficult to determine if this is a consequence of the loading or genuine unsymmetric shell response. As mentioned earlier, SG 13 appeared to be recording uncharacteristic responses. The oblique direction was the only direction in which data was worthy

of consideration. Consequently, its data is not reliable enough to legitimately make conclusions regarding the symmetry of the shell response.

Frequency excitation

A limiting factor in designing the experiments was to minimise the amount of structural damage caused to the prototype. Transient loads were characterised by a pressure magnitude and a pressure pulse. The stress induced by the pressure magnitude relative to the ultimate tensile strength of the prototype's material and the duration of the shock and bubble pulses relative to the shell's periodic times, were the two main factors controlling the dynamic response of the shell to transient loads. If the frequency of the loading is close to one of the natural frequencies at which the shell vibrates then resonance could magnify the loading on the shell. The time duration of the impulse is observed to be of the order of 100μs (10kHz). As stated earlier in chapter 3, the natural frequencies of the prototype shell in a submerged environment were not known. However, earlier investigations estimated structural frequencies in the range 60Hz - 576.17Hz[79] for the first eight modes in air with fixed base conditions. Submerging and tethering the prototype would have the effect of reducing this frequency range. Therefore, the frequency of the shock and bubble pulses are considered too high for resonance to occur although this range of modal frequencies will be excited throughout the UNDEX event. At later times in the event (milliseconds) the frequency of the structural response will reduce, at the risk of exciting lower modes of vibration if significant levels of deformation are experienced.

To determine the frequencies excited by the UNDEX loading on the shell an energy spectral density (ESD) plot, generated by transforming all strain signals into the frequency domain, is a common method of analysis. The ESD for the above signals was found to contain a high level of contamination at the high frequency end of the spectrum (> 20kHz). The contamination was thought to be caused by either electrical noise corrupting the strain signal or secondary pulses emanating from the oscillating bubble superimposing high frequency pulses onto the shell which was still responding to the first shock wave pulse. This would increase the frequency response of the shell making the higher frequencies difficult to determine. One solution to this problem would have been to process the time domain comprising the shock wave pulse only but this would have rendered only a limited representation of the complete structural response throughout the UNDEX event.

Consequently, the strain signals were filtered using a low pass filter with a cut off frequency, f_c, of 20kHz, i.e., all frequency components above 20kHz were removed. An

exponentially decaying window was also applied to gradually decay the amplitudes of the oscillations.

Although the energy of the signal is affected by filtering it is the frequency content that is of primary interest. It is observed that at early time in the strain response to the shock loading (< 15ms) high frequencies (kHz) were recorded from the shell, whereas at late time, (> 15ms) low frequencies (Hz) are evident. Similar observations are evident from the bubble loading. After filtering out all frequencies above 20kHz the resolution of the lower frequencies improved but the higher frequencies were still indeterminate. Hence, only the 0.0 – 1.0 kHz frequency band was considered for frequency response information.

Figs 5.8(a) – (c) illustrate ESDs of the circumferential strain responses recorded at various positions for the 2.0m load case. The frequencies most excited are indicated by the highest energy density which, for the stand off point, apex and base, is 190Hz. At the stand off point and apex a lower frequency of 20Hz is also evident. As the stand off distance increases the most commonly excited frequencies increase to 21Hz and 200Hz, and, 22Hz and 210Hz. These frequencies, when converted back into time correspond to approximately 48ms and 5ms periods and constitute late time response.

5.5 Results of axisymmetric loading

5.5.1 Free field fluid response

Pressure

The free field pressure gauges, PGs 8 and 9, shown in Fig. 4.3, displayed similar characteristics for free field fluid response at 1.0m stand off for 5g EDC-1 as recorded in the symmetric load cases. As Figs 5.9(a) and (b) show, the arrival of the shock front is identified by a rapid increase in pressure to a peak value of 4.325MPa (PG 9) followed by a rapid exponential decay for approximately 100μs, after which, secondary peaks of a considerably lower magnitude are observed. The pressure then decays at a slower exponential rate. As in the symmetric load cases, this irregularity in the decay makes it difficult to determine a single decay constant. However, the decay rate, θ, was estimated to be 33ms.

Data relating to the free field response is listed in table 5.4. The average initial peak pressure, at 1.0m stand off from 5g EDC-1, is similar to that of the 10g charge at the same stand off distance (see table 5.2). Using the shock factor relationship a peak

Gauge no.	Peak pressure (MPa)		Impulse, I (Pa.s)		Energy, E_f (Pa.m)	
	Shock	Bubble	Shock	Bubble	Shock	Bubble
8	4.080	0.699	189.61	160.95	124.35	23.84
9	4.325	0.694	186.49	168.02	121.38	24.13

Table 5.4: Comparison of shock wave and first bubble pulse characteristics at 1.0m stand off from 5g EDC-1

pressure of 3.6MPa for a 1.0m stand off from 5g EDC-1 is estimated from the average of the 10g EDC-1 results, 20% lower than that recorded. The shock factor is only an approximate guide, but it is possible the 5g charge may have been more successful in detonating than the 10g. Reversing the use of the shock factor relationship, a peak pressure of 6.12MPa is estimated for the peak pressure at 1.0m stand off from 10g EDC-1 which correlates with the higher free field pressures recorded for 10g EDC-1.

A difference in shock front arrival times of 30μs was recorded. This time variance corresponds to a distance of 40mm (assuming $c = 1500\text{ms}^{-1}$) which, divided over two gauges, would mean an offset of 20mm in the positioning of each gauge. Experimental errors of this magnitude were also found to occur in the 2.0m symmetric load case.

Incorrect setting of a gauge response level resulted in clipping, i.e. a loss of the recording of peak pressure data, at PG 15. A plateau is evident from Fig. 5.10 signifying that the pressure at this distance exceeded 5.6MPa. Fig. 5.10 does give evidence of bulk cavitation being recorded by this pressure gauge. Negative pressure is observed for a sustained period of time after 0.35ms rising again on arrival of a reflection. The ability of the pressure gauge to quantify this cavitation is in question since pressures below absolute zero are being recorded. Consultation with DERA (Rosyth) confirmed this.

Bubble pulses

The pressure at PGs 8 and 9 is observed to increase 45ms after the initial shock pulse, indicating the arrival of the first bubble pulse. Table 5.4 compares the parameters relating to the shock and first bubble pulses at 1.0m stand off from 5g EDC-1. A second bubble pulse was detected at 79ms.

As is evident in table 5.4, the pressure loading from the bubble is approximately 15% that of the shock wave. The impulse per unit area for the bubble pulse is of the same order as the shock pulse but not higher, as recorded for 10g EDC-1. The radiated

bubble energy is observed to be of the order of one-fifth of the radiated shock energy. These results suggest it is unlikely that bubble loading would contribute further to any shock induced structural damage.

Reflections

Fig. 5.10 records evidence that reflections from the boundary surfaces are being observed by PG 15. The pressure magnitudes are approximately 36% of the peak pressure at the shock front. Taking the shortest path from the charge to PG 15 as a reflection from the back wall of the tank the average shock wave speed was estimated to be $1761 ms^{-1}$.

5.5.2 Fluid response at shell

Total pressure

The early response pressure-time histories of the fluid response in the vicinity of the shell are depicted in Figs 5.11 and 5.12. Despite the presence of electrical noise, due to voltage gains being set at too high a level for the measuring station, filters were not used on the pressure records as they carried the risk of filtering out the peak pressure responses.

PGs 1 and 2 recorded the total pressure at and near the apex of the shell. The characteristic sharp rise followed by a rapid decay to negative pressures, possibly indicating cavitation in the apex region, is evident. The total pressure peak is observed to be approximately 20% higher than that recorded at the free field gauges which suggests that the initial radiated tensile pressures are lower under axisymmetric loading than symmetric loading. For the symmetric direction the total pressure at the stand off position was lower than the incident pressure in three out of four load cases. Further loading studies would be necessary to determine the exact cause of the lower scattered pressure levels in the symmetric cases.

The pressure-time histories recorded by PGs 3, 4 and 6 indicate an initial gradual form of loading at the maximum diameter of the shell with several sharp peaks, similar to that observed at the apex during the symmetric load cases. The duration of this loading is such that it would appear to the prototype shell as an application of quasi-static load on the maximum diameter for a period of almost 1.0ms. It is difficult to account for why the sharp peak recorded at approximately 1.1ms at PG 3 was not recorded at PG 6. A similar pulse was observed slightly later in time at PG 4. The pulse recorded

at PGs 2 and 3, prior to the peak total pressure, could be due to the arrival of the detonation pulse prior to that of the shock wave. For the axisymmetric direction, the detonator is approximately the same distance from the shell as the charge and, as it detonates first, the pulse from the detonator will arrive at the shell before the shock wave. This highlights a further difficulty with utilising this detonation technique for axisymmetric load cases. The ability of the pressure gauges to quantify cavitation pressures was questioned earlier and the experimental data for PGs 3, 4 and 6 add further uncertainties. The negative pressures recorded here are below absolute zero (-0.1MPa) which is physically impossible. The data does however, strongly indicate that significant cavitation is occurring.

Axisymmetry of loading

Fig. 5.12 also indicates some variation in the axisymmetry of the loading around the maximum diameter of the shell. Ignoring the initial peak in the pressure-time record for PG 6, the shock wave peak pressure for PG 3 is 0.620MPa, compared to 0.540MPa for PG 6. Also, the arrival time of the shock wave differs by approximately 15μs, which corresponds to a distance of 26mm (assuming $c = 1761\text{ms}^{-1}$). Such variations in time and pressure magnitude might be related to the variations recorded in PGs 8 and 9. Conversely, the gauge placement on the shell might have been inexact, or PG 3 may have been orientated slightly more towards the charge.

5.5.3 Shell response

After the symmetric load cases there was confidence from the strain levels recorded that no damage had been invoked in the shell. Therefore it could be assumed that the shell had the same material and geometric characteristics for the axisymmetric load case.

Primary peak strains

Initial peak strains along the $\theta = 0^{\circ}$ meridian are summarised in table 5.5. The region around the apex of the shell is subjected to the highest shock impulse per unit area, since this part of the shell sees the shock impulse first. Consequently, the strains are highest in this region. The strain-time history for the apex stand off point is shown in Fig. 5.13 and is seen to exhibit a rise in initial peak response, reducing prior to peak response. As with the symmetric load case a more detailed presentation of strain records

Position	Initial peak strain ($\times 10^6$)			Max. principal	Principal
ϕ, θ	Circum.	Merid.	Oblique	strain ($\times 10^6$)	angle
$0^o, 0^o$	-3164	-2368	-2971	-3214	13.6^o
$30^o, 0^o$	-1766	-2123	-1873	-2137	10.9^o
$60^o, 0^o$	-997	-754	-828	-1006	-10.7^o
$90^o, 0^o$	-1224	-1003	-918	-1338	-30.3^o
$90^o, 180^o$	-1010	-661	-778	-1020	-9.1^o
$120^o, 0^o$	-1034	-807	-926	-1034	1.4^o
$150^o, 0^o$	-1833	-1439	-1314	-2013	-29.3^o
$150^o, 180^o$	-1602	-696	-1300	-1627	9.2^o

Table 5.5: Initial peak strains, maximum prinicpal strains and principal angles under axisymmetric loading from 5g EDC-1 at 1.0m stand off

at other positions is given in chapter 6 when compared with numerical predictions.

The strain levels are observed to reduce with distance from the apex. At the maximum diameter (along meridian $\theta = 0^o$) peak strains are observed to be higher than $\pm 30^o$ either side, a phenomenon observed at the apex and base regions for the symmetric load case. As well as causing localised displacements, the shell tries to undergo rigid body motion downwards, impelling the shell against the water. Resistance provided by the surrounding water would result in a squashing effect as reaction pressure would push against the shell compressing it. The pressure of the propagating shock wave down the shell contributes further to the compression of the entire shell.

Towards the base, strains are observed to increase at $\phi = 150^o$, indicating further bending in this part of the shell. Bending in this region could be caused by a combination of the deformation due to squashing, and the influence of the stiffer tufnol base, as in the symmetric load cases. Under this loading the base provides a large flat surface that would result in large reaction forces as the shell tries to move downwards against the surrounding water. The transfer of these forces into the weaker GRP laminate, combined with the higher frequencies excited in the base, as observed in the response to the symmetric loading, would contribute to bending in this region.

The trend observed in the direction of peak strains for the symmetric load case is not evident for the axisymmetric load case. Under axisymmetric loading, the apex is noticeably stiffer in the circumferential direction due to the presence of the seam making the shell more flexible meridionally. For a monolithic shell the strain records

for the circumferential and meridional directions at this position would be expected to be the same. At $\phi = 30^o$, dominant peak strains are in the stiffer meridional direction suggesting that the shell laminate is conforming to the earlier trend noted in the symmetric load cases. However, from $\phi = 60^o - 150^o$, the circumferential peak strains dominate. Given that the radius of curvature is larger over this region it is difficult to explain why the meridional strains are not higher.

The maximum principal compressive strains indicate the base and apex require strengthening under axisymmetric UNDEX loading as well as symmetric loading. The response in the base region was expected to be the same, however, the principal strain levels at $\phi = 150^o, \theta = 0^o$ and 180^o indicate the shell is stiffer at $\theta = 0^o$. However, the principal strain at the apex exceeds that of the base region. Consequently, under higher axisymmetric UNDEX loads the critical strain level of the laminate would most likely be exceeded at this position first. Several positions suggest that, for a full scale concrete shell, reinforcement bars would be required for strengthening purposes in the 45^o direction, as well as the 0^o and 90^o directions, namely in the maximum diameter and base regions. Elsewhere bars in the 0^o and 90^o directions would be sufficient.

As an interesting aside, previous microstructural studies done on GRP laminates have indicated that an air backed GRP structure is more prone to damage than a liquid backed GRP structure[82,83]. The large impedance mismatch between the laminate and air causes the shock wave to be almost entirely reflected off the inner surface of the laminate, effectively doubling the shock loading. For liquid backed structures, there is a lower impedance mismatch between the liquid and laminate permitting the shock wave to pass through, and continue into the liquid. The liquid also provides a cushion for the GRP when hit by a shock wave reducing the amount of bending, and hence tensile and compressive stresses, on the laminate. Membrane strain responses from a liquid backed echinodome would be expected to be higher than those above as a consequence of increased stiffness due to the presence of the liquid inside. Experiments from the same work also found that the isotropic nature of the random fibre orientation of the chopped strand mat GRP contributed greatly to ultimate strength of the material.

Other sensitivity studies have reported that stiffness and ultimate tensile strength are increased when strain rate is increased. This suggests that GRP laminates could withstand higher loads under shock loading than quasi-static loading[82,84].

Secondary peak strains

The significance of the bubble pulse is again clearly evident from Fig. 5.13. The severity of the bubble pulse loading generates strain rates and peak strains of the same order of magnitude, and in some instances higher, e.g. at the stand off position.

At no position did the initial or secondary peak strains exceed the maximum allowable strain of the GRP material (-6295$\mu\varepsilon$) under axisymmetric loading conditions. The highest peak strain recorded, in the apex region, came to within 53% of the ultimate value.

Axisymmetry of response

Variations in the axisymmetry of the structural response are apparent when analysing the strain responses located around the maximum diameter, as seen in Fig. 5.14. The initial peak structural responses at SGs 4, 9 and 12 occur at different times by as much as 300μs. This would result if the shock front were to arrive at these parts of the shell at different times, or it could be a consequence of the fact that the shell was not monolithic. The elastic properties of the seam would permit the two halves of the shell to respond differently when loaded. Also, the two halves were not a perfect match, particularly around the seam, due to variations in thickness and geometrical form over the entire shell surface. Such discontinuities would also contribute to variations in shell response throughout the GRP laminate.

Frequency excitation

Fig. 5.15 illustrates an ESD of the filtered strain response shown in Fig. 5.13. The main responses excited by 5g EDC-1 at 1.0m stand off distance are 35Hz at the apex and 400Hz at the base (not shown), corresponding to time periods of 28ms and 5ms respectively. From the filtered signal, shown in Fig. 5.13, they equate with the periods of structural response after 130ms. The effect of the stiffer tufnol plate attached to the base is evident under axisymmetric loading also.

Higher frequencies were recorded under axisymmetric UNDEX loading than symmetric. Although both charge size and stand off distance were different in each case, the trend in frequency response follows that observed previously[4] with a modal analysis performed on the shell in air. The frequency for the axisymmetric mode (243.69Hz) was higher than for the symmetric mode (60.67Hz). The different operating environment, boundary conditions and loading conditions make it difficult to take this comparison

any further. A modal analysis in the underwater environment would be required to determine fundamental frequencies for symmetric and axisymmetric modes.

As in the symmetric load case it was concluded that secondary pulses emanating from the oscillating bubble were superimposing high frequency pulses making the high frequency response difficult to determine.

5.6 Correction of experimentally measured loads

It is intended to extract peak pressure and decay values from all free field results of the axisymmetric and symmetric load cases to provide a more accurate description of the load for numerical simulations. Using experimentally measured peak pressure decay values as input to DAA simulations could provide a stronger quantitative verification of the predictive capabilities of USA-DYNA3D.

Using exponential curve fitting techniques on the collation of pressure-time signals recorded at various stand off distances, a decay rate can be estimated over a specified time period. However, experience has shown that the measured peak pressures might not correspond to the actual peak pressures. The finite size of the pressure gauge requires an averaging of the pressure over the width of the gauge. Also there is a time lag of approximately 10μs, known to occur at the measuring station, between each reading. The averaging procedure and time lag mean a higher peak pressure could fail to be recorded.

To account for the time interval it is common practice to apply a correction to the experimental signals[73]. This correction involves fitting a linear curve over the rise time, t_r, between the limits $t_{0.1P_{max}} < t_r < t_{0.9P_{max}}$, and an exponential fit over the decay time, t_d, between the limits $t_{0.9P_{max}} < t_d < t_{0.1P_{max}}$. The time at which the corrected peak pressure occurs, t_2, is taken as midway between the time the two fitted curves intersect, t_3, and the time at which $P = 0$ in the linear fit equation, t_1. Once t_2 is known it is substituted back into the exponential fit equation and the corrected peak pressure P_{cmax} evaluated. Fig. 5.16 illustrates the correction technique graphically. The peak pressure decay values, along with resulting impulse and energy quantities (integrated over $t_{pmax} - t_{\frac{pmax}{100}}$) are compared in table 5.6. Empirical equivalents are shown for comparison purposes.

The effect of the averaging and time delay on 5g EDC-1 at 1.0m stand off is clear from table 5.6. The rapid decay rate causes a 27% increase from the experimentally measured to corrected peak pressures. The empirical peak pressure decay values generate a higher

Value	P_{max} (MPa)	θ (μs)	I (Pa.s)	E_f Pa.m)
Exptl (measured)	4.200	33.000	170.68	122.71
Exptl (corrected)	5.812	49.184	285.50	314.86
Empirical	7.0096	25.500	178.53	237.54
Power law	3.799	32.482	26.562	22.016

Table 5.6: Comparison of empirical and experimental shock wave quantities at 1.0m stand off from 5g EDC-1

peak pressure than the corrected values. However, the lower empirical decay rate results in a lower impulse value than the experimentally corrected impulse.

5.7 Power laws

Data from experimental free field pressure-time curves could assist in the generation of similarity curves for the EDC-1 explosive material. Similarity curves provide a means of producing power laws to predict the dependence of shock wave parameters over a range of charge masses and distances. These power laws could be used in the design of future experiments using EDC-1.

Using the decay constants fitted to the experimental data, pressure decay curves were integrated to time $t = 6.7\theta$, to provide corresponding shock wave impulse and energy flux density values. Each of these shock wave parameters was then reduced by the respective charge mass and plotted against $\frac{W^{\frac{1}{3}}}{R}$ to generate the similarity curves illustrated in Fig. 5.17.

The quality of the power fits is influenced by the quantity of experimental data available, which, apart from 10g EDC-1 at 1.0m stand off, was considered to be low. Also the accuracy of the data is influential. The scatter of data points observed on the peak pressure and decay similarity curves for each $\frac{W^{\frac{1}{3}}}{R}$, particularly for 10g at 1.0m, indicates a low correlation between the data. Nonetheless, from these curves the following power laws for peak pressure, decay constant, impulse and energy flux density of the EDC-1 explosive material, were obtained.

$$P_m = 34.5\left(\frac{W^{\frac{1}{3}}}{R}\right)^{1.249} \tag{5.1}$$

$$\theta = 521.7W^{\frac{1}{3}}\left(\frac{W^{\frac{1}{3}}}{R}\right)^{0.572} \tag{5.2}$$

$$I = 2316.3W^{\frac{1}{3}}\left(\frac{W^{\frac{1}{3}}}{R}\right)^{1.530} \tag{5.3}$$

$$E_f = 6137.0W^{\frac{1}{3}}\left(\frac{W^{\frac{1}{3}}}{R}\right)^{2.188} \tag{5.4}$$

The above power laws are empirical and should be used with caution when calculating design loads. As is clear from table 5.6 the impulse and energy power laws yield predicted shock wave parameters much lower than those measured. Equations 5.1 – 5.4 are approximate but could be used for larger charge sizes and/or stand off distances, provided all other linear dimensions are scaled according to the principle of similarity. It should be borne in mind that these relationships were obtained from a cylindrical charge shape. Deviations from this shape and/or material may lead to variations in loading severity and a different set of constants would need to be defined.

5.8 Conclusions

Experimental studies, subjecting the prototype echinodome to UNDEX loading were conducted under symmetric and axisymmetric conditions. The subsequent fluid responses were examined and compared with empirical results.

After correction, the free field fluid response data was utilised to produce power law relationships to assist in the design of future experiments using the EDC-1 explosive material.

The free field fluid response produced characteristic pressure peaks and exponential decays, subsequently followed at later times by bubble pulses. However, the total fluid pressures at the shell were lower than expected. For the majority of cases the total pressure was less than the incident pressure. It was evident that bulk cavitation was recorded close to the free surface and local cavitation at the apex, maximum diameter and base in both loading directions. Longer duration shock pulses were observed on the shadow side of the shell which, for higher UNDEX loading, could cause more damage than the shorter duration pulses.

Analysis of the shell response revealed that, under both symmetric and axisymmetric loading, the apex and base regions of the shell were most critical, undergoing the highest strain levels. The axisymmetric load case generated the most severe loading on the shell. At 90^o from the stand off point, in both loading directions, a longer duration transient load was observed. At no position were strain levels found to exceed the maximum static material failure strain. The tufnol plate was seen to generate higher frequency vibrations in the base region under both symmetric and axisymmetric loading, contributing to increased bending at the base. The direction of the principal strains suggested that under higher loads reinforcement bars would be required at 45^o, as well as 0^o and 90^o, in the region $\phi = 60^o$ to the base to strengthen this area of a full scale shell. Elsewhere bars at 0^o and 90^o would be sufficient.

Several aspects of the experimental results were unsatisfactory and their consideration in future experiments would be worthwhile.

1. The sphericity of the shock wave upon impingement with the shell is in question. Care should be taken over pressure gauge placement as small variations in gauge placement would lead to large variations in resultant pressure at the shell due to the rapid decay rates involved.

2. Incomplete detonation of the charges or degradation of pressure gauges led to a large variation in loading. An alternative method of charge detonation or gauge replacement after each load case could reduce this inconsistency. The detonation technique also proved to be unsuitable for axisymmetric load case due to the pulse emanating from the detonator contaminating both the free field and total pressure results.

3. The imperfections of the shell generate discontinuities along the seam which influenced local peak strain levels, particularly at the apex. The overall structural response was observed to contain inconsistencies in the direction of peak strain expected for each load direction. A monolithic structure with minimal imperfections could overcome both these problems.

Despite these irregularities, the fluid and shell response data is concluded to be of sufficient reliability to validate LS-DYNA and USA-DYNA3D in modelling both these UNDEX load cases.

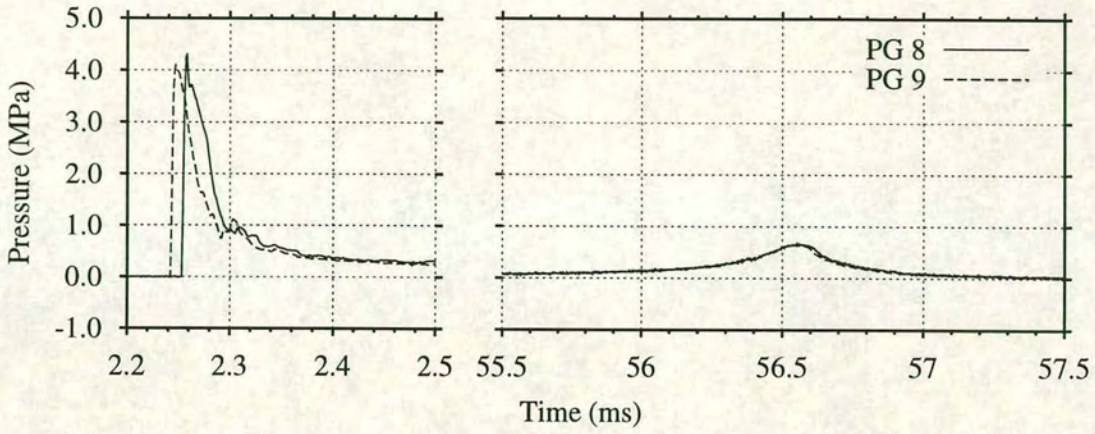

(a) Shock and bubble pulses

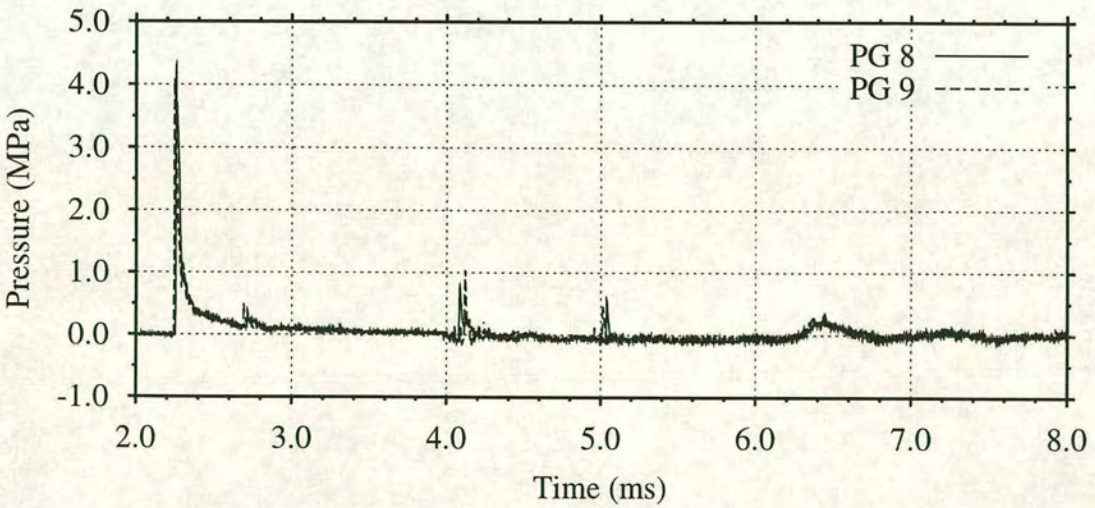

(b) Reflections

Figure 5.1: Free field fluid response to 10g EDC-1 at 1.0m stand off

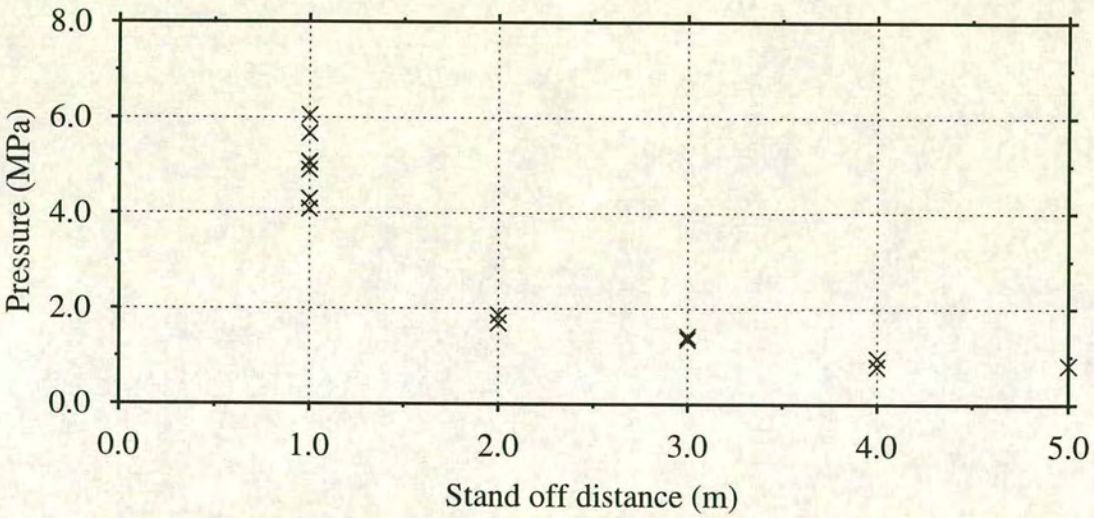

Figure 5.2: Incident peak pressure at various stand off distances (1.0 – 5.0m)

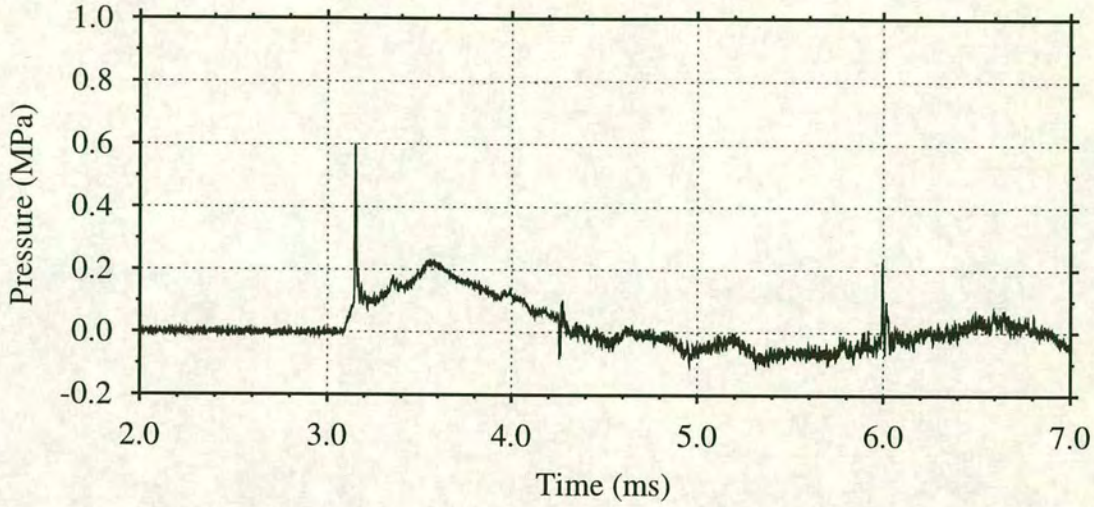

(a) $\phi = 0°, \theta = 0°$ (PG 1)

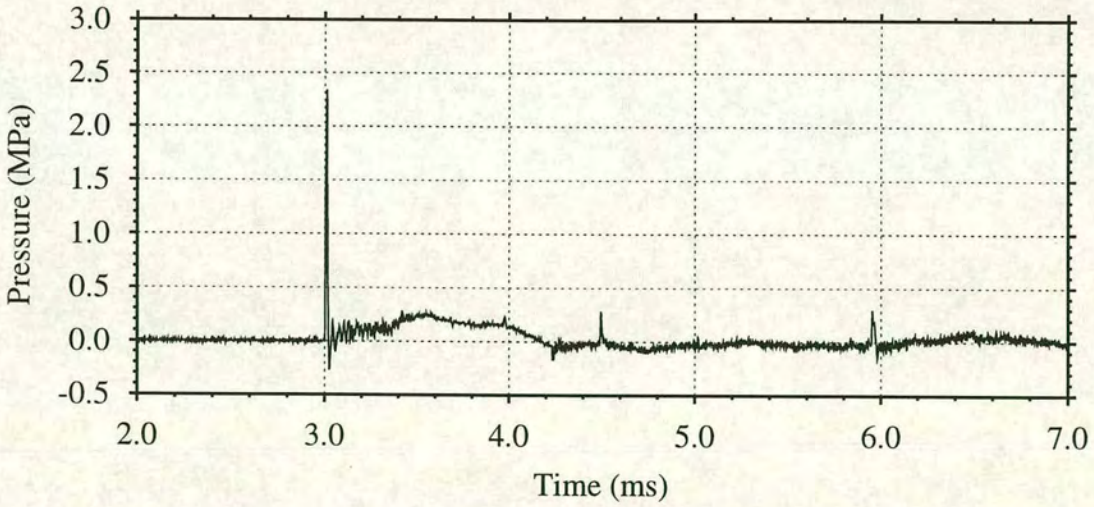

(b) $\phi = 45°, \theta = 0°$ (PG 2)

Figure 5.3: Fluid response at shell to 10g EDC-1 at 2.0m stand off (symmetric)

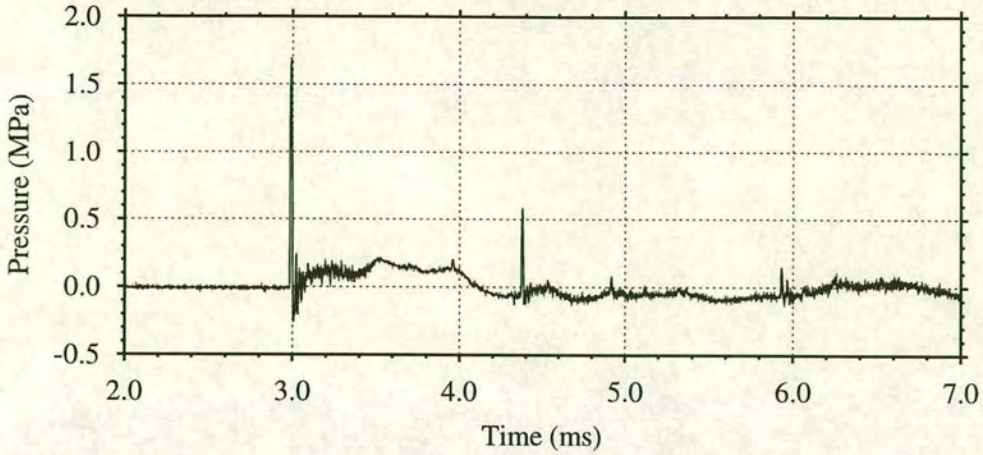

(a) $\phi = 90°, \theta = 0°$ (PG 3)

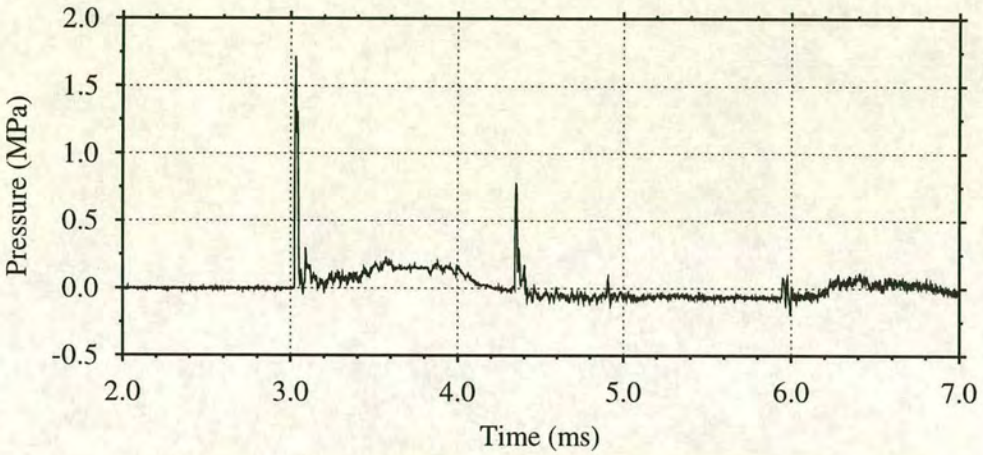

(b) $\phi = 135°, \theta = 0°$ (PG 4)

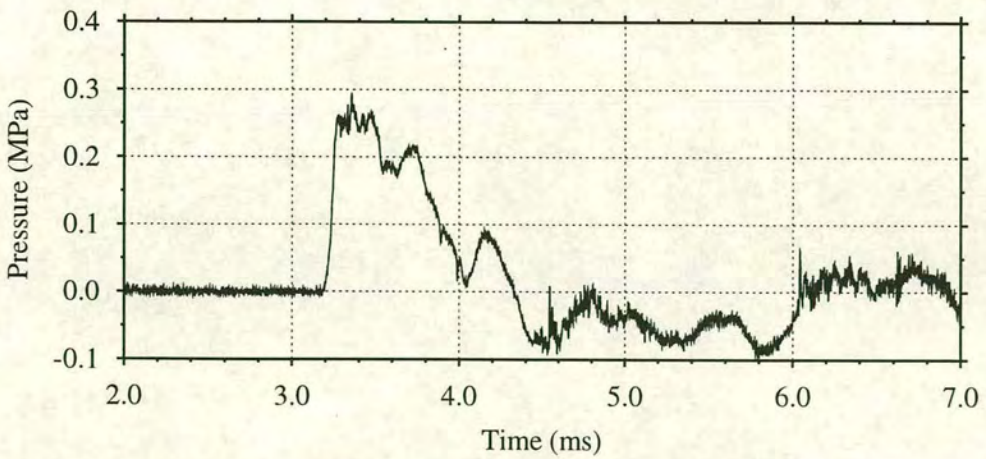

(c) $\phi = 90°, \theta = 180°$ (PG 6)

Figure 5.4: Fluid response at shell to 10g EDC-1 at 2.0m stand off (symmetric)

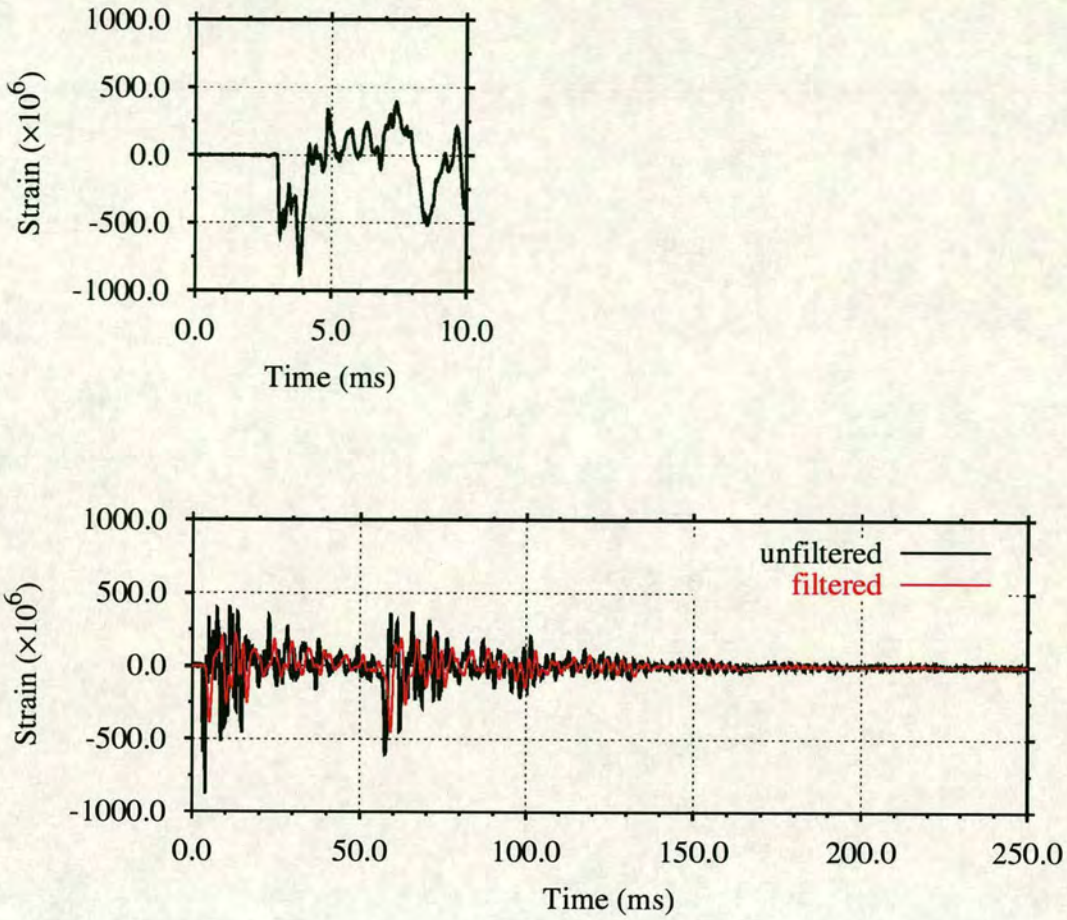

Figure 5.5: Circumferential strain response at $\phi = 90^o, \theta = 0^o$ to 10g EDC-1 at 2.0m stand off (symmetric)

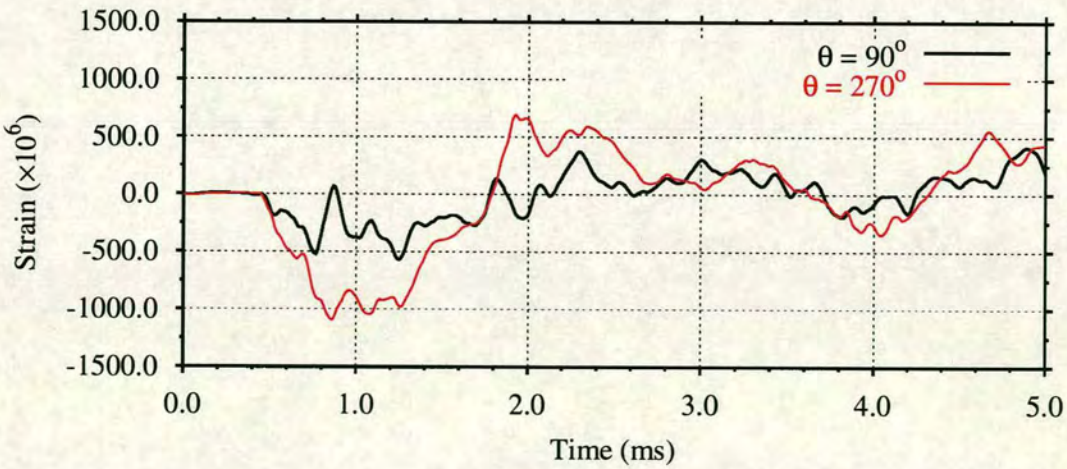

Figure 5.6: Symmetry of shell response (oblique strain) at $\phi = 90^o$ to 10g EDC-1 at 2.0m stand off (symmetric)

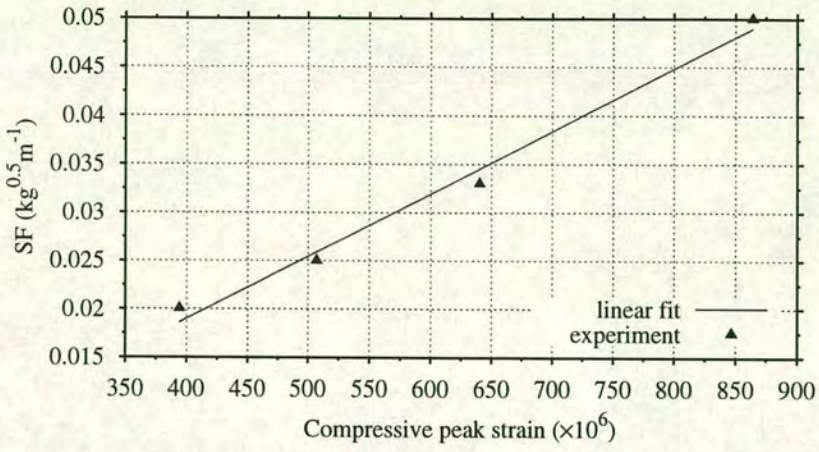

(a) $\phi = 90^o, \theta = 0^o$ (circumferential)

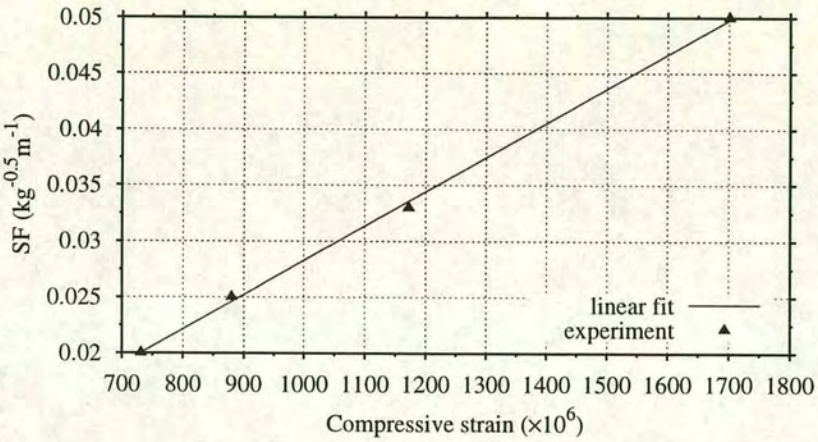

(b) $\phi = 0^o, \theta = 0^o$ (oblique)

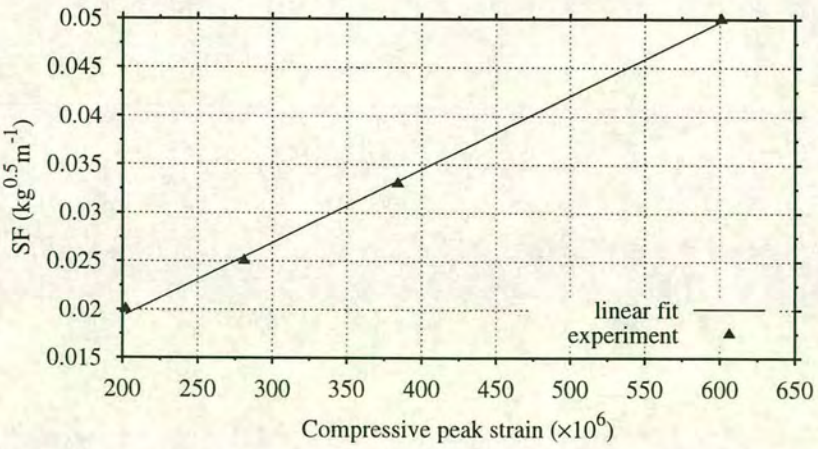

(c) $\phi = 150^o, \theta = 0^o$ (oblique)

Figure 5.7: Load vs strain relationships at various positions on the shell for symmetric loading from 10g EDC-1 at 2.0m stand off

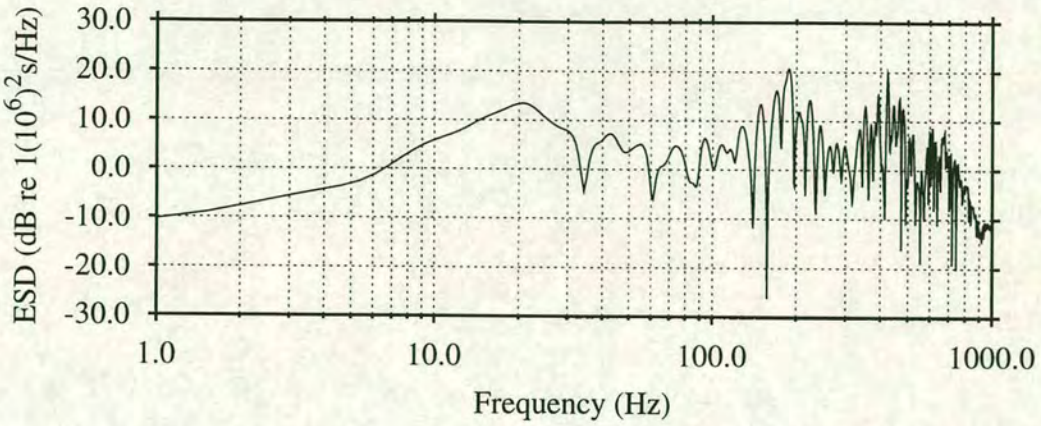

(a) $\phi = 0°, \theta = 0°$

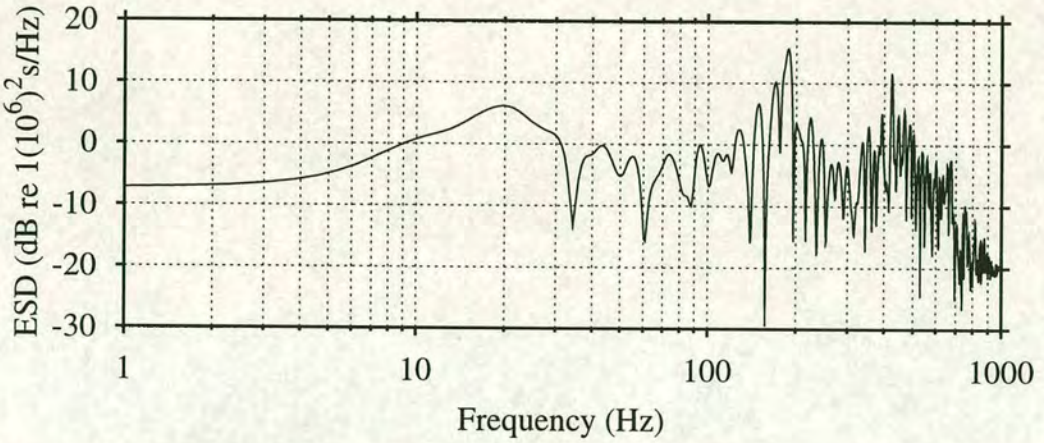

(b) $\phi = 90°, \theta = 0°$

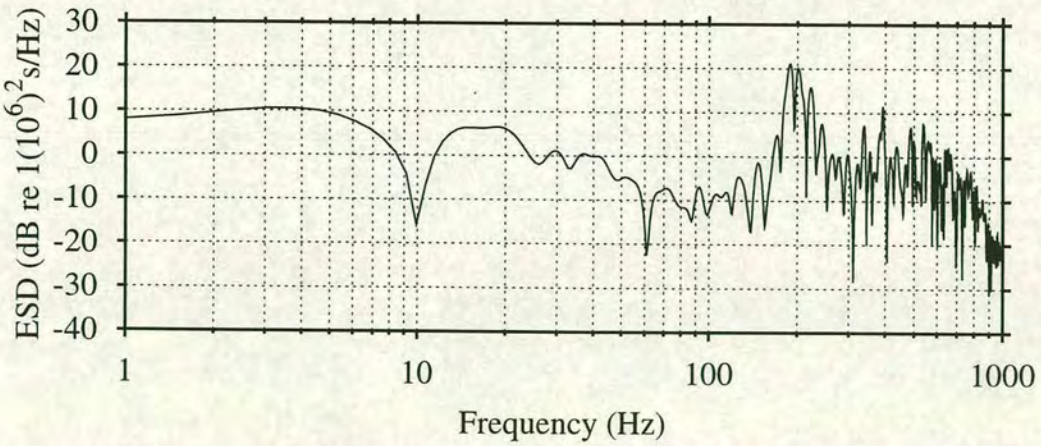

(c) $\phi = 150°, \theta = 0°$

Figure 5.8: Energy spectral densities of circumferential strain response at various positions under symmetric loading from 10g EDC-1 at 2.0m stand off

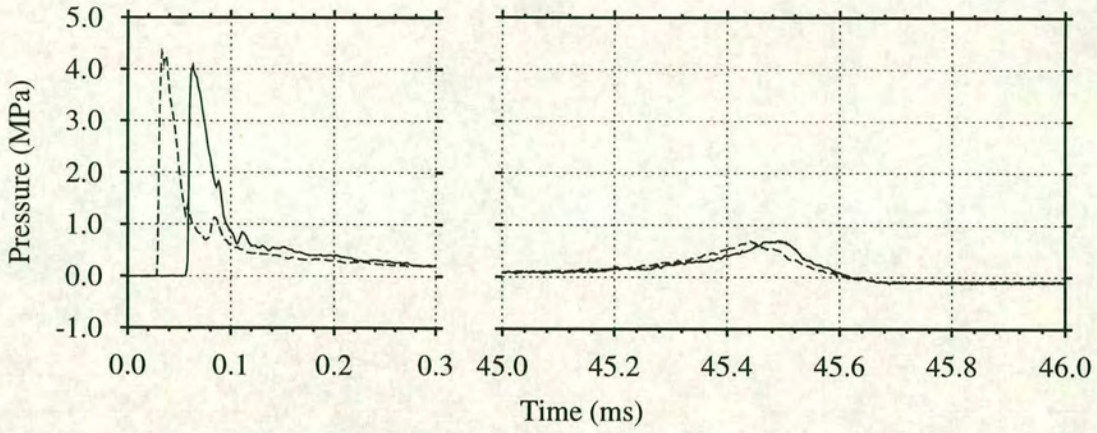

(a) Shock and bubble pulses

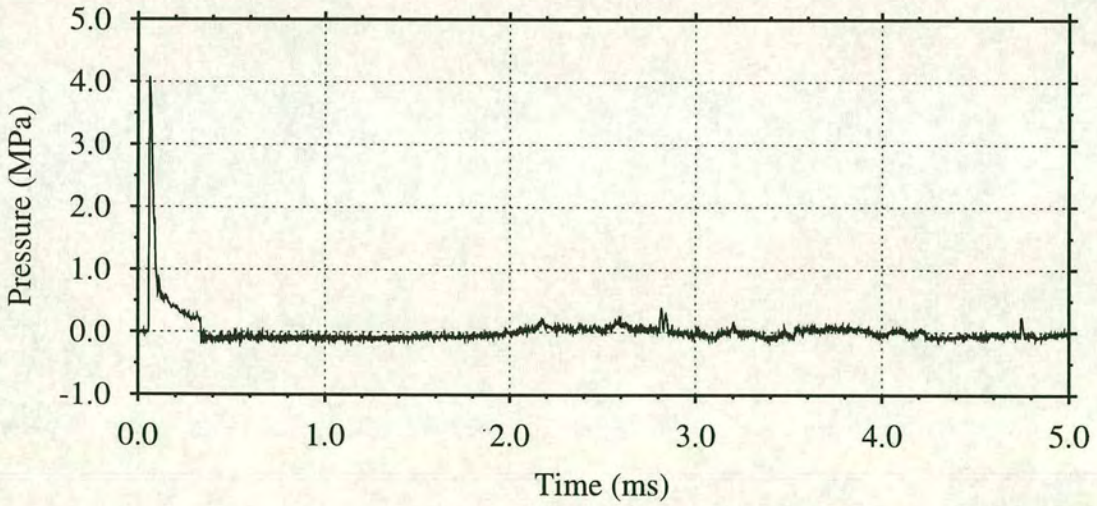

(b) Reflections

Figure 5.9: Free field fluid response to 5g EDC-1 at 1.0m stand off (axisymmetric)

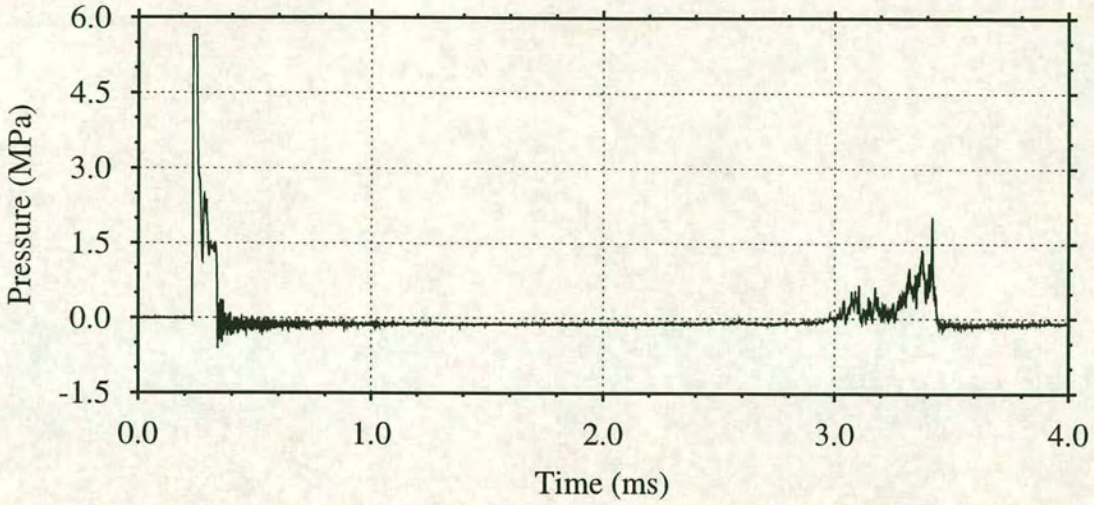

Figure 5.10: Clipping due to low gauge setting (PG 15), at 0.45m stand off from 5g EDC-1

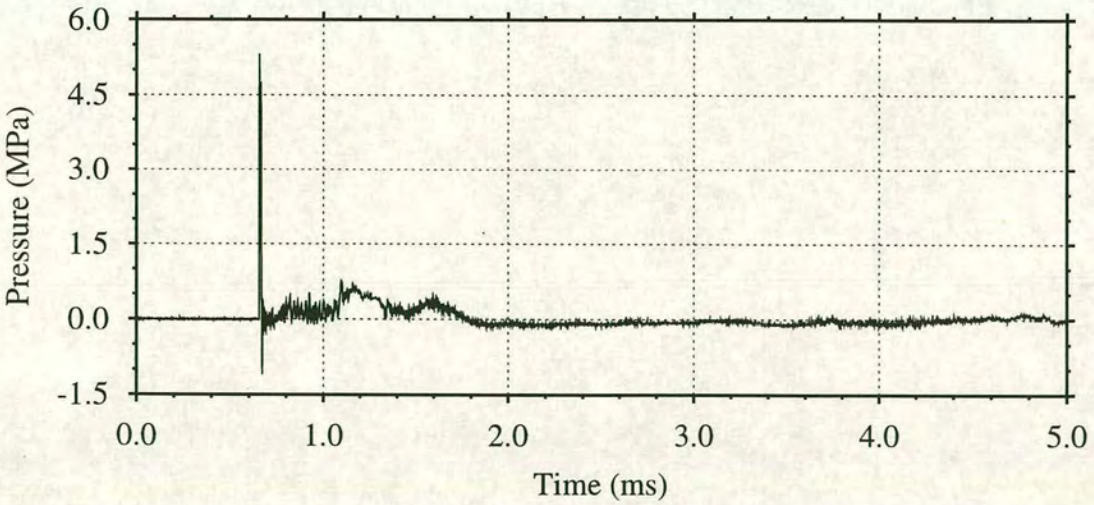

Figure 5.11: Fluid response at $\phi = 0^o, \theta = 0^o$ on shell (PG 1) to 5g EDC-1 at 1.0m stand off (axisymmetric)

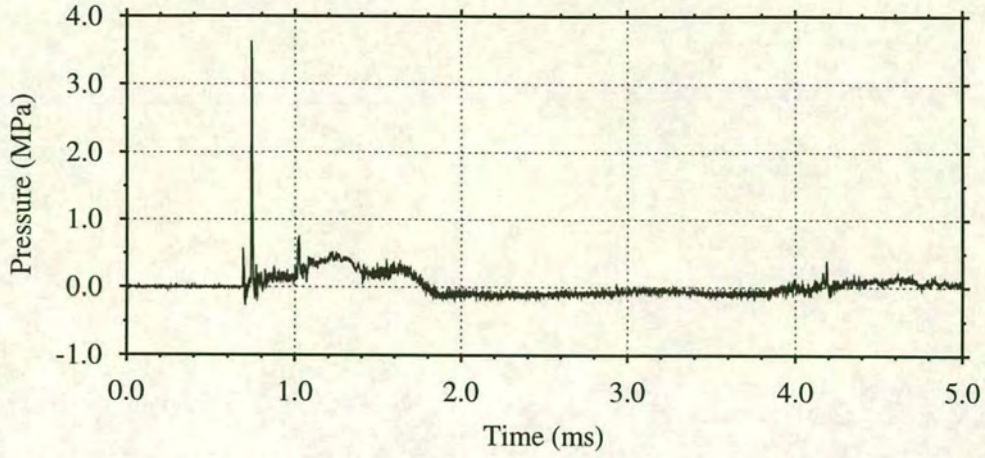

(a) $\phi = 0°, \theta = 0°$ (PG 2)

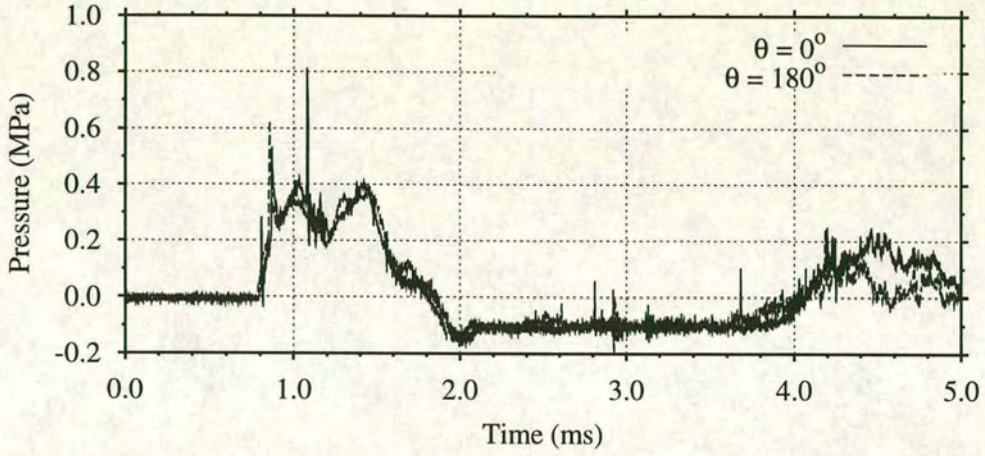

(b) Axisymmetry of loading at $\phi = 90°$ (PGs 3 and 6)

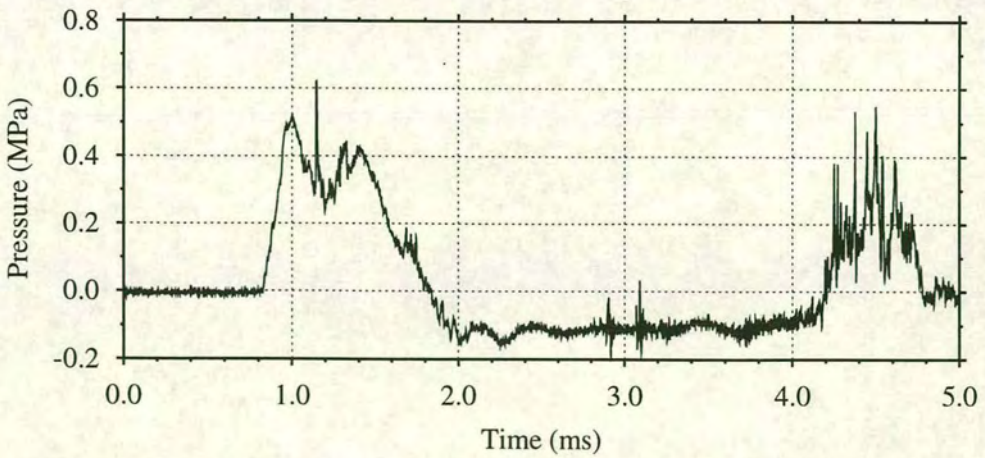

(c) $\phi = 135°, \theta = 0°$ (PG 4)

Figure 5.12: Fluid response at various positions on shell to 5g EDC-1 at 1.0m stand off (axisymmetric)

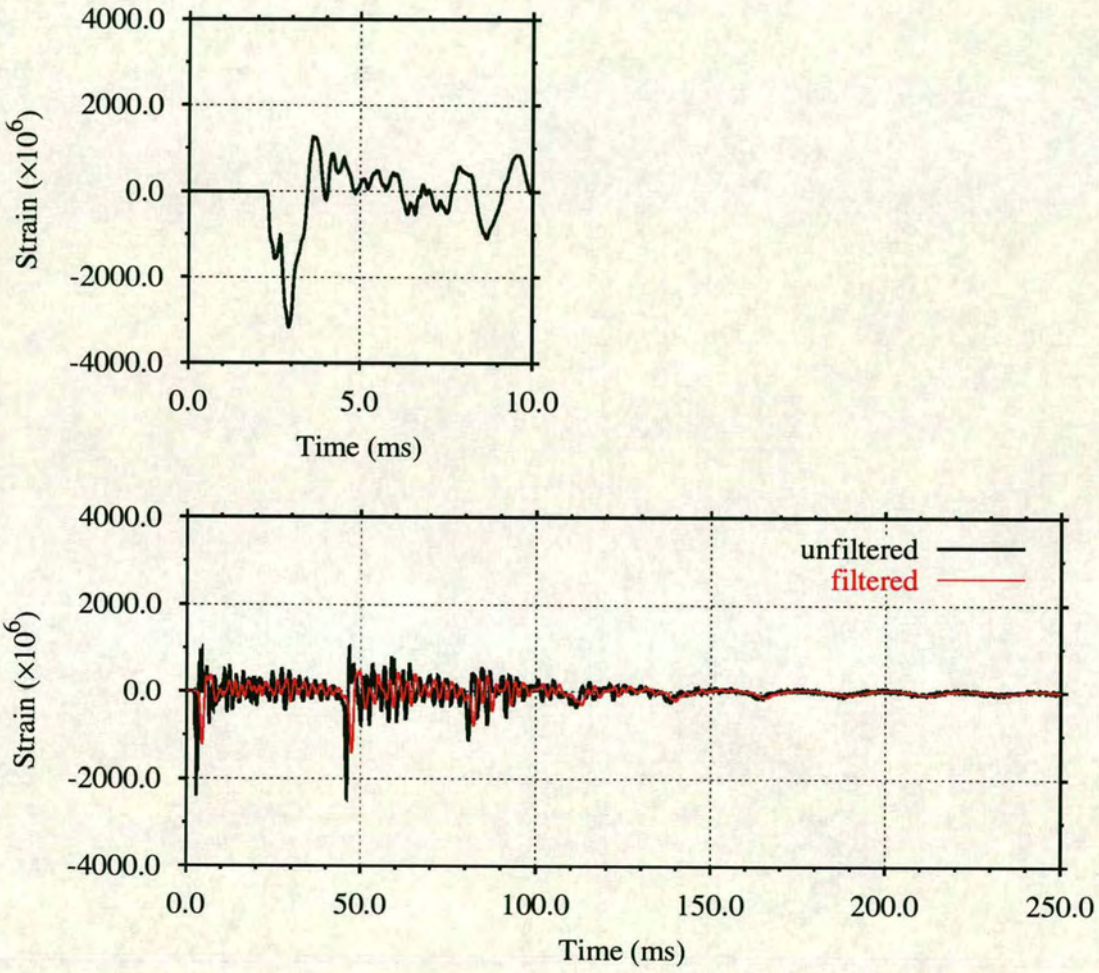

Figure 5.13: Circumferential strain response at $\phi = 0^o, \theta = 0^o$ to 5g EDC-1 at 1.0m stand off (axisymmetric)

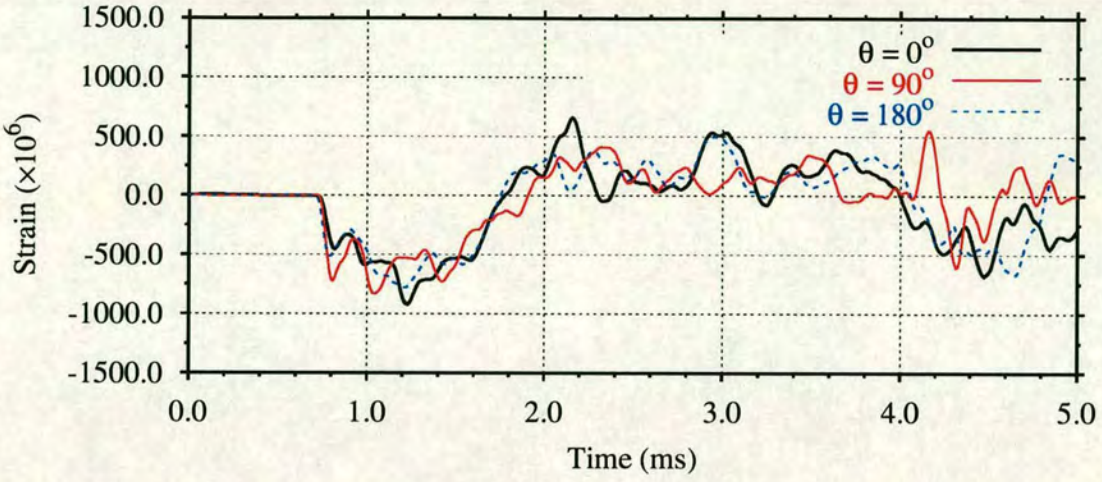

Figure 5.14: Axisymmetry of shell response at $\phi = 90^o$ to 5g EDC-1 at 1.0m stand off (axisymmetric)

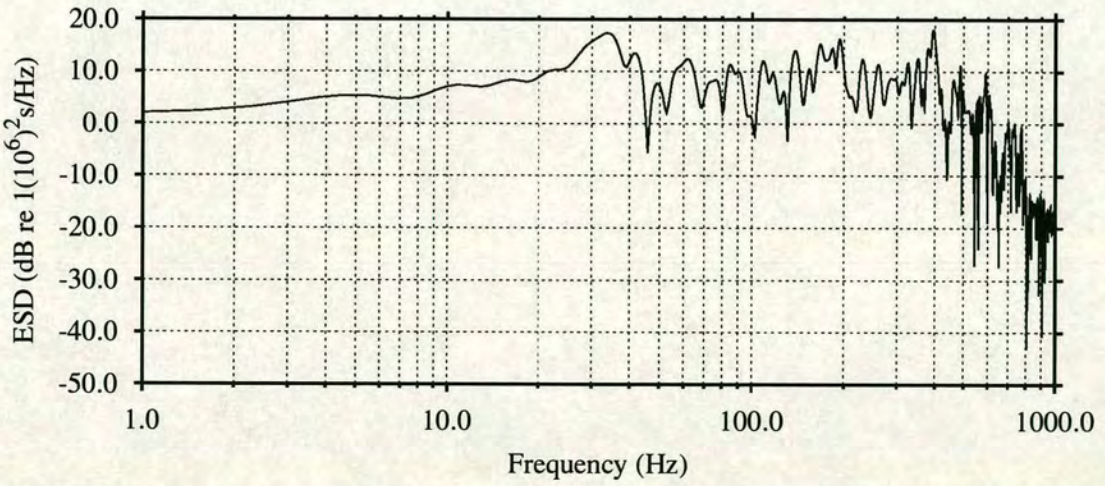

Figure 5.15: Energy spectral density of circumferential strain response at $\phi = 0^o, \theta = 0^o$ to 5g EDC-1 at 1.0m stand off (axisymmetric)

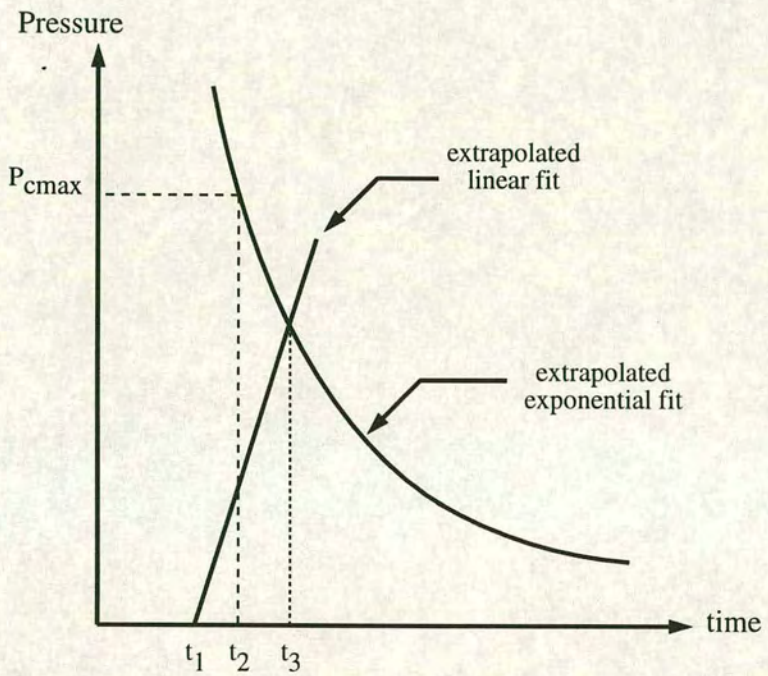

Figure 5.16: Determination of corrected experimental peak pressure decay values

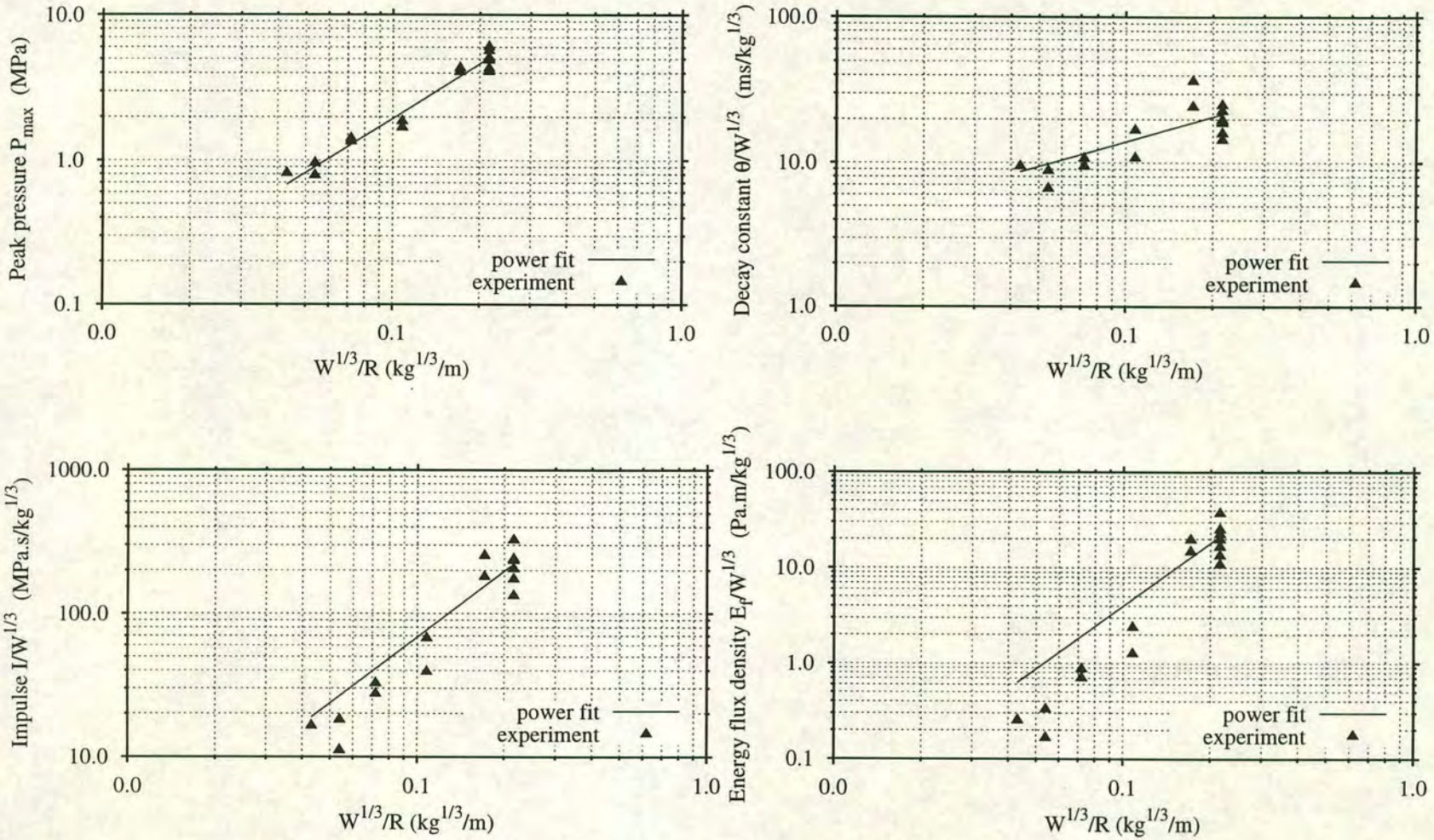

Figure 5.17: Power fits to determine empirical constants for EDC-1 explosive

Chapter 6

Validation of numerical simulation of UNDEX loading

6.1 Introduction

Experimental tests described in chapter 5 have provided fluid and shell response data for the validation of LS-DYNA and USA-DYNA3D for modelling UNDEX-FSI. The prototype echinodome was subject to symmetric and axisymmetric forms of UNDEX loading at various stand off distances. For the symmetric loading, four load cases, each using 10g EDC-1, were examined. For the axisymmetric loading, one load case, using 5g EDC-1, was examined. Reliable free field fluid response data has been acquired. The total pressure was noticed to be less than the incident pressure for most cases. Analysis of the shell response revealed that the axisymmetric load case generated the most severe strain levels on the shell, and that the most critical regions accentuated under both axisymmetric and symmetric loading were the apex and the base.

Sufficient data is now available to quantitatively and qualitatively evaluate the ability of the MMALE and DAA approaches to simulate the response of the free field fluid and the fluid at the shell to 5g and 10g charges. Validation of LS-DYNA and USA-DYNA3D for predicting the shell response could provide confidence in the use of these techniques to predict dynamic buckling loads.

The development of numerical models to simulate the axisymmetric and symmetric load cases, based on modifications of the models constructed in chapter 4, is presented in the current chapter. A detailed comparison of the numerical and experimental results for the symmetric and axisymmetric load cases is then discussed and the predictive capabilities of the finite element models assessed.

6.2 Validation limitations

A comparison of numerical predictions with all experimental results is not possible due to the symmetry conditions used on the numerical models. Such a detailed comparison is also considered unnecessarily exhaustive and time consuming with limited benefit. To satisfactorily validate LS-DYNA and USA-DYNA3D the main issues for comparison are the free field response at the various stand off points, the fluid pressure at the surface of the shell and the strain responses. The most critical positions on the prototype shell are the points at which the shell is most likely to undergo material failure first. From the analysis of the experimental results pertaining to the meridians $\theta = 0^o$ and 180^o, it was clear that $\phi = 0^o$ and 150^o were experiencing the highest strain levels under axisymmetric loading conditions, and $\phi = 0^o$, 90^o and 150^o under symmetric loading conditions. Although accurate prediction of the strain levels at the other positions would strengthen the validation of the numerical techniques, the positions chosen should provide a sufficient level of confidence in using the numerical techniques for dynamic buckling predictions.

As was observed in chapter 5, the initial peak response to shock loading occurred within the first 5.0ms, and bubble pulse loading at 45.0ms. The poor results from the bubble simulations performed in chapter 3 reduced confidence in using the MMALE technique for predicting bubble loading on the prototype, and consequently it was decided not to run a simulation to bubble time with this technique. Bubble pulse loading is possible with the DAA technique (DAA_2), however, previous application of the DAA_2 approach to a problem involving bubble loading found the transition between shock and bubble loading on a structure difficult to model due to the different frequencies involved[85]. Bubble pulse simulations are not possible with the DAA-MAT90 technique at the time of writing. In view of these limitations the 5.0ms analysis time adopted in chapter 4 will be sufficient for all the numerical simulations performed here.

6.3 Numerical models of experiments

In chapter 4 three numerical approaches and their suitability for modelling axisymmetric UNDEX loading against the prototype echinodome were presented. Models utilising each approach were modified to simulate the experiments performed in chapter 5.

Using TrueGrid several geometrical adjustments and mesh refinements were made to the pseudo-wedge MMALE mesh of chapter 4. This led to the generation of a model for the axisymmetric load case comprising 76422 brick elements to represent the fluid, 8

elements discretising the 5g charge and, initially, 93 Belytschko-Lin-Tsay shell elements for the prototype shell. The angle of the pseudo-wedge was 22.5^o, as in the 10g model. The model was initialised to detonate the charge at time $t = 0$ and all advection schemes were tested for accuracy and efficiency. The pressure cut off was set to zero. The boundary conditions for the tank floor and walls, and the free surface remained unchanged,

The infinite and semi-infinite fluid domain models constructed for the DAA approaches in chapter 4 were also adapted to simulate the axisymmetric experiment. No physical alterations to the meshes were required, only changes to the input of the pressure decay values and the charge location. The experimentally corrected values of chapter 5 were utilised, representing the UNDEX loading perceived by the shell. The 15mm offset down the $\theta = 0^o$ meridian, imposed on the strain gauge at the apex of the shell during the experiment, was accounted for by requesting output from a shell element at the same distance from the apex. The difference in strain response between this shell and the one at the apex was found to be negligible.

For the symmetric load case the nature of the loading and subsequent shell response meant that it was necessary to model half the shell. In view of the complications encountered in constructing the MMALE model for the axisymmetric load case it was decided not to use this technique for the symmetric load case for the following reasons.

1. The restriction of using the ALE coupling method to couple the shell to the surrounding fluid would make this a complex model to construct.

2. The size of the fluid elements would be dictated by the charge, and the distances involved (2.0 – 5.0m) would necessitate a large number of fluid elements to track the shock wave accurately. The number of fluid elements would be further increased by the need to incorporate the free surface, tank walls and floor, as non-reflecting boundary elements would lead to fluid mass flow out of the mesh which is undesirable because of the presence of inertia effects of the surrounding fluid.

3. The large number of elements would result in a computationally expensive analysis using the current computing resources. Parallelisation of the MMALE technique within LS-DYNA would greatly assist in reducing execution times but, at the time of writing, a parallel version of the Eulerian formulation was not available.

4. Use of any pre-processing techniques to reduce the number of elements, e.g., transitioning, biasing or large element sizes, introduces the risk of inaccurate

loading being applied to the shell due to smearing of shock wave, or reflections from numerical boundaries.

Suitable adaptations to the DAA models developed for the axisymmetric load case provides a much simpler and cost effective approach to the symmetric load case. The fluid mesh was shown to be of adequate discretisation to track a shock wave, and extend sufficiently far away from the shell to have allowed the shock wave to propagate around it. Consequently, the existing DAA-MAT90 and DAA meshes were adopted for the symmetric load cases, the only changes required being the location of the charge, with respect to the shell and the free surface, and the pressure decay input values. For each DAA approach the corrected experimental load obtained from the symmetric load cases was applied to the models.

The default Belytschko-Lin-Tsay shell formulation was initially used for the shell model based on the findings from chapter 3. The shock wave was initialised a distance equivalent to one element away from the shell boundary in all DAA models at time $t = 0$. The damping factor for the acoustic elements, β, was set to 0.1, as in chapter 4, and the cavitation option activated. Reflections from the floor and walls of the tank were not taken into account.

For all simulations comparisons were made using circumferential and meridional strains only as oblique strains could not be obtained directly from the shell elements available in the numerical simulations. A comparison of direct strains is considered adequate for the validation of LS-DYNA and USA-DYNA3D.

6.4 Comparison of results for symmetric loading

To analyse all symmetric load cases is considered too time consuming and repetitive to discuss. Therefore only the most severe load case (2.0m stand off) is chosen for comparison of numerical and experimental results, and is sufficient to determine the predictive capabilities of USA-DYNA3D. The predicted fluid and shell responses from both techniques are discussed below.

The computing resources utilised to solve the DAA models required approximately 120Mb of memory, and 30000 – 40000s of CPU time*, the DAA technique requiring less memory but more solution time.

*executed on SGI ORIGIN 200, R10000 processor; minimum output requested

6.4.1 Experiment – DAA

The response times predicted by the DAA approach provided a suitable time datum for the fluid and shell results. The 3.0ms pre-trigger of experimental response times was reduced further to ensure the times coincided with those predicted by the DAA approaches.

Fluid response at shell

A satisfactory representation of the physical propagation of the shock wave around the shell, predicted by the DAA-MAT90 technique, is illustrated in Figs 6.1(a) – (d). The shock wave maintains its sphericity as it engulfs the shell, and the shock front is well defined whilst in the vicinity of the shell. Diffraction of the shock front is observed close to the surface of the shell. Beyond the shell, the shock front becomes smeared due to the discretisation. Predicted pressures observed in the fluid at 0.9ms may be attributed to scattered pressures as the shell oscillates after the impingement of the shock wave.

An attempt to extract the fluid pressures at the shell from the USA package was not possible due to the unavailability of the appropriate software. However, the acoustic elements available in LS-DYNA permitted predicted pressure records to be obtained. Figs 6.2 – 6.6 depict the total pressures predicted initially using $\beta = 0.1$ at $\phi = 0^o$, 45^o, 90^o and 135^o, compared with the measured results. The time domain of 3.0ms was chosen to enhance the clarity of the comparison. The atmospheric and hydrostatic pressures were deleted from these records when it was discovered that the strain levels were zero initially indicating that it was not being applied to the shell model, only to the acoustic elements. This, combined with the fact that the pressure gauges in the experiment did not account for atmospheric and hydrostatic pressures, meant it could be removed from the numerical results without affecting the comparison. Doing so results in negative pressures in the pressure records which may or may not be due to cavitation.

Each pressure-time history exhibits an initial peak response followed by a rapid decay to zero. The predicted pressure peaks are listed against experimental values in table 6.1. At the stand off point the predicted peak pressure is within 10% of that measured. The peak pressure near the base is overpredicted, and at all other positions are considerably underpredicted. The maximum total pressure measured experimentally occurred at $\phi = 45^o$. Numerically it is predicted to occur at the stand off point, as was expected experimentally. A prevailing rise in pressure, although obscured by numerical

Position θ, ϕ	Exptl total pressure (MPa)	Peak total pressure (MPa)		
		$\beta = 0.1$	$\beta = 0.5$	$\beta = 0.9$
$0^o, 0^o$	0.600	0.48	0.49	0.43
$45^o, 0^o$	2.340	1.16	1.23	1.08
$90^o, 0^o$	1.693	1.84	1.81	1.79
$135^o, 0^o$	1.719	0.93	1.07	1.00
$90^o, 180^o$	0.292	0.57	0.67	0.53

Table 6.1: Comparison of experimental and DAA-MAT90 predicted peak total pressures under 10g EDC-1 at 2.0m stand off (symmetric)

oscillations, is noticeable after the initial peak at all locations, particularly at the apex and maximum diameter on the shadow side. The rise time of the pressure at the maximum diameter on the shadow side is seen from Fig. 6.6 to exhibit a slower rate, as observed experimentally, showing that the simulated shock front has thickened as a result of diffracting around the shell. It is also encouraging to observe that the pressure is sustained for a period of time, albeit less than in the experiment. The peak pressure magnitudes are overpredicted by approximately 50% suggesting that the diffraction of the shock wave has not reduced the peak pressures by as much as in the experiment. The arrival of the shock wave is almost $50.0\mu s$ behind that measured on the shadow side, indicating the shock wave is propagating at a slower rate than observed in the experiment.

Where cavitation was recorded experimentally the pressure was found to be negative, however, the correction made for the atmospheric and hydrostatic pressures makes it difficult to determine if cavitation is predicted to occur at the points where predictions were made. There are short periods of time after the initial peak pressure at the stand off point, when the predicted pressure is zero. This may be an indication the fluid was cavitating in this region, however, no cavitation was visible from the pressure contour plots.

All pressure-time histories predicted for $\beta = 0.1$ are observed to oscillate excessively pertaining to numerical fluctuations. The frequency and amplitude of oscillations are observed to be high compared to those of the experimental results. This was thought to be a feature of the first order acoustic elements being used, however, altering the damping factor was found to improve the results. The damping factor was increased from 0.1 to values of 0.5 and 0.9 in the DAA-MAT90 model and the results are plotted

on the same figures for comparison. The values of the total peak pressures are listed in table 6.1. The amplitudes of the oscillations are observed to diminish with increasing values of β. The peak pressure values are observed to increase for $\beta = 0.5$ and reduce for $\beta = 0.9$, except at the stand off point, where the pressure appears to converge towards the measured value. Pressures are now observed to exist in the short periods where zero pressures were observed previously as a result of increasing β suggesting that these were not evidence of cavitation.

Since reflections from the walls and tank floor were not accounted for in the DAA models the second experimental peak, occurring at 1.35ms at $\phi = 135^o$, $\theta = 0^o$ (see Fig. 6.5, is not predicted. The peaks appearing around this time in the predicted record are most likely delayed radiated pressures from the behaviour of the shell.

Only at the maximum diameter is the peak pressure predicted with sufficient accuracy by the DAA-MAT90 technique. The propagation rate of the shock wave and the peak pressures predicted elsewhere are in question. It is possible that the shell element positions did not correspond exactly with the positions in the experiment due to the approximate discretisation used for the FE model. However, the prediction of the longer duration pulses at the apex and shadow sides are particularly noteworthy, as they indicate some agreement in physical propagation of the shock wave around the shell. The effect of the damping factor in reducing the amplitude of the numerical oscillations on the pressure records is clear, however, its influence on the strain records must also be examined before a suitable value can be concluded for use in future models.

Shell response

A comparison of selected predicted shell responses to symmetric loading using both DAA approaches, for positions $\phi = 0^o$, 90^o, near side, and 150^o, near and shadow sides, are shown in Figs 6.7 – 6.12. The DAA approaches show poor quality predictions for strain results compared to the pressure results. The DAA technique grossly underpredicts the strain levels at all positions. For example, at the stand off point the predicted circumferential strain is 60% lower than that measured (see Fig. 6.7). A possible source of numerical error is the direct line of sight approach, used by the DAA technique to calculate pressure, which will produce an inaccurate fluid response for a structure such as the prototype echinodome which exhibits a shadow zone due to the convex curvature of the shell. Accounting for diffraction using the DAA-MAT90 technique around the shell is physically a more accurate method of tracking the pressure at the shock wave front as has been observed.

The DAA-MAT90 technique follows the trend of the measured response at the stand off point for the first 0.5ms suggesting that the predicted geometrical influence on the strain response is in good agreement with that observed experimentally. The initial rise in compressive strain, followed by a decrease, then a second rise, is evident from Fig. 6.7. The initial peak strain levels were predicted well meridionally, as shown in Fig. 6.8, however, circumferentially they are 30% lower than those measured. Similarly, at the other positions shown, the DAA-MAT90 model underpredicts the peak strains and the quality of the records is generally poor. Encouragingly though, in the regions where high strain levels were recorded, i.e., at $\phi = 0^o$ and 150^o near and shadow sides, the numerical model is predicting the highest strain response. The reader is reminded that the measured peak response at $\phi = 0^o$ is believed to be abnormally high due to the mismatch of the seam. To assess the quality of strain results for a different position a DAA-MAT90 simulation was performed at a stand off distance of 5.0m using the same charge size. The circumferential and meridional strain results are compared to experimental results in Fig. 6.12. The underprediction of the DAA-MAT90 technique is clearly evident.

Any contributions to the strain response that the circumferential imperfections may have added were not simulated. Had the thickness variation in the circumferential direction been included, the strain response under symmetric loading may have been even lower. However, inclusion of geometric imperfections in the circumferential direction would make a finite element model complicated to construct.

The elastic material model used for the echinodome shell could also be too simplified for the GRP material. The shear modulus is assumed to follow the elasticity theory with this material model which may not necessarily be the case. LS-DYNA contains more complex material models which could be taken advantage of if more details relating to the material characteristics were known. For example, to examine the influence the shear modulus the 10ms 300N ramped loading problem was executed using the *MAT_ORTHOTROPIC_ELASTIC material from chapter 3. A factor of five increase in displacement was observed when the shear modulus was reduced by a factor of ten.

The strain records were not contaminated with numerical oscillations to the same extent as the pressure records. A smoother response was observed by increasing the damping factor to improve the predicted pressures. However, as is evident from table 6.2, the predicted peak strain levels are reduced in most cases, particularly in the critical regions, by increasing the damping factor. Figs 6.13 – 6.14 show that the effect of increasing the damping factor on the trend in strain response at the stand off point is negligible.

In chapter 3 the various shell element formulations were tested under quasi-static

Position ϕ, θ	Exptl peak strain ($\times 10^6$)	DAA-MAT90 peak strain ($\times 10^6$)			DAA peak strain ($\times 10^6$)
		$\beta = 0.1$	$\beta = 0.5$	$\beta = 0.9$	
$0^o, 0^o$	-1921	-657	-608	-595	-385
$30^o, 0^o$	-1405	-497	-478	-463	-341
$60^o, 0^o$	-784	-588	-538	-542	-324
$90^o, 0^o$	-905	-559	-605	-599	-414
$90^o, 180^o$	-924	-955	-930	-907	-421
$120^o, 0^o$	-921	-639	-1294	-609	-333
$150^o, 0^o$	-1433	-892	-861	-834	-435
$150^o, 180^o$	-1621	-919	-900	-875	-448

Table 6.2: Comparison of experimental and DAA predicted initial peak strains under 10g EDC-1 at 2.0m stand off (symmetric)

loading. The default shell, Belytschko-Lin-Tsay, was considered to be computationally the most efficient and accurate for this form of loading. However, it must not be assumed that the same shell efficiency and accuracy is valid under UNDEX loading. The default shell has been utilised in the simulations performed so far. Other suitable shell formulations are listed in table 6.3 along with solution times for a 2.0ms analysis and the percentage difference in predicted peak circumferential strain from experiment for the stand off point.

The solution times are surprising, based on the observations made in chapter 3. Under quasi-static loading the S/R co-rotational Hughes-Liu shell required almost 1200% more solution time than the default shell, while the S/R Hughes-Liu shell required almost 2400%. Under UNDEX loading there is only a nominal difference in solution times between these two particular shell formulations and the default (6% and 20% respectively). The most efficient shell formulation is the Belytschko-Leviathan shell requiring 13470s to solution, compared closely with the solution time for the default shell. The model using the Fast (co-rotational) Hughes-Liu element would not execute. The variations in predicted peak strain response from the Belytschko-Leviathan shell are nominal, ranging from 0.5 – 3%, and, as Fig. 6.15 shows for the default and Belytschko-Leviathan shells, the deviation in strain history is negligible over 2.0ms.

The deformed shape of the prototype shell predicted by the DAA-MAT90 technique is depicted in Fig. 6.16. Inward deformation is observed at the maximum diameter (near side), apex and base regions as the shock wave diffracts around the shell. Once

Shell formulation	Solution time (s)	% difference
Hughes-Liu	14281	-32
Belytschko-Lin-Tsay (default)	13995	-31
S/R Hughes-Liu	16711	-32
S/R co-rotational Hughes-Liu	14875	-31
Belytschko-Leviathan	13470	-30
Belytschko-Wong-Chiang	14087	-30
Fast (co-rotational) Hughes-Liu	—	—
Fully integrated shell	13832	-32

Table 6.3: Comparison of computational cost and accuracy (relative to experiment) of various shell formulations for DAA-MAT90 ($\beta = 0.5$) predicted peak circumferential strain response at $\phi = 90^o, \theta = 0^o$ to 10g EDC-1 at 2.0m stand off (symmetric)

the shock wave has passed the shell the laminate is observed to oscillate particularly in the base region. The stiffer base appears to contribute significantly to the oscillations. There is insufficient data to ascertain from the analysis time of the numerical results for $\phi = 150^o$, near and shadow side, if the strain response exhibits a higher frequency than at $\phi = 0^o$, as was observed experimentally.

The nature of the interface between the shell elements and the acoustic elements is such that deformation of the shell boundary causes a deformation of the layer of acoustic elements next to the boundary. Unlike ALE technology, this mesh deformation is not diffused throughout the acoustic elements. Consequently the layer of acoustic elements next to the shell boundary becomes distorted over the duration of an analysis which can lead to a reduction in the timestep. Fortunately, the displacements in this analysis are sufficiently small to not cause this problem. The deformation is depicted in Fig. 6.17. For large deformation problems this would cause a breakdown of the analysis.

In attempting to improve the results of the DAA-MAT90 model by changing the damping factor and shell formulations only minor improvements in strain response were observed. Since the quality of results for the DAA technique were considered to be less accurate no attempt was made to improve this model.

From the results of the symmetric load case analyses, several parameters could be taken and used in the simulation of the axisymmetric load case. The most suitable shell formulation for this approach was found to be the Belytschko-Leviathan shell and

a damping factor of $\beta = 0.1$ should be used to generate the most accurate peak strain response in the critical regions.

6.5 Comparison of results for axisymmetric loading

Fluid and shell response predictions from the DAA approach and the MMALE technique were obtained for the 5g EDC-1 axisymmetric load case and are presented below. As in the symmetric load case the results from the two DAA approaches are examined to highlight the differences between the DAA-MAT90 and DAA implementations.

The time domain of the MMALE technique, from detonation time to 5.0ms, provides a suitable time datum over which the measured and DAA results could be plotted to trace the time responses of all results. The measured response times are corrupted by pre-trigger such that the detonation time is unknown. The DAA response times correspond to the shock wave initialised at a closer position to the stand off point than in the MMALE analysis which, although also providing a suitable datum, would leave the MMALE predicted signals short of 5.0ms should they be adjusted to the DAA time domain. Consequently, time in the measured and DAA results presented here has been altered to fit with that of the MMALE analysis.

The computing resources used by the axisymmetric DAA simulations were similar to those of the symmetric models. The MMALE analysis was computationally the most expensive of the three techniques, requiring of the order of 90000s CPU time[†] and approximately 140Mb of memory. A more detailed discussion regarding computational cost is given in section 6.6.

6.5.1 Experiment – MMALE

Free field response

All four advection schemes were tested for accurate prediction of the free field peak pressure, 1.0m off to the side of the charge, and the results are listed in table 6.4. All schemes are observed to underpredict the peak pressure by approximately 20% on average. The second order van Leer advection scheme is closest to the experimental value of 4.20MPa. The pressure-time history predicted by the van Leer scheme is compared with the experimentally measured pressure record in Fig. 6.18. On the

[†]executed on SGI ORIGIN 200 R10000; minimum output requested

Advection scheme	Free field pressure (MPa)	Total pressure at $\phi = 0^o$ (MPa)	Solution time (s)
Donor cell	3.28	2.92	68979
van Leer & HIS	3.16	2.54	125225
van Leer	3.38	3.09	94375
Donor cell & HIS	3.08	2.78	70677

Table 6.4: Comparison of MMALE predicted peak pressures for various advection schemes under 5g EDC-1 at 1.0m stand off (axisymmetric)

same plot the experimentally corrected pressure record, used in the DAA analyses, and a pressure-time history predicted by a one eighth sphere model, similar to that developed in chapter 3, are also shown.

The pressure-time curve predicted by the MMALE axisymmetric pseudo-wedge model was simulated poorly compared to the other pressure-time histories. The slow rise time suggests the discontinuity at the shock front is smeared over a number of elements, the aspect ratio of which is poor (≈ 1.5) in the direction of propagation (1.0m to the side of the charge). The peak pressure is consequently reduced by the smearing of the shock front. Also, the small number of elements in the charge may not have permitted the full build-up to detonation pressure, as was concluded necessary from the detonation example in chapter 3. Due to the small element sizes involved, to use a sufficient numbers of elements would have been impractical.

The predicted pressure decay behind the shock front consists of several oscillations of decreasing amplitude, as were observed with 10g EDC-1 in chapter 4. It is noteworthy however, that the measured decay appears to correspond with the mean values of oscillations. If a finer mesh were used the correlation of the predicted and measured decays might improve.

The pressure record from the one eighth sphere model, although an improvement over the pseudo-wedge model, is observed to overpredict the measured peak pressure by approximately 20%, but is closer to the corrected experimental value. That this result is higher than the pseudo-wedge model is expected as the discretisation in the direction of propagation is significantly finer.

Experimentally, the free field pressure-time history is representative of the incident pressure at the apex of the shell. Numerically however, the predicted free field

pressure-time history discussed above is not representative of the incident pressure at the apex as the mesh quality was much superior in the vertical direction of propagation (see Figs 4.6(a) and (b)). Hence it is likely that the incident pressure at the apex is greater, and the pressure record of better quality, than the predicted free field pressure shown.

The MMALE predicted physical propagation of the shock wave around the shell is illustrated in Figs 6.19(a) – (d). The shock wave maintains its sphericity as it engulfs the shell, and the shock front is well defined whilst in the vicinity of the shell. Diffraction of the shock front is observed, manifested by reduced pressure, close to the surface of the shell. Later in time scattered pressures from the apex and base of the shell are seen after the shock wave has passed. Elsewhere the shock front is noticeably smeared, particularly in the region of the mesh off to the side of the charge.

It is concluded from table 6.4 that the van Leer advection scheme is the most accurate scheme to use with this MMALE pseudo-wedge model for applying the shock loading to the shell. Moreover, computationally, the van Leer scheme is noticeably cheaper than the recommended default scheme (van Leer & HIS). Consequently, all further results presented are extracted from the MMALE pseudo-wedge model using the van Leer scheme.

Fluid response at shell

Figs 6.20 – 6.21 depict the total pressures for positions $\phi = 0^o$, 45^o, 90^o and 135^o, predicted using the van Leer advection scheme, compared with the measured results. As in the symmetric load case, the atmospheric and hydrostatic pressures were removed from the pressure records predicted at the shell as they were not being applied to the structural mesh. A simulation was run with $P_c = -0.1$MPa (absolute zero) in an attempt to predict quantitatively negative pressures indicating cavitation. As illustrated in Fig. 6.20(a) the regions where cavitation is occurring is indicated by periods when $P_T = 0$ for $P_c = 0$. When $P_c = -0.1$MPa the total pressure in these periods is observed to shift down to P_T=-0.1MPa with little variation in the predicted results. This suggests that cavitation can be qualified with either $P_c = 0$ or $P_c = -0.1$MPa. The remainder of the total pressure-time histories are predicted for $P_c = 0$. The pressure peaks at each position are listed in table 6.5 for $P_c = 0$. Despite the predicted records exhibiting similar trends to the measured fluid responses, all predicted pressure-time histories are observed to suffer excessively from noise, similar to that observed in the DAA-MAT90 technique for the symmetric loading.

Position ϕ, θ	Experimental pressure (MPa)	Predicted pressure (MPa)	% difference
$0^o, 0^o$	5.320	3.09	-42%
$45^o, 0^o$	3.630	1.62	-55%
$90^o, 0^o$	0.813	0.67	-18%
$135^o, 0^o$	1.678	1.05	-37%

Table 6.5: Comparison of experimental and MMALE predicted peak total pressures under 5g EDC-1 at 1.0m stand off (axisymmetric)

At all positions the peak pressure is underpredicted. For the position $\phi = 0^o$ table 6.4 shows that all advection schemes predicted approximately 10% lower total resultant pressure, on average, compared to the predicted free field pressure, and 30-60% lower than the total pressure measured. The same phenomena was observed experimentally in the symmetric load cases. From table 6.5 and Fig. 6.21(a) the predicted peak pressure at $\phi = 90^o$, although appearing premature by $\approx 200\mu$s, is 80% of the experimental value. The pressure spike representing the experimental peak response is difficult to account for, as mentioned in chapter 5. The earlier response time in the numerical model could indicate that its shock wave was propagating with a faster velocity in the numerical model. These results suggest the MMALE pseudo-wedge model is not accurately simulating the scattered pressure.

It is possible that the pseudo-wedge model of the shell could be resulting in significantly greater initial radiated pressures, which are tensile, thus reducing the level of the scattered pressures to below those of the incident. The same aberration was encountered in the 10g model in chapter 4. Analysis of the DAA results in the same chapter strengthened this postulation when higher total pressures were predicted at the apex for a more accurate model which included circumferential response as well as meridional. A comparison of the DAA results for this load case is required (see section 6.5.2) to determine if the problem lies with the MMALE model.

It is concluded that the MMALE pseudo-wedge model was unsuccessful in predicting the peak pressure responses for the axisymmetric load case. Nevertheless, it is encouraging to observe that the general trends over the first millisecond were modelled well. Peaks superseded by a rapid decay and subsequent oscillations were evident at $\phi = 0^o$ and 45^o. The longer duration pulses at $\phi = 90^o$ and 135^o were also clearly simulated.

Position ϕ, θ	Initial peak strain ($\times 10^6$)			
	Circum.		Merid.	
	Expt	MMALE	Expt	MMALE
$0^o, 0^o$	-3164	-1955	-2368	-3696
$30^o, 0^o$	-1766	-1871	-2123	-1731
$60^o, 0^o$	-997	-1349	-754	-1337
$90^o, 0^o$	-1224	-741	-1003	-1451
$120^o, 0^o$	-1034	-1080	-926	-1877
$150^o, 0^o$	-1439	-1250	-1833	-2347

Table 6.6: Comparison of experimental and MMALE predicted initial peak strains under 5g EDC-1 at 1.0m stand off (axisymmetric)

Shell response

A comparison of measured and predicted shell response at $\phi = 0^o$ and 150^o, for the meridional and circumferential directions, is presented in Figs 6.22 – 6.25 for three advection schemes, to observe the effect of the advection scheme on the predicted strain response.

Qualitatively, the general trend at $\phi = 0^o$ over the first millisecond is well reproduced suggesting the simulated shell behaviour associated with the UNDEX loading is in good agreement with the experimentally observed behaviour. Over 5.0ms the predicted signal is observed to exhibit the initial peak and decaying response that the measured signals possess. This is an indication of the damping effect of the inertia of the surrounding fluid. Also, as observed experimentally, the rise to the initial peak at the apex features a small reduction in strain prior to peak response.

The sequence in peak strain levels down the $\theta = 0^o$ meridian recorded experimentally is predicted well by the van Leer advection scheme and is listed in table 6.6[‡]. The highest peak strain is observed at the apex, although an identical level of strain was expected in both directions under axisymmetric UNDEX loading. Towards the maximum diameter the peak strain level reduces before increasing again in the base region. Compared with experimental values however, the initial peak strains for the circumferential direction are underpredicted by 38% at $\phi = 0^o$ and overpredicted in the meridional direction by 56%. Experimentally the greater peak strains were observed to occur meridionally at $\phi = 30^o$ and 150^o, and from $\phi = 60^o - 120^o$ circumferentially. However, the predicted

[‡]executed on SGI ORIGIN 200 R10000

Shell formulation	Solution time (s)	% difference
Hughes-Liu	25938	-40
Belytschko-Lin-Tsay (default)	24541	-41
S/R Hughes-Liu	25177	-38
S/R co-rotational Hughes-Liu	24987	-43
Belytschko-Leviathan	25566	-43
Belytschko-Wong-Chiang	25748	-50
Fast (co-rotational) Hughes-Liu	25436	-53
Fully integrated shell	25621	-47

Table 6.7: Comparison of computational cost and accuracy (relative to experiment) of various shell formulations for MMALE predicted peak meridional strain response at $\phi = 0^o, \theta = 0^o$ to 5g EDC-1 at 1.0m stand off (axisymmetric)

results show poor agreement with this trend, particularly at $\phi = 150^o$, where the higher strain was predicted to occur in the circumferential direction, although it is significantly overpredicted. Interestingly, the predicted results do agree with the earlier observations made under symmetric loading, i.e., that the shell is stiffer in the meridional direction.

Although the various shell element formulations were tested for the DAA-MAT90 technique, the conclusions drawn can not be assumed to apply to the MMALE approach. All MMALE simulations have been performed up to this point using the default shell. The same shell formulations tested by the DAA-MAT90 technique were also tested on the MMALE technique. However, as table 6.7[§] shows, there are only minor differences observed between the various shell formulations, in both cost and accuracy. On this basis, the default shell formulation was considered suitable for dynamic buckling predictions with this technique.

The deformed shape of the prototype shell predicted by the MMALE analysis is depicted in Fig. 6.26. It is clear why the base is predicted as a critical regions of the shell given the degree of bending it undergoes. The sudden large increase in thickness may have resulted in high localised bending at the interface between the GRP membrane (3.44mm) and the base (19.0mm, see section 3.8.1). No experimental measurements were made near to this interface to experimentally determine the effect of the stiffer base on the shell in this region, however such a response could be expected in reality.

[§]executed on DEC ALPHA 8400 625MHz (RAL)

The rigid body motion after 5.0ms is clearly evident.

6.5.2 Experiment – DAA

Fluid response at shell

Figs 6.27 and 6.28 compare the pressure response predictions with experimental measurements for the axisymmetric load case. The total pressure response at the stand off point, Fig. 6.27(a), corresponds well with that recorded experimentally. A sharp rise to the peak total pressure is followed by a rapid decay to zero. The predicted peak total pressure is in good agreement with the measured value and is greater than the input free field peak pressure, illustrated in Fig. 6.18, as expected. This suggests the scattered pressure is simulated correctly with this technique, which was not the case in the MMALE technique. This is most likely due to the fact that the incident pressure at the apex is more representative of the experimental value in the DAA-MAT90 analysis since it is initialised one element away from the stand off position.

This confirms the findings in chapter 4, that the lower resultant pressure predicted by the MMALE model is unlikely to be a consequence of the material definition, since the same definition was used by both techniques. A more probable cause of the discrepancy between the resultant pressures for each technique is the accuracy of the incident pressure at the stand off position. The diffusion of the shock front will be greater for the MMALE technique since the shock wave has travelled further. A second source of inaccuracy could be attributed to the equation of state used for the fluid in the MMALE technique. The acoustic formulations assumed by the DAA approach and the acoustic element could generate higher values of pressure around the shell than the MMALE model. A more accurate equation of state and finer fluid mesh would most likely improve the MMALE predicted peak pressures in this region.

Multiple peaks caused by numerical fluctuations are observed after the total pressure has decayed to zero. Their presence suggests prevailing pressures in this region, as observed experimentally.

At $\phi = 45^o$, 90^o and 135^o the DAA-MAT90 analysis was unsuccessful in capturing the total peak pressure value, predicting just over 50% of that measured at $\phi = 45^o$, and overpredicting by 80% at $\phi = 135^o$. Despite this, it is encouraging to observe the general trend of the predicted records imitating what happened in reality. A slow rise in pressure, perceived 0.5ms after the arrival of the shock wave at $\phi = 45^o$, and the

Position ϕ, θ	Exptl total pressure (MPa)	Peak total pressure (MPa) ($\beta = 0.1$)
$0^o, 0^o$	5.320	5.30
$45^o, 0^o$	3.630	2.07
$90^o, 0^o$	0.813	0.67
$135^o, 0^o$	0.623	1.13
$90^o, 180^o$	0.628	0.67

Table 6.8: Comparison of experimental and DAA predicted peak total pressures under 5g EDC-1 at 1.0m stand off (axisymmetric)

longer duration impulses at $\phi = 90^o$ and 135^o, are all simulated in accordance with what was measured.

Axisymmetry of loading is evident in Fig. 6.29 when comparing the predicted pressure records at $\phi = 90^o$ for the $\theta = 0^o$ and 180^o meridians. As is clear from table 6.8 the experiment was less successful in ensuring the UNDEX loading was axisymmetric.

Shell response

Despite evidence of numerical noise in the signals the rise to the peak response at the apex clearly exhibits the characteristic drop in strain level prior to the peak, as illustrated in Figs 6.30 – 6.33. With the exception of one result, the DAA-MAT90 approach predicts higher initial peak strains in both directions.

As with the MMALE technique the sequence of peak strain levels down the $\theta = 0^o$ meridian, listed in tables 6.9 and 6.10, is predicted well by both DAA approaches for the circumferential and meridional directions and follows the pattern of the experiment. The strains are observed to be highest at the apex reducing towards the maximum diameter, then increasing again towards the base. The predicted peak strain levels occur in the meridional direction, as observed in the MMALE pseudo-wedge model, confirming that the numerical model is stiffer meridionally, as observed experimentally under symmetric loading, but contradicting what was observed experimentally under axisymmetric loading. The peak response in the circumferential direction predicted by the DAA-MAT90 technique compares well with the measured response except at the maximum diameter and in the base region where significant underprediction is evident. Overall the peak responses in the meridional direction are overpredicted

Position ϕ, θ	Initial peak strain ($\times 10^6$)			
	Circum.		Merid.	
	Expt	DAA-MAT90	Expt	DAA-MAT90
$0^o, 0^o$	-3164	-3125	-2368	-3133
$30^o, 0^o$	-1766	-1990	-2123	-1987
$60^o, 0^o$	-997	-1195	-754	-1659
$90^o, 0^o$	-1224	-693	-1003	-1897
$120^o, 0^o$	-1034	-1231	-926	-2234
$150^o, 0^o$	-1833	-1402	-1439	-2632

Table 6.9: Comparison of experimental and DAA-MAT90 predicted initial peak strains under 5g EDC-1 at 1.0m stand off (axisymmetric)

Position ϕ, θ	Initial peak strain ($\times 10^6$)			
	Circum.		Merid.	
	Expt	DAA	Expt	DAA
$0^o, 0^o$	-3164	-1952	-2368	-2252
$30^o, 0^o$	-1766	-1289	-2123	-1212
$60^o, 0^o$	-997	-883	-754	-1046
$90^o, 0^o$	-1224	-912	-1003	-1071
$120^o, 0^o$	-1034	-1088	-926	-1319
$150^o, 0^o$	-1833	-1391	-1439	-1546

Table 6.10: Comparison of experimental and DAA predicted initial peak strains under 5g EDC-1 at 1.0m stand off (axisymmetric)

significantly. The DAA technique tended to underpredict circumferentially but overpredict meridionally in the lower two thirds of the meridian.

At $\phi = 0^o$ the predicted strain records are almost identical in each direction for both techniques. This was the response expected with the MMALE technique but not achieved (see table 6.6). This is further evidence supporting the more detailed discretisation of the DAA shell model. The higher strain occurred in the circumferential direction experimentally, but in the meridional direction numerically. The peak strain levels predicted by the DAA-MAT90 technique are in quite good agreement with experimental values. Unfortunately, at $\phi = 150^o$ the peak strains are underpredicted circumferentially and overpredicted meridionally. On the other hand, the DAA technique predicts a closer agreement with the measured response for the

circumferential direction. Such inconsistencies as these make the DAA results difficult to interpret.

Peak strains levels close to the initial peak are observed with the DAA technique in both directions long after the arrival of the shock wave, indicating the response has failed to dampen. This distinct lack of damping is common to all strain records predicted with this technique. The numerical noise is more evident under axisymmetric loading than in the symmetric load case, although it is confined to regions of maximum response, i.e., the apex and the base.

Fig. 6.34 depicts the deformed shape of the prototype shell predicted by the DAA-MAT90 technique. The shell is observed to have undergone rigid body motion after 5.0ms. The resistance applied by the surrounding water is evident from the squashed form exhibited by the shell. Later in time, at 0.8ms, the base of the shell is subjected to severe bending, which is reversed by 2.5ms. These oscillations could cause weakening of the shell in this region. An animated response of the shell clearly shows the base oscillations migrating upwards through the GRP laminate.

6.6 Architecture performance and solution times

For such computationally intensive simulations it is beneficial to assess the performance of LS-DYNA and USA-DYNA3D on various computer architectures and operating systems to examine not only differences in solution times, but also variations in solutions.

Versions of LS-DYNA were made available for three architectures: SGI, DEC ALPHA and an eight processor CRAY[¶]. Only an SGI version of USA-DYNA3D was available at the time of writing. Hence an architecture comparison could only be performed on the quasi-static loading and the MMALE axisymmetric UNDEX loading models. The various architecture performance and solutions of these models for the SGI and DEC ALPHA architectures are presented in tables 6.11 and 6.12. The analysis time of the UNDEX simulations was 2.0ms. Minimum output was requested in each case. The performance of the CRAY processor was found to be three times slower than the other processors available, and the UNDEX simulation could not be executed over multiple processors because the Eulerian formulation within LS-DYNA had not been parallelised at the time of writing.

It is clear that for both problems the 625MHz DEC ALPHA processor is the cheapest

[¶]CRAY J90 (RAL)

Architecture	Average time per zone cycle (ns)	CPU time (s)	Mean disp. (mm)
SGI Origin 200 (R10000)	11081	4306	0.57
DEC ALPHA 8400 EV5 (300MHz)	12202	4741	0.57
DEC ALPHA 8400 EV5 (625MHz)	7800	3031	0.57

Table 6.11: Comparison of various architecture performance and solutions for quasi-static loading

Architecture	Average time per zone cycle (ns)	CPU time (s)	Peak strain ($\times 10^6$)
SGI Origin 200 (1 × R10000)	85757	48879	-3696
DEC ALPHA 8400 EV5 (300MHz)	68674	39174	-3332
DEC ALPHA 8400 EV5 (625MHz)	43038	24541	-3332

Table 6.12: Comparison of various architecture performance and solutions for MMALE axisymmetric UNDEX loading

architecture at the time of writing. For the quasi-static loading model it is 30% faster and for the UNDEX loading model it is almost 50% faster than the SGI. It is interesting to note that the 300MHz DEC ALPHA is more expensive than the SGI Origin to compute the quasi-static model, but less expensive for the UNDEX model. No variation in the mean displacement is evident for the quasi-static model. A 10% difference in the peak strain at the apex was observed for the MMALE UNDEX simulation between on the SGI and the DEC ALPHA architectures. This might be attributed to the fact that the Eulerian formulation in LS-DYNA is being developed on DEC ALPHA architecture. The DEC ALPHA solution reduces the difference between simulation and experiment from 56% to 41%.

6.7 Conclusions

A detailed comparison of numerical simulations with experimental results from symmetric and axisymmetric UNDEX loading on the prototype echinodome has been undertaken. The three numerical procedures - MMALE, DAA-MAT90 and DAA - were utilised and validated for fluid and shell response predictive capabilities. Several conclusions can be drawn from the application of each procedure to the various load cases.

Under symmetric UNDEX loading the DAA approach predicted good agreement with the fluid response but poor shell response.

1. Overall, the DAA approaches appeared to simulate the physical fluid and shell response well, predicting the critical regions under symmetric loading with good correspondence between experiment and numerical modelling.
2. Quantitatively, the DAA technique underpredicted the shell response.
3. The fluid response at the shell predicted by the DAA-MAT90 technique was encouraging, and increasing the damping factor provided a reduction in the amplitude of numerical oscillations in the predicted pressure records.
4. The DAA-MAT90 technique also underpredicted the peak shell response. Increasing the damping factor reduced the predicted peak strains further.

An accurate prediction of strain response is more essential if either DAA technique is to be considered reliable for predicting dynamic buckling loads under symmetric UNDEX loading. That an accurate response was recorded at the stand off point for the first

0.3ms in the meridional direction only, and failure to predict the peak response at any other position, reduces confidence in this technique's capabilities for dynamic buckling load predictions under symmetric loading. Moreover, insufficient pressure decay value data is available to perform a suitable number of simulations to obtain the required information for prediction of dynamic buckling criteria. As a result the use of a second predictive technique in any numerically predicted results would be required, introducing further errors into a buckling analysis. Consequently, a numerical prediction of dynamic buckling loads is not considered viable using either DAA approach.

The MMALE pseudo-wedge model clearly demonstrated a capability for predicting the peak response of the prototype echinodome under axisymmetric loading.

1. The predicted physical propagation of the shock wave up to, and around, the shell was in good agreement with previous observations.

2. The quality of the pressure-time history associated with the shock wave at the stand off point is in question, being characterised by a series of slow rising oscillations of decreasing amplitude at the free field position. The peak pressure is within 10% of the measured experimental value.

3. The fluid response at the shell was underpredicted compared to experimental measurements and found to be less than the incident pressure at the apex.

4. The sequence of peak strains down the $\theta = 0^o$ meridian is well reproduced. However, the direction in which the experimental peak strains were found to occur was not replicated.

5. The predicted response of the shell was generally found to be overpredicted compared with experimental results. The highest strains however, did coincide with the critical regions observed experimentally.

The overpredicted shell response does not necessarily render the MMALE technique incapable of being utilised to make dynamic buckling load predictions. The MMALE technique provides a good representation of the physics of an UNDEX event and generates an approximate loading for the desired charge size at a given stand off distance. The fact that the strains were generally overpredicted implies a conservative estimate could be obtained to determine at what load failure would occur geometrically, and to compare with the load required to invoke material failure.

The DAA approach can be concluded to have predicted the shell response under axisymmetric loading much more accurately than under symmetric loading. For the axisymmetric load case:

1. Overall, the DAA approaches predicted credible physical fluid and shell response, predicting where the critical regions under axisymmetric loading would occur, namely the apex and the base.

2. The predicted fluid response at the shell is in excellent agreement with that observed experimentally, particularly at the stand off point.

3. The sequence of peak strains predicted by both DAA approaches followed that observed in the experiment.

4. The peak shell response predicted by the DAA-MAT90 technique was in better agreement with the experiment than the DAA technique, particularly at the stand off point. Both techniques overpredicted the response around the maximum diameter.

The DAA-MAT90 approach is concluded to be suitable for predicting dynamic buckling loads under axisymmetric loading as it provides an accurate prediction of the strain response at the critical regions of the shell. However, in order to utilise the DAA approach, experimental pressure decay values are required for various charge sizes and/or stand off distances to simulate the loading to which the shell is subjected. This data is not available for distances any closer than 1.0m for both 5g and 10g charges. Consequently more data would have to be acquired before undertaking dynamic buckling load predictions.

Several other issues regarding the numerical approaches, architecture performance, and accuracy of numerical models have been examined and the following conclusions can be drawn.

1. Accounting for the thickness variation in the circumferential direction as well as the meridional would be a more accurate representation of the shell. Also a more complex material model could be combined with this to improve the predicted response of the shell model.

2. The material definition used for the shell in both the MMALE and DAA meshes is considered inadequate for predicting scattered pressures, although the higher quality discretisation used in the DAA approaches indicates an improved predicted fluid response.

3. The deformed plots obtainable from numerical simulations provide a better understanding of both the global and local response of the prototype echinodome. Such understanding could not be achieved so readily from experimental studies.

4. The Belytschko-Leviathan shell is the most efficient shell formulation for DAA-MAT90 analyses of UNDEX loading against the prototype echinodome.

5. The default shell formulation and the van Leer advection scheme are sufficiently accurate for MMALE analyses of axisymmetric UNDEX loading.

6. The DEC ALPHA architecture is the cheapest architecture available at the time of writing for the MMALE UNDEX model utilised in the simulations presented in this work. It also computes a more accurate solution, i.e., closer to the experimental result.

The analyses performed in this chapter provide sufficient confidence in utilising the MMALE approach for dynamic buckling load predictions under axisymmetric UNDEX loading.

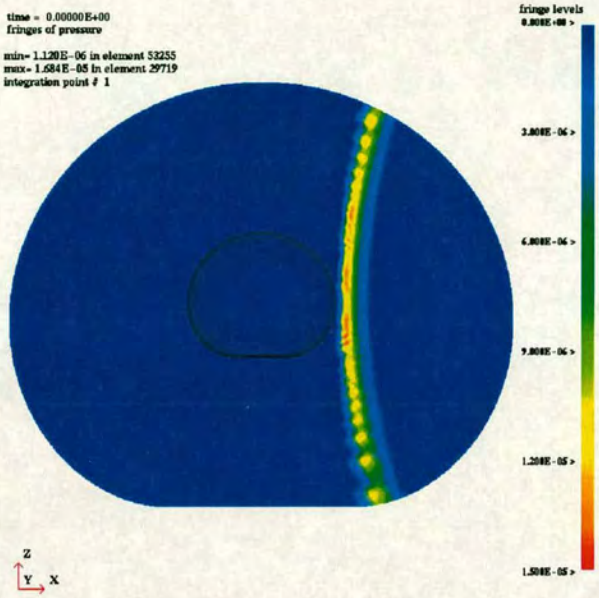

(a) Impact (t = 0.0ms)

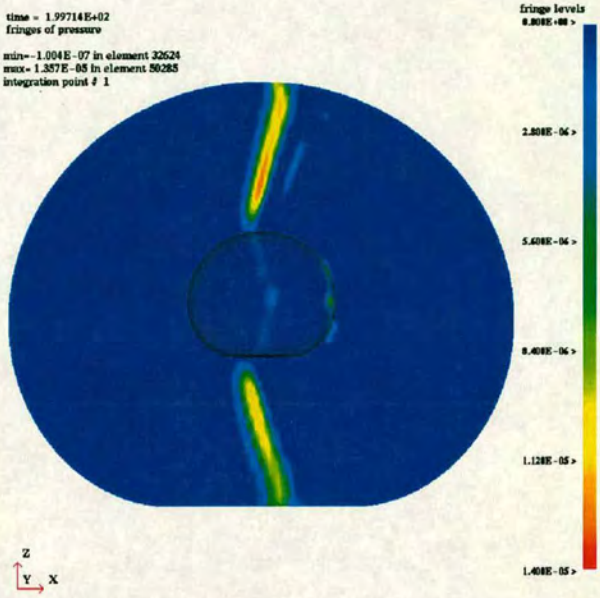

(b) Diffraction (t = 0.2ms)

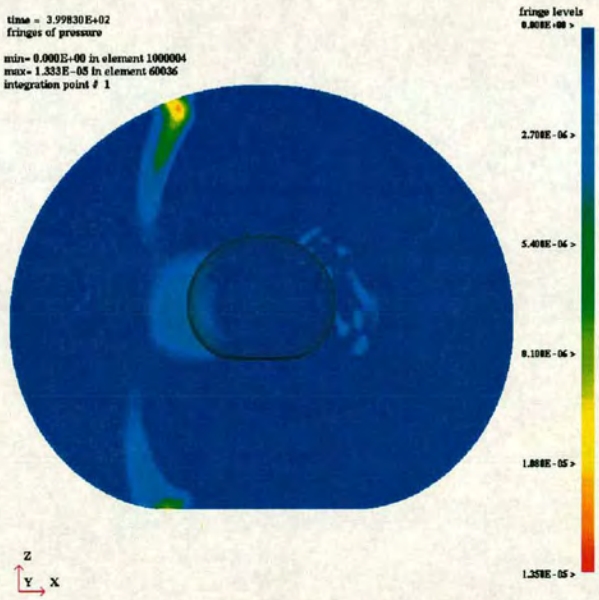

(c) Distorted shock front (t = 0.4ms)

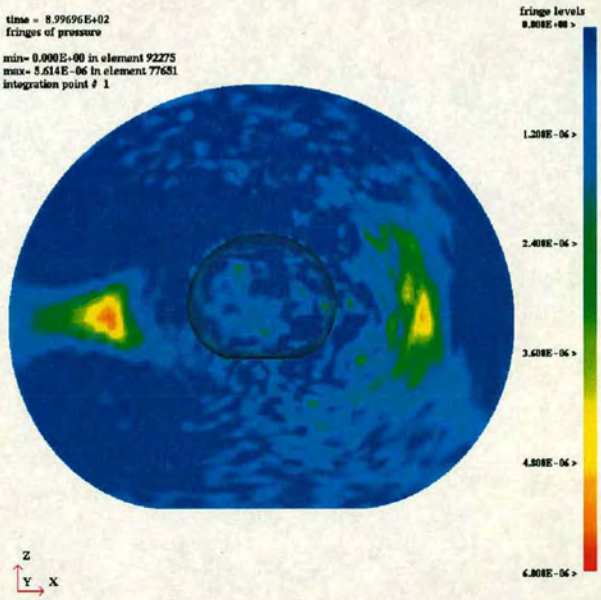

(d) Scattered pressure (t = 0.9ms)

Figure 6.1: DAA-MAT90 predicted propagation of shock wave around shell under symmetric loading from 10g EDC-1 at 2.0m stand off (pressure units = Pa $\times 10^{-11}$)

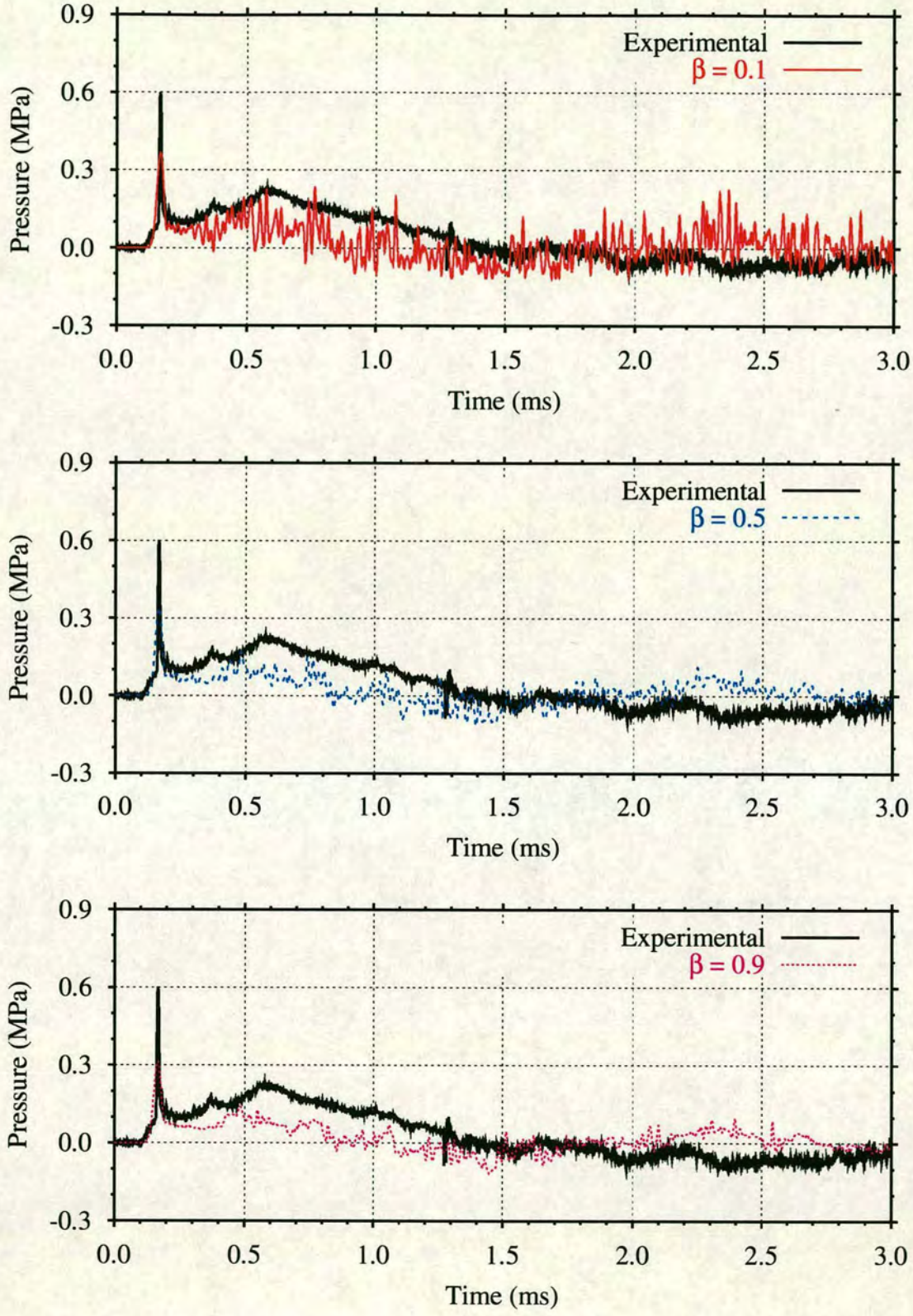

Figure 6.2: Comparison of DAA-MAT90 predicted and measured fluid response at $\phi = 0^o$, $\theta = 0^o$ (PG 1) to 10g EDC-1 at 2.0m stand off (symmetric)

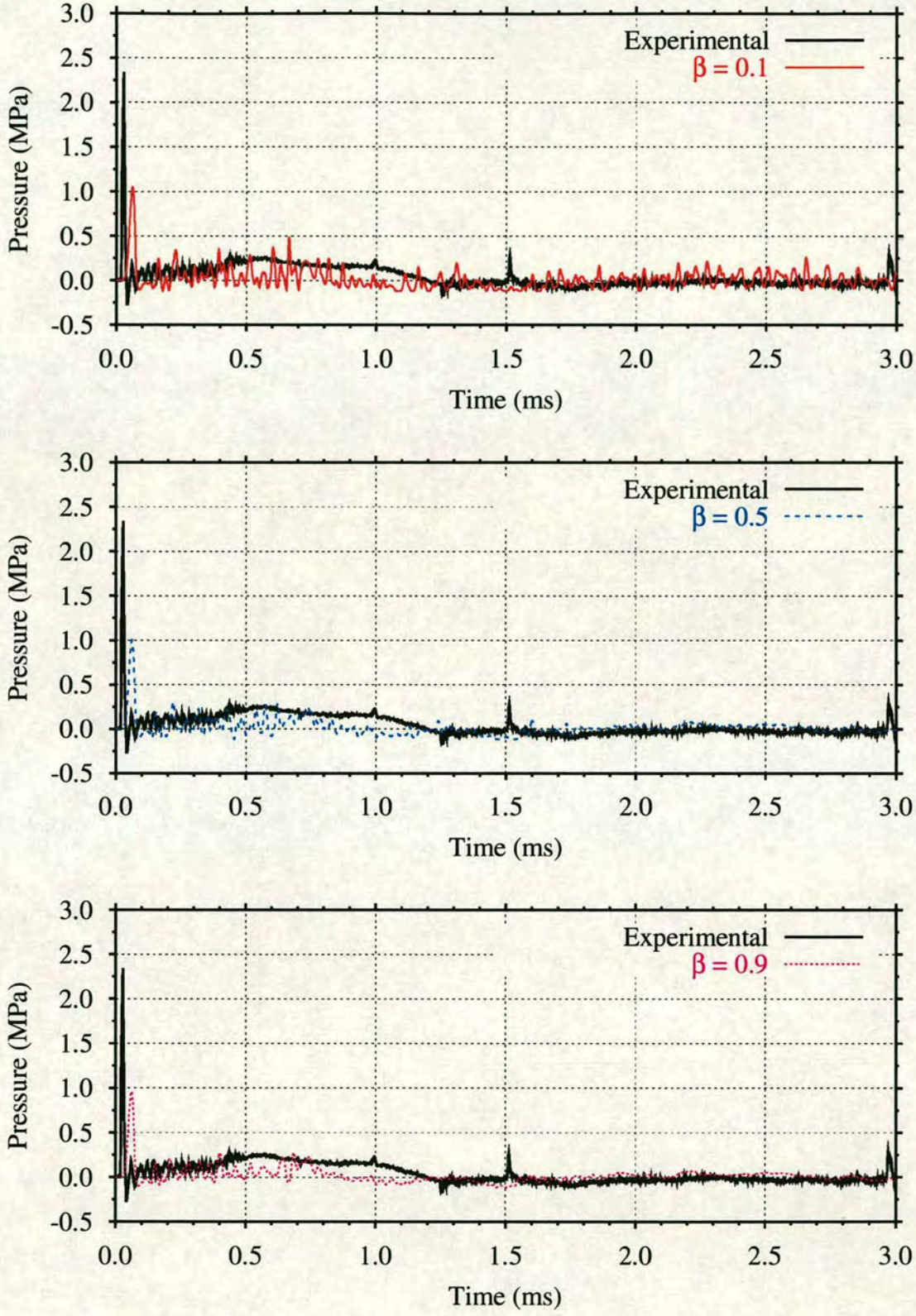

Figure 6.3: Comparison of DAA-MAT90 predicted and measured fluid response at $\phi = 45^o$, $\theta = 0^o$ (PG 2) to 10g EDC-1 at 2.0m stand off (symmetric)

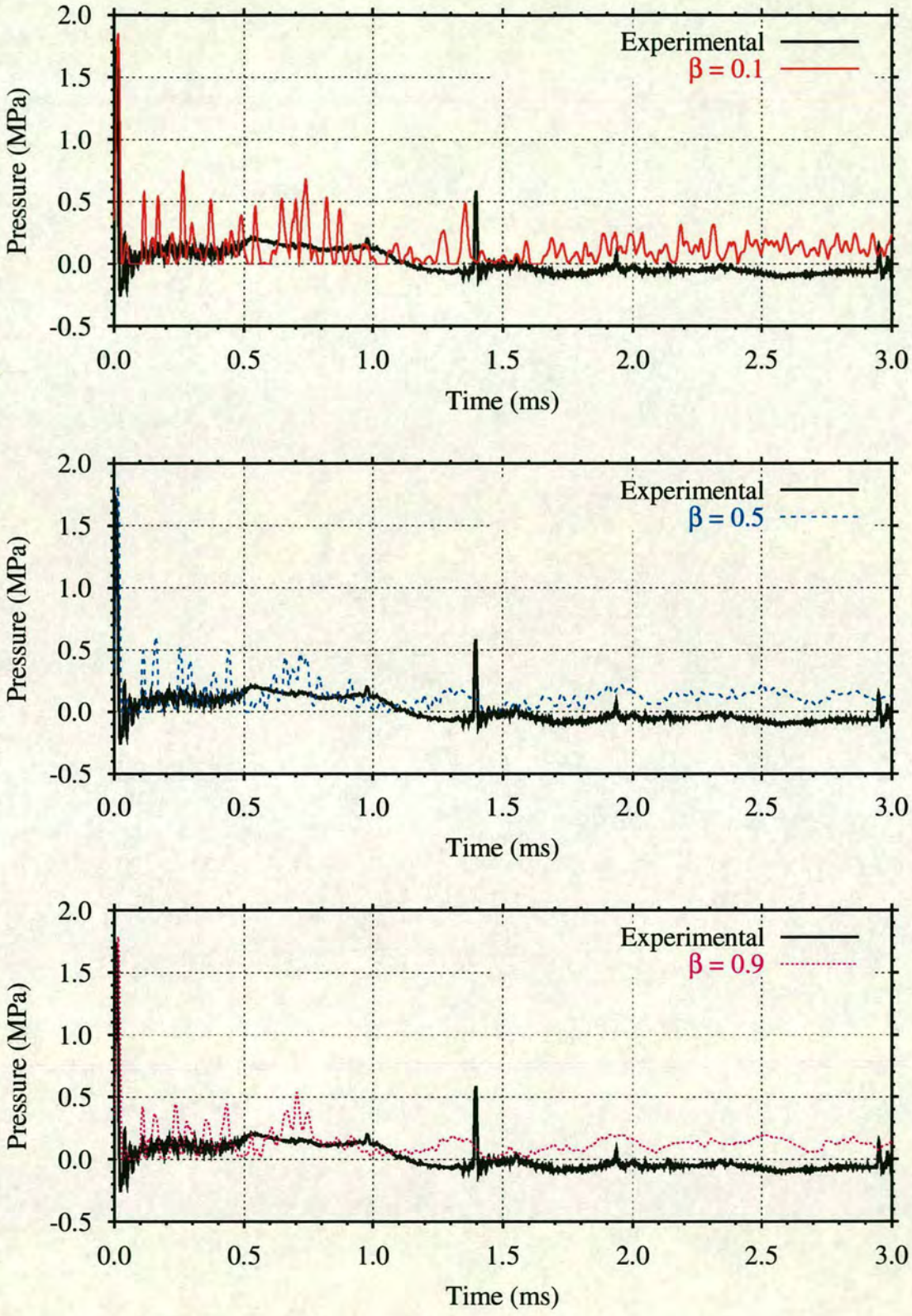

Figure 6.4: Comparison of DAA-MAT90 predicted and measured fluid response at $\phi = 90^o$, $\theta = 0^o$ (PG 3) to 10g EDC-1 at 2.0m stand off (symmetric)

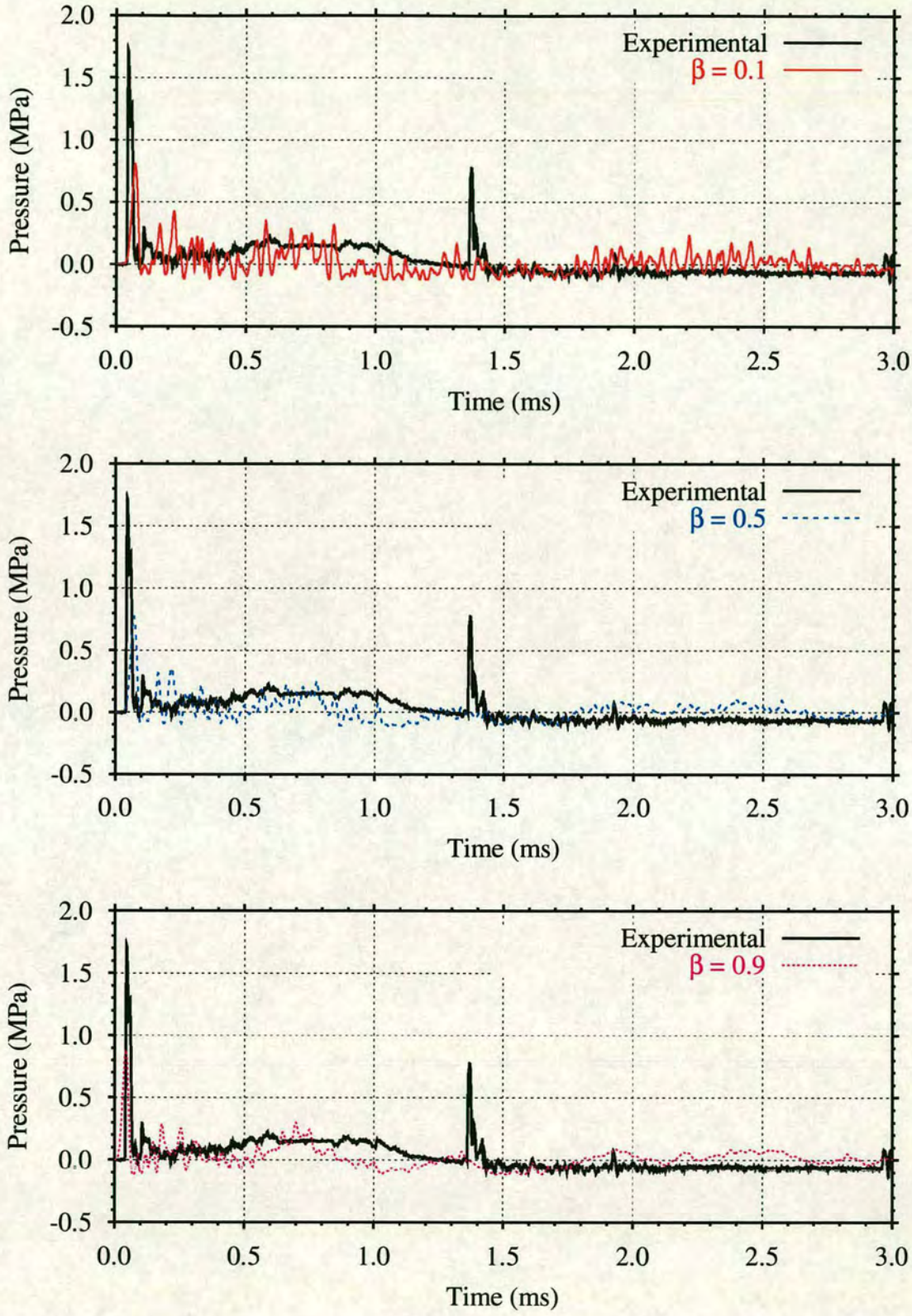

Figure 6.5: Comparison of DAA-MAT90 predicted and measured fluid response at $\phi = 135^o$, $\theta = 0^o$ (PG 4) to 10g EDC-1 at 2.0m stand off (symmetric)

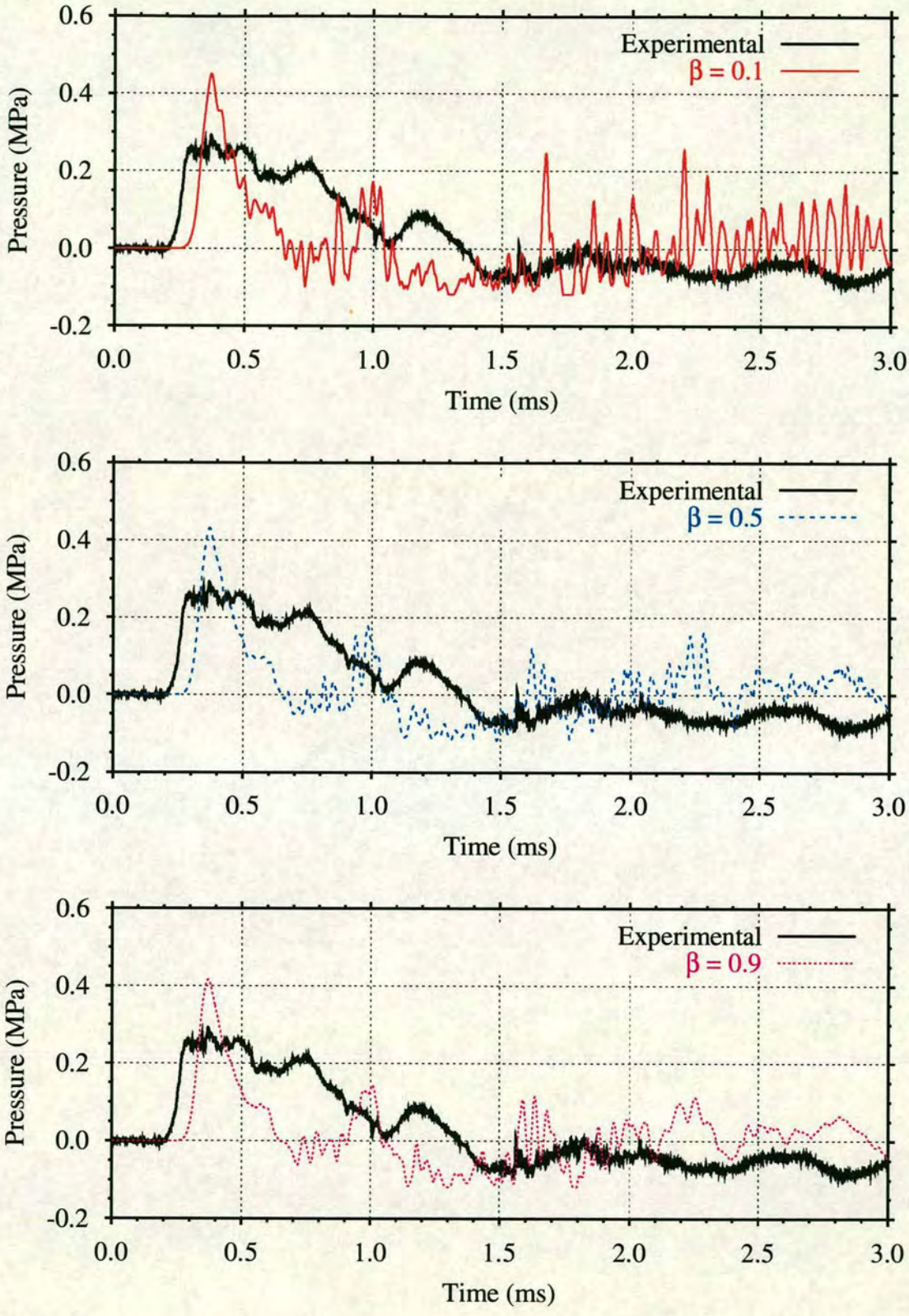

Figure 6.6: Comparison of DAA-MAT90 predicted and measured fluid response at $\phi = 90^o$, $\theta = 180^o$ (PG 6) to 10g EDC-1 at 2.0m stand off (symmetric)

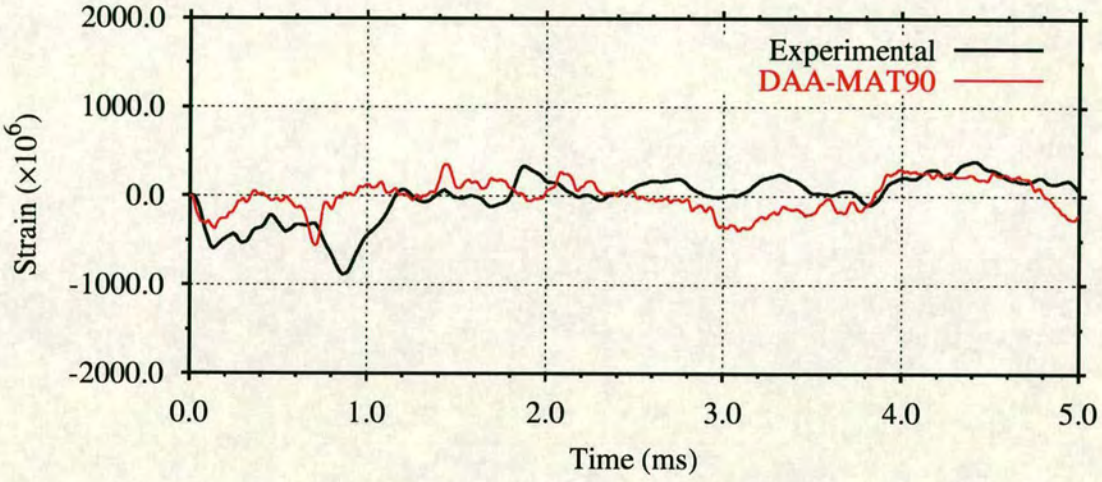

(a) DAA-MAT90 vs experiment

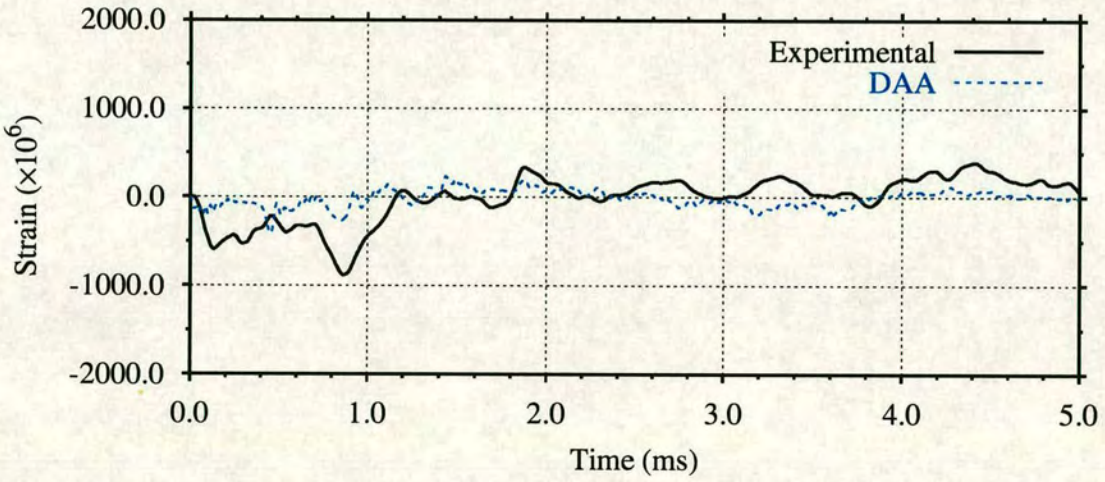

(b) DAA vs experiment

Figure 6.7: Comparison of predicted and measured circumferential strain response at $\phi = 90°$, $\theta = 0°$ to 10g EDC-1 at 2.0m stand off (symmetric)

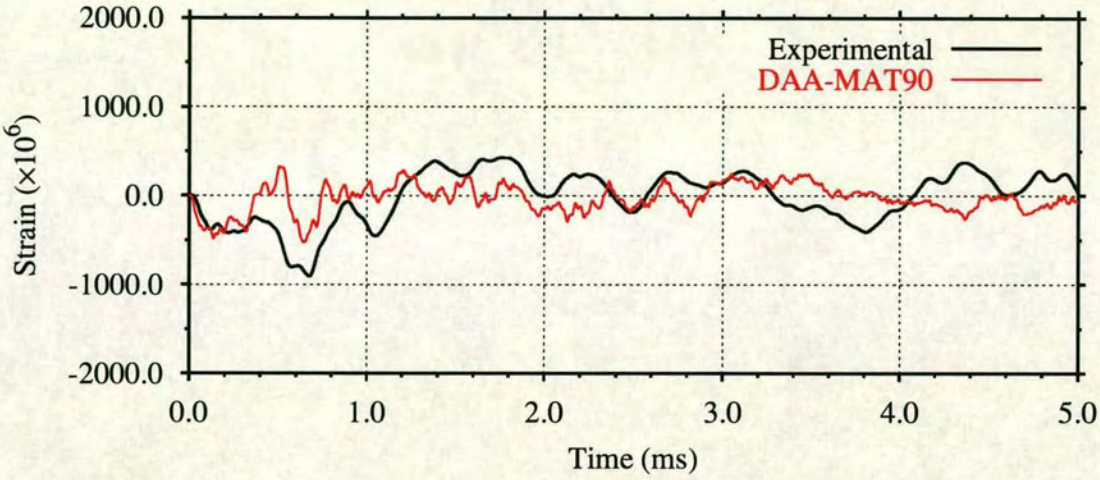

(a) DAA-MAT90 vs experiment

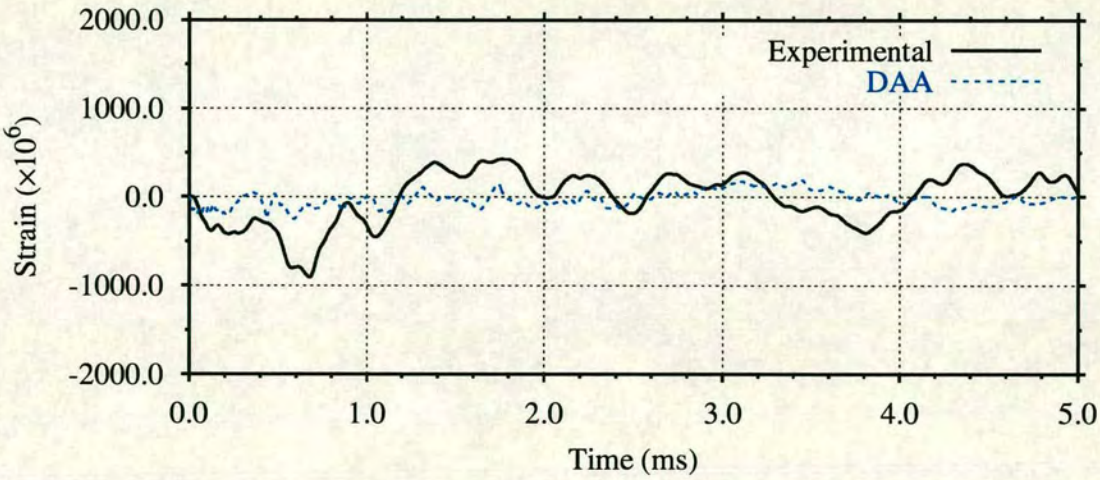

(b) DAA vs experiment

Figure 6.8: Comparison of predicted and measured meridional strain response at $\phi = 90^o$, $\theta = 0^o$ to 10g EDC-1 at 2.0m stand off (symmetric)

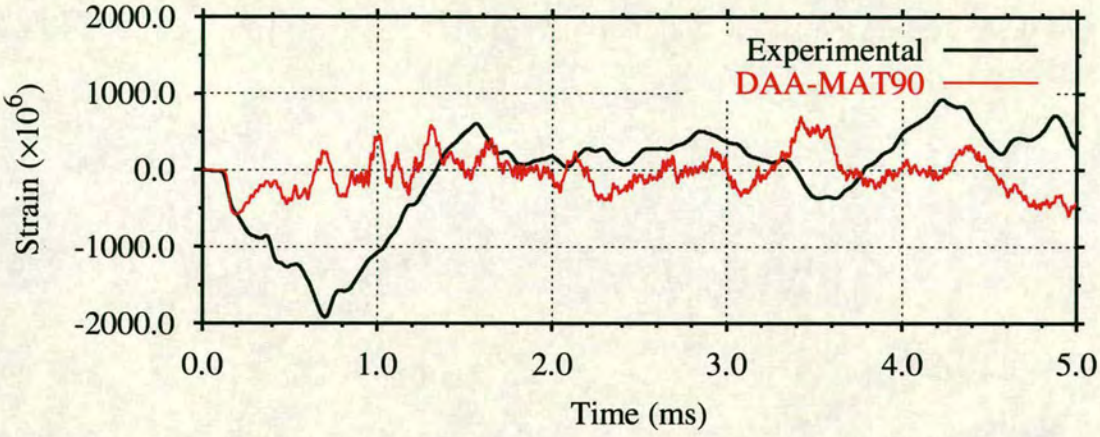

(a) DAA-MAT90 vs experiment

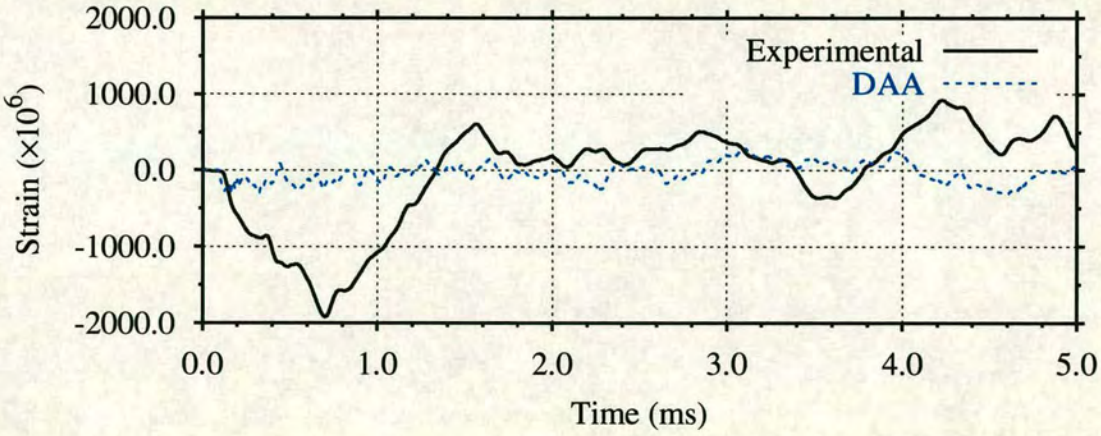

(b) DAA vs experiment

Figure 6.9: Comparison of predicted and measured circumferential strain response at $\phi = 0^o$, $\theta = 0^o$ to 10g EDC-1 at 2.0m stand off (symmetric)

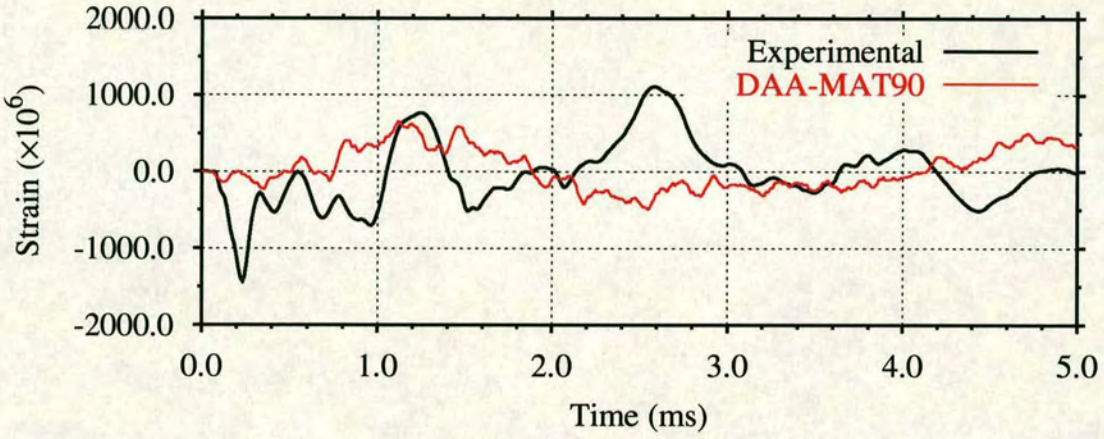

(a) DAA-MAT90 vs experiment

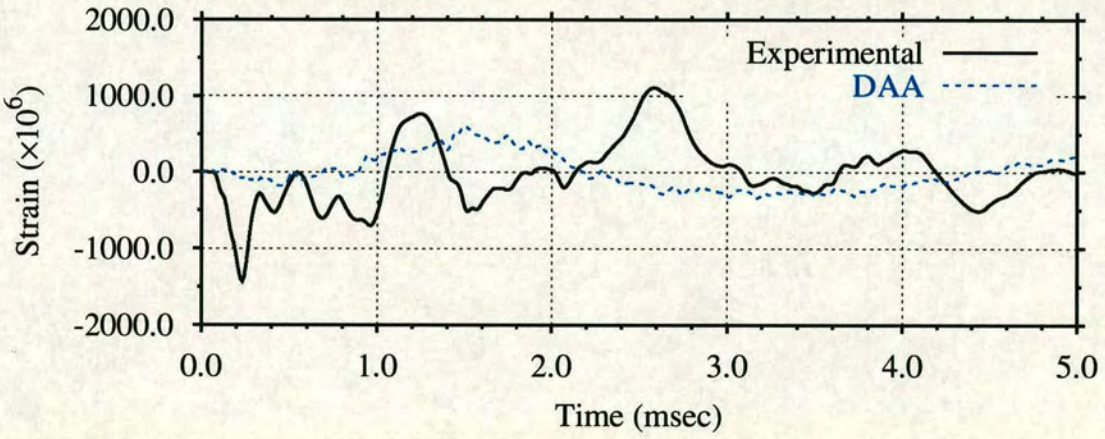

(b) DAA vs experiment

Figure 6.10: Comparison of predicted and measured circumferential strain response at $\phi = 150^o$, $\theta = 0^o$ to 10g EDC-1 at 2.0m stand off (symmetric)

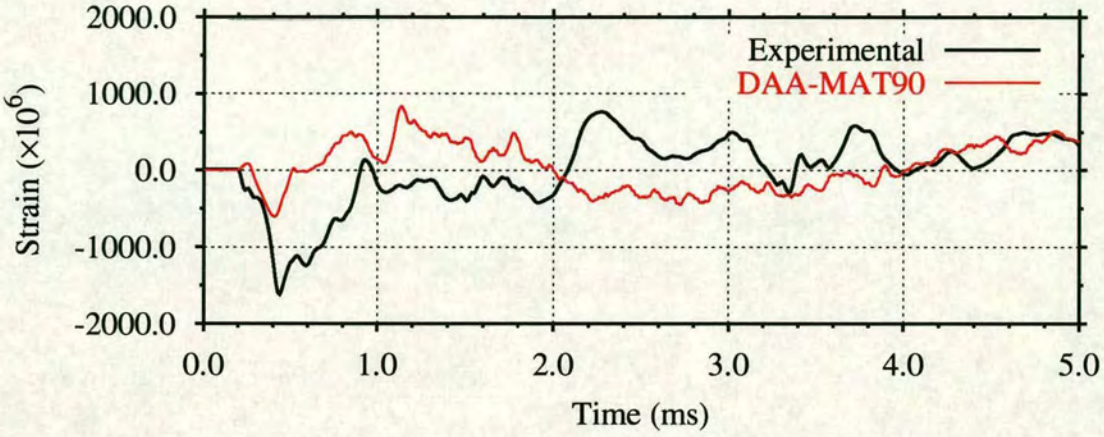

(a) DAA-MAT90 vs experiment

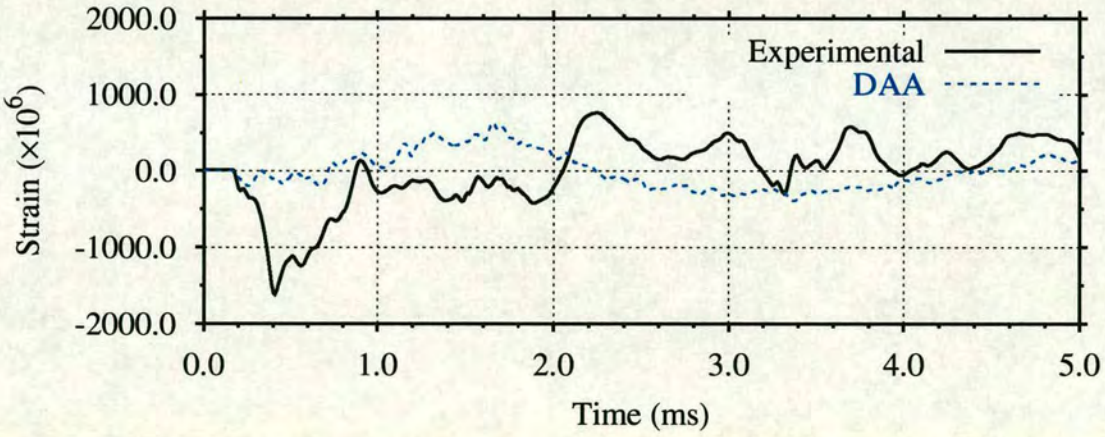

(b) DAA vs experiment

Figure 6.11: Comparison of predicted and measured circumferential strain response at $\phi = 150^o$, $\theta = 180^o$ to 10g EDC-1 at 2.0m stand off (symmetric)

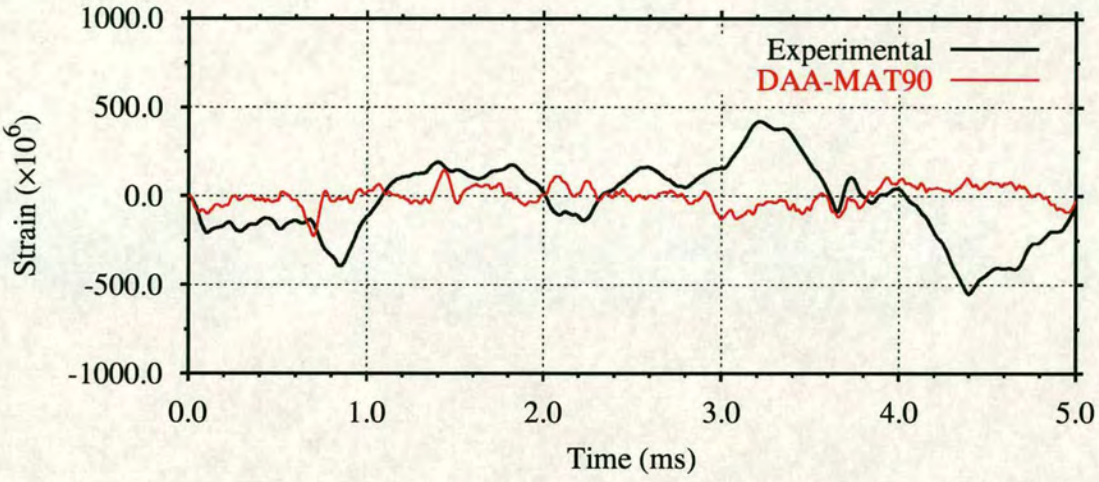

(a) Circumferential strain

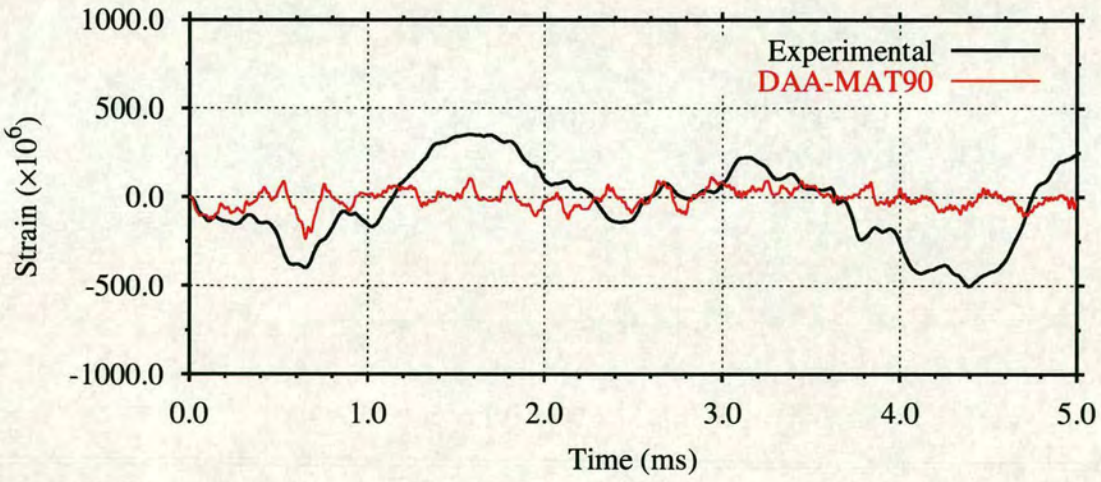

(b) Meridional strain

Figure 6.12: Comparison of DAA-MAT90 predicted and measured meridional strain response at $\phi = 90^o$, $\theta = 0^o$ to 10g EDC-1 at 5.0m stand off (symmetric)

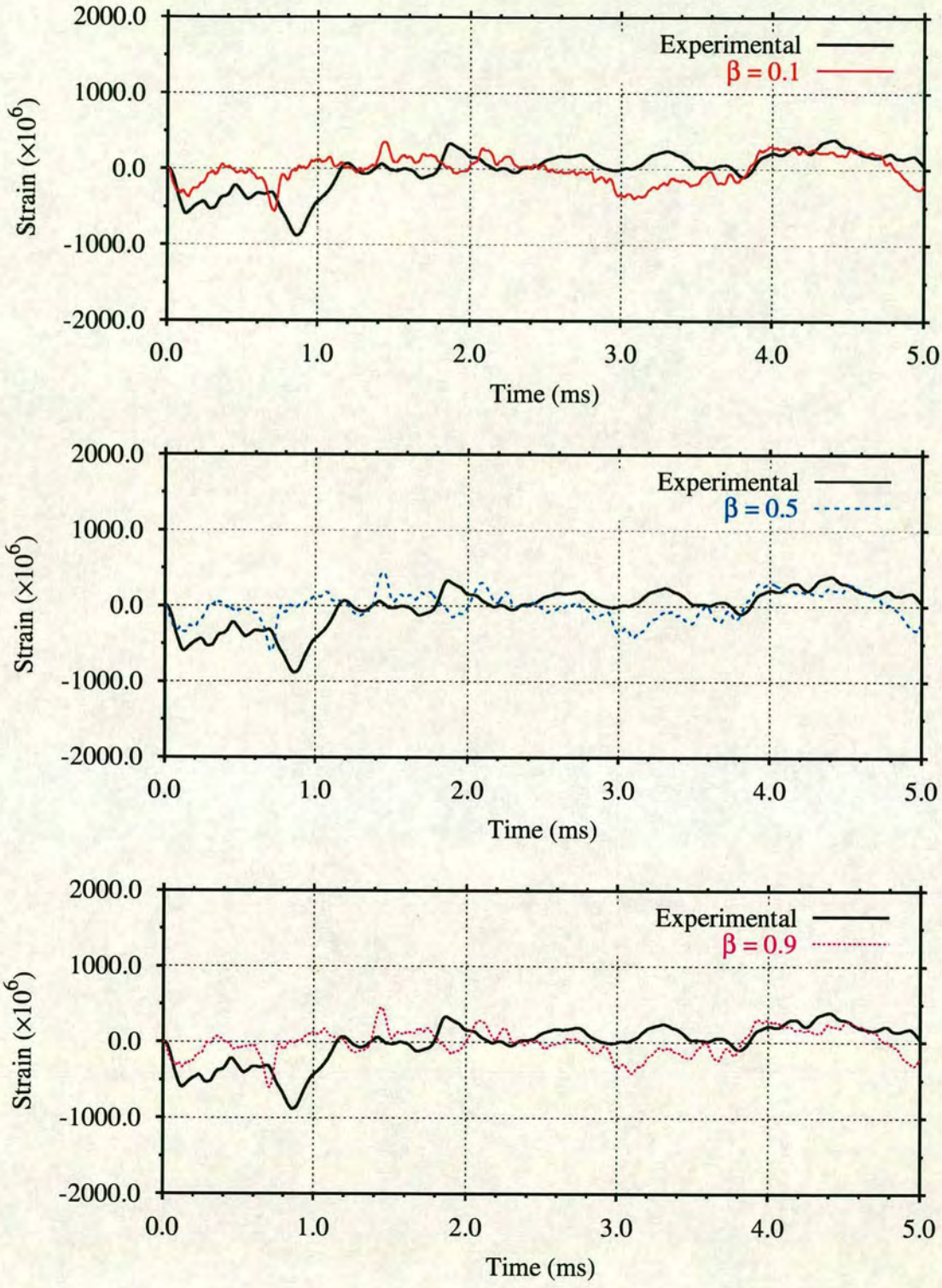

Figure 6.13: Effect of damping factor, β, on DAA-MAT90 predicted circumferential strain response at $\phi = 90^o$, $\theta = 0^o$ to 10g EDC-1 at 2.0m stand off (symmetric)

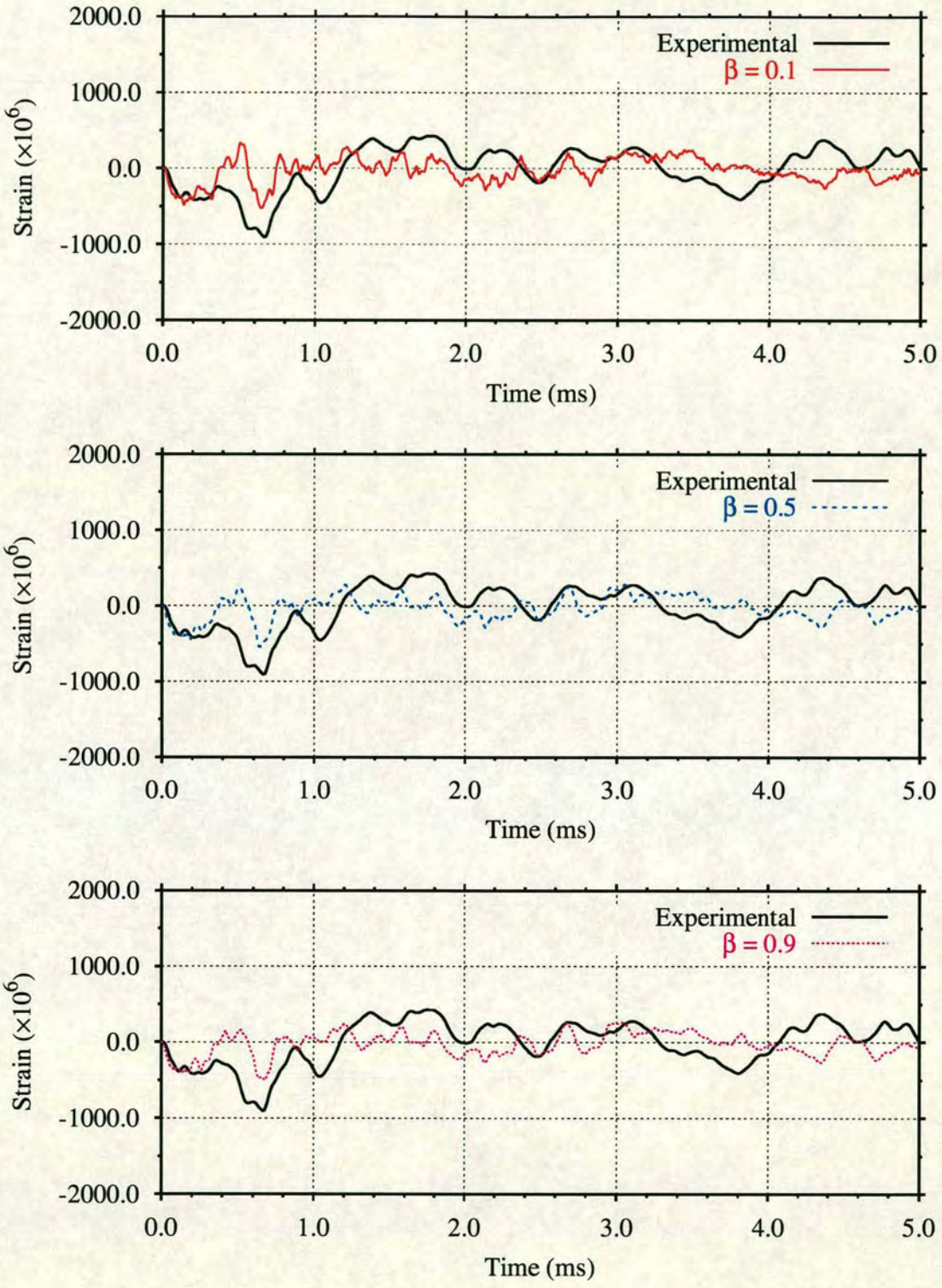

Figure 6.14: Effect of damping factor, β, on DAA-MAT90 predicted meridional strain response at $\phi = 90^o$, $\theta = 0^o$ to 10g EDC-1 at 2.0m stand off (symmetric)

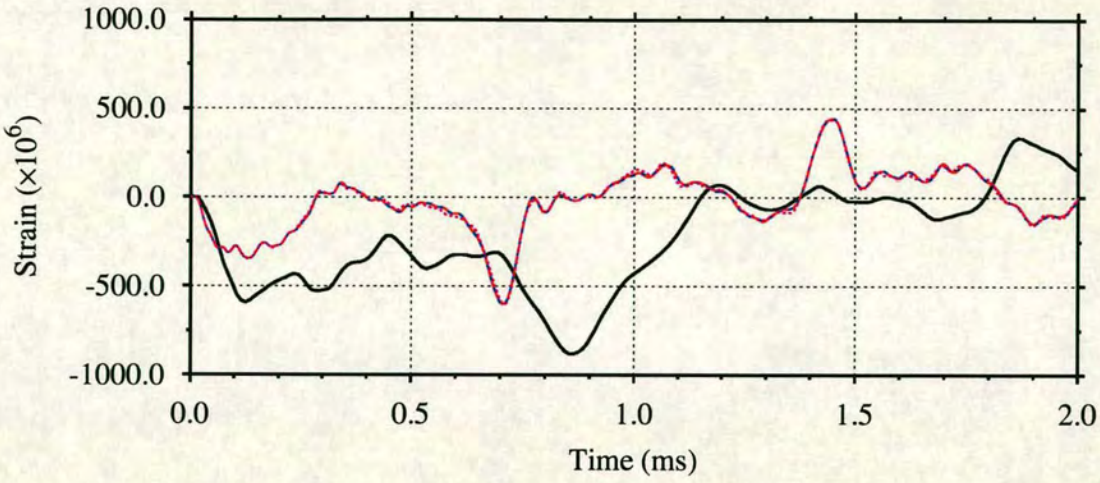

(a) Circumferential strain

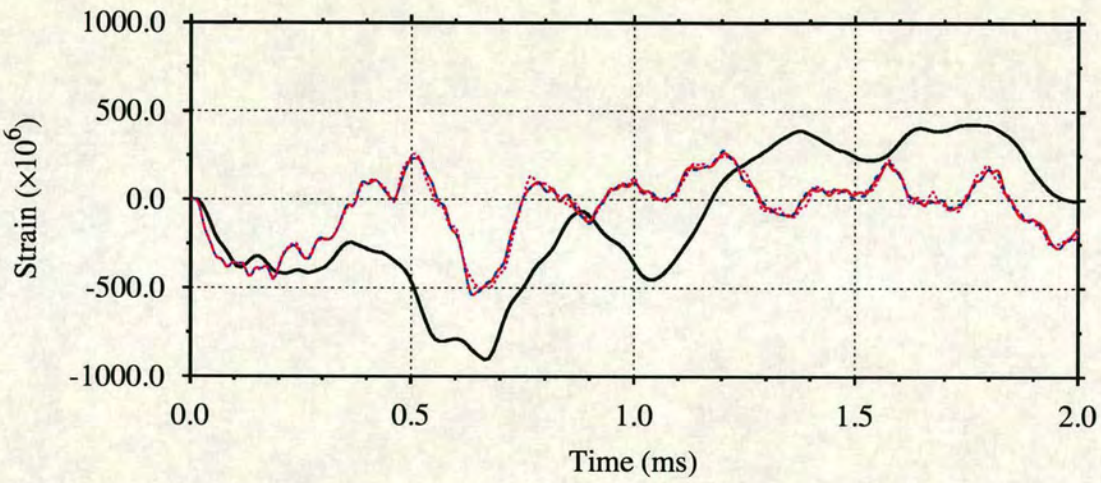

(b) Meridional strain

Figure 6.15: Effect of shell formulations on DAA-MAT90 predicted strain response at $\phi = 90^o$, $\theta = 0^o$ to 10g EDC-1 at 2.0m stand off (symmetric)

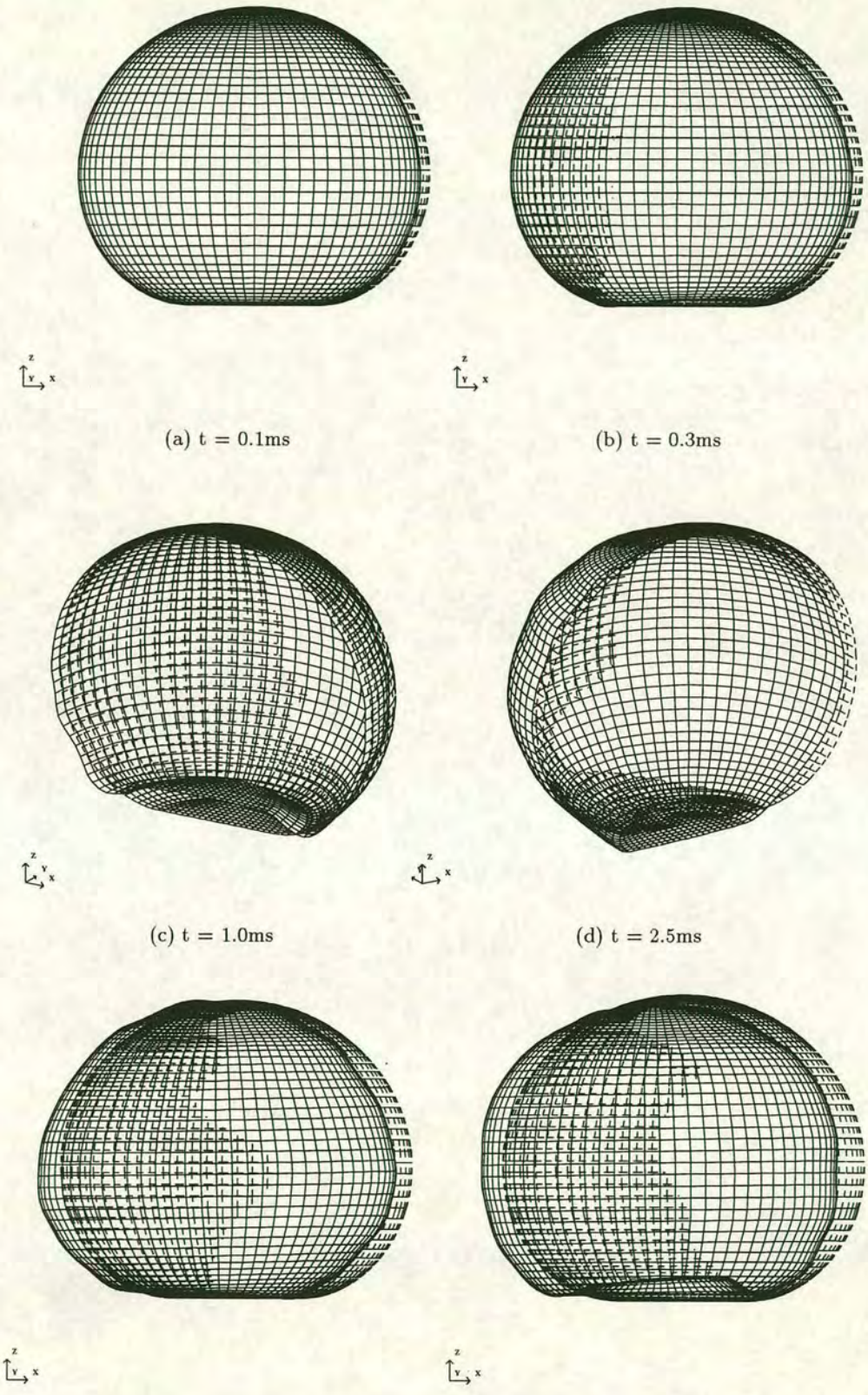

(a) t = 0.1ms

(b) t = 0.3ms

(c) t = 1.0ms

(d) t = 2.5ms

(e) t = 4.0ms

(f) t = 5.0ms

Figure 6.16: DAA-MAT90 predicted shell deformation under symmetric loading from 10g EDC-1 at 2.0m stand off (disp. $\times 100$)

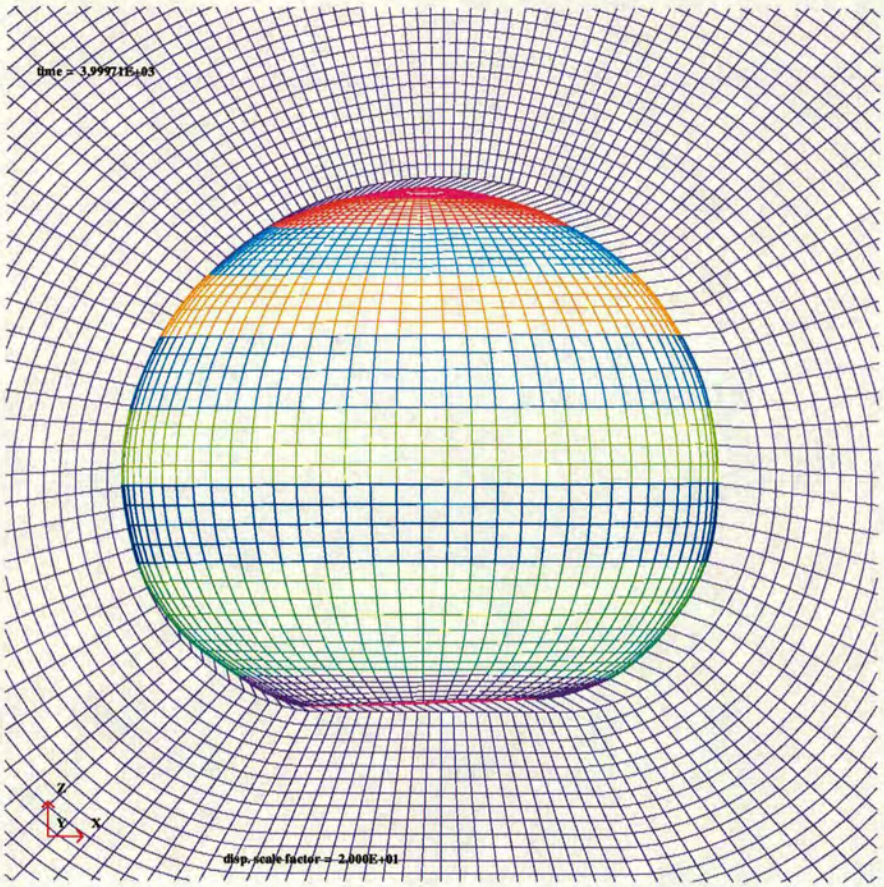

Figure 6.17: Deformation of acoustic elements at $t = 4.0$ms (disp. $\times$ 20)

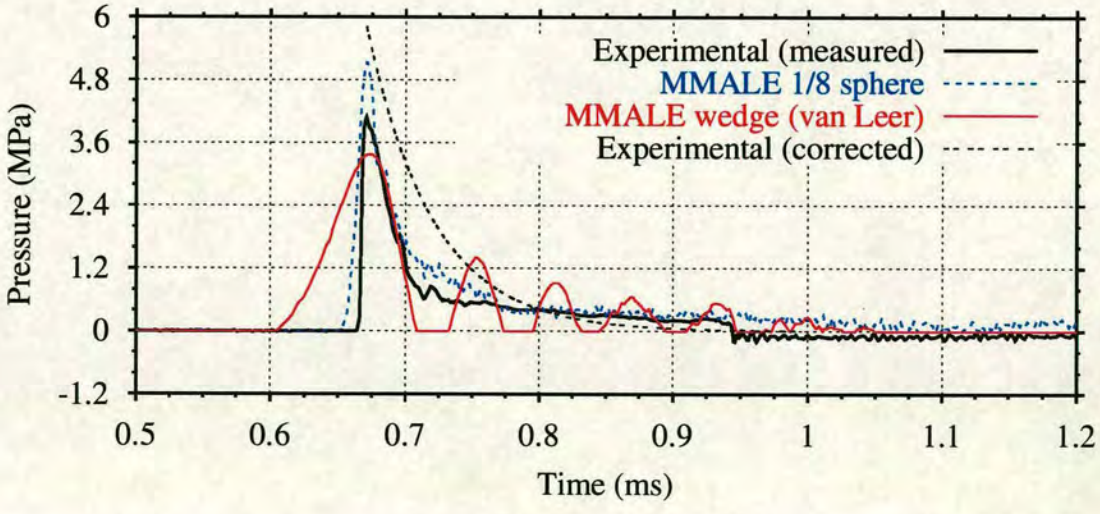

Figure 6.18: Comparison of free field fluid response at 1.0m stand off from 5g EDC-1

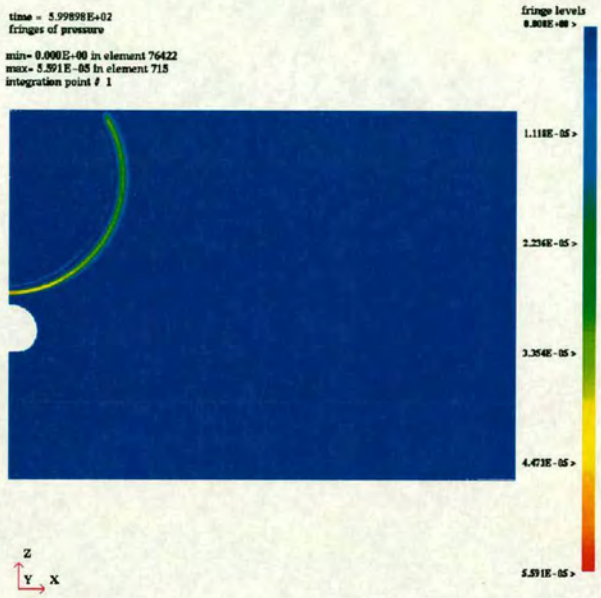

(a) Impact (t = 0.6ms)

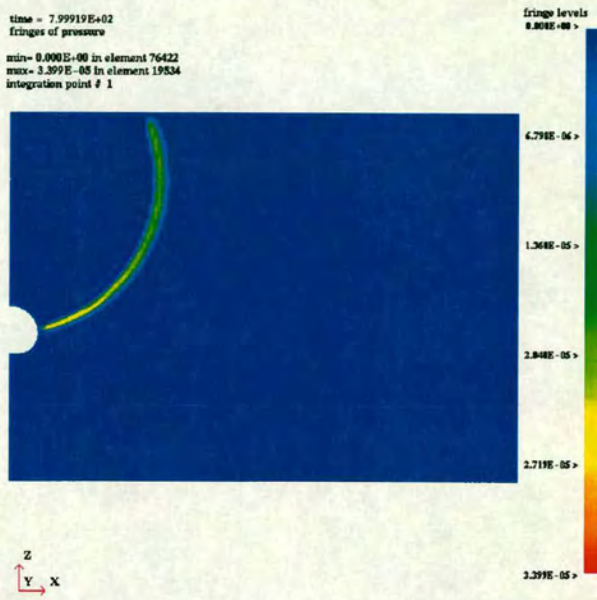

(b) Diffraction (t = 0.8ms)

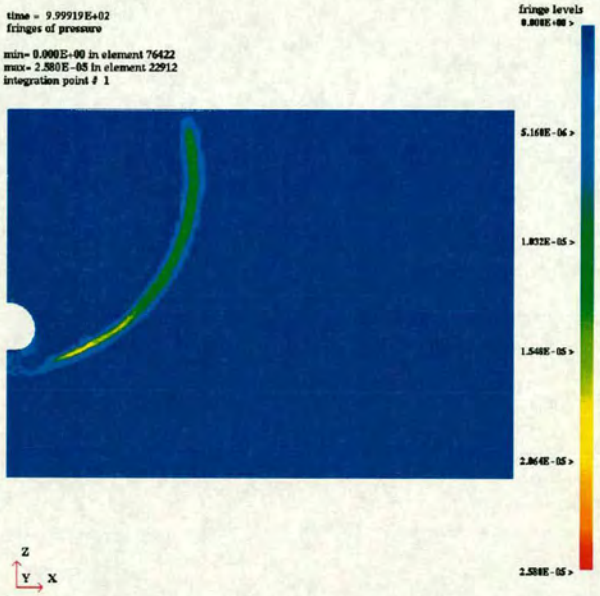

(c) Smeared shock front (t = 1.0ms)

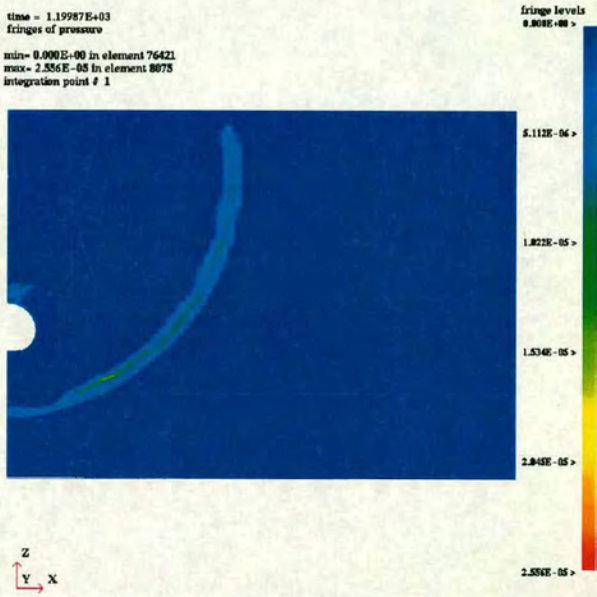

(d) Reflection (t = 1.2ms)

Figure 6.19: MMALE predicted propagation of shock wave around shell under axisymmetric loading from 5g EDC-1 at 1.0m stand off (pressure units = Pa $\times 10^{-11}$)

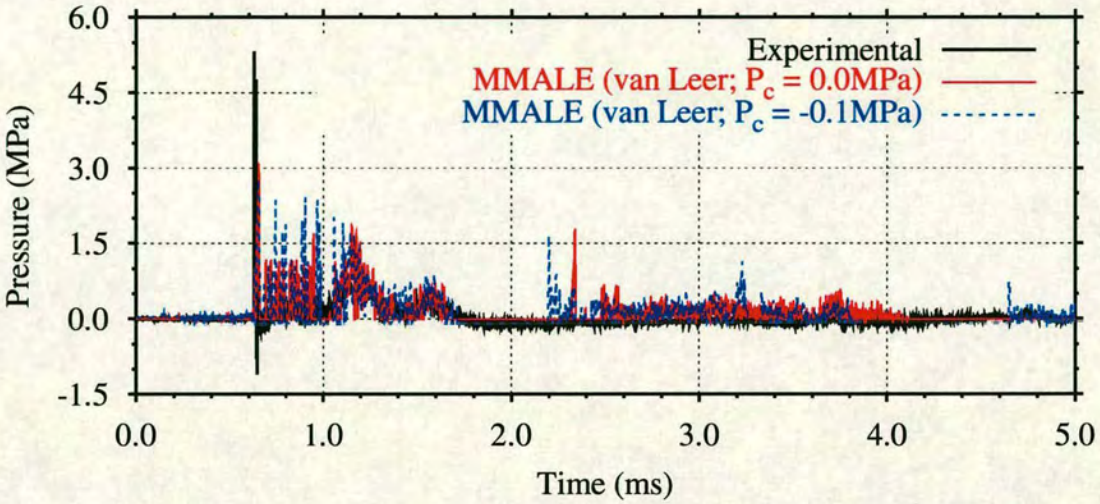

(a) $\phi = 0^o$, $\theta = 0^o$ (PG 1)

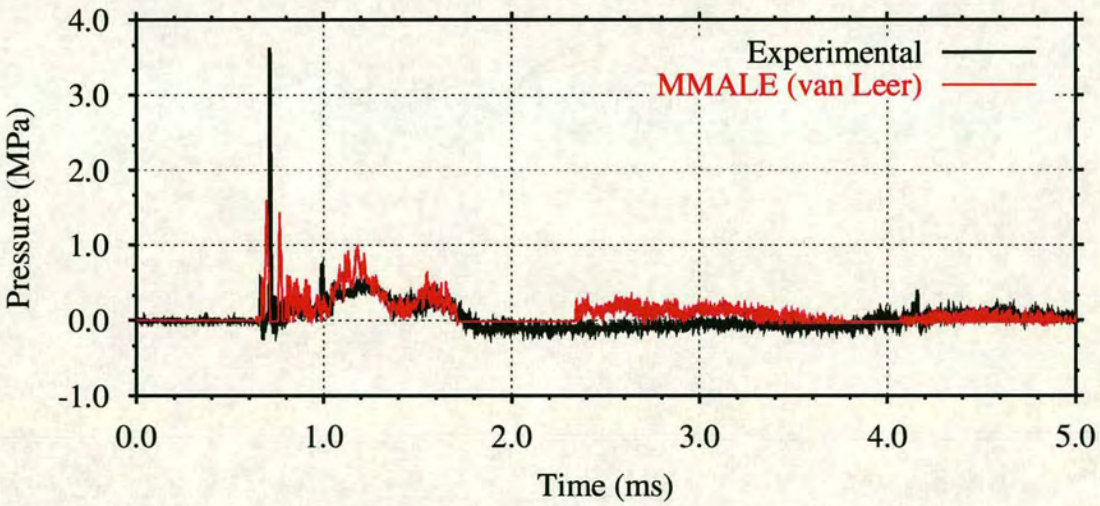

(b) $\phi = 45^o$, $\theta = 0^o$ (PG 2)

Figure 6.20: Comparison of MMALE predicted and measured fluid response at PGs 1 and 2 to 5g EDC-1 at 1.0m stand off (axisymmetric)

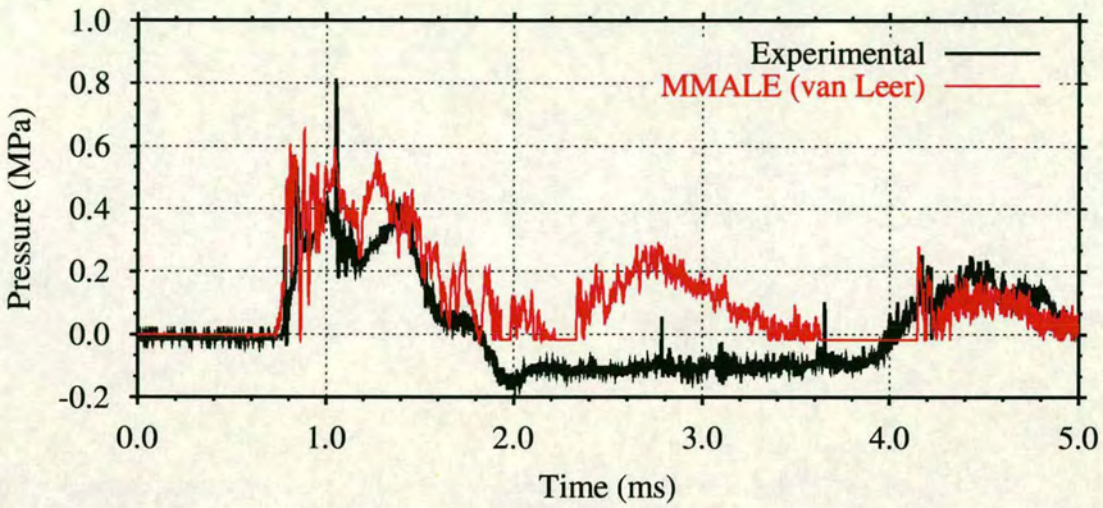

(a) $\phi = 90^o$, $\theta = 0^o$ (PG 3)

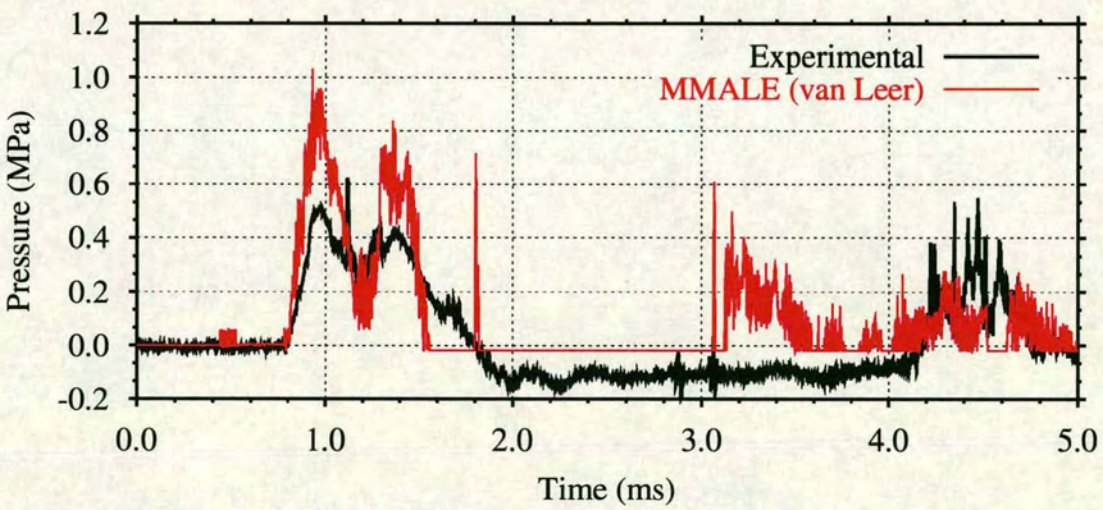

(b) $\phi = 135^o$, $\theta = 0^o$ (PG 4)

Figure 6.21: Comparison of MMALE predicted and measured fluid response at PGs 3 and 4 to 5g EDC-1 at 1.0m stand off (axisymmetric)

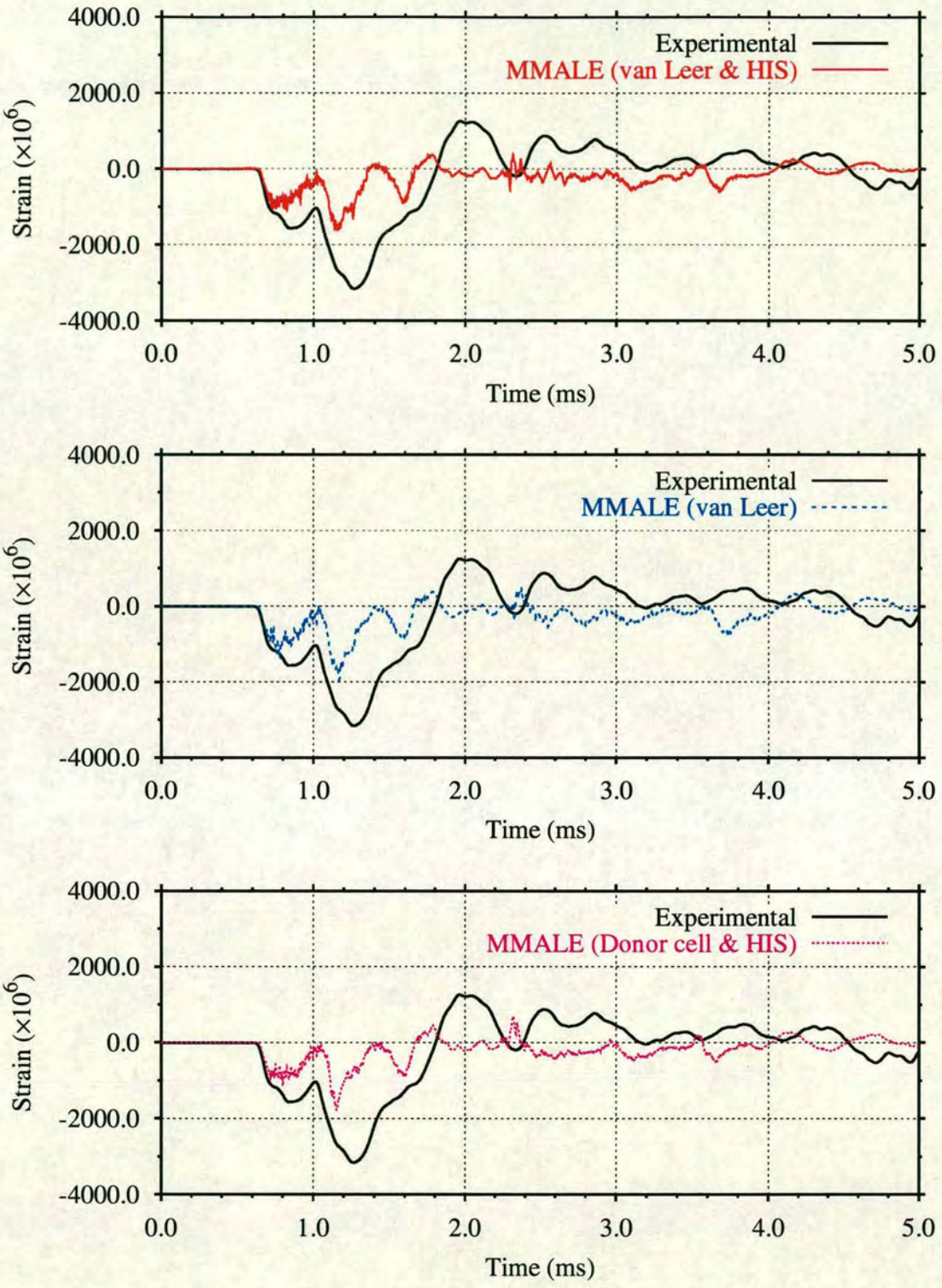

Figure 6.22: Comparison of MMALE predicted and measured circumferential strain response at $\phi = 0^o$, $\theta = 0^o$ to 5g EDC-1 at 1.0m stand off (axisymmetric)

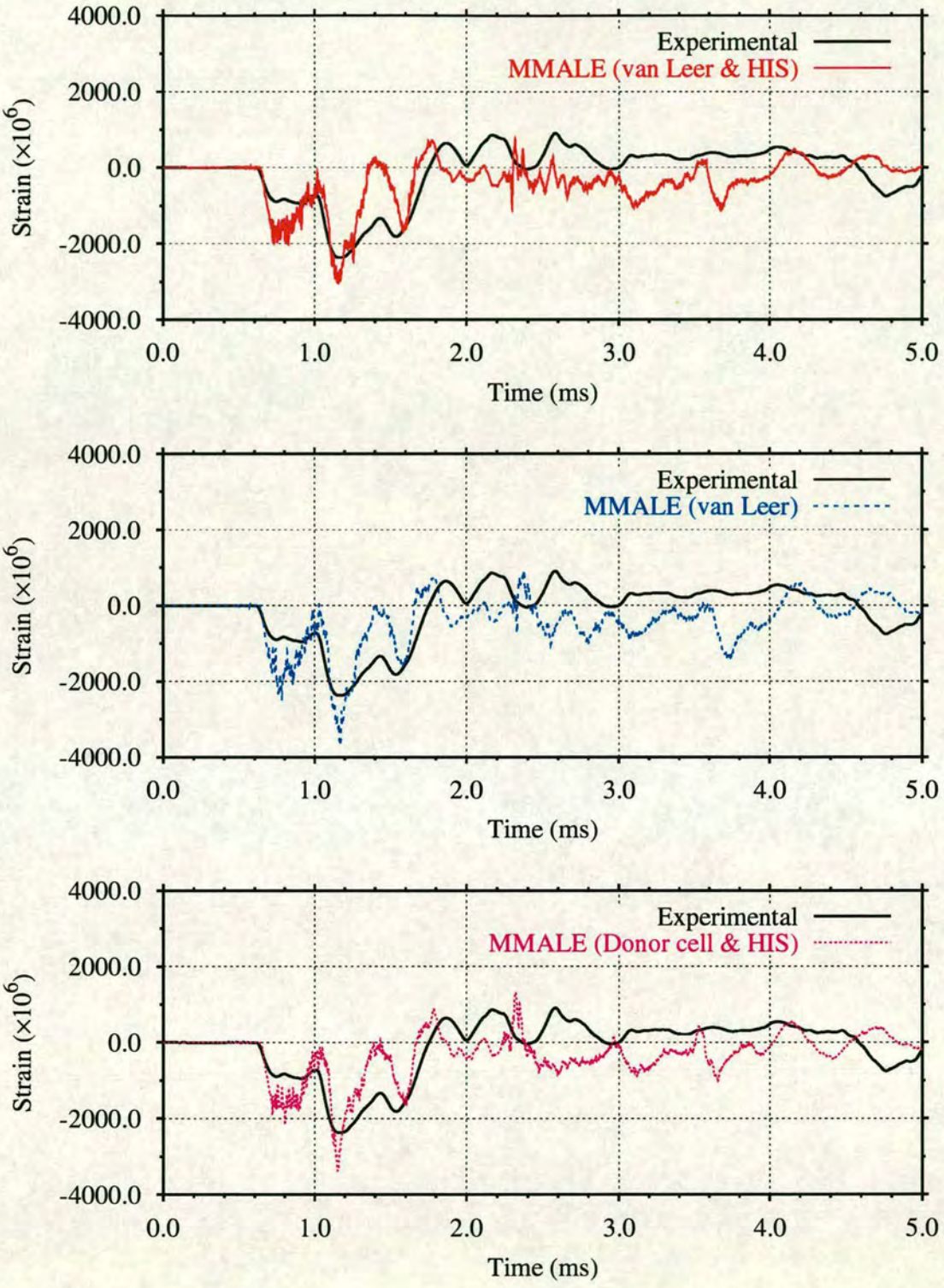

Figure 6.23: Comparison of MMALE predicted and measured meridional strain response at $\phi = 0^o$, $\theta = 0^o$ to 5g EDC-1 at 1.0m stand off (axisymmetric)

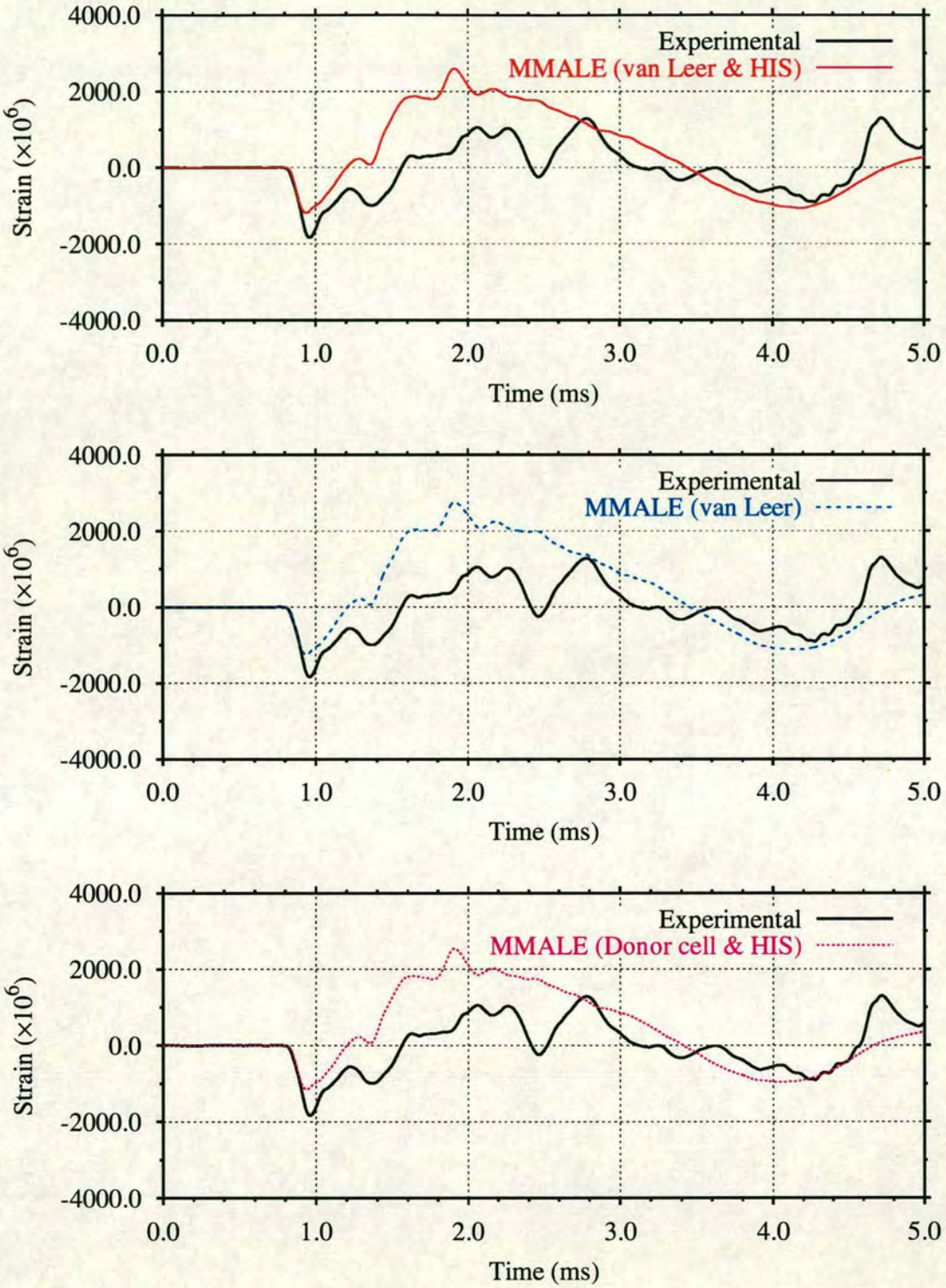

Figure 6.24: Comparison of MMALE predicted and measured circumferential strain response at $\phi = 150^o$, $\theta = 0^o$ to 5g EDC-1 at 1.0m stand off (axisymmetric)

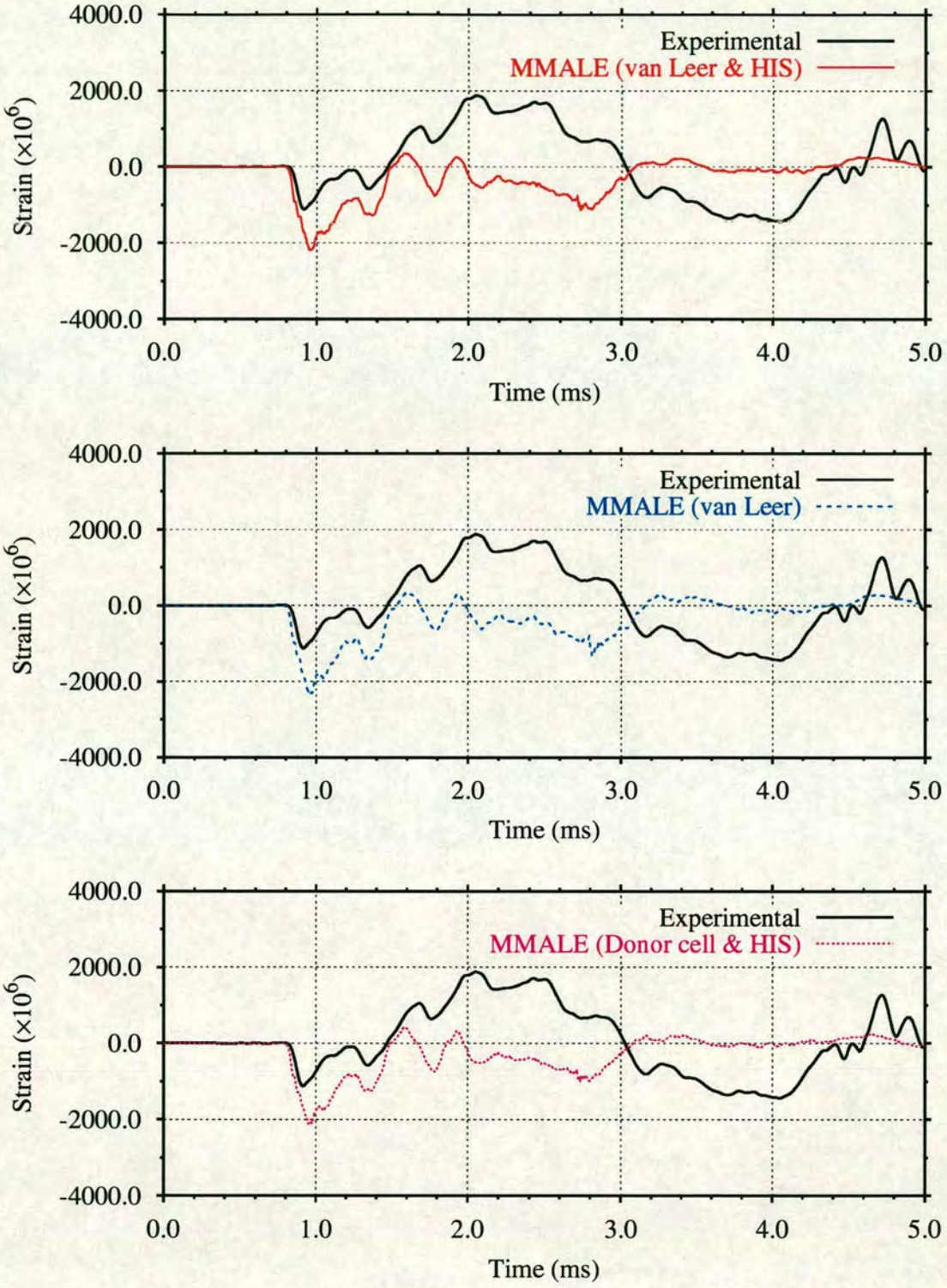

Figure 6.25: Comparison of MMALE predicted and measured meridional strain response at $\phi = 150^o$, $\theta = 0^o$ to 5g EDC-1 at 1.0m stand off (axisymmetric)

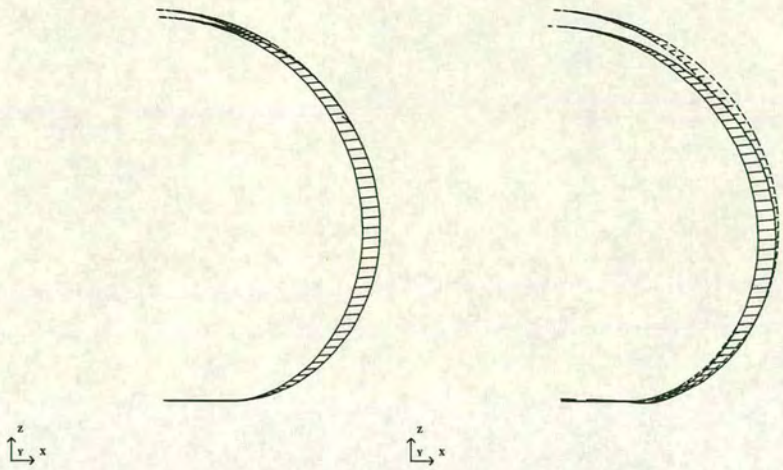

(a) t = 0.7ms (b) t = 1.0ms

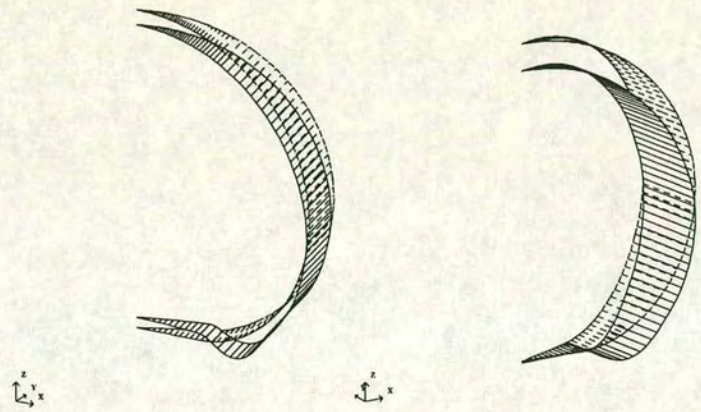

(c) t = 1.5ms (d) t = 2.5ms

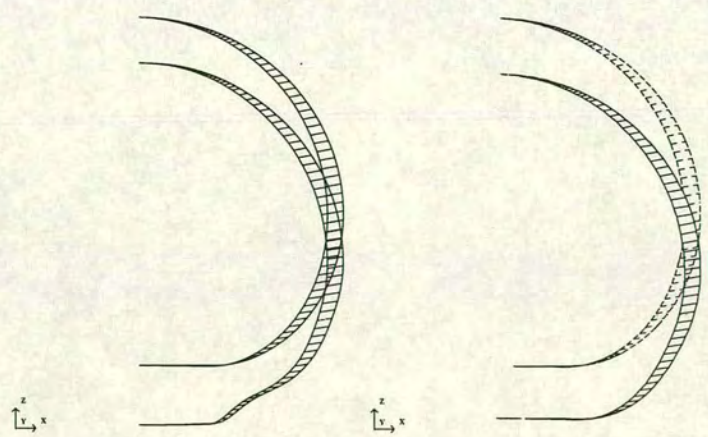

(e) t = 4.0ms (f) t = 5.0ms

Figure 6.26: MMALE predicted shell deformation under axisymmetric loading from 5g EDC-1 at 1.0m stand off (disp. $\times 20$)

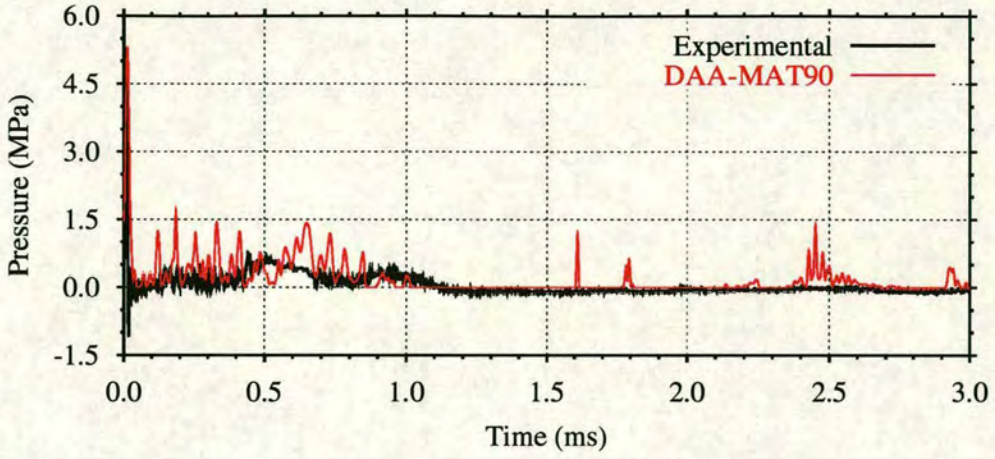

(a) $\phi = 0^o$, $\theta = 0^o$ (PG 1)

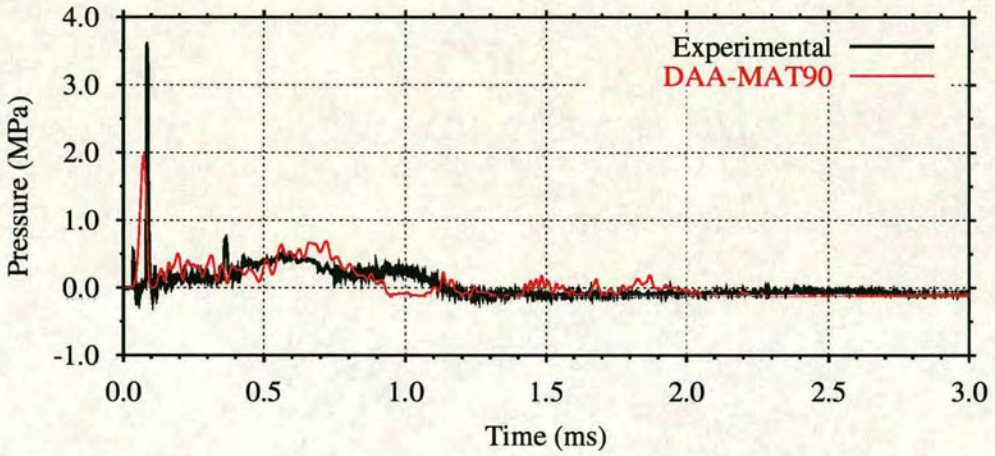

(b) $\phi = 45^o$, $\theta = 0^o$ (PG 2)

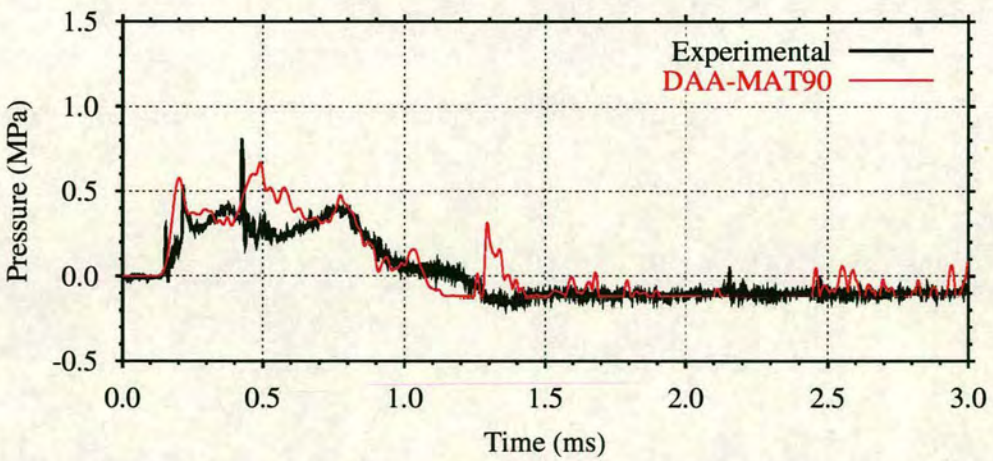

(c) $\phi = 90^o$, $\theta = 0^o$ (PG 3)

Figure 6.27: Comparison of DAA-MAT90 predicted and measured fluid responses at $\phi = 0^o - 90^o, \theta = 0^o$ to 5g EDC-1 at 1.0m stand off (axisymmetric)

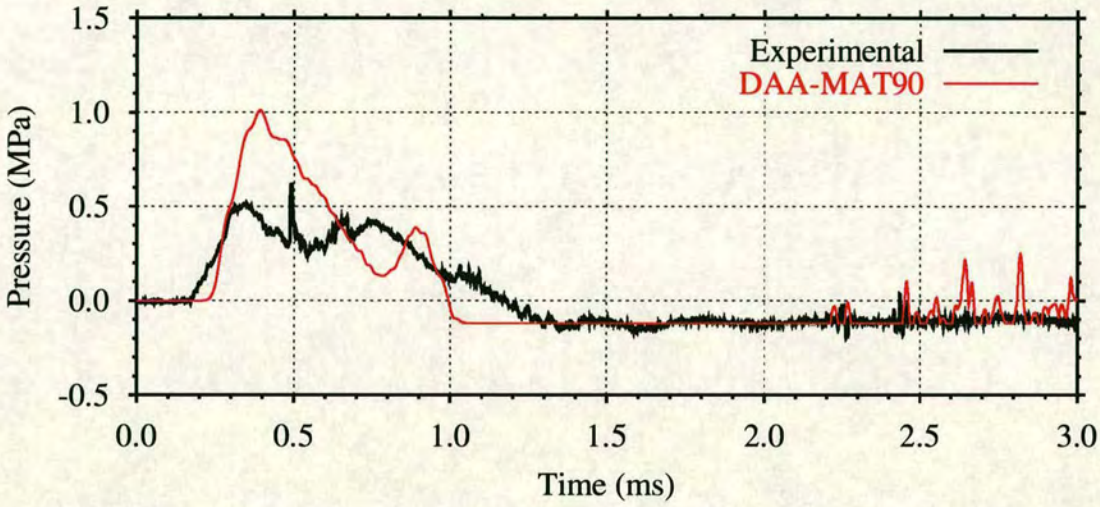

(a) $\phi = 135°$, $\theta = 0°$ (PG 4)

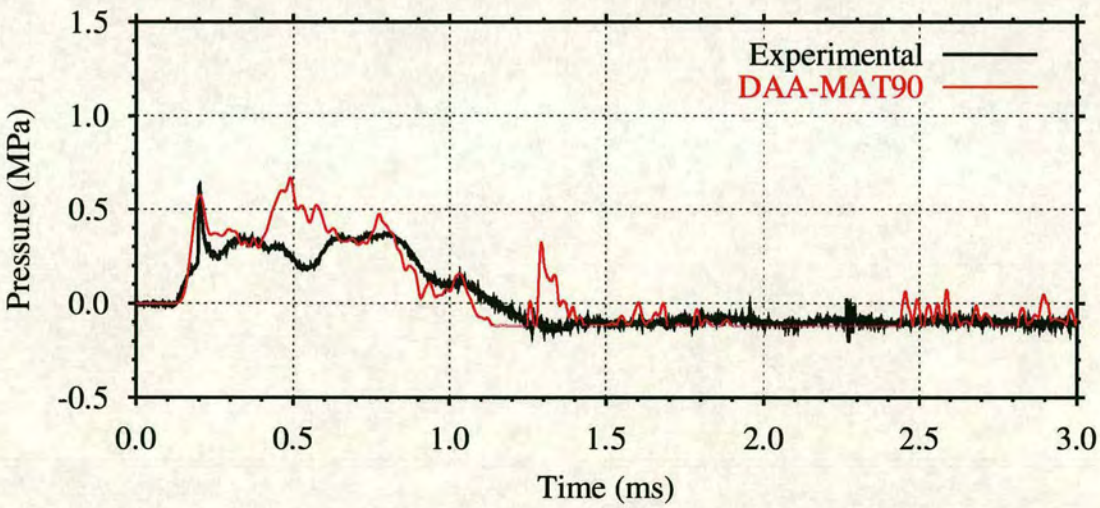

(b) $\phi = 90°$, $\theta = 180°$ (PG 6)

Figure 6.28: Comparison of DAA-MAT90 predicted and measured fluid responses at $\phi = 135^o, \theta = 0^o$ and $\phi = 90^o, \theta = 180^o$ to 5g EDC-1 at 1.0m stand off (axisymmetric)

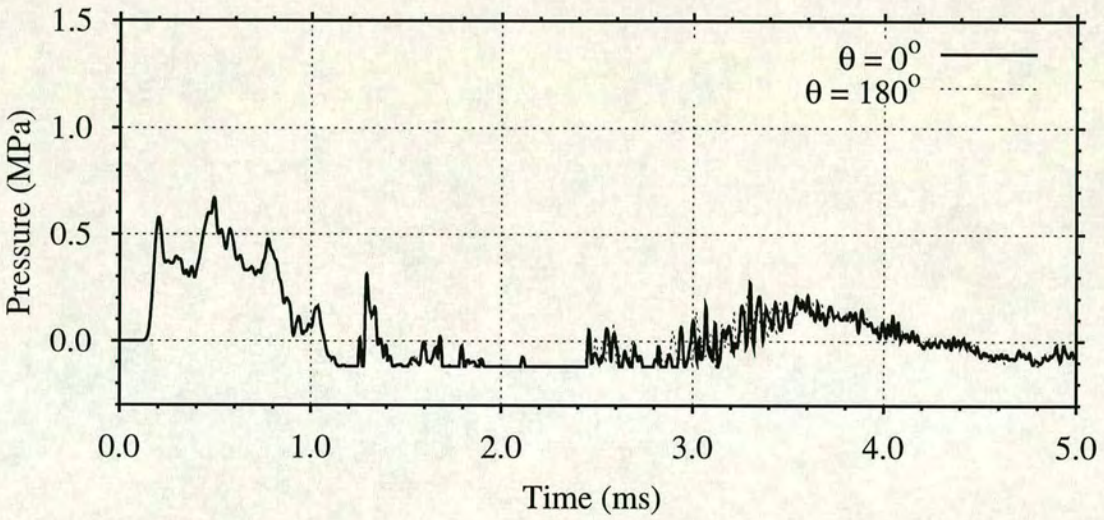

Figure 6.29: Axisymmetry of loading at $\phi = 90^o$ under axisymmetric loading from 5g EDC-1 at 1.0m stand off

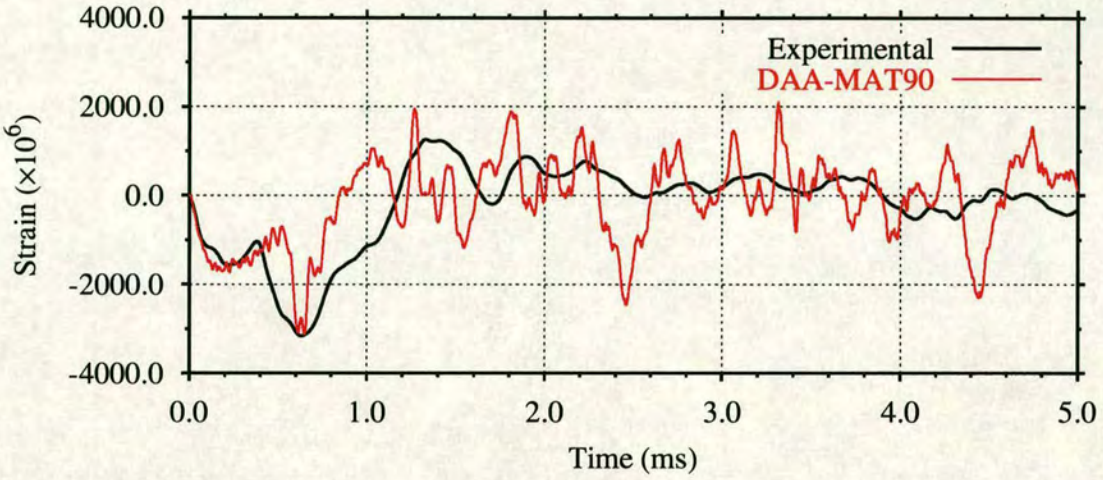

(a) DAA-MAT90 vs experiment

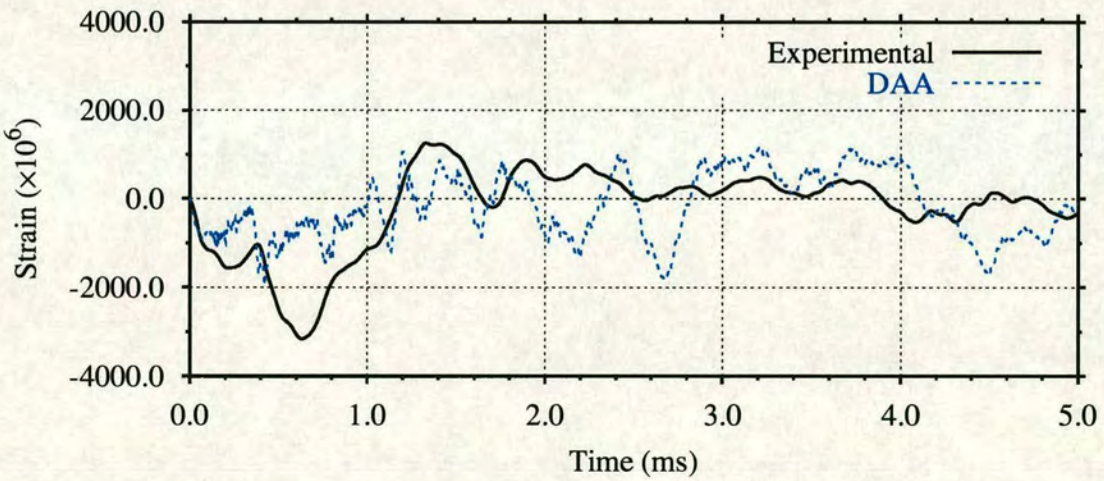

(b) DAA vs experiment

Figure 6.30: Comparison of predicted and measured circumferential strain response at $\phi = 0^o$, $\theta = 0^o$ to 5g EDC-1 at 1.0m stand off (axisymmetric)

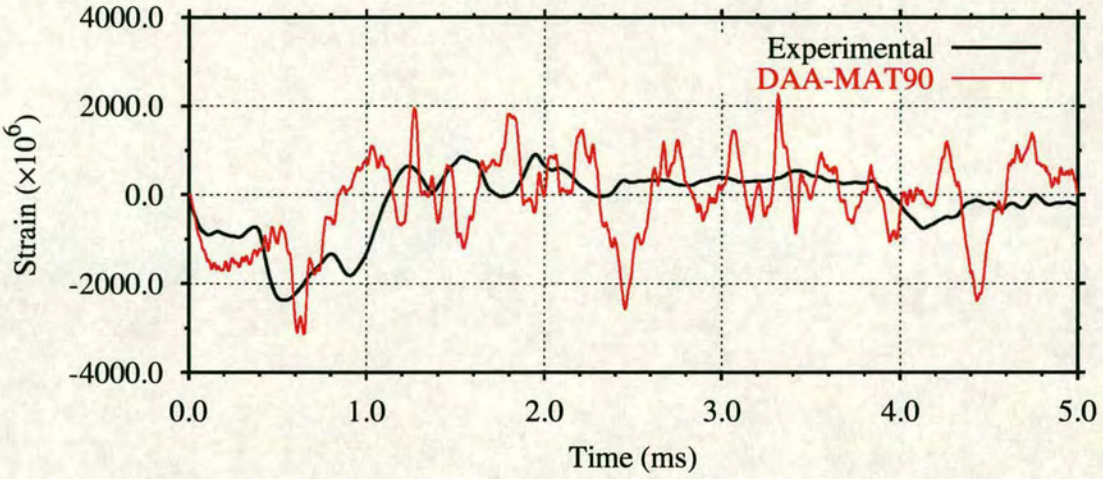

(a) DAA-MAT90 vs experiment

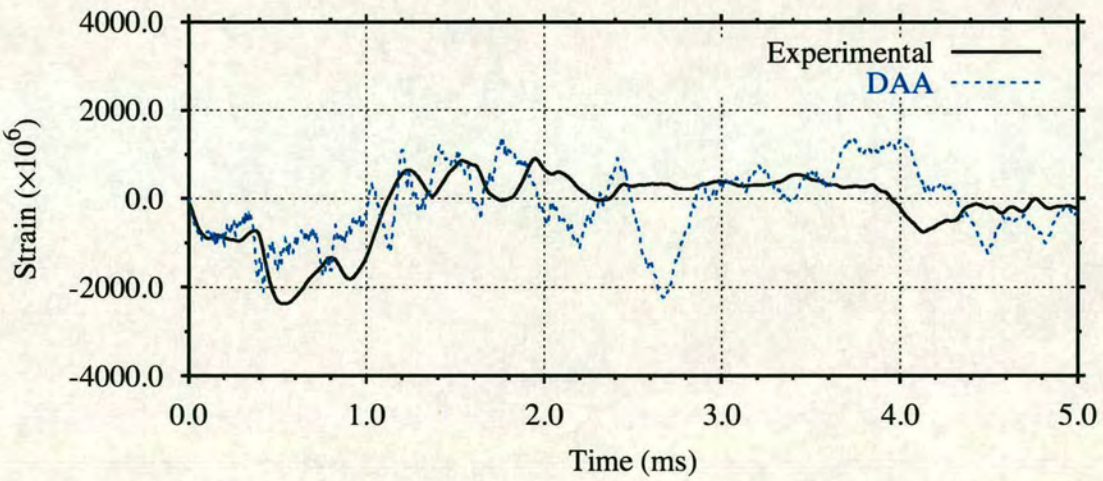

(b) DAA vs experiment

Figure 6.31: Comparison of predicted and measured meridional strain response at $\phi = 0^o$, $\theta = 0^o$ to 5g EDC-1 at 1.0m stand off (axisymmetric)

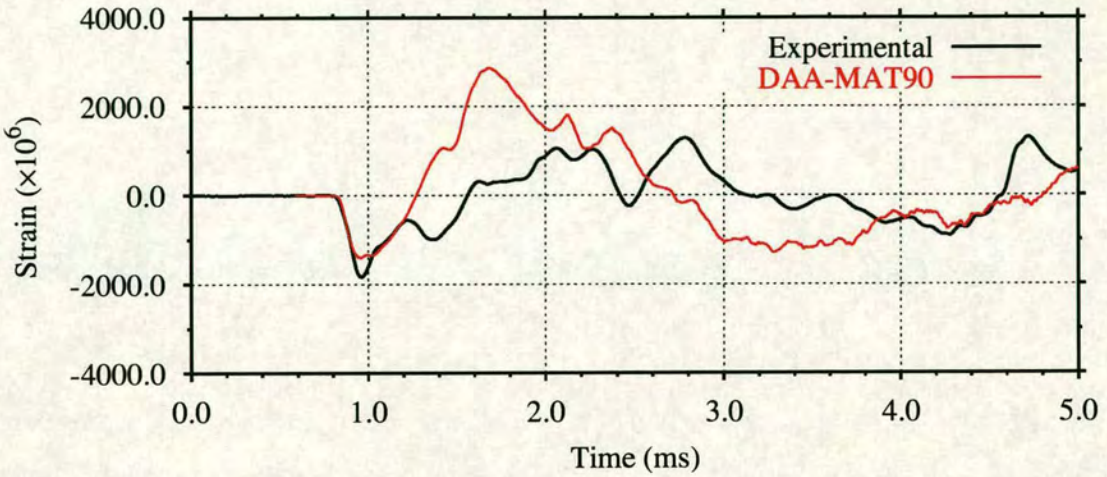

(a) DAA-MAT90 vs experiment

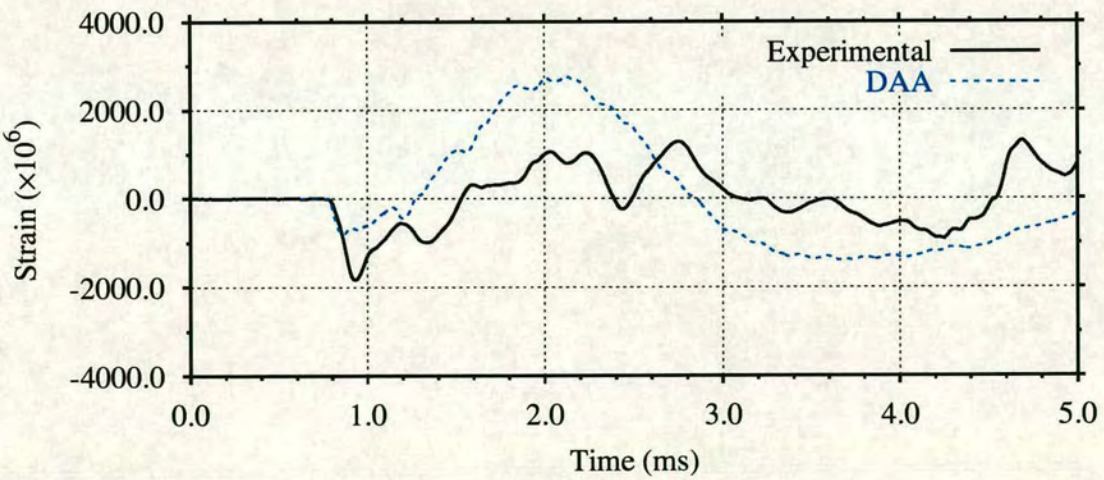

(b) DAA vs experiment

Figure 6.32: Comparison of predicted and measured circumferential strain response at $\phi = 150^o$, $\theta = 0^o$ to 5g EDC-1 at 1.0m stand off (axisymmetric)

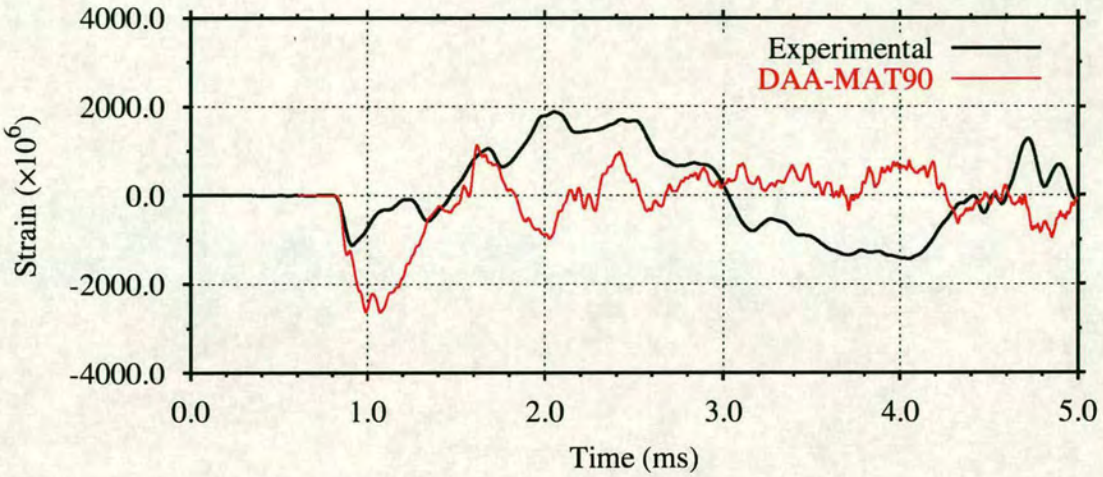

(a) DAA-MAT90 vs experiment

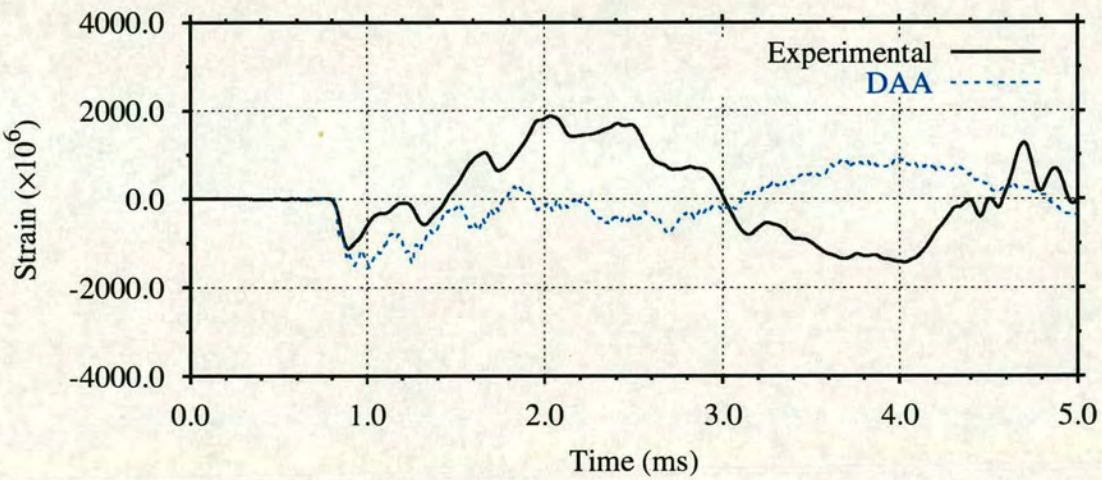

(b) DAA vs experiment

Figure 6.33: Comparison of predicted and measured meridional strain response at $\phi = 150^o$, $\theta = 0^o$ to 5g EDC-1 at 1.0m stand off (axisymmetric)

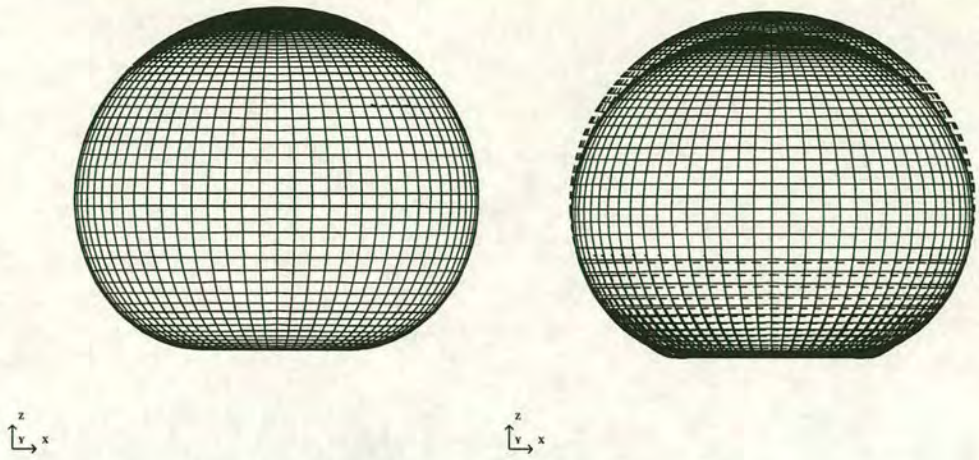

(a) t = 0.1ms

(b) t = 0.5ms

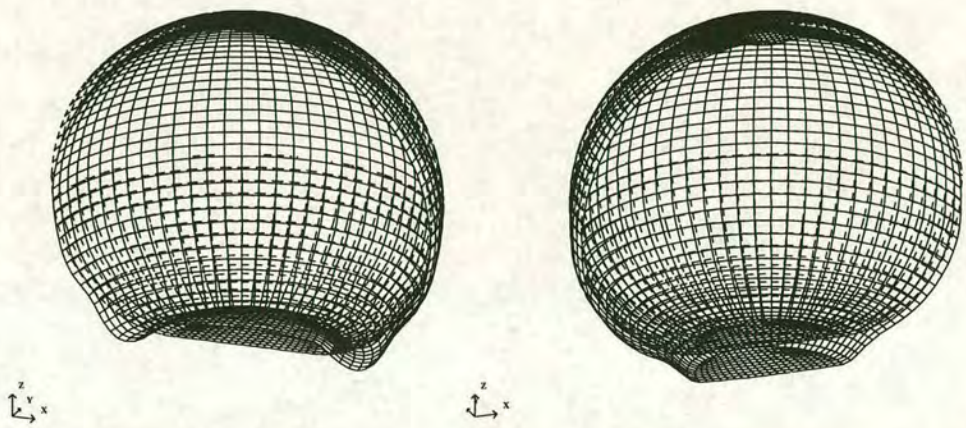

(c) t = 1.0ms

(d) t = 2.5ms

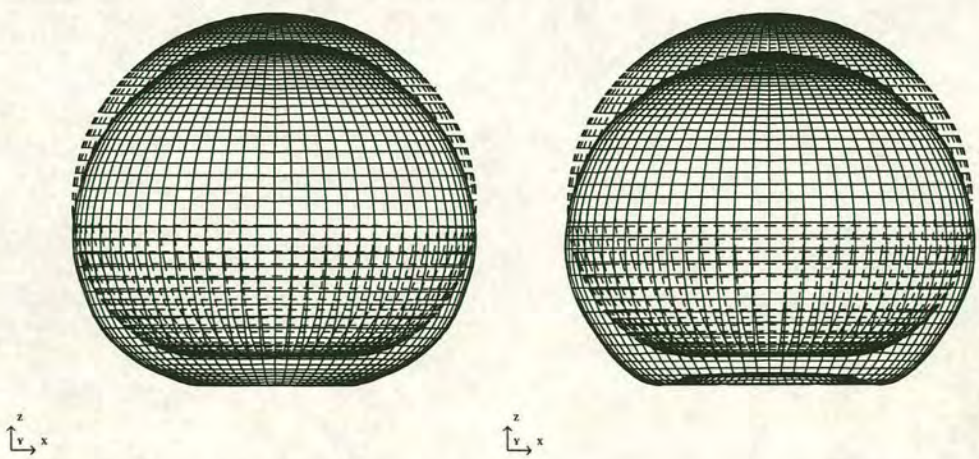

(e) t = 4.0ms

(f) t = 5.0ms

Figure 6.34: DAA-MAT90 predicted shell deformation under axisymmetric loading from 5g EDC-1 at 1.0m stand off (disp. $\times 20$)

Chapter 7

Dynamic buckling predictions under UNDEX loading

7.1 Introduction

Validation of LS-DYNA and USA-DYNA3D performed in chapter 6 concluded that neither DAA approach available through USA-DYNA3D could be used reliably to simulate symmetric UNDEX loading on the prototype echinodome. The shell response was underpredicted for a 2.0m stand off distance. As has been mentioned earlier the MMALE technique is not a practical approach to solving the symmetric load case owing to the current complexity of constructing and cost of analysing a suitable FE model.

The DAA approaches produced much improved results under axisymmetric loading. However, insufficient experimental free field pressure decay data is available for 5g and 10g EDC-1 charges to undertake a theoretical dynamic buckling analysis using the DAA approach. The MMALE model validated well for the axisymmetric UNDEX load case producing a shell response in good agreement with or, at some positions, an overprediction of experimental response.

Sufficient experimental data is available to determine dynamic buckling criteria for symmetric UNDEX loading using predictive techniques. For axisymmetric UNDEX loading evaluation of theoretical buckling criteria using the MMALE approach is possible.

Non-destructive techniques suitable for predicting dynamic buckling criteria from experimental or theoretical data are presented in this chapter. A buckling analysis is then performed on the experimental data obtained for the symmetric UNDEX load

cases. The numerical techniques suitable for making predictions from theoretical results are first evaluated for static and dynamic buckling assessments performed previously. The techniques are then adopted for a buckling assessment under axisymmetric UNDEX loading, performed using models modified from chapter 6.

7.2 Dynamic buckling

Thin spherical shells exhibit a high ratio of membrane to bending stiffness. Under compressive loads a considerable amount of membrane strain energy can be stored before large deformation occurs. The equivalent in bending strain energy would generate appreciable bending. When a shell is loaded, if the strain energy stored as membrane energy were to be transformed into bending energy then the shell could become unstable and undergo an overall change in configuration. Furthermore, it would cease to perform the primary function for which it was designed. Such changes to system behaviour are characterised by a sudden large increase in deformation when a critical load, and associated failure mode, is reached. Although the critical load and failure modes under dynamic loading may differ from those under static loading, similar behaviour may be observed which often leads to a reduction in load carrying capacity or structural failure. Under dynamic loading conditions this system behaviour is termed dynamic buckling.

The buckling process is determined by the form of applied loading and, geometrical and material properties. For perfect shells buckling can occur in one of two ways.

1. **Non-linear collapse** - also termed *snap through* or *limit load*, this is the point at which the load-deflection curve has zero slope, i.e. the structure has zero stiffness. It is usually predicted by means of a non-linear stress analysis.

2. **Bifurcation buckling** - the load at which the shell starts to deform with different behaviour from the pre-buckled state. These are termed post-buckling and pre-buckling paths respectively. Failure is said to have occurred if the post-bifurcation load-deflection curve has a negative slope, and the amplitude of deformation is independent of the applied load.

As a shell under loading buckles, different stages of deformation, known as deformation modes, are experienced. The first, or fundamental, deformation mode occurs at the lowest load termed the critical, or buckling, load. If bifurcation buckling occurs the deformation modes are orthogonal to those of the pre-buckled state and, consequently,

they are equal to zero throughout the pre-buckling path[86]. Once bifurcation buckling has occurred it can be categorised in four ways according to the structure.

1. **Neutral** - the load carrying capacity remains constant with increasing deformation, e.g. centrally loaded struts.
2. **Asymmetric** - the load carrying capacity can increase or decrease depending on deformation path, e.g. eccentrically loaded riveted sheets.
3. **Stable** - the load carrying capacity increases with increasing deformation, e.g. flat plates.
4. **Unstable** - the load carrying capacity decreases with increasing deformation, e.g. cylindrical or spherical shells.

For real structures failure by bifurcation buckling alone is unrealistic due to the presence of geometric imperfections which can have a strong influence on the collapse load. It is more likely that failure would be observed to progress through both the non-linear collapse and bifurcation buckling processes.

7.3 Estimating buckling loads

Experimental tests performed on complete spherical shells subjected to uniform external pressure revealed that buckling initiates at a point where a small dimple forms[86,87]. In an attempt to simplify the problem the classical buckling load of a spherical shell was compared to that of a spherical cap clamped at its edge. However it was concluded that, even for deep caps, the pre-buckling behaviour could never equal that of a complete spherical shell due to the presence of the edge boundary. Buckling was observed to occur at loads 80-90% of the classical shell value. Such work did, however, serve to highlight the sensitivity of initial imperfections affecting the load carrying capacity of shell structures[88].

A prediction of critical buckling loads on a structure, whether full size or scale model, can only be achieved accurately through well controlled experimental tests which are expensive and difficult to perform depending on the load under consideration. Observations made from experiments have assisted in the characterisation of buckling and led to the development of several non-destructive techniques for predicting critical loads of shell structures.

1. **Southwell plot** - Prediction of shell static buckling loads were initially extensions of investigations by Euler into the deformation of simple struts. This work led to the development of a method for predicting the theoretical buckling load, P_{cr}, of struts with initial imperfections, δ_o, by Southwell[89]. Southwell noted that for small deflection experiments, i.e. the deflections are small compared to the overall geometry, the lateral deflection at the centre of a uniaxially loaded strut, δ, is dominated by the fundamental deformation mode at loads approaching P_{cr} and is equal to the first term in the Fourier solution,

$$\delta = \frac{\delta_0}{\frac{P_{cr}}{P} - 1} \tag{7.1}$$

where,

δ_0 = initial geometrical imperfections; and
δ = deflection under load.

This can be rewritten to represent the equation of a straight line in a plot of $\frac{\delta}{P}$ vs δ whose inverse slope gives the critical load and it is known as the Southwell plot,

$$\frac{\delta}{P} = \frac{\delta}{P_{cr}} + \frac{\delta_0}{P_{cr}} \tag{7.2}$$

Eqn 7.1 mathematically describes the neutral post-buckling path of centrally loaded struts. This technique has been extended to the deflection of plane frameworks, plates and shells, all assuming small deflections occurred. Roorda[90] highlighted the importance of initial imperfections on the predicted critical load. Initial imperfections could be of such magnitude that displacements must be taken well beyond the small deflection range to obtain meaningful results. In doing so there was a danger of invoking non-linearities in the structure requiring care in the applicability and interpretation of the Southwell plot. If the initial imperfections were such that they encouraged positive or negative deflections to occur, the critical load could be over- or underpredicted respectively. Non-linearities were also argued to occur at low load levels due to inherent zero errors in the deflection[91] which prompted the use of the pivot point concept. This was found to increase data scatter in previous work on the echinodome[4] and consequently was rejected.

The Southwell plot has been used in previous predictions of static buckling loads for the echinodome with limited success[4]. Although overpredicting the critical

loads at most points, the base was correctly predicted as having the minimum P_{cr} value, and thus it was highlighted as a critical region. The applicability of the technique for predicting critical loads under dynamic loading such as UNDEX loads on the echinodome will be discussed later.

Several time-dependent techniques have been utilised specifically for predicting critical loads under dynamic loading[92,93] and have been used on a variety of structural systems[94,95].

2. **Equation of motion approach** - monitoring the structural response under increasing load levels, Budiansky and Roth[92] defined a critical load level step criterion in which a sudden increase in localised displacement response is observed. Under dynamic loading the displacement response is characterised by oscillations. At the stage where these oscillations experience a large jump the critical load has been reached and a local buckling load determined.

3. **Volume approach** - by replacing displacement with volume, a global buckling load could be determined for the prototype echinodome. The volume of an FE model can be traced in LS-DYNA using an airbag. The airbag is modelled geometrically using the parts comprising the FE model, hence no additional elements are required to physically represent the airbag. Time history data relating to the airbag can be output in a similar manner to nodal or element data.

4. **Phase plane approach** - localised system response parameters such as displacement can be described using their phase trajectory. The phase plane is the plane $\frac{dq(t)}{dt}$ vs $q(t)$, in which these trajectories lie, where $q(t)$ is the displacement. For loads smaller than the critical load, the system trajectory oscillates about a stable equilibrium point. At loads equal to or greater than the critical load the system trajectory passes through an unstable equilibrium point and the response is said to have undergone escaped motion.

Akkas and Jackson[96] observed that for dynamic buckling of a structure interacting with a fluid medium to be possible, the static load-deflection curve must have a limit point. A theoretical investigation revealed that such a point did exist for the prototype echinodome[12] thus allowing a dynamic buckling load to be determined. Akkas and Jackson utilised the Budiansky and Roth method[92], and the phase plane approach, to demonstrate when buckling was being observed with the FE method. Similar studies are reported elsewhere[97].

The validity of the above approaches for predicting buckling criteria is assessed for

Strain gauge no.	Linear regression model	Standard deviation (s)
SG 4	$y = 7.2 \times 10^{-5}x$	$\pm 3.3 \times 10^{-6}$
SG 6	$y = 8.6 \times 10^{-5}x$	$\pm 3.3 \times 10^{-6}$
SG 12	$y = 6.7 \times 10^{-5}x$	$\pm 2.0 \times 10^{-6}$
SG 14	$y = 3.2 \times 10^{-5}x$	$\pm 8.4 \times 10^{-6}$

Table 7.1: Linear regression analysis for SF vs $\mu\varepsilon$

theoretical response data of the echinodome under quasi-static and dynamic loading, acquired in previous analyses[4], and for the theoretical responses to UNDEX loading.

7.4 Experimental prediction

No data were available to permit use of the equation of motion or volume approaches. The phase plane approach could be utilised on existing data using the $\frac{d(\mu\varepsilon)}{dt}$ vs $\mu\varepsilon$ plane (where $\mu\varepsilon$ = microstrain), however, the shell response is well within the failure limit and hence no escaped motion would be observed. To obtain such data experimentally without overshooting the critical load would prove difficult. If such data did exist the bubble loading would be superimposed onto the response to shock loading rendering the phase trajectories difficult to interpret although an analysis of the individual shock and bubble phases would give an indication of the true response of the shell. Overall the applicability of the phase plane approach on making predictions from experimental data is in doubt.

The Southwell technique is thought to be suitable for predicting the critical stand off distance for the initial part of the shock phase of symmetric UNDEX loading on the shell. Plots of shock factor (SF) vs $\mu\varepsilon$, and $\frac{\mu\varepsilon}{SF}$ vs $\mu\varepsilon$, are shown for several positions in Figs 7.1 – 7.4. Initial peak compressive strains associated with the shock factor from each UNDEX load case were used as data for these plots. Under tensile strains, material delamination is the more likely mode of failure.

The linear regression models of table 7.1 are assumed to pass through zero as pre-trigger data obtained prior to the arrival of the shock wave is observed to oscillate about the zero strain level. The standard deviation is given for a 90% confidence interval. The quality of the linear fit between SF and $\mu\varepsilon$ was found to be excellent.

The results from the Southwell plots performed on each direction at each measuring

Position	Critical stand off (m)		
ϕ, θ	Circum.	Merid.	Oblique
$0^o, 0^o$	—	—	—
$30^o, 0^o$	—	—	—
$60^o, 0^o$	—	—	—
$60^o, 0^o$	—	—	—
$90^o, 0^o$	—	—	—
$120^o, 0^o$	—	—	—
$150^o, 0^o$ (ext.)	0.21	—	0.42
$90^o, 30^o$	—	—	0.033
$90^o, 60^o$	—	—	—
$90^o, 60^o$	—	—	—
$90^o, 90^o$	—	—	—
$90^o, 120^o$	—	—	—
$90^o, 150^o$	—	0.077	0.15
$90^o, 180^o$	—	0.13	0.23
$90^o, 270^o$	—	—	—
$150^o, 180^o$ (ext.)	0.18	—	—
$150^o, 180^o$ (int.)	X	X	X
$150^o, 180^o$ (int.)	X	X	X

— stiffening

X data corrupt or non-existent

Table 7.2: Predictions from Southwell plots for symmetric UNDEX loading

point are presented in table 7.2. The majority of the shell is observed to be stiffening, particularly on the near side of the shell. The critical positions predicted by the Southwell plot are noticeably the base on both the near and shadow sides, and the shadow side of the maximum diameter.

The critical stand off distance using 10g EDC-1 is estimated as 0.42m for a symmetric UNDEX load case. A peak experimental strain of -1921$\mu\varepsilon$ was recorded at the apex of the shell during the 2.0m symmetric load case. Using the shock factor relationship approach, similar to that used in appendix A, this peak strain would increase to approximately -9150$\mu\varepsilon$ at a stand off distance of 0.42m exceeding the static material failure strain. Using the same relationship the static material failure strain would be obtained with a 10g charge located at an estimated stand off distance of 0.61m.

The critical regions of the shell predicted by the Southwell plot are in agreement with previous observations. The initial load from the shock wave highlights the base region as the first area to fail by dynamic buckling. The shadow side of the shell at the maximum diameter has also been identified as being a critical area, although at a much closer stand off distance. However, as the stand off distance is reduced below 1.0m under symmetric UNDEX loading from 10g EDC-1, it can be concluded that the prototype shell would fail materially before failing due to dynamic buckling.

The complexity of the transient loading and dynamic response makes it impossible to capture one particular instant in time when maximum compressive peak strain occurs for every load case. Also, throughout an UNDEX event the loading is not only due to the impulse of the shock and the bubble but, for close stand off distances (10 – 20 $\times$ charge radius[15]) energy from afterflow also contributes a major portion of the load. This highlights limitations of using the Southwell method to characterise dynamic buckling resulting from time-dependent loading. As mentioned earlier, it is difficult to obtain reliable experimental data to use alternative methods, such as the phase plane approach, which take into consideration the dynamic nature of the response.

7.5 Theoretical predictions

Critical loads of the echinodome have been studied previously under various static and transient dynamic loads[4]. From this work collapse buckling loads under static and dynamic symmetric point loads were evaluated. It was found that linear static bifurcation buckling loads were in excess of non-linear static collapse loads and, consequently, bifurcation buckling under static loading was ignored. Step loading with infinite duration and zero ramping time was evaluated to be the most severe

dynamic load to be applied to the prototype shell and the dynamic collapse buckling load was concluded to be more critical than its static counterpart. The geometry of the echinodome was concluded to be too complex to estimate a dynamic bifurcation buckling load with any degree of reliability.

In an attempt to assess LS-DYNA's capability for predicting static and dynamic collapse buckling loads, the half symmetry echinodome model, developed in chapter 3, was subjected to increasing levels of quasi-static and dynamic loading in the form of ramped and step symmetric pressure point loads (see Fig. 7.5) applied normal to the surface at $\phi = 60^o$ from the apex. The buckling loads were predicted, using trial and error, to the nearest 250N and compared with those evaluated previously[4] to determine the best technique to use for estimating critical loads.

Subsequently, the MMALE pseudo-wedge model was utilised to predict a critical charge size under axisymmetric UNDEX loading at 1.0m stand off distance.

7.5.1 Buckling under point loads

Static loading

Under the ramped symmetric pressure point load at $\phi = 60^o$ there is evidence of geometric non-linearity. The displacement-time histories at the load point position and at $\phi = 150^o$, under various loads, are plotted in Fig. 7.6. An obvious change in shell response for half the structure is indicated beyond 8.0kN. The frequency of the oscillations associated with the normal displacement response reduces from 35Hz at 8.0kN to 7.14Hz at 8.25kN, and the oscillation range increases from $\pm 10\%$ to $\pm 20\%$ at both 60^o and 150^o. A marked reduction in the stiffness of the shell is observed, from Fig. 7.7, at 8.0kN. However, beyond 9.0kN, the shell is observed to stiffen again, highlighting the difficulty of tracking the nature of the response using applied load and a limitation of the material model used to represent the shell. Previously, a non-linear collapse load was evaluated using prescribed displacements and a point of zero stiffness on the load-deflection curve was reached beyond which the displacements were found to increase at much lower loads. Consequently, it would be more accurate to apply prescribed displacements and evaluate the reaction to determine the load at which zero stiffness is recorded. However, this approach is not suitable for UNDEX loading problems involving a distributed transient pressure loading and an irregular dynamic response and so will not be pursued here.

Tracing the volume using the airbag incorporated into the model provided supporting

evidence for the 8.0kN estimated from the mean displacement response at the load point. As Figs 7.8(a) and 7.8(b) show, a sudden reduction in mean volume is observed after this load. This jump comprises a reduction in volume of only 0.24% of the mean.

The phase trajectory for the displacement at the load point is shown in Fig. 7.9. Below the 8.0kN load the oscillations are observed to be regular and elliptical about the mean displacement. At 8.0kN a change in the elliptical nature of the oscillations is noticeable. However, it cannot be concluded that this is escaped motion as a sudden jump to an unstable equilibrium point is not possible with the elastic material model used.

As the same ramping time was being used for higher loads it was questioned if the increasing load rate was affecting the response of the shell. Thus ramping times of 100ms and 200ms were applied to the 8.0kN load. The volume-time histories are plotted in Fig. 7.10. It is clear that the loading rate does not affect the mean volume, merely the range of oscillations in the response.

From the equations of motion[92] and volume approaches the static collapse buckling load for the full shell, P_{sc}, is calculated to be twice the predicted load (since only half the shell was modelled), i.e., 16.0kN. The lack of evidence for zero stiffness makes it difficult to conclude from this approach that this is a reliable prediction of a non-linear static collapse load. However, it is interesting that the local and global values coincide. It is noted to be considerably higher than the value of 9.3kN predicted in earlier work[4]. The deformed shape under the estimated static critical load is shown in Fig. 7.11. The excessive deformation predicted at the load point evidently highlights this position as a critical region under ramped pressure point loading, in agreement with earlier predictions[4].

Dynamic loading

The shell response at the load point, $\phi = 60^o$, and at $\phi = 150^o$ to dynamic step loading is illustrated in Fig. 7.12. A sudden jump in the amplitude of the oscillations, indicating a change in the shell behaviour, is apparent after 6.5kN. In earlier investigations[4] the response after the critical load was characterised in a similar manner.

The mean normal displacement at the load point was observed to be higher than those obtained earlier[4]. Utilising the mean displacement of the shell response as a method of predicting a dynamic failure load was considered inaccurate as the ranges of the displacement oscillations are observed to increase with load and, consequently, the mean displacement may not increase proportionately resulting in an overprediction of the buckling load for dynamic step loading. A sudden increase in the range of

oscillations would be more indicative of a critical load. The load is plotted against the oscillation range and, as Fig. 7.13 shows, the rate of increase in shell response reaches a maximum at approximately 7.0kN.

A marked change in volume range with increasing step load is less clear. From Fig. 7.14 the volume range is observed to increase non-linearly with load, evidence that the shell is weakening up to a maximum of 7.25kN after which the volume range curve indicates uniform stiffness. At this load the mean volume has reduced by approximately 0.62%.

The phase trajectories for displacements at the load point, illustrated in Fig. 7.15, do not indicate any sudden change in shell behaviour as was observed for the quasi-static load case.

For the full shell the dynamic collapse buckling load, P_{dc}, is calculated to be 14.5kN. As with the static buckling analyses the lack of evidence for zero stiffness makes it difficult to conclude from the equations of motion approach that 13.0kN is a reliable prediction for the dynamic buckling load. However, this local value lies within the range of loads under which the volume is observed to increase non-linearly. The predicted load is noted to be higher than that predicted in earlier work[12], however the ratio of the dynamic to static collapse buckling loads, $\frac{P_{dc}}{P_{sc}}$ is 0.91, compared with 0.833 predicted earlier[12]. Fig. 7.16 illustrates the deformed shape under the estimated dynamic critical load.

It can be concluded from both the above static and dynamic buckling assessments that the volume and the equation of motion approaches are a reliable indicator for estimating local or global buckling loads. The applicability of the phase plane approach to predicting critical loads under dynamic loading is in question. The approach supported the buckling load predicted by the volume under the static loading but not under the dynamic step loading.

7.5.2 Buckling under UNDEX loading

The pseudo-wedge FE model of chapter 6 was adapted to incorporate various charge sizes ranging from 5g to 100g and an airbag was also included in the shell model to trace the changes in predicted volume with time. Both the volume and phase plane approaches were examined for predicting a critical charge size globally and locally for axisymmetric UNDEX loading. The phase plane approach described the phase trajectory of localised predicted strain responses at various positions on the $\theta = 0^o$ meridian using the phase plane, $\frac{d(\mu\varepsilon)}{dt}$ vs $\mu\varepsilon$.

A plot of a typical predicted volume-time history (volume normalised with initial volume, V_o) under a 25g charge is illustrated in Fig. 7.17. The minimum volume under shock loading was taken as representing the critical response for a particular charge size. The minimum normalised volume-load relationship for a range of charge sizes is plotted in Fig. 7.18 and it is clear that a sudden reduction in minimum volume is observed after a shock factor of $0.2449\text{kg}^{0.5}\text{m}^{-1}$ ($\equiv$ 60g). The minimum volume under a 60g charge is seen to have reduced by approximately 1.0%. This is greater than the reduction observed under the dynamic step loading suggesting that, due to the different nature of the loading, the shell can deform significantly more under UNDEX loading than under step loading before any sudden change in shell behaviour is observed.

The phase trajectories of predicted localised strain responses did not appear to support the critical charge size predicted by the volume-load curve. At no position was there any indication of escaped motion at 60g and similar phase trajectories were observed up to 90g, as Fig. 7.19 illustrates. However, at 100g the strain levels in the phase trajectories for $\phi = 60^o$ (not shown) and 90^o experience a sudden jump (see Fig. 7.20). Meanwhile, at these high loads the strain levels nearer the base are $\approx 32000\mu\varepsilon$, well beyond the failure strain of the material (-6295$\mu\varepsilon$).

In a further attempt to predict buckling criteria Southwell plots were produced for the positions $\phi = 90^o$ and 150^o. The results for $\phi = 90^o$ are shown in Fig. 7.21. Stiffening was indicated for the base region in the circumferential direction along with a very high critical charge size (> 10000kg) for the meridional direction. This stiffening is consistent with the lack of escaped motion predicted by the phase trajectory approach for the same position. At the maximum diameter the Southwell plot predicted a critical charge size of 350g for the circumferential direction compared with the onset of escaped motion at 100g shown by the phase trajectory approach. As mentioned earlier the Southwell plot only considers an instantaneous value of peak strain compared to the phase trajectory approach which considers the entire dynamic response of a local position. For this reason the phase trajectory approach could be considered a more reliable method for dynamic loading.

A limitation of the numerical model was highlighted when modelling larger charge sizes. To ensure the minimum volume had been calculated it was necessary to increase the analysis time from 5.0ms to 15.0ms. The radius of the bubble increases with charge size such that its expanding boundary intersects the free surface before the maximum radius has been reached. At this point the timestep in the analyses reduces by several orders of magnitude rendering the solution time impractical. In reality the bubble intersecting the free surface causes a plume of water to be thrown radially outwards. This is not possible under these boundary conditions (see section 4.5.1.3).

The boundary conditions at the free surface (vertical motion only) are only relevant for shock waves. When three materials are permitted in one element this will allow air to be modelled above the free surface giving the correct boundary conditions for both the shock wave and the bubble. Several analyses were attempted beyond 100g, however, the calculation had to be terminated before it could be ascertained if the minimum volume had been reached.

The use of the phase plane approach in determining critical loads under UNDEX loading conditions is limited owing to the material model used to represent the shell. The stable equilibrium point for the FE model of the prototype shell under UNDEX loading is the zero strain level. All phase trajectories exhibit either oscillations about the zero strain level or indicate a return to the zero strain level. The elastic material model cannot exhibit any escaped motion to an unstable equilibrium point as the material model assumes perfect elasticity independent of the nature of the loading. Even at high loads and high loading rates the response will always return to the zero strain level.

The local critical charge size predicted by the phase plane approach was expected to be lower than the global one predicted by the volume approach, as globally structures can generally sustain higher loads. It is possible that a lower critical charge size may have been observed had the phase trajectories for other elements, i.e., other positions on the shell, been examined. Taking the lower of the two predicted charge sizes as the critical charge size, at 60g the predicted strain levels are observed to exceed the static material failure strain. From the validation in chapter 6 the highest strain level was predicted to occur in the meridional direction for the apex, and thus this is taken for comparison against the static material failure strain. For 60g EDC-1 at 1.0m stand off distance the predicted peak strain is observed from Fig. 7.22 to be -12853$\mu\varepsilon$, well in excess of the static material failure strain. The predicted strain record in Fig. 7.23 suggests that the static material failure strain would be obtained with 20g EDC-1 at 1.0m stand off distance. Despite the limitations of the MMALE model it can be concluded from the above predictions that, under axisymmetric UNDEX loading at 1.0m stand off distance, the prototype shell will fail materially at the apex before buckling.

7.6 Conclusions

Dynamic buckling predictions for the prototype echinodome subject to symmetric and axisymmetric UNDEX loading have been undertaken using both experimental and numerical data. From the various non-destructive techniques utilised the following conclusions can be drawn regarding the critical buckling criteria for the shell.

Experimental tests of symmetric UNDEX loading from 10g EDC-1:

1. The Southwell plot highlighted the base and the shadow side of the maximum diameter as critical regions of the shell.
2. The base was predicted as more critical than the shadow side of the maximum diameter. A critical stand off distance of 0.42m was predicted before buckling would occur in the base region, compared to 0.23m at the maximum diameter.
3. At this predicted critical stand off distance 10g EDC-1 will generate strains well in excess of static material failure strain.
4. Strain levels are predicted to reach the static material failure strain in the base region at a stand off distance of 0.61m.

From experimental data the prototype shell is expected to suffer material failure before buckling occurs due to symmetric UNDEX loading from 10g EDC-1. The applicability of the Southwell plot is limited as it only considers the shell response at a particular instant in time. For this work the peak response upon arrival of the shock wave was used.

Numerical simulation of axisymmetric UNDEX loading at a stand off distance of 1.0m:

1. The volume approach predicted that, geometrically, the shell is able to withstand loads up to a charge size of 60g EDC-1 prior to global buckling occurring. For 60g the volume is observed to reduce by 1.0%.
2. At 1.0m stand off distance 60g EDC-1 would generate strains well in excess of static material failure strain.
3. Strain levels are predicted to exceed the static material failure strain at the apex for 20g EDC-1 at 1.0m stand off.
4. The phase plane approach predicts a higher buckling charge size than the volume approach. Evidence of escaped motion is observed for $\phi = 60^o, 90^o$ and 150^o at 100g EDC-1.

Limitations of the elastic material model chosen from LS-DYNA to represent the GRP material of the shell put the predictions by both the phase plane and volume approaches into question. However, the results do indicate that under axisymmetric UNDEX loading at 1.0m stand off distance the shell is expected to fail materially before buckling occurs.

Under dynamic loading the results, and comparisons with available data, suggest that a combination of the volume approach, and either the equations of motion or phase plane approaches, could be used to establish dynamic buckling criteria for theoretical models.

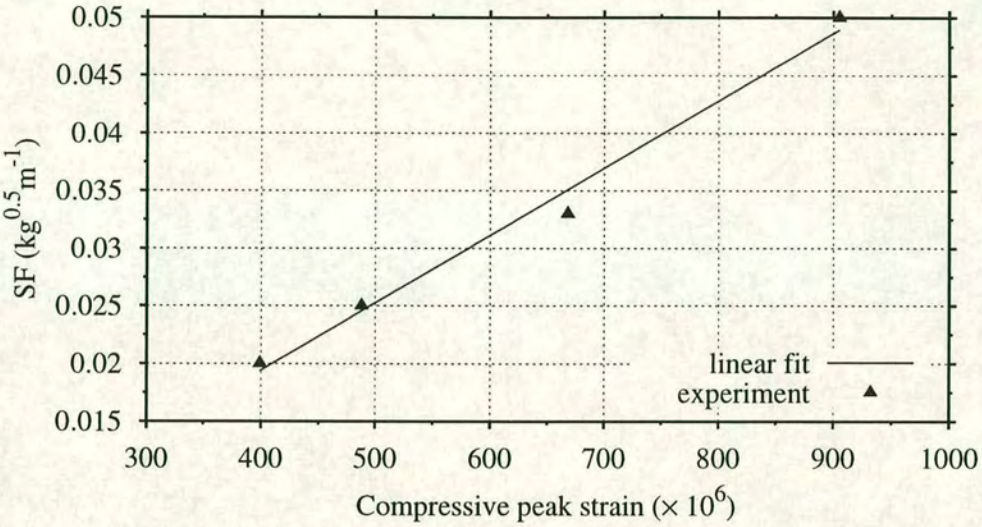

(a) Shock factor vs $\mu\varepsilon$ for $\phi = 90^o, \theta = 0^o$

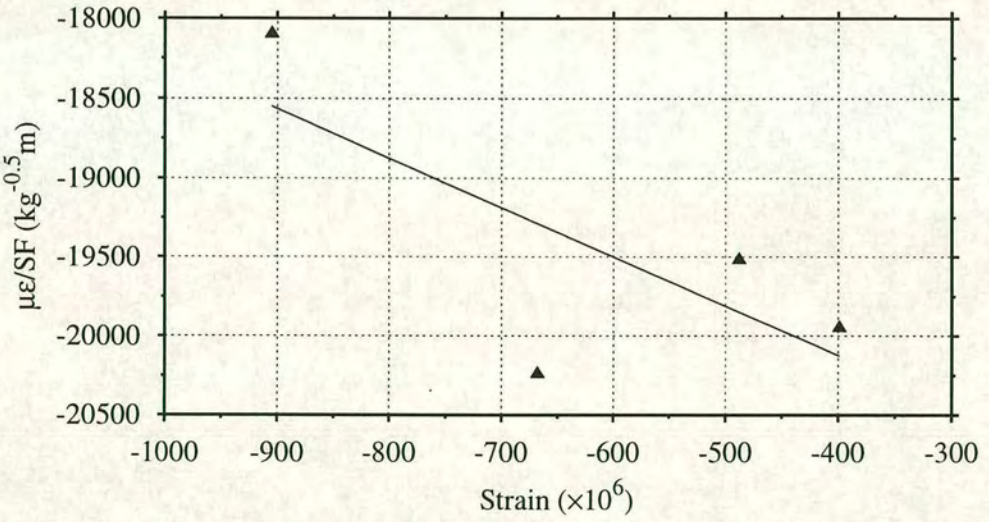

(b) Southwell plot for $\phi = 90^o, \theta = 0^o$ (tension positive)

Figure 7.1: Predicted buckling at $\phi = 90^o, \theta = 0^o$ (meridional direction) under 10g EDC-1 symmetric UNDEX loading – ***Stiffening***

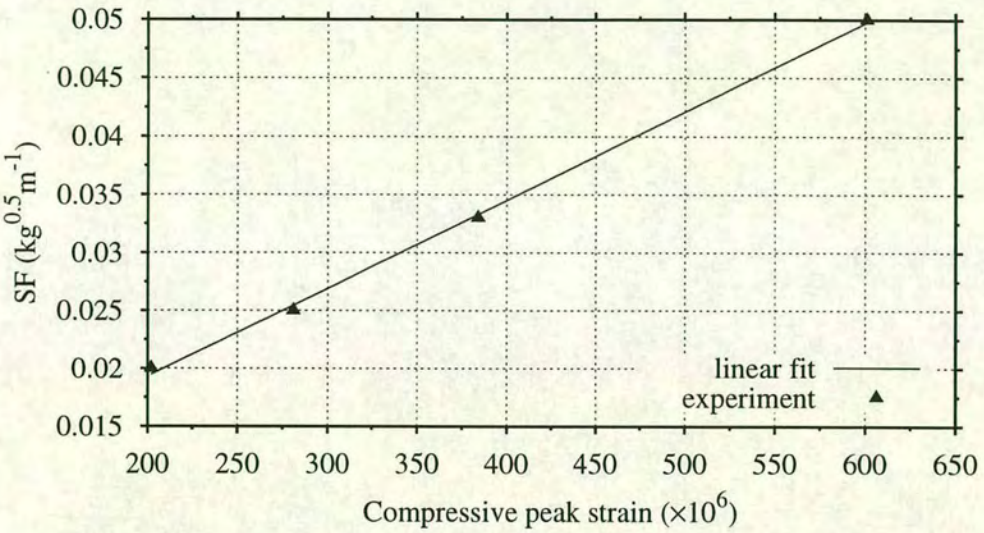

(a) Shock factor vs $\mu\varepsilon$ for $\phi = 150^o, \theta = 0^o$

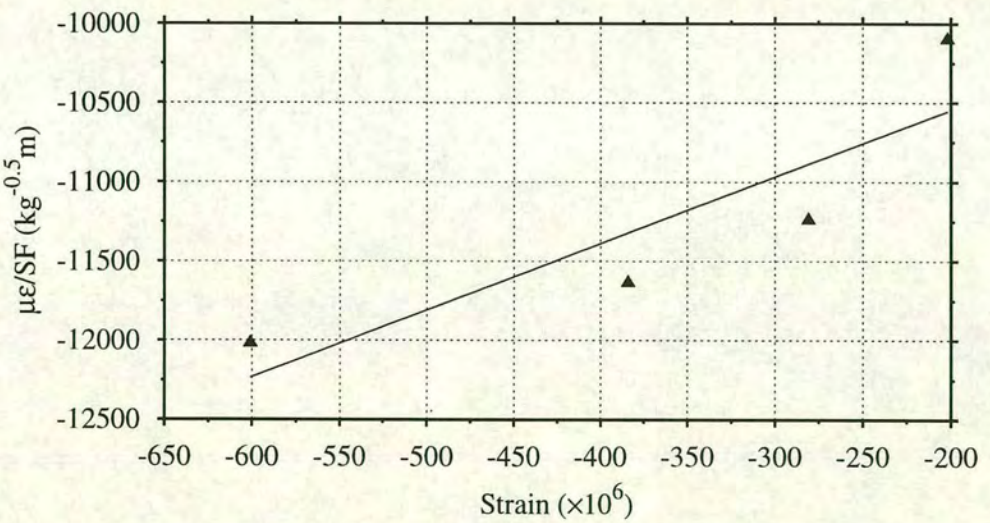

(b) Southwell plot for $\phi = 150^o, \theta = 0^o$ (tension positive)

Figure 7.2: Predicted buckling at $\phi = 150^o, \theta = 0^o$ (oblique direction) under 10g EDC-1 symmetric UNDEX loading – ***Critical stand off = 0.42m***

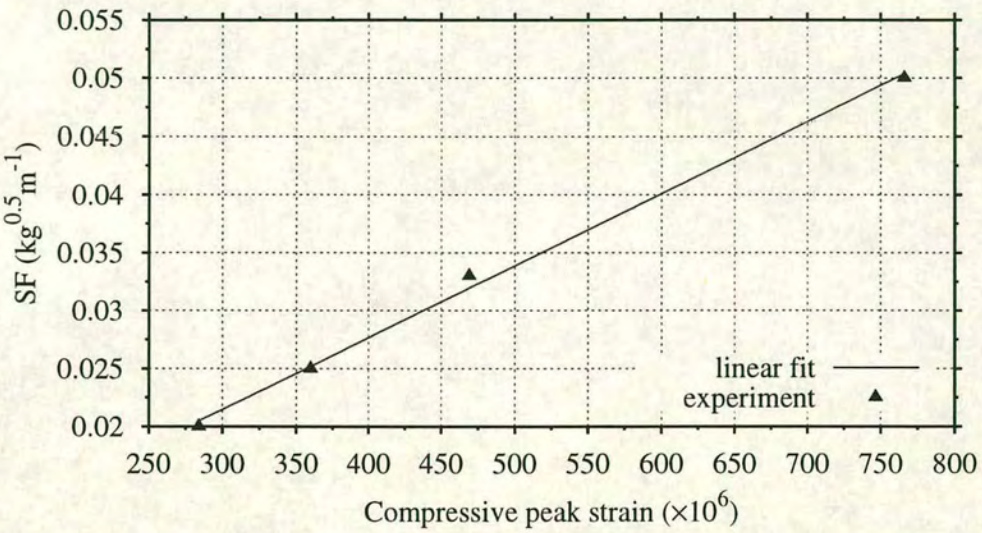

(a) Shock factor vs $\mu\varepsilon$ for $\phi = 90^o, \theta = 180^o$

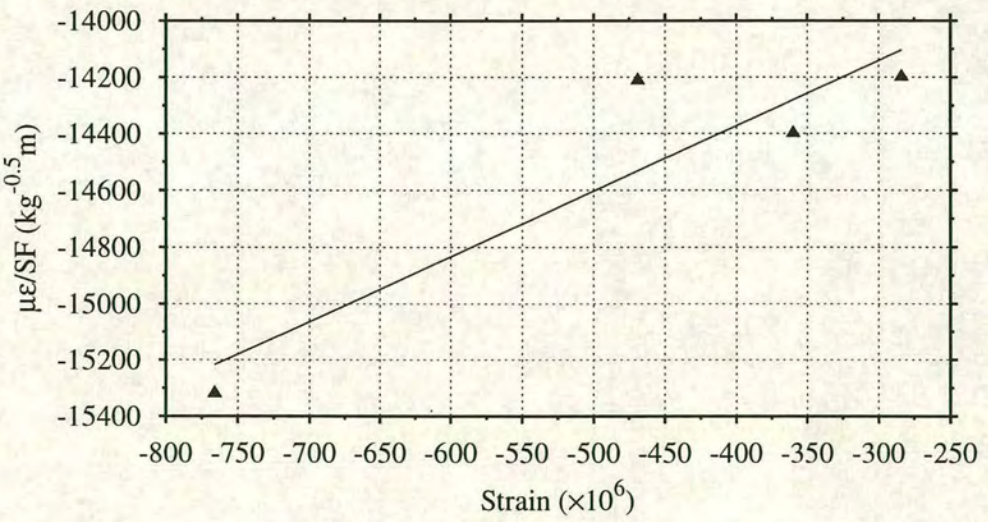

(b) Southwell plot for $\phi = 90^o, \theta = 180^o$ (tension positive)

Figure 7.3: Predicted buckling at $\phi = 90^o, \theta = 180^o$ (oblique direction) under 10g EDC-1 symmetric UNDEX loading – ***Critical stand off = 0.23m***

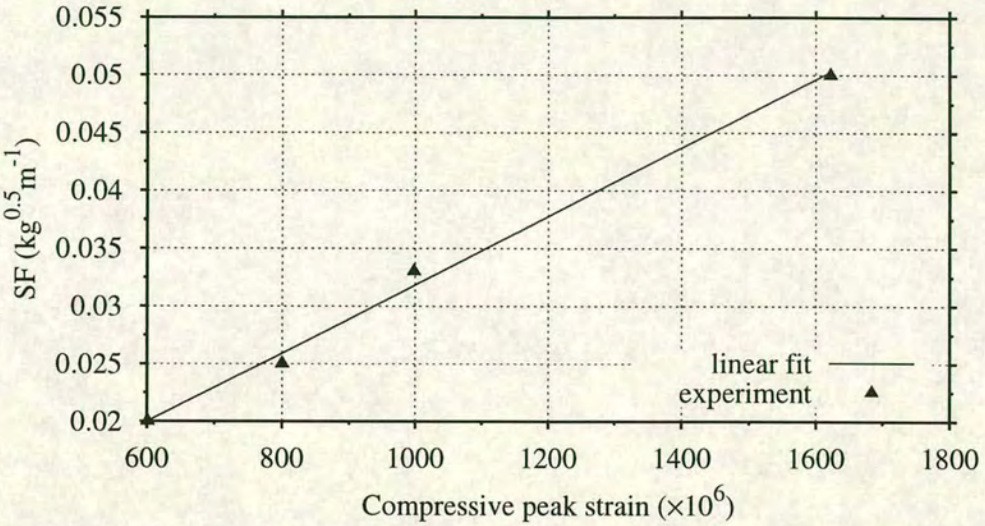

(a) Shock factor vs $\mu\varepsilon$ for $\phi = 150^o, \theta = 180^o$

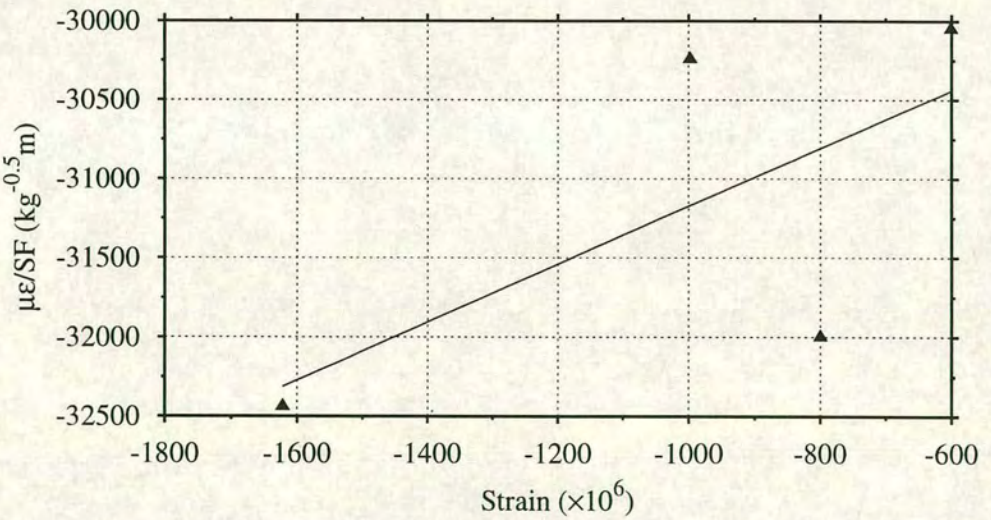

(b) Southwell plot for $\phi = 150^o, \theta = 180^o$ (tension positive)

Figure 7.4: Predicted buckling at $\phi = 150^o, \theta = 180^o$ (circumferential direction) under 10g EDC-1 symmetric UNDEX loading – ***Critical stand off = 0.18m***

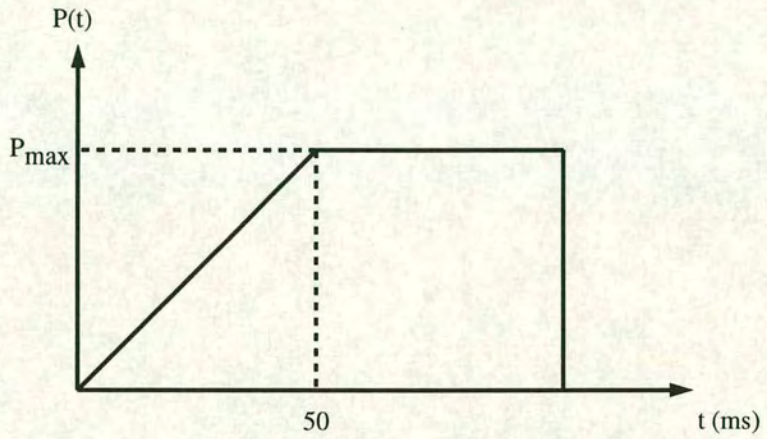

(a) Quasi-static ramped load

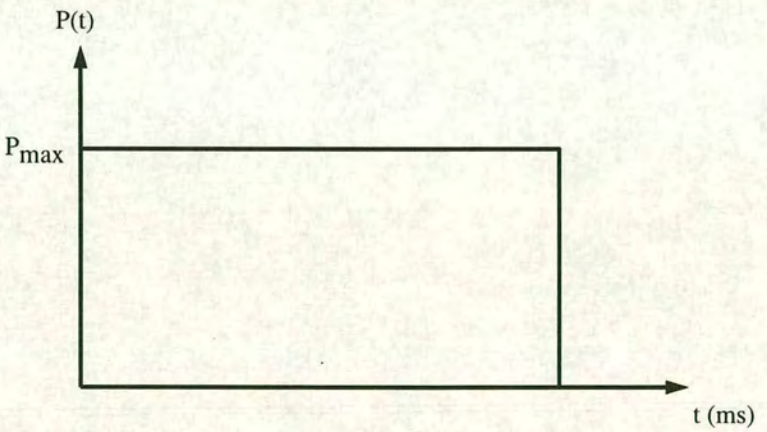

(b) Dynamic step load

Figure 7.5: Quasi-static and dynamic point loading configurations

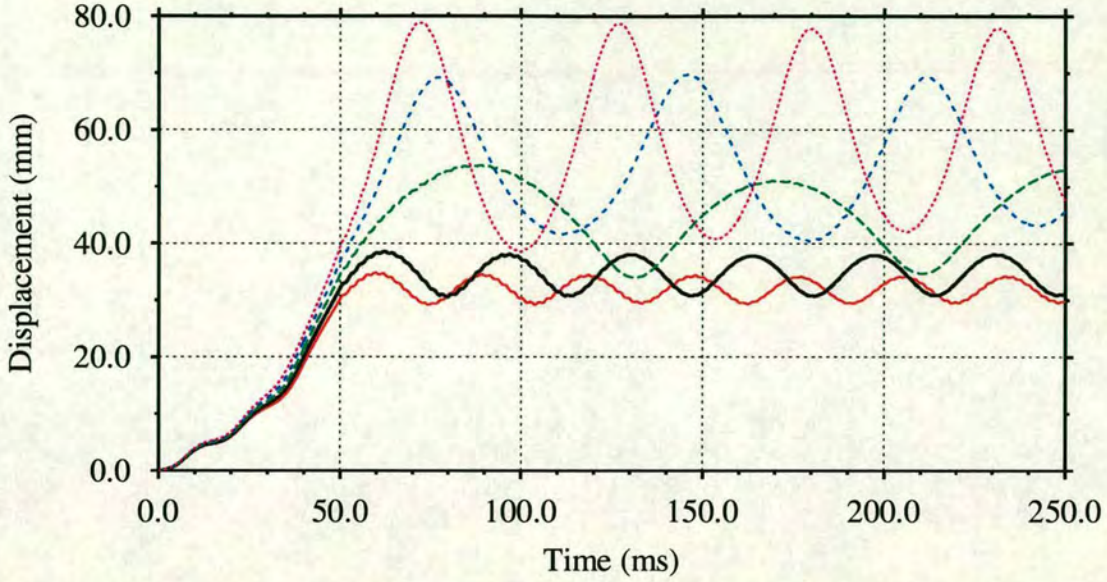

(a) Load point ($\phi = 60^o$)

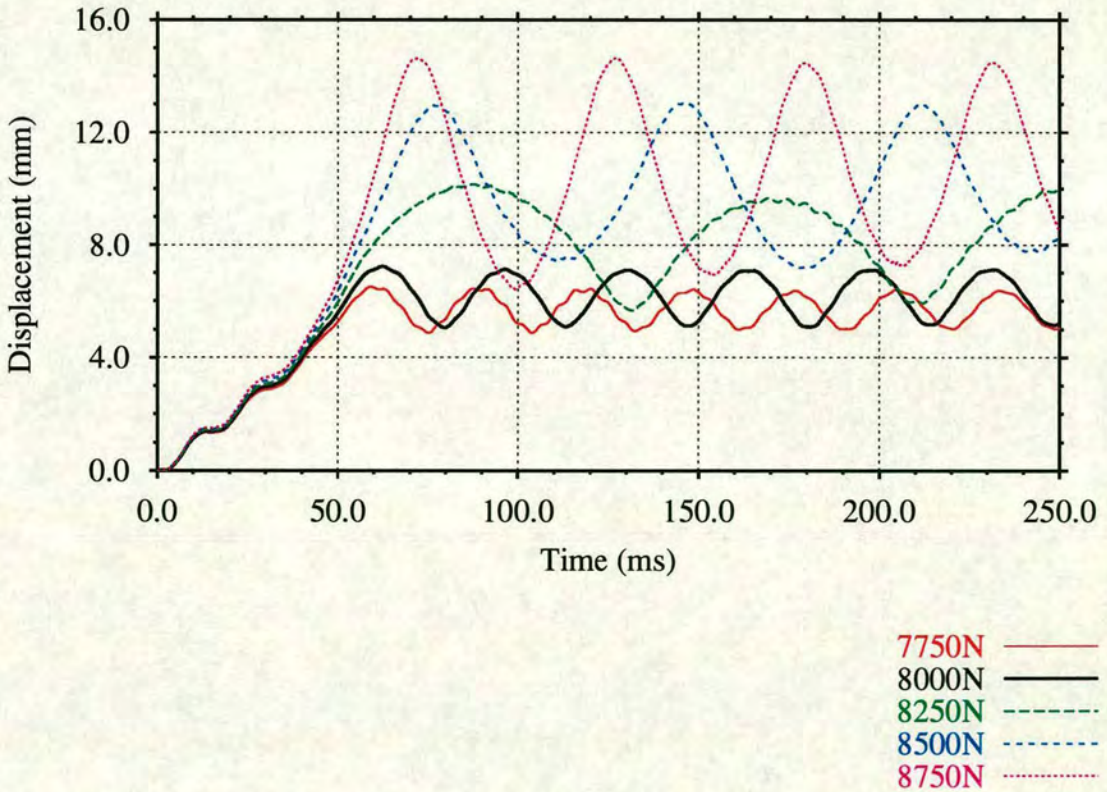

(b) Base ($\phi = 150^o$)

Figure 7.6: Normal displacement responses to quasi-static ramped loading applied at $\phi = 60^o, \theta = 0^o$

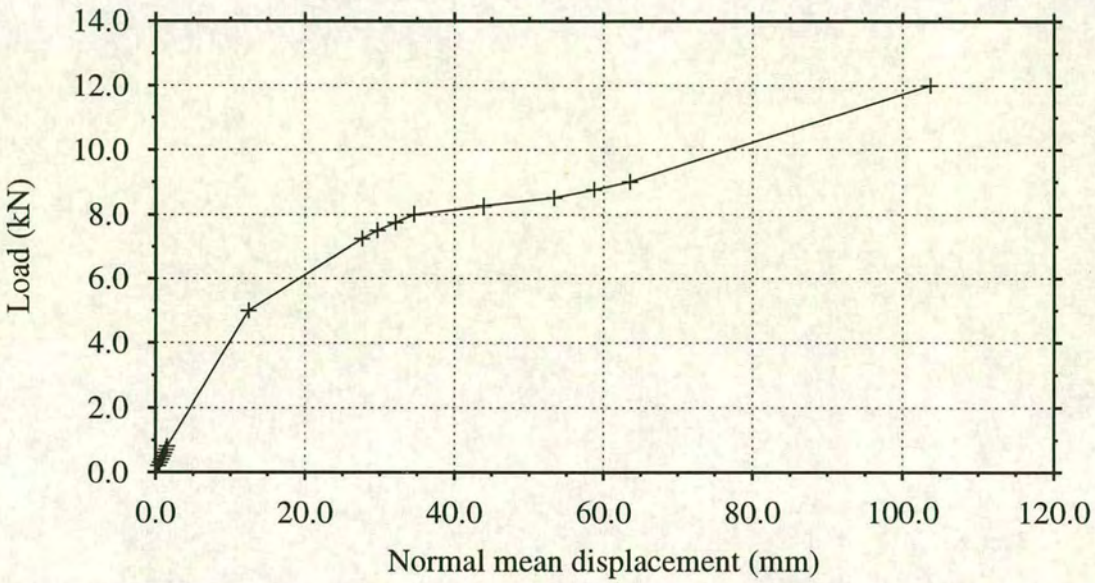

Figure 7.7: Load vs normal mean displacement at load point for quasi-static ramped loading applied at $\phi = 60^o, \theta = 0^o$

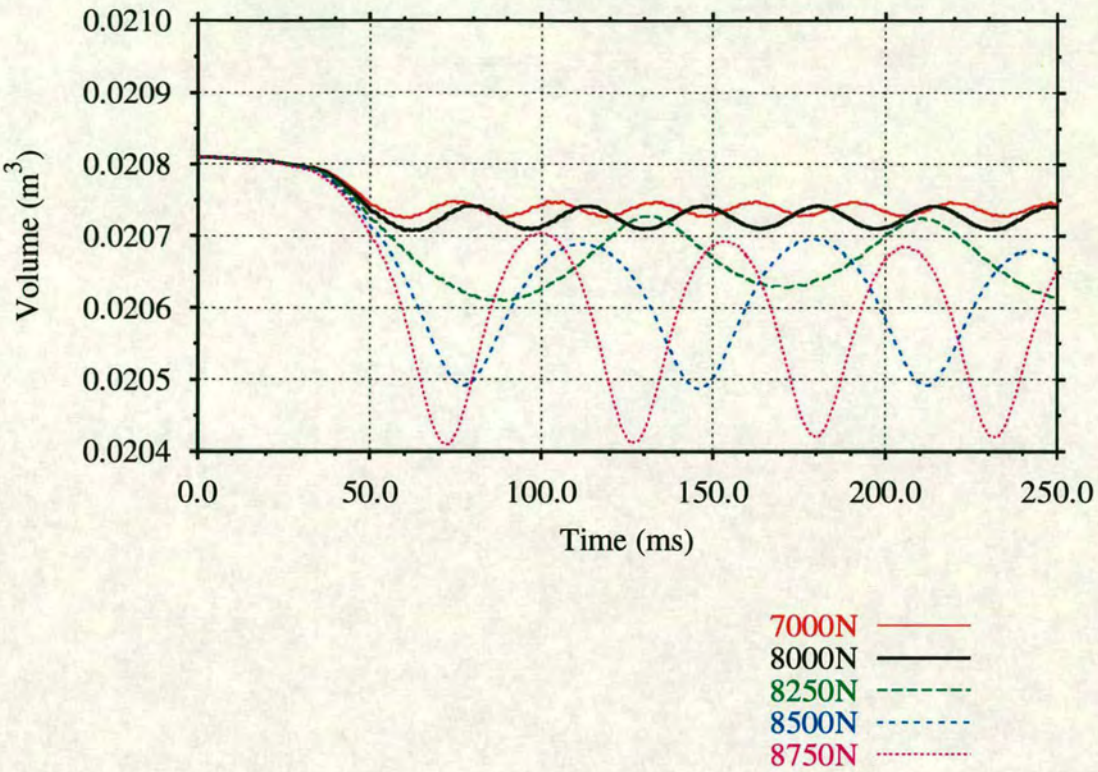

(a) Volume response

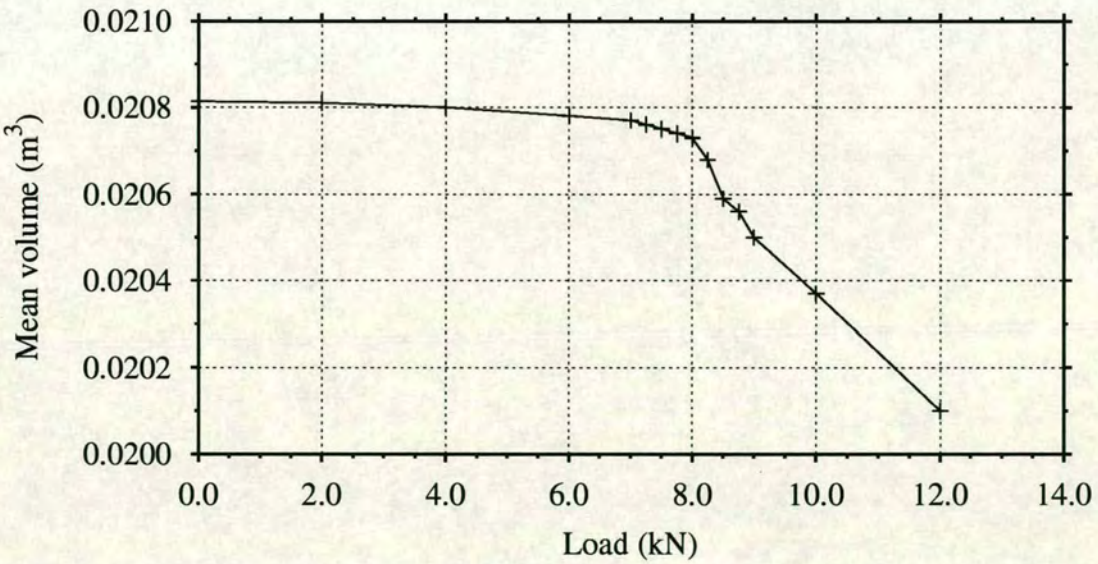

(b) Volume vs load

Figure 7.8: Volume response to quasi-static ramped loading applied at $\phi = 60^o, \theta = 0^o$

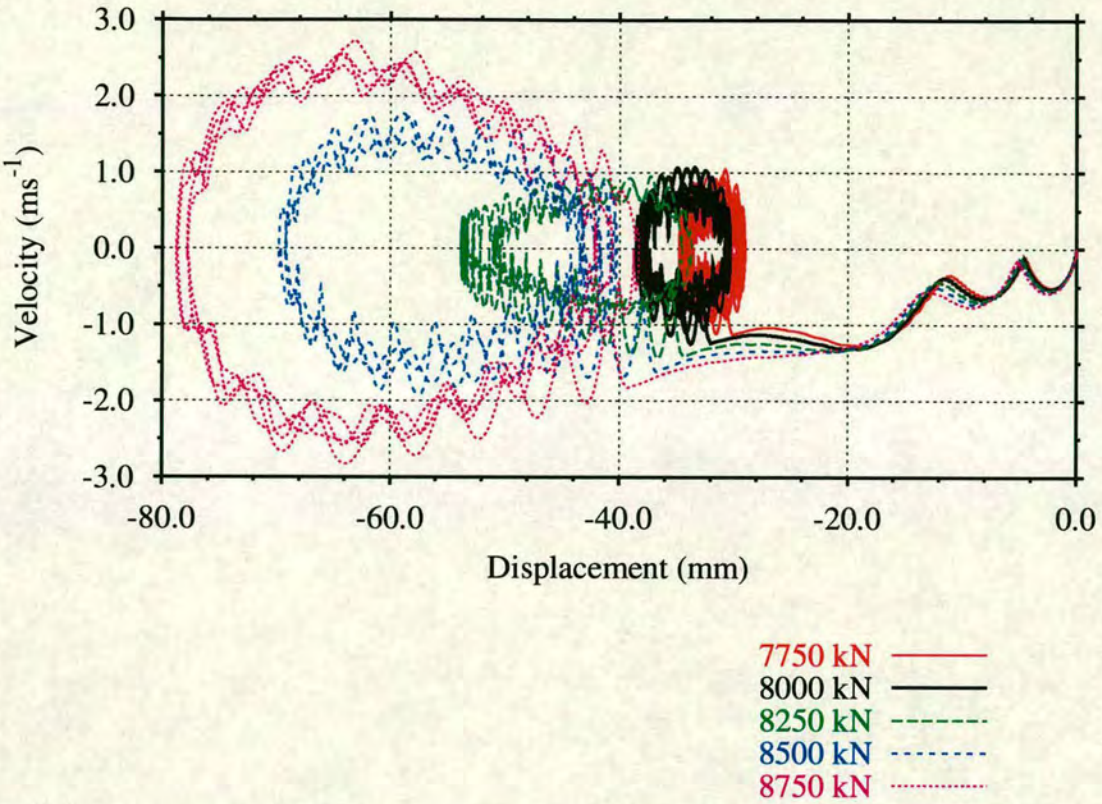

Figure 7.9: Normal displacement (outwards positive) phase trajectories to quasi-static ramped loading applied at $\phi = 60^o, \theta = 0^o$

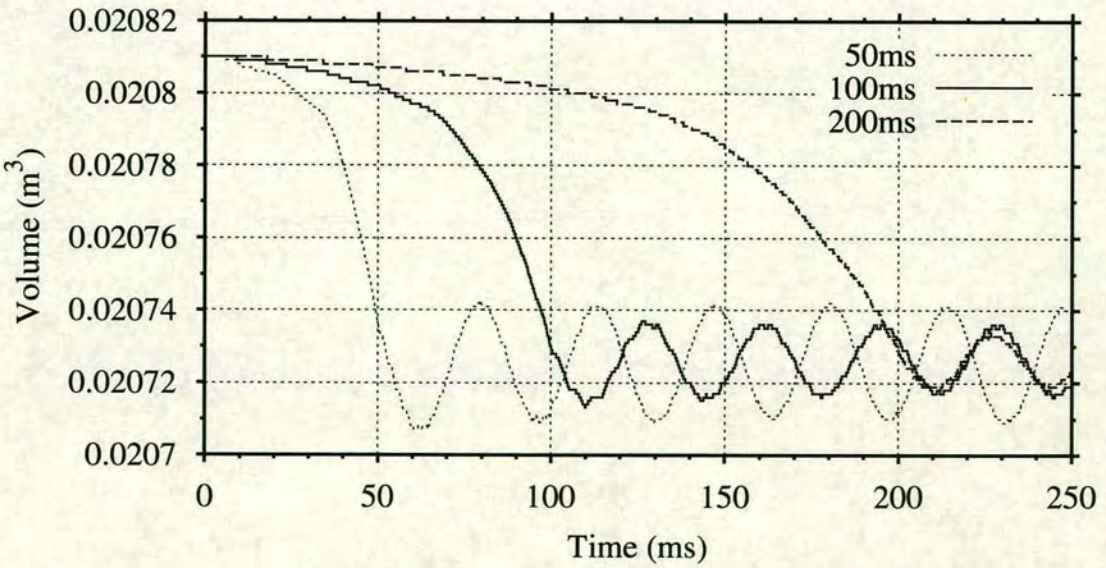

Figure 7.10: Effect of ramping time on volume response

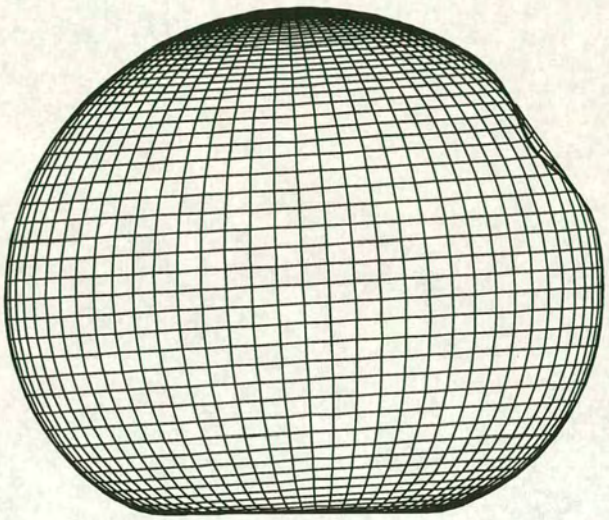

Figure 7.11: Non-linear static collapse deformation for quasi-static ramped loading applied at $\phi = 60^o, \theta = 0^o$ – ***Limit load = 16.0kN*** (disp. $\times 1$)

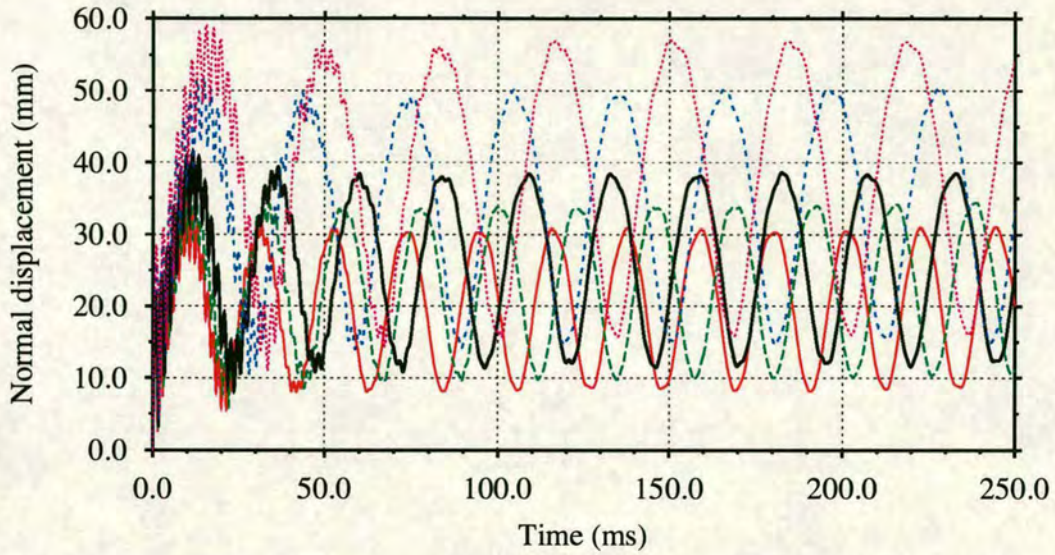

(a) Load point ($\phi = 60^o, \theta = 0^o$)

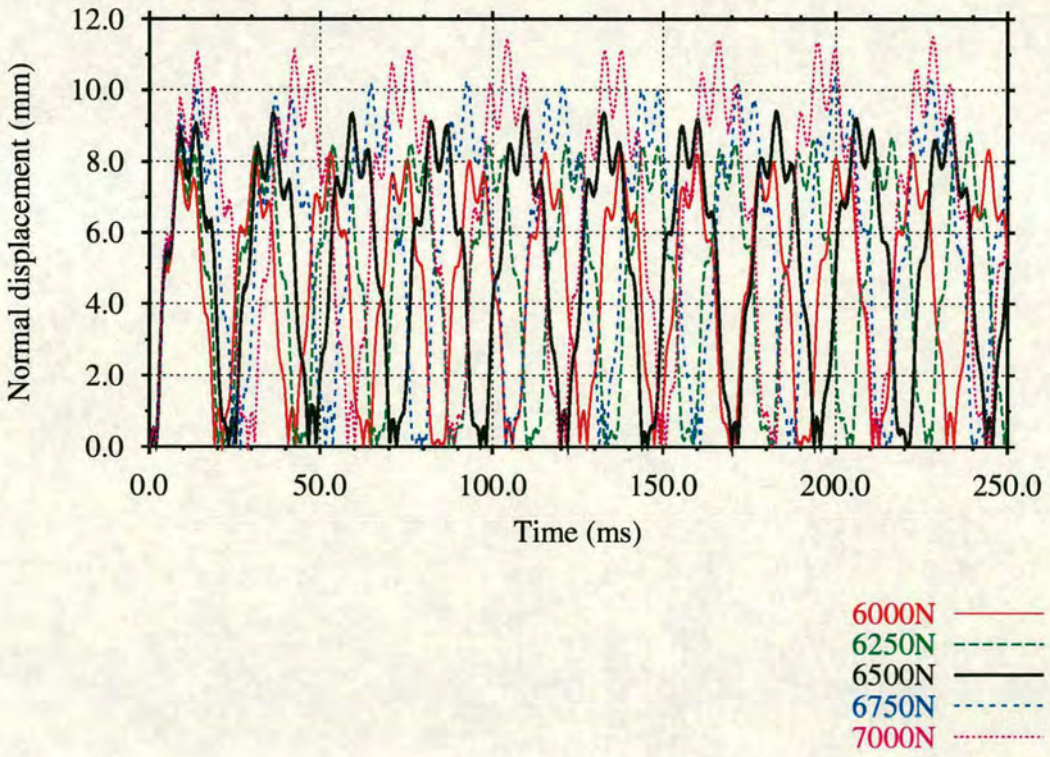

(b) Base region ($\phi = 150^o, \theta = 0^o$)

Figure 7.12: Normal displacement responses to dynamic step loading applied at $\phi = 60^o, \theta = 0^o$

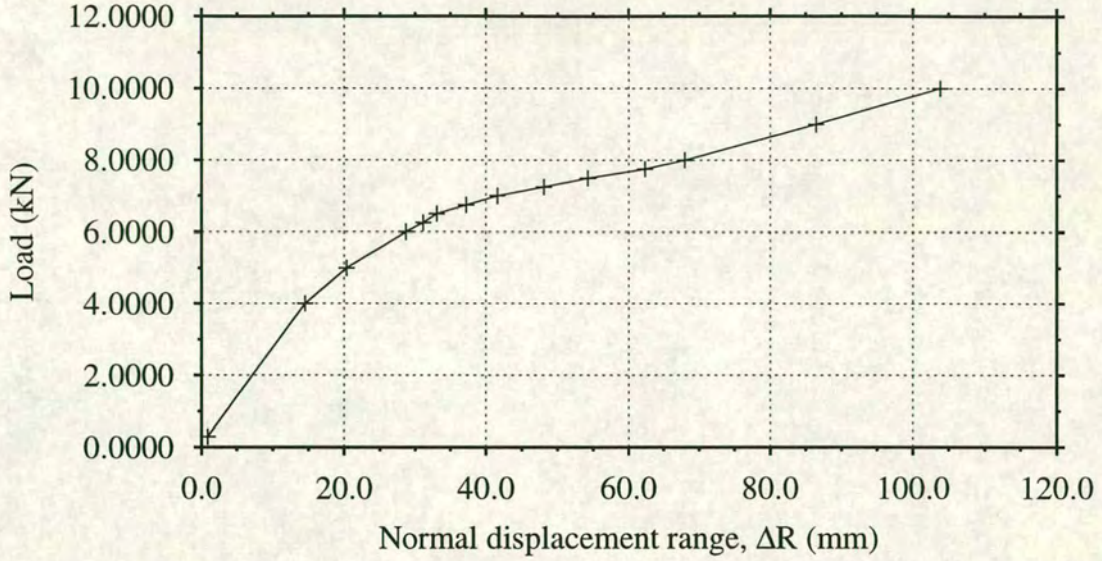

Figure 7.13: Load vs normal displacement range at $\phi = 60^o, \theta = 0^o$ for dynamic step loading applied at $\phi = 60^o, \theta = 0^o$

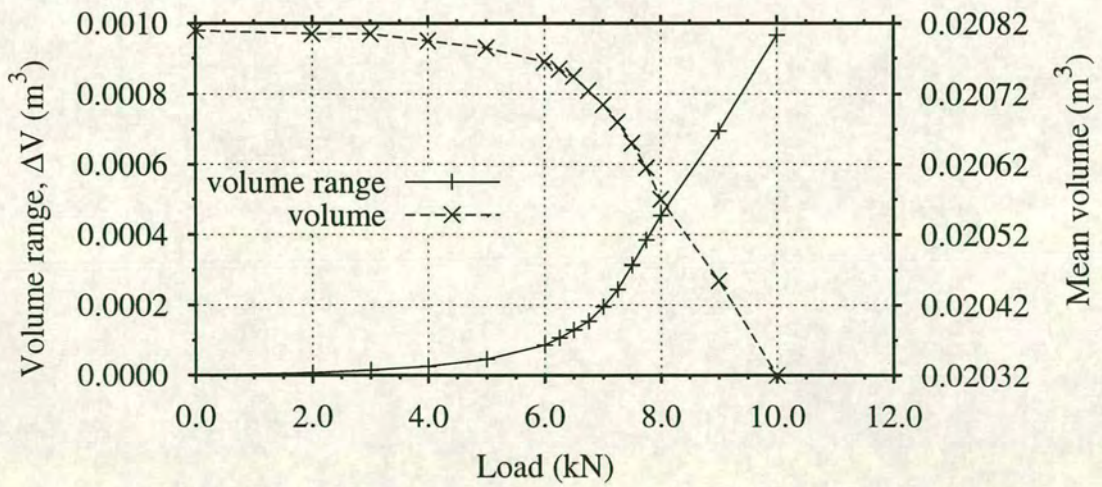

Figure 7.14: Volume vs load for dynamic step loading applied at $\phi = 60^o, \theta = 0^o$

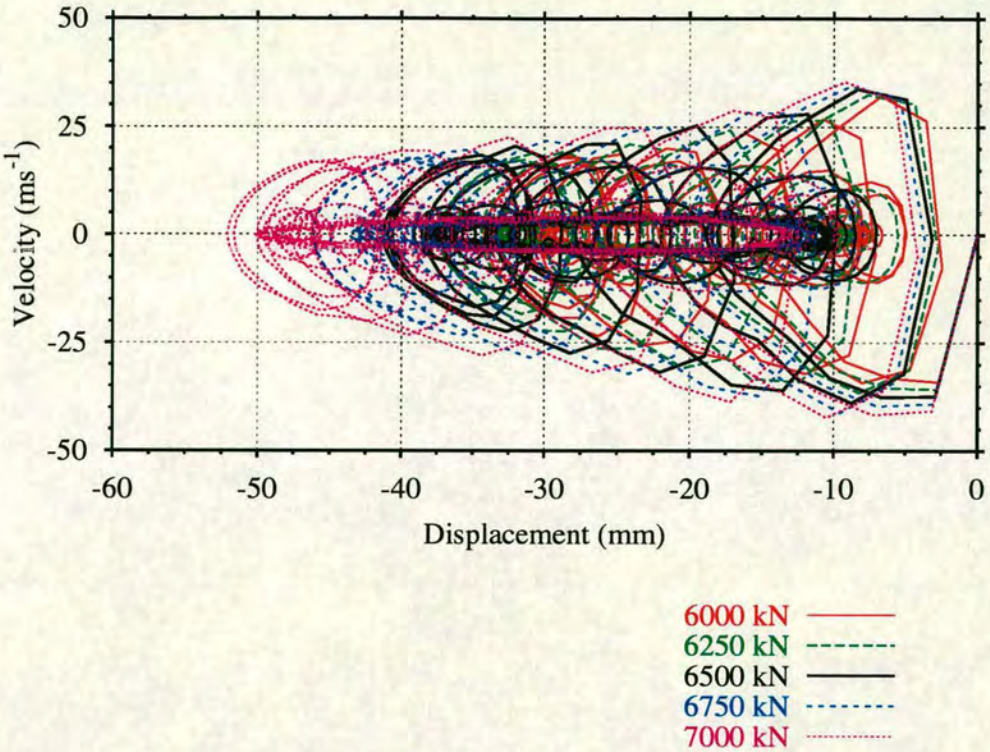

Figure 7.15: Displacement (outwards positive) phase trajectories at $\phi = 60^o, \theta = 0^o$ for dynamic step loading applied at $\phi = 60^o, \theta = 0^o$

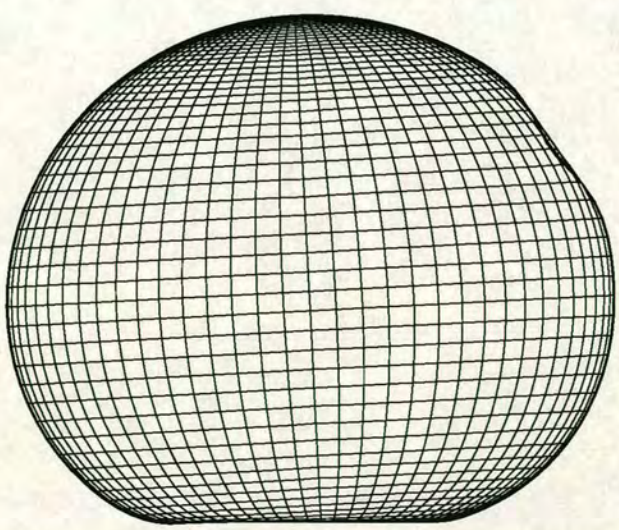

Figure 7.16: Non-linear dynamic collapse deformation for dynamic step loading applied at $\phi = 60^o, \theta = 0^o$ – ***Limit load = 14.5kN*** (displacement $\times 1$)

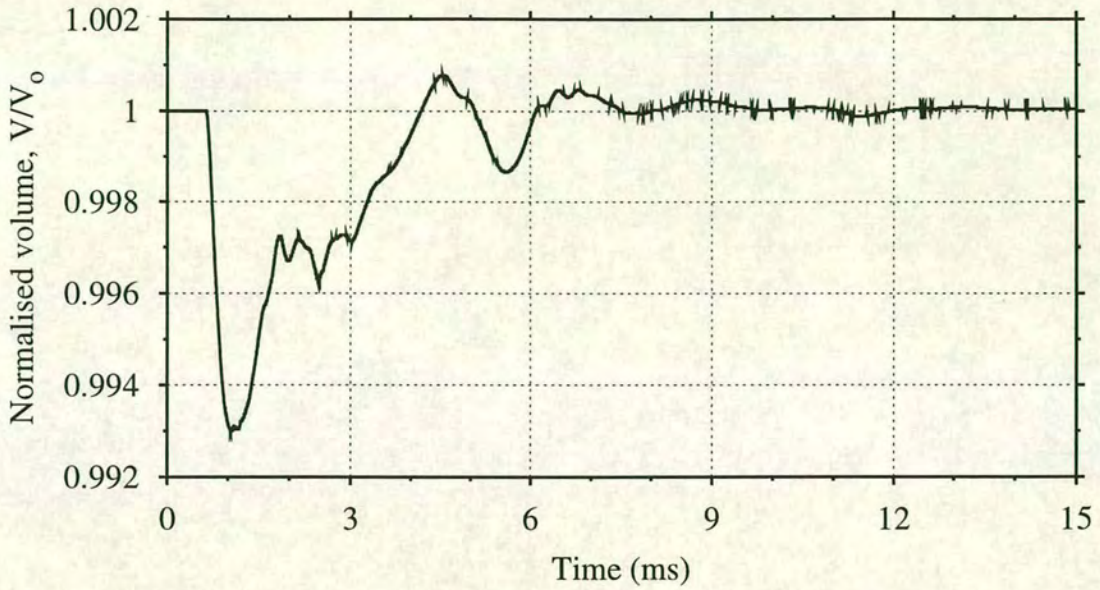

Figure 7.17: Volume response for axisymmetric UNDEX loading from 25g EDC-1 at 1.0m stand off

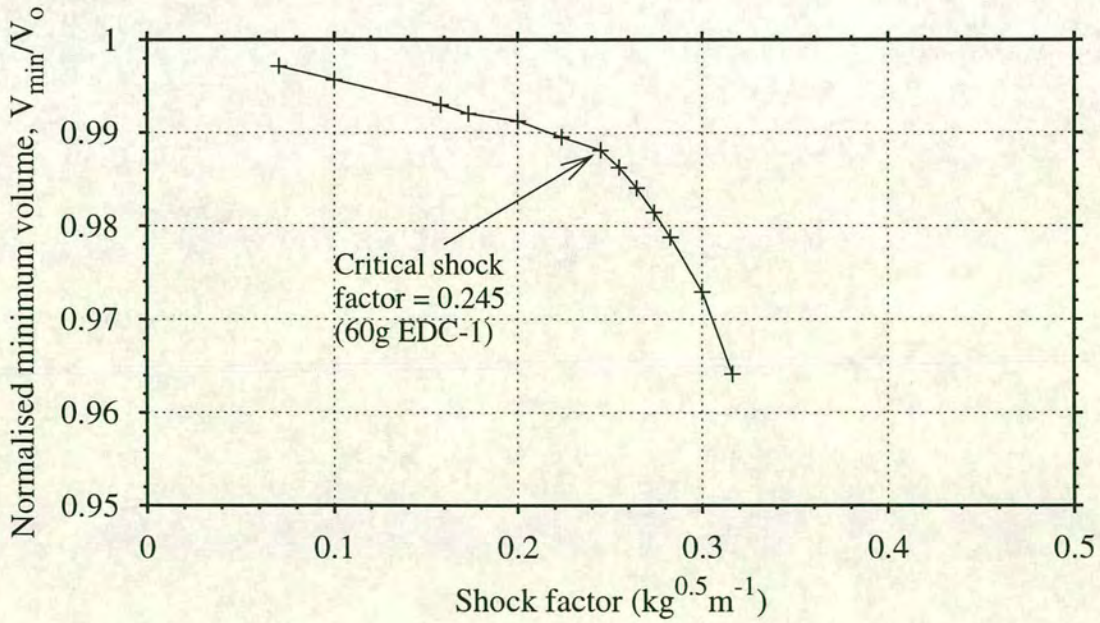

Figure 7.18: Normalised minimum volume vs load for axisymmetric UNDEX loading at 1.0m stand off

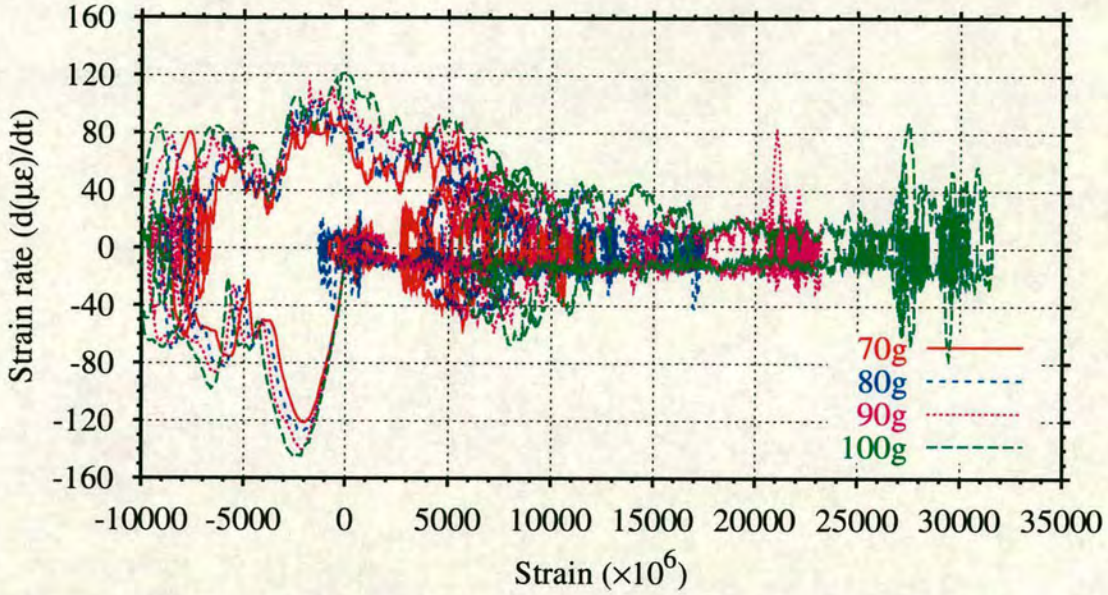

Figure 7.19: Meridional strain phase trajectories (tension positive) at $\phi = 150^o, \theta = 0^o$

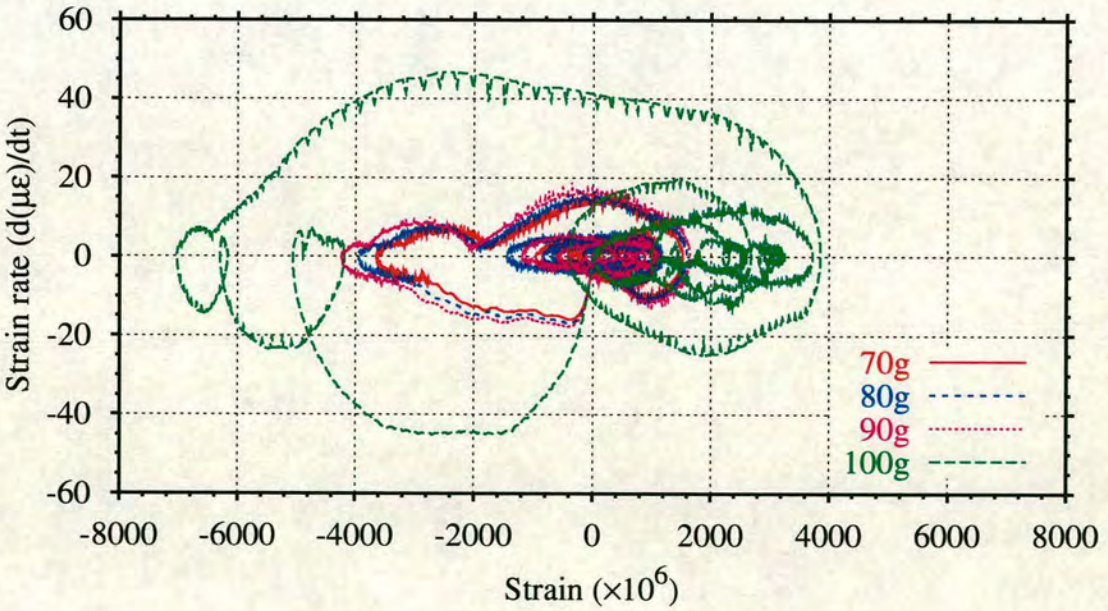

Figure 7.20: Circumferential strain phase trajectories (tension positive) at $\phi = 90^o, \theta = 0^o$

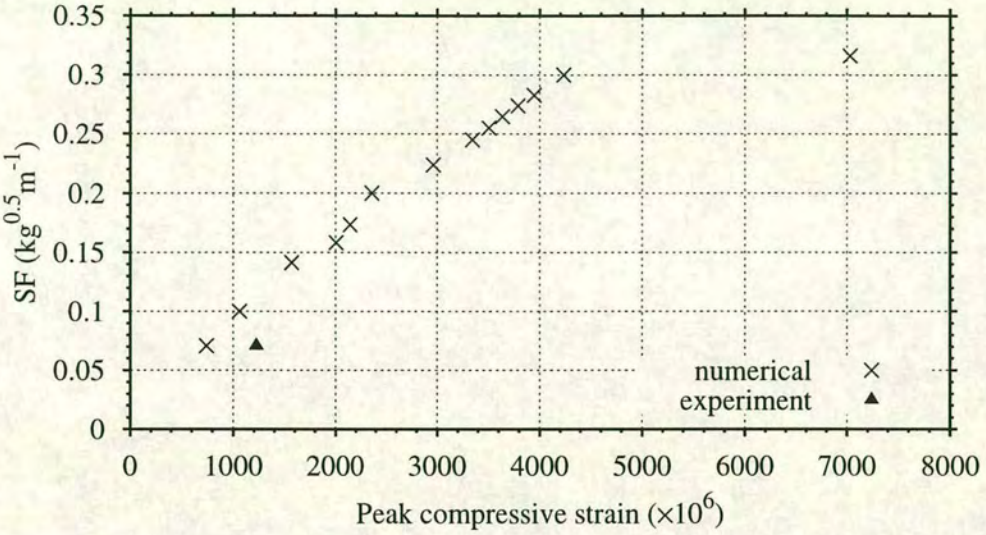

(a) Shock factor vs MMALE predicted circum. strain for $\phi = 90^o, \theta = 0^o$

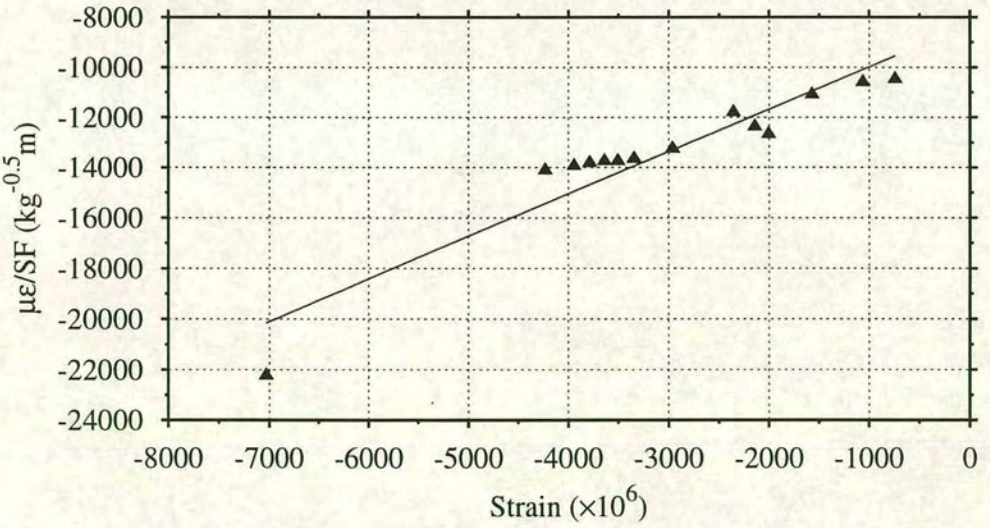

(b) Southwell plot for $\phi = 90^o, \theta = 0^o$ (tension positive)

Figure 7.21: Predicted buckling at $\phi = 90^o, \theta = 0^o$ (circumferential direction) under axisymmetric UNDEX loading at 1.0m stand off – ***Critical charge size = 350g***

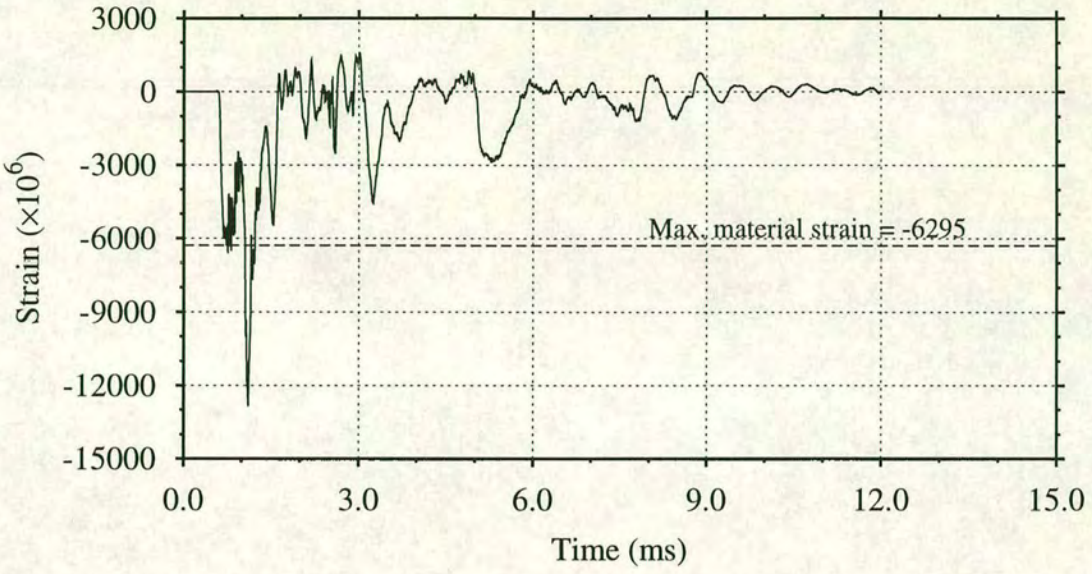

Figure 7.22: Meridional strain response at $\phi = 0^o, \theta = 0^o$ to 60g EDC-1 at 1.0m stand off

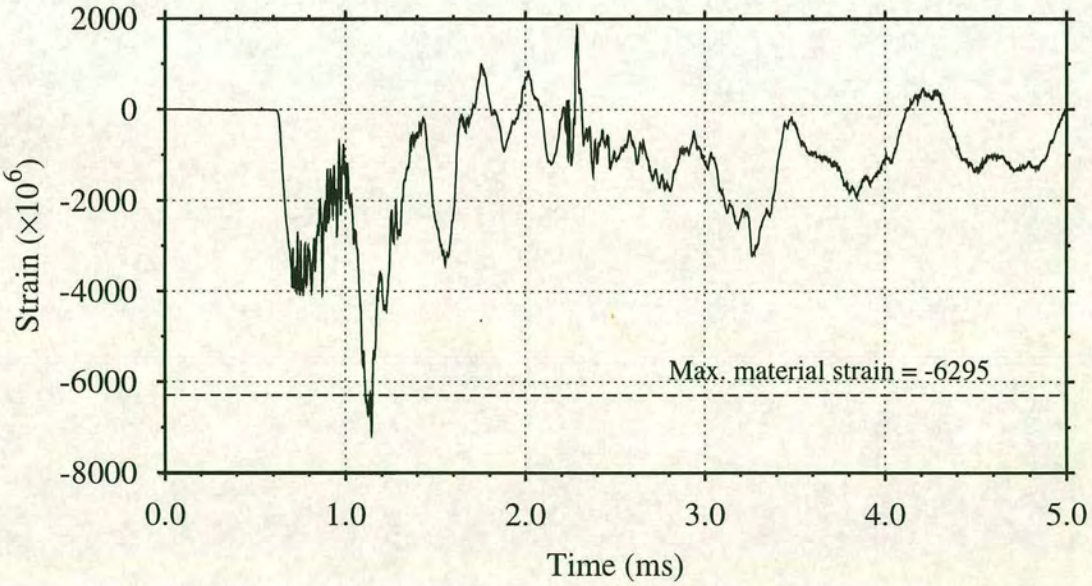

Figure 7.23: Meridional strain response at $\phi = 0^o, \theta = 0^o$ to 20g EDC-1 at 1.0m stand off

Chapter 8

Conclusions and discussion

8.1 Conclusions

The purpose of this thesis was to verify and validate FE and BE technology currently available to simulate UNDEX loading on a prototype echinodome shell. FE models of both the free field environment and the shell were constructed, prior to performing experimental tests, to assist in the design of numerically reproducible experiments. Results from these simulations were verified against empirical and existing experimental data.

The shell was then subjected to axisymmetric and symmetric UNDEX loading from 5g and 10g EDC-1 respectively at various stand off distances, and analysis of data relating to fluid and shell response was undertaken to gain an understanding of the associated behaviour.

Structural response data were‘ presented for quantitative and qualitative validation of the FE and BE approaches to determine the most accurate approach for predicting dynamic buckling criteria under UNDEX loading conditions. In combination with this numerical and experimental data, several non-destructive techniques were then utilised to establish a critical stand off distance under symmetric loading, and a critical charge size under axisymmetric loading.

Conclusions drawn from the completed work have been subdivided into those regarding the experimental tests, those regarding simulations undertaken with the FE approach, available through LS-DYNA, and those regarding simulations undertaken with the BE approach, available through USA-DYNA3D.

8.1.1 Experimental UNDEX loading tests

1. A large spread of free field data for a 1.0m stand off distance from 10g EDC-1 evidently pointed to either an inconsistency in percentage of detonation, attributed to the remote detonation technique, or a degradation of the pressure gauges after each load case.

2. The power laws derived for the EDC-1 charges should be used with caution. Higher quality data from both the 5g and 10g charges would need to be obtained to improve the usefulness of these laws, particularly for energy magnitudes.

3. Peak total pressures at the stand off point under axisymmetric loading were higher than the incident pressure, however, under symmetric loading all cases recorded lower values than the incident pressure except the 4.0m load case. This is attributed to the radiated pressure under symmetric loading being significantly more tensile than under axisymmetric.

4. Whilst the peak total pressure magnitude reduced as the shock wave diffracted around the shell the rise time and duration of the pressure pulse were observed to increase generating a more sustained loading on the shadow regions of the echinodome. This can be explained by the initial impingement of the shock wave against the shell pushing the shadow side of the shell against the water, creating a pressure which is later combined with the arrival of the shock wave pressure. At all positions there was evidence of local cavitation in both symmetric and axisymmetric load cases, and, in the axisymmetric load case, there was also evidence of bulk cavitation.

5. At all positions the initial strain response was observed to be compressive. The impingement of the shock wave at the stand off point initiates a stress wave in the material which travels faster than the shock wave propagating through the fluid. This stress wave will result in compressive strains being observed at various positions in the shell prior to the arrival of the shock wave.

6. The frequency of the strain response in the base region was much higher than that at the apex indicating the influence of the stiffer tufnol plate attached to the base. In the design of an echinodome the stiffness and mass effects of temporary or permanent connections to the base should be considered under UNDEX loading.

7. The highest strains were recorded at the apex and base region revealing that these are the most critical regions under axisymmetric and symmetric UNDEX loading. Some mismatch in the fitting of the two shell halves contributed significantly to the high strain levels recorded at the apex. Despite this the experimental

strain results provide supporting evidence for the earlier recommendation of extra reinforcement in the base region[4].

8. The strain results from the symmetric load cases appeared to indicate that the prototype shell was stiffer in the meridional direction than the circumferential. This was attributed to the smaller radius of curvature in this direction. However, this was not found to be the case under axisymmetric loading.

9. At no position were strain levels found to exceed the maximum static material failure strain. Consequently, the prototype shell was assumed to exhibit the same structural properties after the completion of the tests as before.

10. Use of the non-destructive Southwell plot technique is limited in predicting dynamic buckling criteria from structural response to UNDEX loading due to the dynamic nature of the response and the complexity of the loading comprising shock and bubble.

11. Using the Southwell plot on the results of the symmetric load cases, it was established that, under symmetric UNDEX loading from 10g EDC-1, the prototype echinodome would fail materially at the maximum diameter before dynamic buckling occurs. Using the shock factor relationship the static material failure strain is predicted to be achieved at a stand off distance of 0.61m.

8.1.2 Simulation of UNDEX loading using LS-DYNA

1. The use of the FE method in modelling isolated free field UNDEX phenomena gave good agreement with theoretical and experimental observations. LS-DYNA has been validated for detonation, shock wave propagation and pressure-time predictions up to 1.2m stand off distance from 2kg EDC-1. The ideal solution for detonation is to use a sufficient number of elements to allow the pressure at the detonation front to build up to the P_{cj} value. The optimum solution for detonation is a function of computational cost and required accuracy.

2. For accurate shock wave propagation the ideal solution is for the element dimension to be less than the thickness of the shock front. The optimum solution is for the fluid elements to have the same dimension as the charge, and ensure a constant mesh density throughout the region of interest.

3. The Donor Cell & HIS advection scheme gave the most accurate prediction of peak pressures for free field UNDEX problems. To reduce smearing effects it was necessary for the element sizes of the charge and fluid meshes to be of equal dimension in the propagation direction.

4. For problems involving small magnitudes of timestep (microseconds) the efficiency of LS-DYNA's performance was improved by using equivalent non-standard units of the same order as the timestep.

5. At the time of writing LS-DYNA could not be validated for UNDEX related bubble phenomena. Pressure-time histories were distorted with numerical noise and the tracking of the boundary of the exploded charge material lost accuracy after one expansion and contraction cycle.

6. For static load cases the slow transient approach was computationally more efficient, and numerically more accurate, than the dynamic relaxation approach. Compared to the solution time of a static code both approaches are very computationally expensive.

7. The use of LS-DYNA combined with empirical shock wave relationships demonstrated the capabilities of LS-DYNA to assist in the design of experiments.

8. The following features were found to impose restrictions on simulating UNDEX-FSI using the FE method at the time of writing:

    - **Material initialisation** – the initialisation of materials by element restricted the element sizes to those of the charge. This was overcome in the axisymmetric load case by exploiting axisymmetry. However, the number of elements that would have been required to accurately track the shock wave over the stand off distances involved in the symmetric UNDEX load cases would have lead to impractical solution times. Consequently LS-DYNA was not used to simulate the symmetric load cases.
    - **Coupling** – the general coupling approach failed to initialise void elements on the interior of the coupling surface making ALE coupling the only option. A mesh suitable for ALE coupling is more difficult to construct.
    - **Transitioning and biasing** – mesh construction techniques generated numerical reflections which would ultimately interfere with bubble expansion.
    - **Multi-material capabilities** – accurate representation of the free surface was not possible due to only two materials being permitted to mix in one element. For an entire UNDEX analysis, involving bubble interaction at the free surface, three materials are required per element. After several different approaches were tried, nodal constraints were used to restrict flow normal to the free surface.
    - **Wedge element** – for axisymmetric problems the formulation of the wedge element as a collapsed brick element generated variations in shock wave

pressure and bubble shape along the collapsed edge, and also generated unacceptably small timesteps increasing the computational cost of a mesh considerably. This problem necessitated a hole along the axis of symmetry forcing a reduction in the energy of the charge and inaccuracies in the structural model at the apex and base.

- **Non-reflecting boundaries** – the non-reflecting boundary segments implemented to simulate infinite fluid domains cannot be utilised for UNDEX problems involving bubble pulses. Mass flow is permitted beyond the boundary but any reversal of flow is not simulated. As a result the mass of fluid material within a mesh is not conserved. This forces large volumes of fluid to be modelled for such analyses adding further computational cost to simulations.
- **Subcycling** – the subcycling feature did not function for the Eulerian simulations performed in this work. Consequently, the smallest timestep within the numerical model was used for the entire domain, and for all materials within the domain, throughout the simulation.
- **Adaptivity** – the adaptivity feature available for the Lagrangian formulation could not be exploited due to the malfunction of the general coupling technique. The ALE coupling approach would have required adaptivity for the Eulerian formulation to maintain element connectivity.
- **Parallel processing** – the parallel capabilities of LS-DYNA did not extend to the Eulerian formulation and hence reductions in computation time could not be obtained.

9. From the final FE model constructed, the predicted peak free field and scattered pressures from the UNDEX loading were poor. The peak magnitudes were underpredicted, however, the trends of the total pressure-time histories did resemble that recorded experimentally.

10. The peak strain response of the echinodome to UNDEX loading was overpredicted compared to experimentally measured values. The sequence of peak strains around the shell was not in agreement with experiment but the highest strains predicted did coincide with the critical regions observed experimentally, ignoring imperfection-sensitive regions such as the apex.

11. The van Leer advection scheme was found to be computationally the most efficient and accurate for UNDEX-FSI problems.

12. The volume approach to predicting global dynamic buckling criteria predicted a

lower buckling charge size than the local phase-plane approach. Both can be used reliably to indicate a sudden change in system behaviour.

13. Observing global and local system behaviour, LS-DYNA predicted that the echinodome would undergo material failure before dynamic buckling occurs. The strain levels generated by 20g EDC-1 at 1.0m stand off were predicted to exceed the static material failure strain.

14. For a full scale echinodome structure comprising a different profile, and material properties for which accurate numerical models existed, the quality of experiment-theory comparisons could be improved and relied upon to provide both a qualitative and quantitative assessment of fluid-structure interaction under UNDEX loading.

8.1.3 Simulation of UNDEX loading using USA-DYNA3D

1. The BE DAA-MAT90 approach provided a more physically accurate propagation of the shock wave around the echinodome than the DAA approach. Both approaches assisted in improving the understanding of the physical behaviour of the prototype echinodome when subjected to UNDEX loading.

2. The predicted peak total pressure was in good agreement at most positions with that recorded experimentally under both symmetric and axisymmetric UNDEX loading conditions. The peak pressure in the shadow regions of the shell were overpredicted, although the sustained pressure pulse measured was apparent from the simulation results.

3. The DAA-MAT90 approach overpredicted the peak strain response for the axisymmetric load case and for the symmetric load case the response was underpredicted compared to experimentally measured values. The numerical model of the shell accounted for imperfections favourable to the axisymmetric loading only, thereby making the model more flexible under symmetric loading conditions. The positions where highest predicted peak strain occurred were in accordance with experimental observations and the sequence of peak strain levels around the shell resembled that observed in the experiments.

4. The underpredictions of the symmetric load case combined with the lack of experimental pressure decay values rendered USA-DYNA3D unsuitable for predicting dynamic buckling criteria under either loading condition.

5. For a full scale echinodome structure USA-DYNA3D could be used reliably for

axisymmetric response to UNDEX loading, but should be used with caution under symmetric loading conditions.

8.2 Improvements

From the aforementioned conclusions suggested improvements pertaining to the numerical simulation capabilities and experimental tests may be established.

8.2.1 Improvements to experimental tests

- The variation in percentage detonation of the explosive material requires much improvement to obtain reliable data relating to the shock wave and bubble characteristics. The use of detonators in earlier work[4] proved successful in generating measurable fluid and shell responses to those obtained in this work. Detonators of a similar weight to the charges used in this work would provide reliable data for input to USA-DYNA3D and also for comparison with LS-DYNA and USA-DYNA3D results. The material characteristics of the detonators would have to be related to those of an explosive material for which JWL constants are well established to permit accurate simulation of the detonation using LS-DYNA.

- Also, associated with obtaining reliable free field pressure data, an investigation into the reliability of pressure gauges for repeated use would be worthwhile, considering the spread of data observed experimentally.

- Care in placement of pressure and strain gauges on the shell for recording axisymmetric and symmetric responses should increase the understanding of the effect of imperfections.

- The imperfections of the shell not only generated a variation in axisymmetric and symmetric response, but also provided difficulties for comparison of experimental and numerical data. A reconstruction of the shell using the same design head but not necessarily the same material properties, and aimed at curtailing these imperfections, would minimise both these problems. Current techniques suitable for constructing another prototype echinodome are discussed further in the following section.

8.2.2 Improvements to LS-DYNA

- Initialisation of materials by geometry rather than by elements would remove the restrictions of constructing an FE model with element sizes controlled by the charge and subsequently the control that has on the timestep of the simulation. The charge could be modelled geometrically within the existing fluid elements and initialised at the start of the simulation. For small charge sizes (grams) sufficient elements would still be required to ensure that the detonation pressure of the material is reached. For large charge sizes (kilograms) this would ease construction of the fluid mesh around cylindrical or spherical charge shapes which, in combination with ALE coupling, can become complex and time consuming, and assist in reducing the computational cost of the simulation.

- The wedge element should be included in the element library as an element with its own shape function, not as a degraded hexahedral element. This could dramatically reduce the computational cost of a simulation for axisymmetric problems.

- A fully functional multi-material Eulerian capability of three or more materials being allowed to mix in one element would extend the application of LS-DYNA considerably, e.g., to be able to include air at the free surface would provide the correct boundary conditions for an entire UNDEX event. Such capabilities would also permit the simulation of more complex problems, e.g., multi-material explosives, soil-structure interaction, etc.

- In connection with the multi-material capabilities, the formation of voids within an element for local and bulk cavitation regions would allow a detailed numerical investigation of cavitation to be undertaken. To closely study the growth of cavitation regions and methods of minimising their impact on structural integrity would greatly enhance structural design.

- Void initialisation on the interior of the coupling surface within the general coupling feature is essential if this feature is to be exploited. This feature dramatically reduces the time spent on pre-processing, particularly for complex geometry involving air backed structures. A further enhancement of this feature for storage tanks would be to initialise the material on the interior of the coupling surface with material properties. This would require material initialisation by geometry.

- The numerical simulation of bubble behaviour requires accurate tracking of the explosive gas boundary, particularly at the phases of bubble collapse and

separation. Also bubble migration towards and interaction with proximate rigid boundaries are often features of fluid-structure interaction associated with an UNDEX event. Material interface tracking algorithms, e.g., simple line interface calculation (SLIC) and high resolution interface tracking (HRIT), have been developed elsewhere to provide numerical accuracy in tracking material boundaries[28].

- The tracking of material mass flow occurring beyond non-reflecting boundary segments and the capability of replacing the mass should flow reversal occur is essential for problems such as accurate growth and collapse of the bubble in an UNDEX event.

- The subcycling feature could considerably reduce the computational cost of UNDEX simulations if fully functional for Eulerian domains. The restrictions on mesh density, and hence accuracy, caused by potentially small timesteps involved in these simulations has been made evident. Integration over elements grouped according to dimension and material, using multiples of the smallest timestep, could be easily exploited in UNDEX analyses.

- Adaptivity for Eulerian domains could be utilised to automatically reduce mesh density in regions where accuracy was no longer required. Used in combination with an accurate advection scheme this feature would greatly reduce the computational cost for problems involving large charge sizes and stand off distances. Also, used in conjunction with the general coupling technique, adaptivity would improve the accuracy of the structural response in regions experiencing high strain levels.

- A parallelised version of the multi-material Eulerian capabilities would extend the applicability of LS-DYNA to symmetric UNDEX loading problems. It would also encourage more accurate models, with smaller element sizes and consequently smaller timesteps, to be constructed without fear of computational cost.

8.2.3 Improvements to USA-DYNA3D

- The ability to input direct experimental pressure-time history data rather than theoretical fits to such data would improve the authenticity between the simulation and the experiment.

- The distortion of the LS-DYNA acoustic elements could be reduced by adopting a similar smoothing technique to that used for ALE regions. This would

enhance the performance and applicability of this approach for large deformation problems.

8.3 Recommendations for further work

The work undertaken in this thesis has highlighted possibilities for further work relating to the prototype echinodome that would improve experiment-theory simulations. The capabilities of LS-DYNA also introduce further predictive studies relating to other loading conditions to which the echinodome could be subject.

1. More complex material models are available in LS-DYNA for elastic composites such as the prototype echinodome, e.g., *MAT_ORTHOTROPIC_ELASTIC, *MAT_ENHANCED_COMPOSITE_DAMAGE, which may improve the predicted response of the shell. Further material tests and imperfection measurements would need to be performed to gather more detailed information regarding circumferential imperfections, the shear modulus, temperature effects and the behaviour of the material under high strain rates. Recent UNDEX studies performed using LS-DYNA have shown excellent experiment-theory comparison for thin shell structures for which material properties at high strain rates were well characterised and detailed geometrical imperfections were also modelled[73].

2. Further examination of the unexpectedly low scattered pressures predicted by the MMALE pseudo-wedge model could be undertaken. A quarter symmetry model could be run to determine whether the pseudo-wedge structural mesh or the Eulerian elements are the source of the inaccuracy.

3. Further experimental results pertaining to the prototype echinodome response to axisymmetric UNDEX loading would be required to understand why the shell indicated more stiffness in the circumferential direction than the meridional, as the symmetric load cases indicated and all numerical results predicted.

4. A numerical simulation of a full scale echinodome subject to UNDEX loading would assist in developing the design procedures already in place for the echinodome. The inclusion of temporary or permanent fittings would be necessary to examine their influence on structural behaviour. For a full scale echinodome constructed for a different design head and material properties an examination of critical buckling criteria would be essential.

5. In reality a full scale echinodome storage vessel would be liquid backed at some stage in its operation. The structural response of a liquid backed echinodome

to UNDEX loading would be expected to be less critical than for an air backed one. A numerical dynamic buckling study could be performed to ascertain if the response follows similar trends and to determine the difference between air backed to fluid backed response.

6. The effect of combined shock and bubble loading on dynamic buckling criteria would require investigation, particularly for close stand off distances, for an echinodome constructed from an elastic-plastic material. Supplementary damage caused by the bubble pulse would require increased critical stand off distances or reduced critical charge sizes. Also, for close stand off distances, migration of the bubble towards, and subsequent bubble collapse against, the shell would be worthy of investigation to aid understanding of this complex phenomena.

7. Echinodome storage vessels are usually found to be part of a much larger 'storage field' of containers. In such an environment the diffraction of a shock waves around an echinodome would cause loading on vessels located behind the shadow side. Some investigations into numerically predicting the response of spherical shells located in this region have been undertaken using USA-STAGS-CFA[42,47] with moderate success. To examine the behaviour of an echinodome under this form of loading would assist the understanding of diffraction, the severity of loading resulting from such phenomena and more insight into the response of the echinodome to UNDEX loading.

8. The construction of a new prototype echinodome could assist in improving both experimental results and future numerical models. Current technology provides several accurate techniques for the rapid generation of a new prototype using materials for which numerical models exist within LS-DYNA. Fused deposition modelling (FDM) and stereolithography (SL) are two such techniques which are available. A process known as layer manufacturing is used to build a model in horizontal layers from a conceptual geometrical computer aided design (CAD) model. The SL models can be converted into engineering prototypes in a variety of plastics and metals, by a series of secondary processes such as vacuum casting or quickcast investment casting[98,99].

References

[1] Sofoluwe A. B. *Studies of a structural form for underwater structures.* PhD thesis, University of Edinburgh, 1980.

[2] Royles R. Sofoluwe A. B. Baig M. M. Currie A. J. Behaviour of underwater enclosures of optimum design. *Strain*, 16:12–20, 1980.

[3] Llambias J. M. *Response of an underwater structure of optimum shape to general loading.* PhD thesis, University of Edinburgh, 1985.

[4] El-Deeb K. M. M. *Echinodome response to dynamic loading.* PhD thesis, University of Edinburgh, 1990.

[5] Boyd R. The use of high performance computing in echinodome construction. Hons project, School of Civil and Environmental Engineering, University of Edinburgh, May 1995.

[6] Royles R. Llambias J. M. Storage aspects of liquid gases underwater and the structural implications. In *Proc. of Int. Symp. on Storage and Transport of LPG and LNG*, volume 2, pages 55–72. Koninklijke Vlaamse Ingenieursvereniging, Technologisch Institut (Kommissie Metaalbouw), Antwerpen, Belgium, 1984.

[7] Phua Cheung Paio A. The application of zeolites in water storage and treatment systems. Hons project, School of Civil and Environmental Engineering, University of Edinburgh, May 1995.

[8] Westcoast Gas Services Inc. *Newsletter No. 1.* Environmental Assessment Office Project Registry, PO BOX 9426 Stn. Prov. Govt., Victoria, BC, V8W 9V1, December 1997. Also available at http://eaoluco-web.eao.gs.gov.bc.ca/PROJECT/energy/wgsi/news2.htm.

[9] Royles R. Llambias J. M. Buckling aspects of the behaviour of an underwater pressure vessel. In *Proc. of Appl. Solid Mech.*, pages 287–303. Elsevier Applied Science, London, 1985.

[10] Royles R. Llambias J. M. Buckling behaviour of an underwater storage vessel. *Expt. Mech.*, 25:421–428, 1985.

[11] Royles R. Llambias J. M. El-Deeb K. M. M. Response of echinodomes to asymmetric loading. In *Proc. of Int. Conf. on the Design and Construction of Non-conventional Structures*, volume 1, pages 167–183. Civil-Comp Press, Edinburgh, 1987.

[12] El-Deeb K. M. M. and Royles R. Dynamic and static buckling assessment of an echinodome. *Comp. and Struct.*, 46:899–904, 1993.

[13] El-Deeb K. M. M. and Royles R. Response of an echinodome to explosive loading. *accepted for publication in J. of Shock and Vibration*, 1999.

[14] Boyd A. R. Royles R. El-Deeb K. M. M. and Haxton R. S. Fast dynamic transient loading of underwater structures. In *Proc. of 11th Int. Conf. on Experimental Mechanics*, volume 1, pages 23–28. Allison, Rotterdam, 24 – 28 Aug., 1998.

[15] Cole R. H. *Underwater Explosions.* Princeton University Press, NJ, USA, 1948.

[16] Smith P. D. and Hetherington J. G. *Blast and Ballistic Loading of Structures*, chapter 5. Butterworth Heinemann, London, UK, 1994.

[17] Didham E. F. J. Final report on free field experimental and simulation studies of the IEPG PA29 standard omnidirectional charge. Memorandum 25/92 (unclassified), DERA (Fort Halstead), England, UK, 1992.

[18] Langhammer J. and Landrø M. High-speed photography of the bubble generated by an airgun. *Geophysical Prospecting*, 44:153–173, 1996.

[19] Mair H. U. Preliminary compilation of underwater explosion benchmarks. In *Proc. of 67th Shock and Vibration Symposium*, volume 1, pages 361–379. SAVIAC, Arlington, VA, 1996.

[20] Cobolli G. Damonte R. Figari M. and Iaccarino R. Theoretical-experimental analysis of hull response to underwater explosions. In *Structural Dynamics - EURODYN 1993*, pages 479–486. Allison, Rotterdam, 1993.

[21] Kwon Y. W. and Fox P. K. Underwater shock response of a cylinder subjected to a side-on explosion. *Comp. and Struct.*, 48:637–646, 1993.

[22] Jiang J. and Olson M. D. Non-linear transient analysis of submerged circular plates subjected to underwater explosions. *Comp. Meth. for Appl. Mech. and Eng.*, 134:163–179, 1996.

[23] Shin Y. S. and Geers T. L. Response of marine structures to underwater explosion. Technical report, Shock and Vibration Research, 10150 Blue Larkspur Lane, Monterey, California, 93940, March 1996.

[24] Mair H. U. Hydrocode methodologies for underwater explosion structure/medium interaction. In *Proc. of 66th Shock and Vibration Symposium*, volume 2, pages 227–248. SAVIAC, San Deigo, CA, 1995.

[25] Zienkiewicz O. C. *The Finite Element Method*, volume 1 & 2. McGraw-Hill, London, 4th edition, 1991.

[26] Rao S. S. *The Finite Element in Engineering.* Pergamon Press, Oxford, 2nd edition, 1989.

[27] Anderson C. E. Jr. An overview of the theory of hydrocodes. *Int. J. Impact Engineering*, 5:33–59, 1987.

[28] Benson D. J. Computational methods in Lagrangian and Eulerian hydrocodes. *Comp. Meth. for Appl. Mech. and Eng.*, 99:235–394, 1992.

[29] Swegle J. W. and Attaway S. W. On the feasibility of using Smoothed Particle Hydrodynamics for underwater explosions calculations (Report SAND95-0311). Technical report, Sandia National Laboratories, February 1995.

[30] Shin Y. S. and Geers T. L. A short course on penetration mechanics. Technical report, Southwest Research Institute, San Antonio, Texas, February 1998.

[31] McGlaun J. M. Thompson S. L. and Elrick M. G. CTH: A three-dimensional shock wave physics code. *Int. J. of Impact Eng.*, 10:351–360, 1990.

[32] McKeown R. M. Grande R. Mentges J. M. and Naval Surface Warfare Center. Simulations of UNDEX against submerged structures using DYSMAS/ELC – Part B: Analysis of an unstiffened cylinder. In *Proc. of 65th Shock and Vibration Symposium*, volume 2, pages 253–261. SAVIAC, San Deigo, CA, Oct. 31 – Nov. 3, 1994.

[33] Huang H. and Kiddy K. C. Transient interaction of a spherical shell with an underwater explosion shock wave and the subsequent bubble. *Dynamic Response of Structures to High-Energy Excitation*, 127:1–11, 1991.

[34] Andelfinger U. Simulations of UNDEX against submerged structures using DYSMAS/ELC – Part A. In *Proc. of 65th Shock and Vibration Symposium*, volume 2, pages 243–251. SAVIAC, San Deigo, CA, Oct. 31 – Nov. 3, 1994.

[35] Fiessler B. and Chwalinski R. On the influence of structural shape and interaction on explosive loads in shock and collapse phases. In *Proc. of 66th Shock and Vibration Symposium*, volume 2, pages 287–295. SAVIAC, San Deigo, CA, 1995.

[36] Donea J. The ALE description in transient fluid-structure problems. *Advances in Simulation and Interaction Techniques*, pages 89–101, 1994.

[37] Shin Y. S. and Chisum J. E. Modelling and simulation of underwater shock problems using a coupled Lagrangian-Eulerian analysis approach. Int. Seminar on Hydroelasticity in Ship Structural Design, February 1996.

[38] Lenselink H. and de Vries E. Analysis of the loading of an aluminium cylinder by an underwater explosion. In *MSC World Users' Conference*, 20 – 24 June, 1994.

[39] Geers T. L. Residual potential and approximate methods for three-dimensional fluid-structure interaction problems. *J. of the Acoust. Soc. of Am.*, 49:1505–1510, May 1971.

[40] Geers T. L. Doubly asymptotic approximations for transient motions of submerged structures. *J. of the Acoust. Soc. of Am.*, 64:1500–1508, November 1978.

[41] Felippa C. A. A family of early time approximations for fluid-structure interaction. *J. of Appl. Mech.*, 47:703–708, 1980.

[42] DeRuntz J. A. Jr. The Underwater Shock Analysis code and its applications. *Proc. of 60th Shock and Vibration Symposium*, 1:89–107, November 1989.

[43] DeRuntz J. A. Jr. DERA Rosyth: Unique Software Applications workshop on applications of the USA code to underwater shock problems, 4 – 7 June, 1997. volumes 1 & 2.

[44] Hamdan F. H. Modelling of unbounded media for fluid-structure interaction problems. *Strain*, 34:51–58, May 1998.

[45] Hamdan F. H. and Hobbs R. E. Far-field fluid-structure interaction: A comparison between the doubly asymptotic and plane wave approximations. In *Proc. of the 5th Int. Offshore and Polar Eng. Conf.*, volume 3, pages 378–383, 11 – 16 June, 1995.

[46] DeRuntz J. A. Jr. Shock analysis of submerged structures with internal fluid volumes. *Sloshing Fluid-structure Interaction and Structural Response due to Shock and Impact Loads*, 272:141–152, 1994.

[47] Geers T. L. and Ruzicka G. C. Transient response analysis of multiple submerged structures. *Finite Elements in Analysis and Design*, 6:153–172, 1989.

[48] Haxton R. S. El-Deeb K. M. M. Royles R. and Hunter I. T. Further assessment of numerical procedures for the study of fluid-structure interaction. *Strain*, 31:107–112, August 1995.

[49] Mäkinen K. Dynamically loaded sandwich structures. Report No. 95-20, Royal Institute of Technology, Stockholm, Sweden, 1995.

[50] Shock and Vibration Information Analysis Center. *Shock and Vibration computer programs - reviews and summaries.* Booz, Allan & Hamilton Inc., 1995.

[51] Mackerle J. Fluid-structure interaction problems – finite element and boundary element approaches: A bibliography (1995–1998). *Finite Elements in Analysis and Design*, 31:231–240, 1999.

[52] Anon. *Oasys LS-DYNA Environment 7.1 Volume 3: User Guide.* Oasys Ltd, 13 Fitzroy Street, London, W1P 6BQ, October 1998.

[53] Hallquist J. O. *LS-DYNA Theoretical Manual.* Livermore Software Technology Corporation, 97 Rickenbacker Circle, Livermore, CA 94550, May 1998.

[54] Benson D. J. Momentum advection on a staggered mesh. *J. of Comp. Phys.*, 100:143–162, 1992.

[55] Anon. *LS-DYNA Keyword User's Manual Version 940.* Livermore Software Technology Corporation, 97 Rickenbacker Circle, Livermore, CA 94550, June 1997.

[56] DeRuntz J. A. Jr. *Underwater Shock Analysis - Flumas, Augmat and Timint Manuals.* Livermore Software Technology Corporation, 97 Rickenbacker Circle, Livermore, CA 94550, October 1997.

[57] Shin Y. S. and Hooker D. T. Damage response of submerged imperfect cylindrical structures subject to underwater explosion. *Comp. and Struct.*, 60:683–693, 1996.

[58] DeRuntz J. A. Jr. and Rankin C. C. Applications of the USA-STAGS-CFA code to non-linear fluid-structure interaction problems in underwater shock of submerged structures. In *Proc. of 60th Shock and Vibration Symposium*, volume 1, pages 121–138. SAVIAC, San Deigo, CA, November 1989.

[59] Miller R. D. and Rasmussin E. A. Comparison of analytical and experimental response of an axisymmetric test fixture due to low severity and high severity UNDEX. In *Proc. of 67th Shock and Vibration Symposium.* SAVIAC, Arlington, VA, 18 – 22 November, 1996.

[60] Nakamura T. DeRuntz J. A. Jr. and Hallquist J. O. Linking the USA code and LS/DYNA code using the acoustic elements to predict underwater explosion

response. In *Proc. of 69th Shock and Vibration Symposium (to be published).* SAVIAC, San Deigo, CA, 12 – 16 Oct. 1998.

[61] Anon. *HyperMesh User's Manual Version 2.1.* Altair Engineering Inc., 1757 Maplelawn Drive, Troy, MI 48084, 1997.

[62] Anon. *TrueGrid Manual Version 1.4.* XYZ Scientific Applications Inc., 1324 Concannon Boulevard, Livermore, CA 94550, July 1997.

[63] Anon. *Oasys LS-DYNA Environment 7.1 Post-processing Volume 2: Oasys D3PLOT.* Oasys Ltd, 13 Fitzroy Street, London, W1P 6BQ, October 1998.

[64] Anon. *LS-TAURUS User's Manual.* Livermore Software Technology Corporation, 97 Rickenbacker Circle, Livermore, CA 94550, June 1997.

[65] Anon. *MSC/DYTRAN Example Problem Manual Version 2.3.* The MacNeal-Schwendler Company Ltd, MSC House, Lyon Way, Frimley, Camberely, Surrey, GU16 5ER, April 1995.

[66] Dobratz B. M. *LLNL Explosives handbook - properties of chemical explosives and explosive simulants (UCRL-52997).* University of California, Lawrence Livermore National Laboratory, Livermore, CA, USA, March 1981.

[67] Wright J. K. *Shock Tubes.* Methuen & Co. Ltd, London, UK, 1961.

[68] Buis J. P. *Analysis of shock tube calculations performed by the PISCES-2DELK/V4 code.* PISCES International, B. V., Netherlands, 1987.

[69] Harlow F. H. and Amsden A. A. Fluid dynamics. Monograph, Los Alamos National Laboratory, NM, USA, 1971.

[70] Jardin S. C. and Hoffman R. Simulation of explosive processes in PISCES-1DL. Technical report, Physics International Company, 1972.

[71] Stillman D. W. Lum L. Hallquist J. O. and Benson D. J. An Arbitrary Lagrangian-Eulerian capability for LS-DYNA3D. *Advances in Numerical Simulation Techniques for Penetration and Perforation of Solids*, 171:67–74, 1993.

[72] Molyneaux T. C. K. Li L. Y. and Firth N. Numerical simulation of underwater explosions. *Comp. and Fluids*, 23:903–911, 1994.

[73] DERA (Rosyth). *Private communications.* DERA Rosyth, South Arm Site, Rosyth Royal Dockyard, Rosyth, Fife, KY11 2XR, 1997.

[74] Anon. *Oasys LS-DYNA3D Training Manual: Introductory Course.* Oasys Ltd, 13 Fitzroy Street, London, W1P 6BQ, March 1996.

[75] LSTC. *Private communications.* Livermore Software Technology Corporation, 97 Rickenbacker Circle, Livermore, CA 94550, May 1997.

[76] Milligan C. D. Duncan J. H. and Stillman D. J. A numerical study of underwater explosion bubble phenomena. *Structures under Extreme Loading Conditions*, 299:27–32, 1995.

[77] Underwood P. Dynamic relaxation. *Comp. Meth. for Trans. Anal.*, pages 245–265, 1983.

[78] Papadrakakis M. A method for the automatic evaluation of the dynamic relaxation parameters. *Comp. Meth. for Appl. Mech. and Eng.*, 25:35–48, 1981.

[79] El-Deeb K. M. M. Royles R. Modal examination of an echinodome. *Int. J. of Anal. and Exp. Modal Analysis*, 7:51–63, 1992.

[80] Anon. *ABAQUS/Standard Version 5.8 User's Manual: Volume 1.* Hibbitt, Karlsson and Sorensen (UK) Ltd, The Genesis Centre, Science Park South, Birchwood, Warrington, Cheshire WA3 7BH, 1998.

[81] Jackson N. and Dhir R. K. *Civil Engineering Materials.* MacMillan, 4th edition, 1992.

[82] Mouritz A. P. The damage and failure of GRP laminates by underwater explosion shock loading. *Composites*, 25:431–437, 1994.

[83] Mouritz A. P. The effect of underwater explosion shock loading on the flexural properties of GRP laminates. *Int. J. of Impact Eng.*, 18:129–139, 1996.

[84] Harding J. The effect of high strain rate on material properties. *Materials at High Strain Rates*, pages 133–186, 1987.

[85] Moyer T. Simulation of UNDEX and bubble loading with USA-DYNA3D. In *Proc. of TTCP Workshop.* DERA Rosyth, Scotland, UK. (to be published), 27 – 29 May, 1997.

[86] Bushnell D. *Computerized Buckling Analysis of Shells.* Martinus Nijhoff, Dordrecht, The Netherlands, 1985.

[87] Kaplan A. *Thin Shell Structures - Theory, Experiment and Design.* Englewood Cliffs, NJ, USA, 1974.

[88] Song B. and Jones N. Dynamic elastic buckling of complete spherical shells with initial imperfections. *J. of Struct. Mech.*, 11:327–350, 1983.

[89] Southwell R. V. On the analysis of experimental observations in problems of elastic stability. In *Proc. Royal Society*, volume 135A, pages 601–616, 1932.

[90] Roorda J. Some thoughts on the southwell plot. *J. of the Eng. Mech. Div.*, 93(EM6):37–48, December 1967.

[91] Spencer H. H. and Walker A. C. Critique of southwell plots with proposals for alternative methods. *Expt. Mech.*, 15(3):303–310, 1975.

[92] Budiansky B. and Roth R. S. Axisymmetric dynamic buckling of clamped shallow spherical shells. Technical report, NASA TN D-1510, 1962.

[93] Svalbonas V. and Kalnins A. Dynamic buckling of shells: Evaluation of various methods. *Nuclear Engineering and Design*, 44:331–356, 1977.

[94] Tanov R. and Tabiei A. Static and dynamic buckling of laminated composite shells. In *Proc. of 5th Int. LS-DYNA Users Conf.* to be published, 1998.

[95] Mu J. C. Wu W. Z. and Yang G. T. A numerical calculation of dynamic buckling of a thin shallow spherical shell under impact. *Appl. Math. and Mech.*, 13:125–134, 1992.

[96] Akkas N. and Jackson J. E. Jr. Structural instability in fluid-structure systems under hydrodynamic shock conditions. *J. of Sound and Vibration*, 97:247–259, 1984.

[97] Mustafa B. Al-Hassani S. T. S. and Reid S. R. Axisymmetric dynamic buckling of submerged cylindrical shells. *Comp. and Struct.*, 47:399–405, 1993.

[98] Jacobs P. F. *Stereolithography and other RP & M: from rapid prototyping to rapid tooling.* SME, Michigan, 1996.

[99] Jacobs P. F. *Rapid Prototyping and Manufacturing - fundamentals of stereolithography.* SME, Michigan, 1st edition, 1992.

Appendix A

Pre-experiment charge size estimate

Previous experiments revealed 1g of detonator 79 at 5.0m stand off generated -250$\mu\varepsilon$ at the stand off point on the prototype shell[4]. The strength of 1g detonator 79 ca be assumed approximately equivalent to 1g TNT. Using this result and the shock factor relationship ($\frac{\sqrt{W}}{R}$) an estimate for the strain levels generated by 10g EDC-1 is outlined below.

At 5.0m stand off, shock factor for 1g TNT, $SF_{1g}^{5.0m}$,

$$SF_{1g}^{5.0m} = \frac{\sqrt{0.001}}{5.0} = 0.00632 \tag{1}$$

At 1.0m stand off, shock factor for 1g TNT,

$$SF_{1g}^{1.0m} = \frac{\sqrt{0.001}}{1.0} = 0.03162 \tag{2}$$

Hence $SF_{1g}^{1.0m} = 5 \times SF_{1g}^{5.0m}$, i.e., $\varepsilon_{10g}^{1.0m} = 3.162 \times \varepsilon_{1g}^{1.0m}$. Thus the strain generated by 1g TNT at 1.0m stand off is equal to -1250$\mu\varepsilon$.

At 1.0m stand off, shock factor for 10g TNT, $SF_{10g}^{1.0m}$,

$$SF_{10g}^{1.0m} = \frac{\sqrt{0.01}}{1.0} = 0.1 \tag{3}$$

Hence $SF_{10g}^{1.0m} = 3.162 \times SF_{1g}^{1.0m}$, i.e., $\varepsilon_{10g}^{1.0m} = 3.162 \times \varepsilon_{1g}^{1.0m}$. Thus the strain generated by 10g TNT at 1.0m stand off is equal to -3953$\mu\varepsilon$.

The shock factor for EDC-1 can be related to the shock factor for TNT using the relationship between the Chapman-Jouget values,

$$P_{cj}^{EDC-1} = 0.625 P_{cj}^{TNT} \tag{4}$$

Therefore, $SF^{EDC-1} = 1.6 \times SF^{TNT}$, i.e., $\varepsilon^{EDC-1} = 1.6 \times \varepsilon^{TNT}$.

Hence, the strain generated by 10g EDC-1 at 1.0m stand off is estimated to be 1.6 $\times$ that of TNT, i.e. $1.6 \times -3953 =$ **-6324**$\mu\varepsilon$

For the prototype shell the maximum tensile strain the GRP material can sustain under static loading can be calculated from the material properties:

Young's modulus (E)	= 8800MPa
Ultimate tensile strength	= 55.4MPa

Therefore the maximum tensile strain under static loading, $\varepsilon_{max} = \frac{\sigma_{max}}{E} =$ **6295**$\mu\varepsilon$.

The compressive strength of GRP materials is generally taken to be slightly higher than the tensile strength. The maximum strain that could be sustained under dynamic compressive loading will be close to the maximum tensile strain, thus as a conservative estimate the compressive strains generated by UNDEX loading should not exceed the ultimate tensile strains of the prototype shell, i.e. **-6295**$\mu\varepsilon$.

Appendix B

Conference papers

During the course of the research the following conference papers were produced.

1. Royles, R and Boyd, R., *Influence of high performance computing on analysis and design of underwater structures*, Proc. of 25th AIAS National and International Conference on Material Engineering, Gallipoli/Lecce, volume 1, pages 583-590, 4 – 7 September 1996.

2. Boyd, R. and Royles, R., *Modelling free field UNDEX using LS-DYNA3D*, Proc. of 1st European LS-DYNA Conference, Stratford-Upon-Avon, 18: S2.1-2.11, 20 – 21 March 1997.

3. Boyd, R., Royles, R., El-Deeb, K. M. M. and Haxton, R. S., *Fast dynamic transient loading of underwater structures*, Proc. of 11th Int. Conf. on Experimental Mechanics, Oxford, volume 1, pages 23-28, 24 – 28 August 1998.

XXV AIAS NATIONAL CONFERENCE
INTERNATIONAL CONFERENCE ON MATERIAL ENGINEERING
Gallipoli - Lecce, 4-7 September 1996

Influence of high performance computing on analysis and design of underwater structures

R. Royles and R. Boyd

The University of Edinburgh, Department of Civil and Environmental Engineering, Crew Building, King's Buildings, West Mains Road, Edinburgh. EH9 3JN Scotland UK

KEYWORDS: High performance computing, echinodomes, underwater storage, fluid-structure interaction, design, dynamic buckling

ABSTRACT

This paper looks at the design of underwater storage vessels and, in particular, that of the echinodome - an axisymmetric shell of revolution. The process of rapid production of a set of design curves for shape selection is demonstrated along with techniques to support construction.

Features of fluid-structure interaction are described and the approach to the numerical analysis of such problems is outlined using the echinodome. Both transient analysis and dynamic relaxation are employed with the explicit code LS-DYNA3D to determine a suitable form of discretisation for the shell. Comparison is made with experimental data.

Attention is drawn to the phenomenon of dynamic buckling and the role to be played by high performance computing in its study. Procedures for experimental validation are outlined.

INTRODUCTION

Recent advances in computer technology have spawned the development of parallel computing and its efforts are being felt throughout engineering and science. The field of civil and structural engineering are being affected markedly as parallel computing offers potential for extreme performance and feeds the demand for higher computational rates in numerically intensive operations.

The shortage of land space, the search for and recovery of marine resources, and the growing awareness of pollution of the seas has led to a heightened interest in underwater storage. A vessel suited to this purpose is the echinodome [1] based on the shape of the common sea urchin. Its structural form is an optimum one depending on depth of location below the sea surface, the shell wall thickness and the material of construction. There is a unique size and shape for each set of these design parameters and in order to facilitate the choice of a suitable vessel to fulfil the requirements of a

client it is very desirable to be able to select quickly from the range of possibilities available. The rapid production of design curves to aid this task and the process of construction is examined here.

Underwater structures of this kind have to contend with a mixture of dynamic and static loading arising from current, hydrostatic, tidal, wave and wind effects which can be compounded by seismic and shock phenomena, accidental or otherwise.

The ability to make response forecasts for structures subjected to fast transient dynamic loads has been limited in the past by the computing power and organisation in existence. Underwater structural response to such loadings is complex involving both fluid and structural non-linearities. This requires a capability for reassessing rapidly changing geometrical and material properties in order to make realistic predictions of structural behaviour. The establishment of acceptable discretisation for an echinodome, in preparation for transient analysis under shock loading is explained in this work.

The advent of explicit finite element codes, which do not involve matrix inversion, has speeded up the solution process and their adaptation to parallel computing and probable benefits are discussed.

STORAGE UNDERWATER

Underwater structures for storage purposes are by no means a new concept with many examples existing, e.g. in support of the oil industry and its offshore operations as part of production facilities. There is a wide variety of needs for such liquid storage systems covering oil, liquefied natural gas (LNG), potable water, polluted water and other wastes as well as their treatment. The optimum shape for tanks of this type have received close attention recently revealing the benefits of the echinodome [2, 3].

The shape of the echinodome is similar to that adopted by the common sea urchin for its test which is an axisymmetric shell of revolution. This shape is based on the membrane theory and is an optimum one in that the product of stress and wall thickness at all points throughout the shell is constant for a given set of design conditions. The design parameters are pressure head at the apex, wall thickness and material design stress, and for each set of these there is a unique shell shape of uniform strength. This structural form has been used above ground operating as a tension skin for storage of liquid petroleum gas (LPG) and water, and it is evident [1-3] that a more rigid compressive membrane could be used submerged.

SHAPE PREDICTION AND PARALLELISATION

The shape of the echinodome is predicted with the aid of a computer program [1-3] from the predefined parameters of hydrostatic pressure head at the apex, material strength and shell wall thickness. The possible range of data incorporated by these parameters made the execution of the original serial code arduous. Hence the input of data was automated to speed up the calculations and the serial code was parallelised to avoid overloading processors.

The form of parallelisation involving one program replicated over several processors, which execute it using different data, is known as the single-program-multiple-data (SPMD) model of parallel computing. The processors communicate by means of the message passing interface [4].

In this case the arrangement adopted was in the form of a task farm comprising a root controller/worker and seven other processors, see Fig. 1. The eight processors were SUN microsparc 1 50MHz chips each mounted individually in a SUN Classic machine having 16Mb RAM and 200Mb of hard disk. All processors were networked to a SUN Sparc 5 fileserver having a 70MHz , 32Mb RAM, 2.6Gb of external hard disk, and using the SOLARIS 2.4 operating system.

The root processor controlled,

(i) reading information from the file on the server;
(ii) broadcasting common parameters including the design stress and wall thickness values to all workers as well as itself;
(iii) scattering design head values to each worker including itself;
(iv) gathering results from each worker including itself; and,
(v) writing results to the fileserver.

All workers executed the shape prediction program from the fileserver to determine their own group of results.

EFFECTS of PARALLELISATION

The comparative efficiency of the parallel code (using several processors) relative to the serial code (using one processor) was tested over a range of workloads from 100 to 100000 runs. A run constituted a shape prediction for one set of parameters - design head (z_0), design stress (ds), and shell wall thickness t_w.

The results were drawn up in the form of job execution time for a total number of runs using a number of processors, n, in the range $2 \leq n \leq 8$. The execution times were compared with those found by running the same work load using the serial code on one processor. Only for workloads in excess of 1000 runs was any speed-up obtained using the parallel code on more than one processor, as demonstrated in Fig. 2.

DESIGN DATA

The parallelised shape prediction program could produce large amounts of design data more quickly than the serial code [1, 3] making possible rapid selection of a shape to meet a brief and its progress for analysis and detailed design.

Design curves produced for a range of z_0, ds and t_w, included,

(a) operating depth vs capacity, V;
(b) z_0 vs V; (NB Maximum shell height H = operating depth - z_0);
(c) z_0 vs maximum diameter, D;
(d) operating depth vs H/D;
(e) operating depth vs volume of shell material; and,
(f) operating depth vs base diameter.

The serial code was expanded to incorporate the determination of cutting patterns in flat sheet material from which the doubly curved petals of a shell could be formed in metallic materials, woven and rubberised fabrics. (The apex angle of a petal controls the smoothness of a shell surface.) A range of such patterns is shown in Fig. 3 for an apex angle of 10° using steel plate with t_w = 12mm and a single design stress.

In order to provide some appreciation of the form of a cross section through the apex (i.e. a double meridian) for the chosen material, design stress and thickness

covering a range of design heads appropriate to the brief, a family of shapes as illustrated in Fig. 4 could be obtained.

FLUID-STRUCTURE INTERACTION

The presence of a structure in a fluid stream disturbs the free flow and affects the resulting pressure exerted on it - flow velocity, shape and size of structure, proximity of neighbouring objects and surfaces all make a contribution. Offshore underwater structures have to resist an assortment of dynamic and static loads caused by current, hydrostatic, tidal, wave and wind effects. Shock phenomena arising from earthquake, impact and explosion are sources of transient dynamic load, particularly fast in the latter case, effects of which can be accentuated by movement of a structure relative to the fluid. Structural response to this type of loading is intricate [5] and accurate predictions of behaviour are not easy to achieve. Hence much emphasis has to be placed on the need for well validated computer modelling.

DISCRETISATION

In preparation for a numerical study of echinodomes subjected to explosive loading underwater it was essential to establish an acceptable form of discretisation. Previously [6, 7] implicit semi-loof thin shell isoparametric elements were used for static loading problems. These elements were mainly eight noded quadrilaterals having 32 degrees of freedom (d.o.f.) per element with a ring of six noded triangles at the apex and a fixed base. By contrast it was felt that the use of four noded thin shell explicit elements (24 d.o.f. per element) would reduce overall computation time considerably.

Using the static loading problem involving a symmetric concentrated load of 300N at $\phi = 60°$ from the apex [6] as a basis for experimental validation the LS-DYNA3D code [8] was employed to simulate the problem numerically. Three element meshes were tried (fine = 27400, medium = 7148, and coarse = 936 elements) along a range of elements from its shell element library; see Fig. 5(a) for the coarse mesh.

The pre-processing was performed with the aid of Hypermesh [9], and the solution carried out using both transient analysis and dynamic relaxation (DR). The point load was simulated both as concentrated at one node and as a pressure distributed over four elements having the load point as a common node.

Little difference in response prediction was found between the various elements types, and the pressure load simulation was economical in solution time and resulted in the most realistic prediction of load point normal deflection, δ_{lp}, of 0.67mm compared with 0.61mm experimentally [6]. In all simulations by means of a concentrated load at a single node the deformed mesh suffered from hourglassing (alternate widening and narrowing of the deformed mesh and rippling of the surface near the load point) but did not do so for pressure load simulations, see Fig. 5(b) and (c). There was little to choose between a pressure ramping and a pressure step loading simulation regarding displacement response prediction as can be seen in Fig. 6.

BUCKLING PHENOMENA AND HPC

Under fast transient dynamic loadings shell structures are able usually to withstand brief applications of stresses very much in excess of their static material strength. However, due to the presence of non-linearities (geometrical and material) in

real thin shell structures there is a danger of buckling occurring under dynamic conditions at loads well below those predicted statically [6, 7, 10] especially in a fluid medium.

High performance computing (HPC) using parallelised versions of codes such as LS-DYNA3D with a coupled Eulerian fluid modeller would be better suited to predicting the response of structures to underwater shock loading than implicit finite element codes. Such predictions would require experimental validation which could be achieved by a combination of destructive and non-destructive testing. Using response data (e.g. from suitably located electrical resistance strain gauges) gathered during the forced excitation predictions could be made of dynamic buckling loads [11] and comparisons drawn with some destructive testing.

DISCUSSION

Benefits from the parallelisation of the shape prediction program (SPMD model) were achieved only at high work loads. In this program the computational demand was not high - a single run required the solution of only one first order differential equation. Spreading of a work load over more than one processor would introduce communication time between processors which would become a dominant proportion of the overall execution time. At some work loads it might be expected that there could be an optimum umber of processors above which no more speed-up in execution time could be obtained. For example in Fig. 2 it can be seen that for the particular work load not much advantage was gained by using more than six processors.

Fig. 4 gives the minimum total water depth required for a shell having a particular design head with uniform stress and wall thickness and an indication of the shape. The actual design head could be dictated by the 100 year wave height for the location as well as the maximum draft of shipping in the area.

In the search for a suitable element type and discretisation to be used in future transient analyses of the echinodome under explosive loading all shell element types in the LS-DYNA3D library [8] seemed to perform well in the appointed task. However concentrated loading applied at a single node caused hourglassing whereas distributing the same load as pressure over four elements having the load point as a common node did not produce such mesh distortions. Little advantage was found in using the fine or medium meshes as opposed to the coarse one, although the medium mesh provided a load intensity very close to that prevailing in the experiment. Interestingly the solutions obtained using the finer meshes suffered from a slight static shift in the transient analyses. Such a shift was not present in the static experimental results and when this shift was removed close agreement was obtained among the results from the three meshes. Transient analysis and dynamic relaxation gave comparable results, the latter method being much more economic in CPU time.

CONCLUSIONS

1. Significant savings in job execution time can be achieved at high work loads ($\geq$ 1000 runs) by parallelising the shape prediction program.
2. A coarse mesh (936 elements) proved adequate for analysis purposes and saved on CPU time.

3. Dynamic relaxation with light damping and transient analysis compared very closely and gave predictions within 10% of the experimental result.

ACKNOWLEDGMENTS

The authors are grateful for the support of the Engineering and Physical Sciences Research Council, the M.o.D. DRA Dunfermline., and OASYS Ltd. Gratitude is expressed to the staff of the Edinburgh University Department of Civil and Environmental Engineering, and those of the Edinburgh University Computing Service who assisted with this work.

REFERENCES

[1] R. Royles, A. B. Sofoluwe, M. M. Baig, & A. J. Currie: "Behaviour of underwater enclosures of optimum design", Strain, 16, 1, (1980), 12-20.

[2] R. Royles & J. M. Llambias: "Storage aspects of liquid gases underwater and the structural implications", Proc. Int. Symp. on 'Storage and transport of LPG and LNG', Koninlijke Vlaamse Ingenieursvereniging, Technologisch Institut (Kommissie Metaalbouw), Antwerpen, Belgium, 2, (1984), 55-72.

[3] K. M. M. El-Deeb: " Echinodome response to dynamic loading", Ph.D. thesis, The University of Edinburgh, (1990).

[4] Message Passing Interface Forum: "MPI: a message passing interface standard", M.P.I.F, The University of Tennessee, Knoxville, Tennessee, USA, (May 1994).

[5] R. Royles & K. M. M. El-Deeb: " Behaviour of an echinodome under fast dynamic transient loads", Proc. of BSSM Annual Conference, University of Sheffield, 5-7 September, 1995, BSSM, Guildford, (1995).

[6] R. Royles & K. M. M. El-Deeb: " Static buckling appraisal of an echinodome", Experimental Mechanics, 33, 4, (1993), 263-269.

[7] K. M. M. El-Deeb & R. Royles: "Dynamic and static buckling assessment of an echinodome", Computers and Structures, 46, 5, (1993), 899-904.

[8] OASYS: "OASYS LS-DYNA3D - user manual", Version 6.1 (LS-DYNA3D 936) London, UK, (Oct 1995).

[9] Altair: "Hypermesh", Version 2.0, Altair Comp. Inc, Troy, Michigan, USA, (1995).

[10] Akkas & J. E. Jackson, jr: "Structural instability in fluid-structure systems under hydrodynamic shock conditions", Journal of Sound and Vibration, 97, 2, (1984), 247-259.

[11] R. Royles: "Non-destructive buckling examination of an echinodome", Proc. 10th Int. Conf. on Experimental Mechanics, Lisbon, 18-22 July 1994, A. A. Balkema, Rotterdam, 1, (July 1994), 599-605.

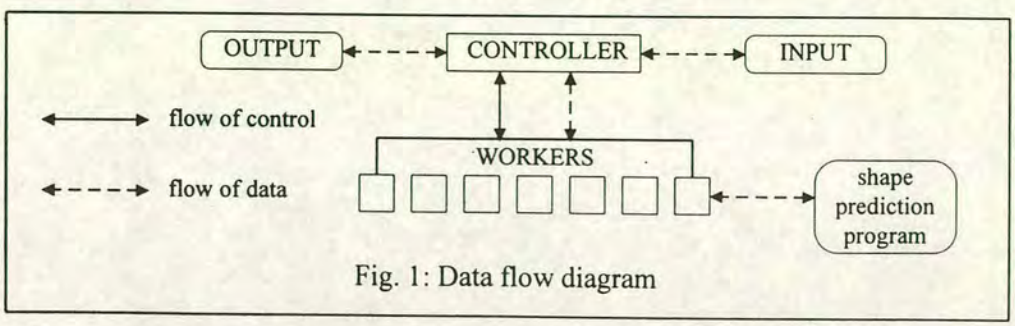

Fig. 1: Data flow diagram

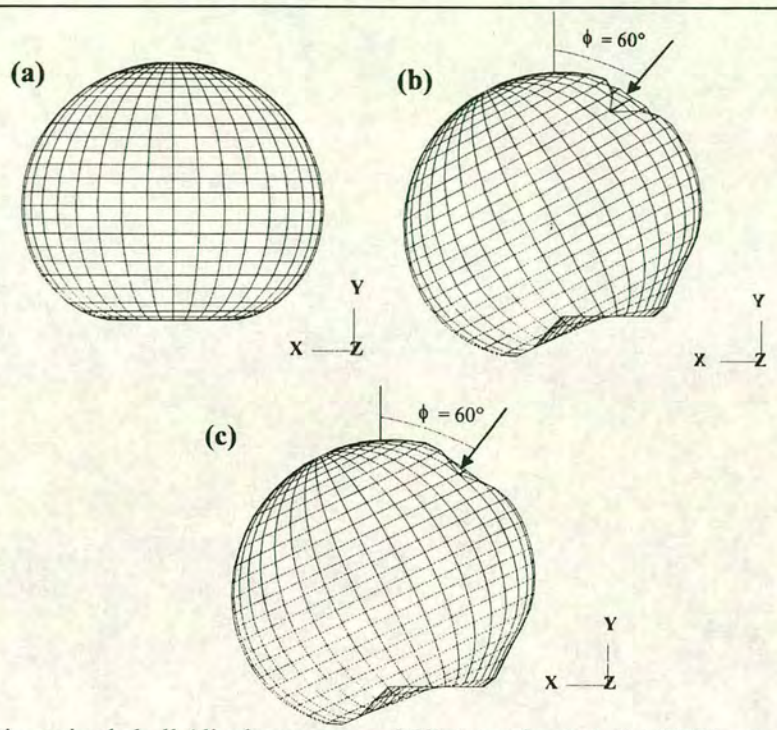

Fig. 7: Discretised shell (displacements × 250) (a) unloaded, (b) 300N concentrated load, (c) 300N pressure load

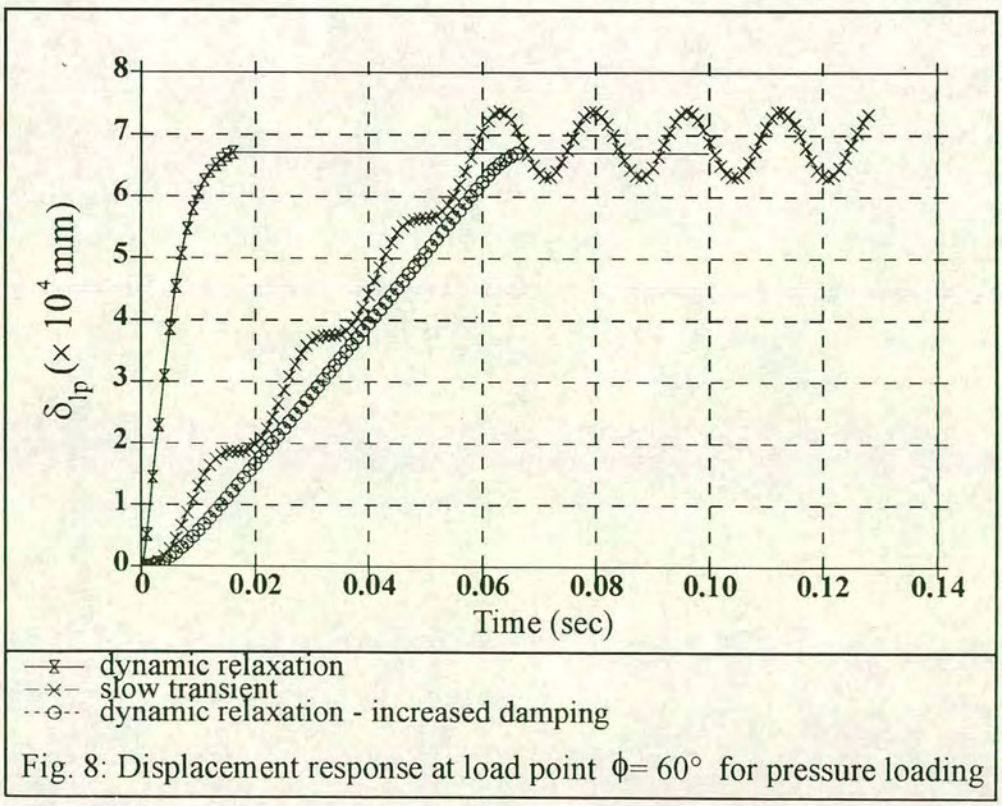

Fig. 8: Displacement response at load point $\phi = 60°$ for pressure loading

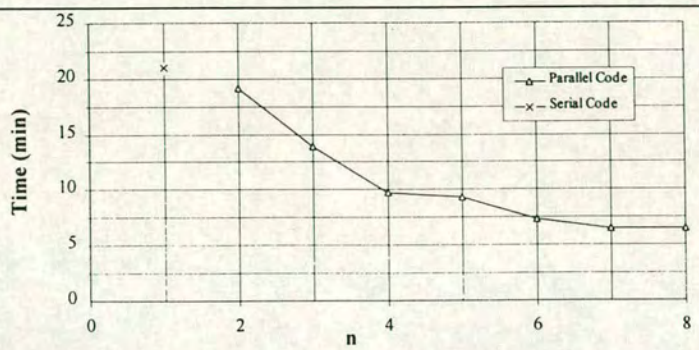

Fig 2: Effect of number of processors, n, on job execution time for 10000 runs

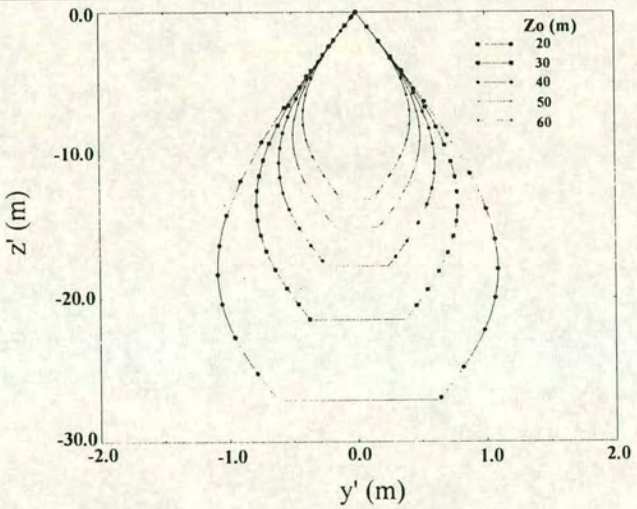

Fig. 5: Cuttings patterns on flat sheet

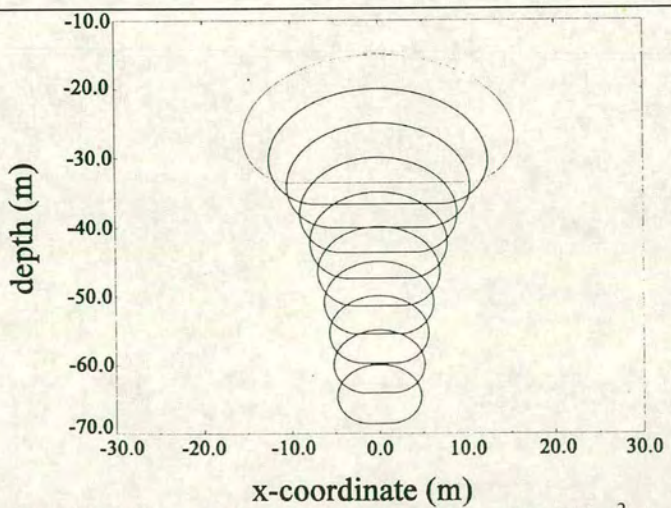

Fig. 6: Family of 2D shapes - double meridian (ds = 120MN/m^2; z_0 = 15-45m)

MODELLING FREE FIELD UNDEX USING LS-DYNA3D

by

R Boyd and R Royles

University of Edinburgh
Scotland

ABSTRACT

This paper examines the capability of LS-DYNA3D v6.1 to model underwater explosion (UNDEX) phenomena in the free field environment.

A free field UNDEX problem consists of many complex phenomena, including detonation and shock wave propagation, which are considered here. Two examples are utilised to examine the modelling of these phenomena under isolated conditions and a third example models the interaction of both phenomena using an infinite cylindrical charge.

All three examples indicate a good comparison with known theoretical results or correlate closely with trends in experimental pressure profiles.

INTRODUCTION

Early developments in the analysis of fluid and structural responses to fast transient dynamic events consisted largely of experimental techniques. Full scale and large model testing were used to measure the physical processes involved and were relied upon heavily as little was understood about the physics of the events. However, recent advances in numerical techniques coupled with a better understanding of the analysis of the physics behind such an event has shifted the reliance on these early techniques to alternative analytical and numerical approaches. Testing techniques are generally very expensive and reduced funding necessitates the search for suitable options.

In a complex submerged structural system the prediction of fluid and structural responses to fast transient dynamic events requires a thorough understanding of the physics of such events. Underwater explosions constitute such an event and the physics of underwater explosion loadings (UNDEX) make it difficult to predict the dynamic forces to which a structure may be subjected.

The research into numerical methods to assist in the study of UNDEX phenomena has led to the development of many general purpose codes (hydrocodes)[1]. LS-DYNA3D is such a code, capable of handling non-linear, large structural response problems. The validation and verification of LS-DYNA3D on a simple numerical model is an essential part of the analysis procedure if results are to be taken as both accurate and reliable at a later stage in the development of a more complex model.

UNDEX PHENOMENA

The physical characteristics of an underwater explosion event and their mathematical treatment have been studied previously[2]. Some of the events are explained briefly below.

Detonation Process

An explosion is a chemical reaction converting the original material of the explosive into gaseous products at very high temperatures and pressures. The process occurs with extreme rapidity and involves a large release of energy. The explosive material is generally an unstable compound which undergoes a reaction initiated by mechanical impact or thermal radiation onto especially sensitive material which in turn initiates the reaction in the main body of the explosive. This is known as detonation. Once initiated a detonation wave propagates through the explosive material behind the shock front at very high speed. The shock front is the narrow region (reaction zone) separating exploded material (hot compressed gases) from unexploded (solid) material. The propagation speed of the detonation wave is a characteristic of each explosive material.

Shock Wave

The result of the detonation process is a disturbance of the surrounding water. This takes the form of a compression wave, or shock wave, propagating radially outwards from the point of detonation. This shock wave is characterised by very steep fronts, separating the exploded material (gases) from the surrounding water. The speed of the wave however decreases rapidly from several thousand m/s close to the detonation point to the speed of sound in water (typically 1400-1500m/s) at some distance from the detonation point. In the vicinity of the detonation a large amount of heat is dissipated as the shock wave propagates outwards. This is due to the steep pressure and velocity gradients characteristic of the shock front.

Other associated events not considered in this paper include the resulting gas bubble and bubble loading, linear and non-linear structural dynamics, fluid-structure interaction, bulk and local cavitation, acoustic wave propagation and ocean effects.

ANALYTICAL MODELS

Following are three example problems which demonstrate clearly the capability of modelling UNDEX phenomena using LS-DYNA3D. Examples 1 and 2 are taken from the DYTRAN examples manual[3].

Example 1: Modelling steady state detonation

The first example models the detonation of an explosive slab and compares the peak pressure behind the shock front against that of the theoretical Chapman-Jouget pressure[2]. The purpose of this example is to illustrate plane wave detonation without the complexities of a fluid medium being present.

A slab of explosive, COMP B, 10mm × 10mm × 500mm, is detonated at one end. A one dimensional mesh of 200 Eulerian elements is used to represent the slab length, entailing an element thickness of 2.5mm, as illustrated in figure 1. The explosive material itself is represented by the Jones-Wilkins-Lee (JWL) equation of state[4] in which the pressure, P, is given as,

$$\left(1-\frac{\omega}{R_1 V}\right)e^{-R_1 V}+B\left(1-\frac{\omega}{R_2 V}\right)e^{-R_2} \qquad (1)$$

where A, B, ω, R_1,R_2 are material constants, E is the internal energy and V the relative volume. All material constants are given in table 1 from the LLNL handbook[5]. A wall (no flow) is declared across all sides of the slab. However nodes are free to move along the longitudinal length of the slab.

Symbol	Parameter	COMP B
ρ_o	density	1717 kg/m^3
D	detonation velocity	7980 m/s
P_{cj}	Chapman-Jouget pressure	29×10^9 Pa
A	material constant	5.24229E11
B	–	0.07978E11
R_1	–	4.2
R_2	–	1.1
ω	–	0.34
E_o	initial internal energy	8.499E9 Pa
V_o	initial relative volume	1.0

Table 1: Properties of explosive charge for JWL test

LS-DYNA3D uses the "programmed + beta burn" technique to model the detonation of the explosive material. This technique involves burn fractions, which multiply the equations of state for high explosives, and control the release of chemical energy over the burn time for each element as the detonation front propagates through the explosive material. Upon ignition a lighting time is computed for each element by dividing the distance from the detonation point to the centre of the element by the detonation velocity[3]. The

detonation front is a plane wave progressing along the length of the slab. The ignition point is the centre of the left face of the mesh, as shown in figure 1(b) and the time of ignition is at the start of the analysis.

The duration of analysis is the 60μsec necessary to burn 500mm of slab at the detonation speed and pressure profiles are requested every 1μsec.

The Chapman-Jouget pressure for a γ-law gas is given by $P_{cj} = 2\,(\gamma_{cj} - 1)\,E_o$.

DISCUSSION OF RESULTS

Figure 2 shows the peak pressure profiles behind the detonation front at various distances along the slab length. The dashed line represents the theoretical Chapman-Jouget pressure. The detonation wave propagates through the explosive material increasing the Chapman-Jouget pressure, converging to a final value of 28.48×10^9 Pa. These results are very acceptable in consideration that JWL equation of state parameters for explosives are valid only for large charges[5]. The shock front is smeared over four elements characteristic of the steep pressure gradient expected. This smearing effect leads to the reduction in final pressure to 98% of the theoretical value (see table 1). The exponential decay is expected behind the shock front.

Example 2: Modelling of a shock tube

A shock tube is a rigid cylinder consisting of two gases separated by a gas tight diaphragm. The two gases are initialised by applying a pressure difference across the diaphragm. The resulting high and low pressure difference regions are known as the compression and expansion chambers respectively. When the diaphragm is ruptured the pressure equalises by means of a shock wave propagating into the expansion chamber and a rarefaction wave propagating into the compression chamber (see figure 3(a)).

This second example models the movement of a shock wave and a rarefaction wave along the length of a shock tube and compares velocity and pressure peak values of the shock tube against analytical values. The purpose of this model is to demonstrate low velocity shock wave propagation.

Symbol	High Pressure, P_1	Low Pressure, P_2
density, ρ (kg/m^3)	1.0	0.125
velocity, u (m/s)	0.0	0.0
specific internal energy, e (Pa)	2.5	2.0
pressure, P (Pa)	1.0	0.1

Table 2: Initial conditions

A shock tube 1m in length and 0.1m in diameter contains two adjacent gases at the initial conditions given in table 2. The gases are separated by a diaphragm at 0.5m. The model comprises 6400 Eulerian elements representing the gases, as illustrated in Figure 3(b). Both ends of the shock tube were closed allowing reflection of both the shock wave in the expansion chamber and of the rarefaction wave in the compression chamber. The gases are represented by the γ-law form of the linear polynomial equation of state[4] for which the pressure, P, is given by

$$P=(\gamma-1)\frac{\rho}{\rho_o}E \qquad (2)$$

where γ is a material constant equal to 1.4 and E is the internal energy. The gases in the shock tube are initialised at time t = 0 and the boundary between them has a single discontinuity. At t > 0 the high pressure gas has a rarefaction front with velocity u_r moving into the compression chamber, and the low pressure gas has a shock front with velocity u_s moving into the expansion chamber. In the region between the shock front and the tail of the rarefaction wave the velocity is constant. There is a contact discontinuity[6] at the position where the gas, originally at the diaphragm, once occupied. On either side of this position the materials are moving with the same velocity u_c.

The analysis lasts for 338ms, time necessary for the shock wave to reflect off the closed end of the expansion chamber.

DISCUSSION OF RESULTS

Figures 4(a) and (b) show pressure-distance and velocity-distance plots respectively for a particular instance in time.

Pressure-distance

The general profile of the pressure-distance curve corresponds with the theoretical prediction. However the oscillations in the pressure-distance profile at the wave fronts (rarefaction and shock) are uncharacteristic with those predicted[6]. The analytical value for the pressure at the point of contact discontinuity P_c is 0.303Pa[7-9] which compares with a numerical value of 0.32Pa at the peak pressure behind the shock front. The plateau behind the peak is closer to the analytical value.

Velocity-distance

The general profile of the velocity-distance curve corresponds with the theoretical prediction. However, at the same points as in the pressure-distance plot oscillations occur in the velocity curve moving towards the wave fronts from the compressed gas to the expanded gas. The analytical value for the velocity at the point of contact discontinuity u_c is 0.927m/s[7-9] which compares with a numerical value of 0.95m/s at the peak velocity behind the shock front. The plateau behind this peak value is closer to the analytical.

The reduction in both pressure and velocity just behind the shock front is not consistent with theory. However, these results are sufficiently close to the predicted value to be acceptable.

Example 3: Free field UNDEX

The third example represents an infinite cylindrical charge (material characteristic as in table 1) with the objective of investigating the modelling of detonation and shock wave propagation at much higher velocities than those experienced in the shock tube example. The purpose of this model is to examine the pressure profiles of the free field UNDEX and compare them with known experimental pressure profiles.

A two dimensional model is constructed of the problem and illustrated in figure 5(a). The model comprises a slice through an infinite cylindrical charge, radius 0.059m and water surrounding the charge to a radius

of 3m, measured from the centre of the charge. The slice is 0.01m in thickness. Gravity is not accounted for in the model, therefore this model is only an approximation.

Thirty two arbitrary Lagrangian-Eulerian (ALE) elements are used to model the charge and a radial mesh extends out from the charge consisting of 160 ALE elements. The ALE elements undergo ALE smoothing permitting periodic rezoning[10] of the large displacements caused by the detonation of the explosive (see figure 5(b)).

DISCUSSION OF RESULTS

Figure 6 shows a plot of pressures measured at five points along the z-axis, i.e. vertically upwards from the charge. peak values are about one tenth of the magnitude of those obtained from the JWL test. As expected, the peak pressure reduces as the shock wave propagates away from the charge. Furthermore, the duration of the transient pressure increases as the peak pressure reduces. Each pressure profile is observed to exhibit multiple peaks or pressure oscillations associated with the exponential decay. These have been observed experimentally by both El-Deeb[11] and Cole[2] but are not generally as pronounced for a typical theoretical pressure-time response. These multiple peaks may be the result of dispersion problems when modelling interference of pressure fronts within the charge, as observed by Molyneaux[12], which are associated with the van Leer MUSCL scheme adopted in LS-DYNA3D. These dispersion problems are known to introduce oscillations[13].

Figure 7 illustrates pressure contour plots at 100μsec,1ms, 1.6ms and 2ms for the model. A cylindrical charge would not normally give rise to a spherically symmetric pressure distribution. However, a spherical pressure wave was expected to be produced since this is a 2D model. In close proximity to the charge the shock wave is seen to be symmetric about the charge and this is maintained throughout the duration of the analysis. At 2ms the pressure wave has moved beyond the confines of the modelling and the remaining pressure contours shown represent the state of the water behind the peak.

CONCLUDING REMARKS

The three examples studied indicate that LS-DYNA3D v6.1 could be applied with some degree of confidence to investigations of UNDEX phenomena involving detonation and propagation of shock waves in a free field situation. However, some peculiarities of behaviour predicted by such numerical simulations do exist and require further close examination.

ACKNOWLEDGEMENTS

The authors are grateful for the support of the M. o.D. DERA, Dunfermline, the EPSRC, Swindon and Ove Arup Systems Ltd, London.

REFERENCES

[1] Mair, H. U.: *Hydrocode methodologies for underwater explosion structure /medium interaction*, SAVIAC, Proceedings of 66th Shock & Vibration Symposium, 2, (1995).

[2] Cole, R. H.: *Underwater explosions*, Princeton University Press, New Jersey, USA, (1948).

[3] MacNeal-Schwendler Corporation: *MSC/DYTRAN example problem manual*, Los Angeles, CA, USA, (April 1995).

[4] Oasys: *LS-DYNA3D User's manual - version 6.1 (LS-DYNA3D 936)*, London, UK, (Oct. 1995).

[5] Dobratz, B. M.: *LLNL Explosives handbook - properties of chemical explosives and explosive simulants*, UCRL-52997, Lawrence Livermore National Laboratory, Livermore, CA, USA, (1981).

[6] Wright, J. K.: *Shock Tubes*, Methuen & Co. Ltd, London, UK, (1961).

[7] Buis, J. P.: *Analysis of Shock Tube Calculations Performed by the PISCES-2DELK/V4 Code*, PISCES International B. V., Netherlands, (1987).

[8] Harlow, F. H. and Amsden, A. A.: *Fluid Dynamics*, Los Alamos Scientific Laboratory Monograph, USA, (1971).

[9] Jardin, S. C. and Hoffman, R.: *Simulation of explosive processes in PISCES-1DL*, Physics International Company, (1972).

[10] Hallquist, J. O.: *LS-DYNA3D Theory Manual - Version 6.1 (LS-DYNA3D 936)*, LSTC, Livermore, CA, USA, (Oct. 1995).

[11] El-Deeb, K. M. M.: *Echinodome response to dynamic loading*, PhD Thesis, University of Edinburgh, (1991), Ch. 5.

[12] Molyneaux, T. C. K., Li, L. and Firth, N.: *Numerical simulation of underwater explosions*, Computers and Fluids, Elsevier Science Ltd., 23, 7, (1994), 903-911.

[13] Benson, D.J.: *Vectorization techniques for explicit arbitrary Lagrangian-Eulerian Calculations*, Computer Methods in Applied Mechanics and Engineering, (1992).

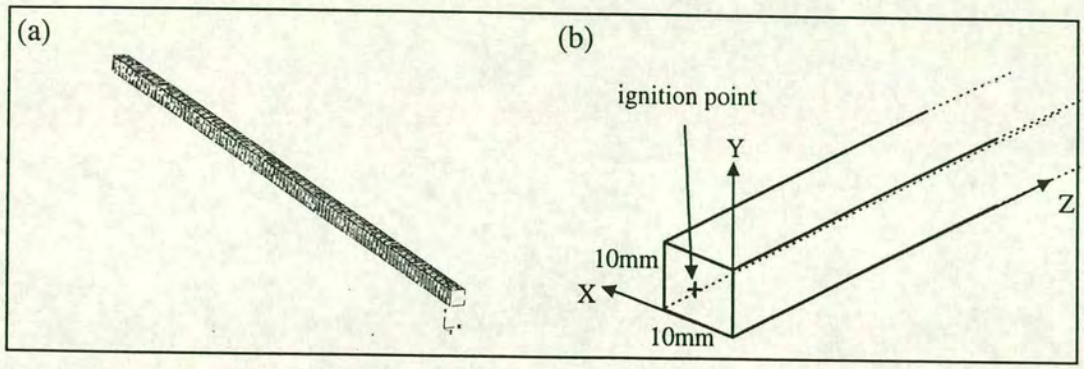

Figure 1: (a) Finite element mesh, (b) geometry of material and detonation point

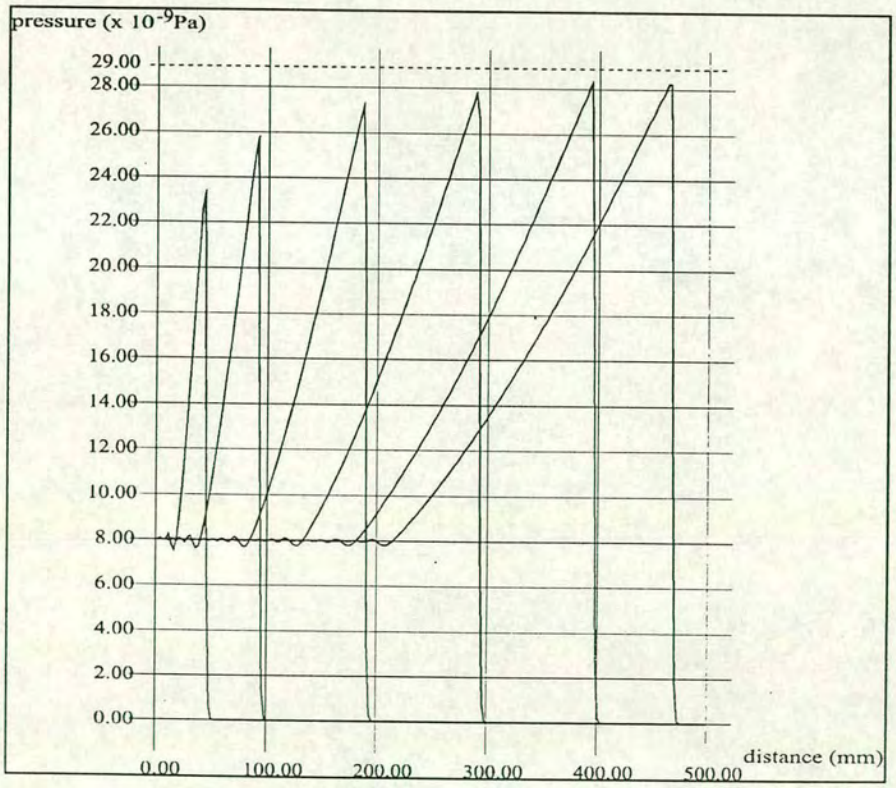

Figure 2: Peak pressure profiles along length of slab

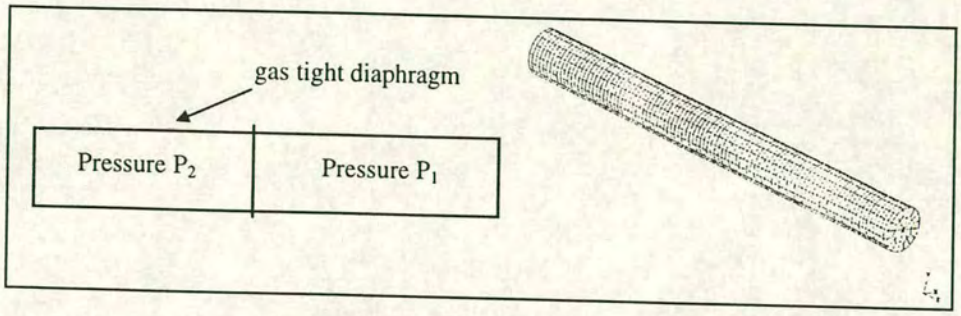

Figure 3: (a) Shock tube, (b) finite element mesh

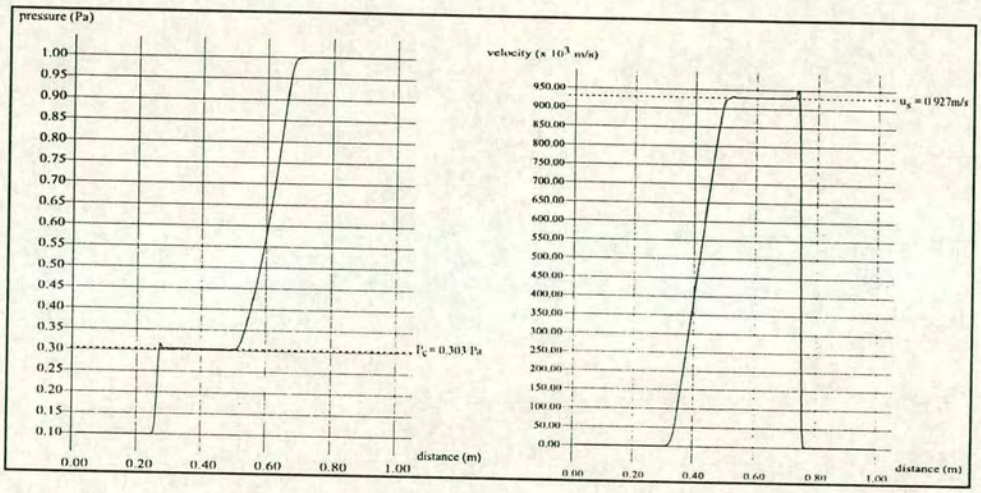

Figure 4: (a) Pressure response along length of shock tube, (b) material velocity along length of shock tube (distance measured from low pressure end)

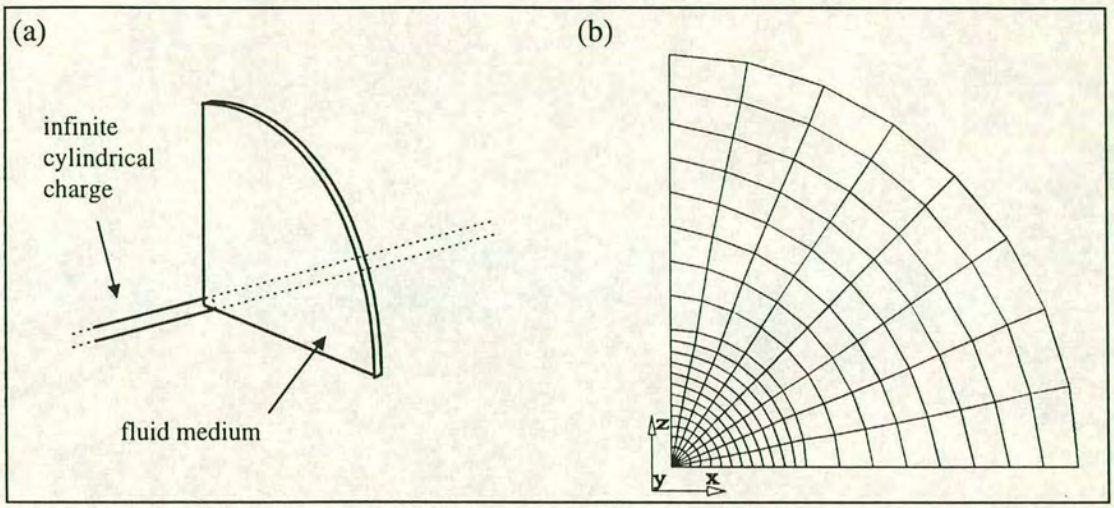

Figure 5: (a) Slice through infinite cylindrical charge, (b) finite element mesh

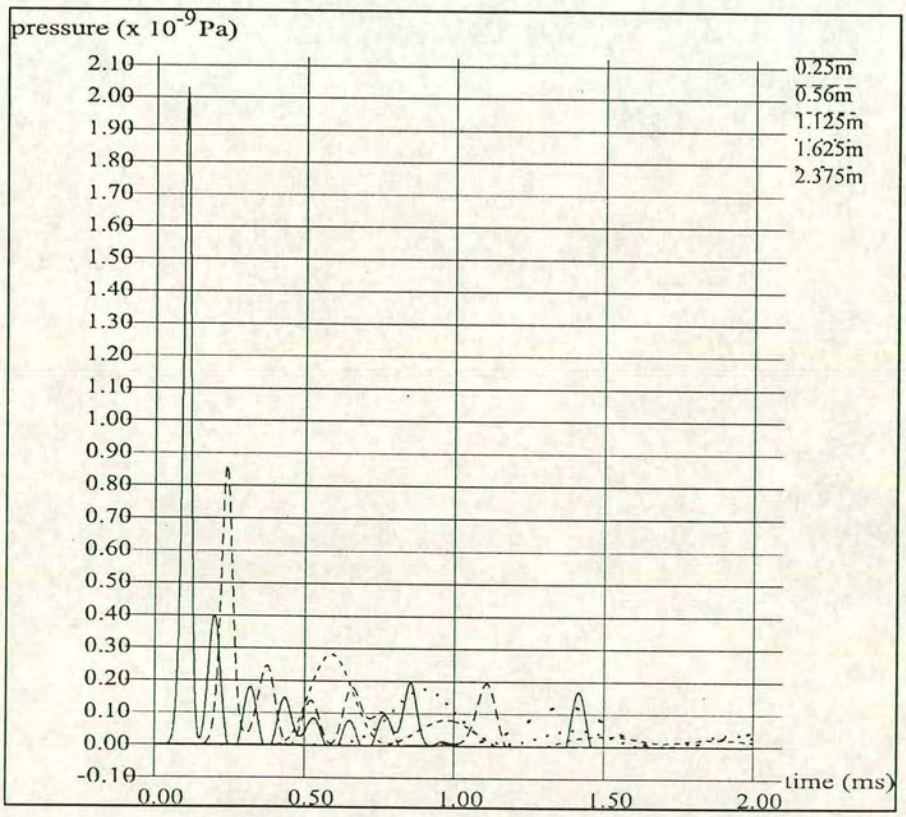

Figure 6: Pressure-time profile for free field UNDEX

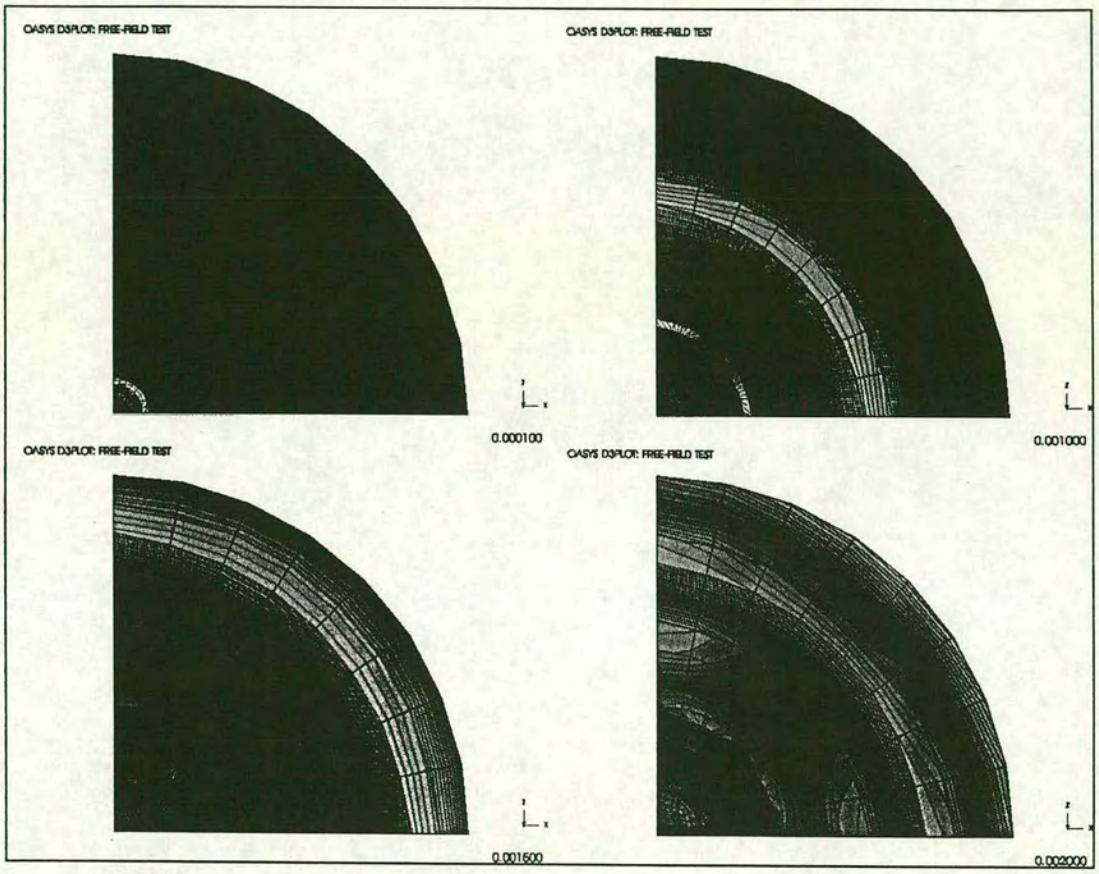

Figure 7: Contour plots at different times for free field UNDEX (unit: secs)

Experimental Mechanics, Allison (ed.) © 1998 Balkema, Rotterdam, ISBN 90 5809 014 0

Fast dynamic transient loading of underwater structures

A.R.Boyd & R.Royles
Department of Civil and Environmental Engineering, University of Edinburgh, UK
K.M.M.El-Deeb
Linear and Non-Linear Structural Dynamics Limited, Edinburgh, UK
R.S.Haxton
DERA, Rosyth, UK

ABSTRACT: The application of a hydrocode, LS-DYNA3D, to the modelling of the response of an underwater structure, an echinodome (axisymmetric thin shell of revolution of optimum form), to UNDEX loading is considered. Comparison is made with experimental data for validation purposes and the phenomenon of dynamic buckling is assessed. A future strategy for assessing the effects of rapid dynamic loadings on underwater structures is outlined.

1 INTRODUCTION

Under fast dynamic transient loads shell structures are able usually to withstand brief application of stresses well in excess of their static material strength. However, due to the presence of non-linearities in real structures - geometrical and material, with emphasis on the former - there is a danger, under dynamic conditions, of buckling failure occurring at loads far below those predicted by static analysis (Akkas & Jackson 1984, El-Deeb & Royles 1993, Royles & El-Deeb 1993, Gourinat & Benyahia 1997).

Dynamic behaviour in these circumstances can be demonstrated by full scale prototype testing (Haxton 1990) although it is expensive to perform especially in relation to underwater structures. As a result numerical modelling of such behaviour is desirable and particularly so in the case of structures subjected to underwater explosive loading, UNDEX which become computationally very intense in their simulation. Predictions of structural response to UNDEX events can be made by the doubly asymptotic approximation, DAA, (Geers 1978, Deruntz 1989, Haxton et al. 1995) a technique in structural dynamics for applying a fluid /structure interaction load onto a structure. It involves the precalculation of the load and represents a decoupling of the structure, from the fluid, approach. In consequence it does not permit the movement of a shock wave through a fluid and subsequent bubble pressure loading to be modelled. Non-linearities which can occur in that type of medium (eg arising from cavitation) are unable to be taken into account by the DAA except at the fluid structure boundary (Miller 1994, Hamdan & Hobbs 1997). Hence, attention is turning towards a mixed method of representation - Eulerian for the fluid and Lagrangian for the structure (Hirt et al. 1974, Belytscho et al. 1978, Donea et al. 1979) - which has been embodied to a varying extent in codes capable of simulating wave propagation in both slid and fluid media, ie hydrocodes. Attempts so far to apply such codings to shock analysis problems (Lenselink & de Vries 1994, McKeown et al. 1994, Chisum & Shin 1995) have met with partial success (Mair 1996).

The advent of high performance computing could aid the prosecution of such complex problems in such more reasonable time-scales than has been possible in the past and offer an opportunity for raising the accuracy of prediction. It was with this in mind that the work reported here was undertaken. The paper describes the application of a hydrocode, LS-DYNA3D (LSTC 1997) to the modelling of the response of an echinodome - an axisymmetric thin shell of revolution of optimum form - to UNDEX loading. The predicted behaviour is compared with physical validation data and buckling tendencies are assessed.

2 OPTIMUM FORM UNDERWATER VESSELS

For some time the use of underwater vessels of optimum form, the echinodome, have been advocated for storage purposes (Royles et al. 1980,

Royles & Llambias 1984). The optimum nature stems from the ability to select a shape giving the required capacity in a particular location at a depth, $z_o \geq 1$ x the prevailing 100 year wave height below the mean sea level such that for a uniform shell wall thickness, t_w, and a design stress, σ_d (suitably factored relative to the ultimate wall material strength), the stressing throughout the shell wall would be uniform and of magnitude σ_d. In addition z_O has to be in excess of the draft of the largest ships capable of operating in the area.

The best method of operation for underwater structures of this type is in a floating, submerged and tethered manner (Figure 1). By so doing anchorage and foundation problems are minimised, vessel recovery is facilitated, and because of the depth prescription relative to the water surface hydrodynamic forces are rendered less dominant than fluctuating static effects. Seismic events would be accommodated more readily by the tethered form of anchorage than by direct location of the structure on an ocean or lake floor.

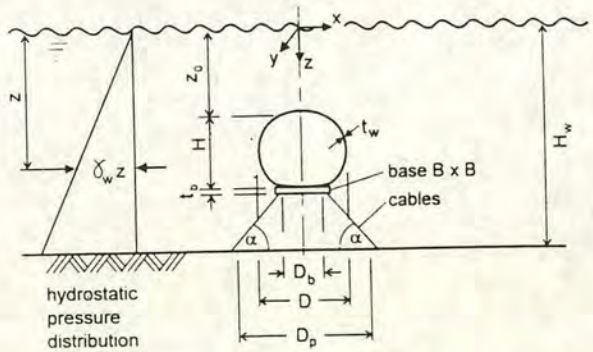

Fig. 1 Tethered form of echinodome

Very significant short duration deformations and stresses could arise in this type of structural system due to impacts from dropped or powered or towed objects even though some mitigation of these effects could be expected due to tethering (El-Deeb & Royles 1993). However, an even greater threat to the structural integrity of an underwater storage system is posed by fast dynamic transient loadings caused by material rapid phase transitions (possibly impact initiated) and explosions. In this report it is the effects of these latter loadings which are examined in more detail.

3 FAST DYNAMIC TRANSIENT LOADS

3.1 *Rapid phase transition*

The spillage of a cryogenic liquid resulting in superheating to an extent that permits homogenous nucleation to occur producing an over pressure is termed a rapid phase transition (RPT), (UKELG 1989).

Liquid natural gas (LNG) is a valuable and hazardous commodity stored either under high pressure or at very low temperatures, or by using an intermediate combination of both conditions. It has been suggested previously (Royles & Llambias 1984) that notable safety advantages could be gained by storing LNG underwater in echinodomes. However, an escape of LNG from an underwater container would lead to an RPT as the cold or high pressure liquid came into contact with the surrounding water. Shock waves would be transmitted to nearby structures including the container itself and the event would resemble in many ways an explosion.

3.2 *Underwater explosions*

An explosion represents a rapid release of energy in a short time. As explosive material is triggered into fast chemical reactions gaseous matter is produced at very great temperatures. When this takes place under water the surrounding fluid compresses the explosive gases into a spherical bubble. Initially during the detonation phase compression waves are generated at the boundary between gas and surrounding water in the form of shock waves travelling at a mean velocity, some distance from the charge, in the range 1400 to 1500 m/s. The time history for such a wave has a very steep pressure front with an exponential decay from the initial peak. Firstly, the gases are under maximum compression occupying minimum volume. After the shock wave emission the pressure drops as the bubble expands with water flowing outwards so long as the internal bubble pressure exceeds the water pressure (ie the sum of the external atmospheric and the hydrostatic pressure). Maximum bubble diameter is achieved when the gas and water pressures equalise and as the gas pressure drops below this level the bubble contracts and inward water flow begins until a minimum radius is achieved. This coincides with the attainment of a second peak pressure much lower in magnitude and broader of crest than the first. It is the first bubble or secondary pulse and a number of

such cycles of expansion and contraction occur before the bubble collapses finally (Cole 1948).

Following detonation the pressure at a particular location can be augmented by reflections of pressure waves from rigid boundaries. In the case of reflections of pressure waves from an air/water boundary (free surface) negative pressures can be set up leading to a phenomenon known as bulk cavitation which can have serious effects on structures in close proximity.

4 FLUID-STRUCTURE INTERACTION MODELLING

The structural type considered in this work was a glass reinforced plastic echinodome (GRP), (Royles et al. 1980), the geometric and material characteristics of which are summarised in Tables 1 and 2.

Preliminary work established the ability of the LS-DYNA3D explicit solver, which is a dynamic program, to deal with hydrostatic effects using either dynamic relaxation or a slow transient approach; and a parallel version of the shape prediction program for an echinodome was developed utilising a series of linked workstations (Royles & Boyd 1996). Subsequently the solver was exercised to demonstrate its capability in simulating the detonation process, shock wave propagation in a fluid, and a complete free field explosive event (Boyd & Royles 1997). This work was carried out on an SGi Indigo2 machine (R4400/150 MHz chip, 320 Mb RAM, Extreme Graphics and 14.9 Gb hard disk).

Table 1. Geometric characteristics of the echinodome (Fig. 1)

Dimension	Value
b	200 mm
D	450 mm
D_b	170 mm
D_p	3260 mm
H	380 mm
H_w	3470 mm
t_b	20 mm
t_w	3.8 mm
z_o	1525 mm

Table 2. Material properties

Property	Value
Shell wall (GRP)	
Ultimate tensile strength	55.4 MPa
Young's modulus, E	8800 MPa
Poisson's ratio, ν	0.36
Mass density, ρ	1100 Kg/m^3
Shell base (Tufnol)	
Young's modulus, E	13200 MPa
Poisson's ratio, ν_b	0.284
Mass density, ρ_b	1360 Kg/m^3
Water	
Unit weight, γ_l	1000 kg/m^3

The modelling of the echinodome structure subjected to a 1g TNT equivalent explosive charge applied symmetrically at a standoff distance R=5m was carried out using LS-DYNA3D with the following features (i) USA (underwater shock analysis), and (ii) USA plus CFA (cavitating fluid analyser). Appropriate pressures to apply at the node points of the boundary segments surrounding the structure were deduced from the field tests (El-Deeb & Royles 1998) assuming an exponential decay from the peak. The discretisation for the USA/CFA simulation (Fig. 2, structure emphasised) included 2124 Belytscho Tsay four noded thin shell structural elements and a 500mm band of acoustic (fluid) elements each of 10 mm radial thickness surrounding the structure. The tethers, indicated in Figure 1, four in all at 90° azimuth separation, were found experimentally (El-Deeb & Royles 1998) to have little influence on response at low charge magnitudes and were ignored in the numerical modelling.

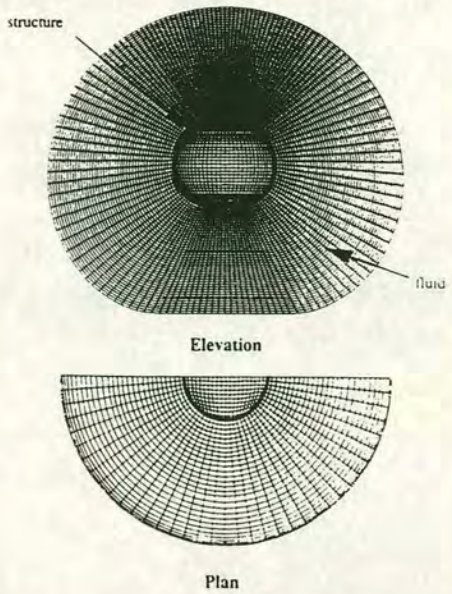

Fig. 2 Discretisation for USA-DYNA3D (acoustic analysis)

The simulation using USA alone was similar to that for the USA/CFA approach but omitted the fluid elements. In both simulations shell thickness variations were taken into account.

These models were run on an SGi Origin 2 workstation having 2 N° R10000/180MHz processors, 512 Mb RAM, Impact Graphics and 18Gb hard disk (external).

5 EXPERIMENTAL VALIDATION

The experimental work referred to here is reported in more detail elsewhere (El-Deeb & Royles 1998). The general arrangement of the structure was as shown in Figure 1 with the associated dimensions and material properties as given in Tables 1 and 2.

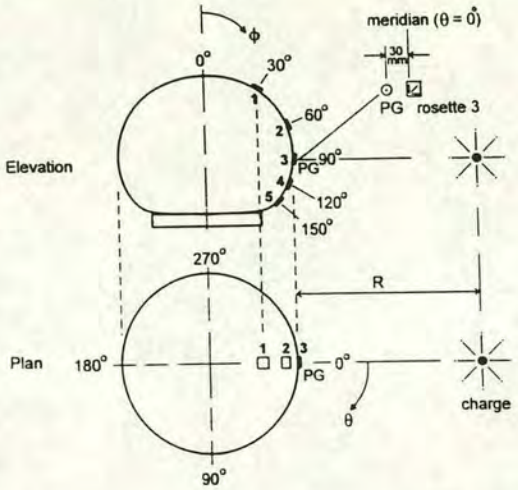

Fig. 3 Disposition of strain gauge rosettes 1 to 5 and miniature pressure gauge (PG)

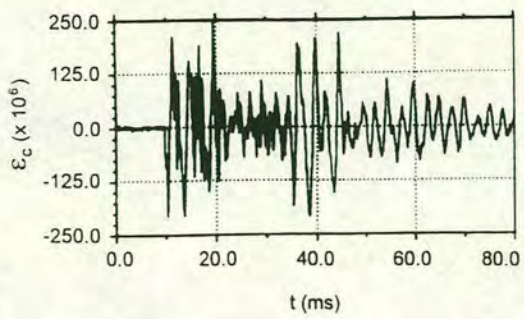

Fig. 4 Typical filtered strain record, rosette 3(θ= 0°, φ =90°) - circumferential direction (El-Deeb & Royles 1998)

The structural responses were measured by means of 45° strain gauge rosettes (foil, elements not superimposed), of 350 ± 0.01Ω resistance, 3mm gauge length, gauge factor = 2.15, temperature compensated for steel and used in a quarter bridge three leadwire arrangement. The environment was seawater at 15°C, constant. Additionally a miniature tourmaline pressure gauge was attached almost flush with the shell surface at its nearest approach to the explosive charge position. Orientation of these transducers was as indicated in Figure 3 and all were waterproofed including leadwires. Signals were recorded automatically and individually on FM analogue tape recorders from which digitised filtered data were obtained. A typical filtered strain record is displayed in Figure 4.

6 DISCUSSION

6.1 *Response Assessment*

Measurable signals were obtained from all channels and, as might be expected from the gauge locations chosen, the greatest response occurred at the nearest approach to the explosion. The pressure-time history for the θ= 0° , φ =90° position measured on the shell agreed quite well with the free field measurements (El-Deeb & Royles 1998) giving confidence in the pressure loads deduced for use in the numerical modelling.

Considering the response at (θ=0°, φ=90°), rosette 3, the measured response was slightly greater in the circumferential direction which is depicted in Figure 4. This tendency is indicated also in the predicted responses shown in Figure 5.

Comparing the measured behaviour over the period (10ms ≤ t ≤ 15ms (see Fig. 4) with the predicted response shown in Figure 5, it can be seen that the USA analysis over predicted with the maximum peak occurring at approximately 3.2 ms into the measuring period, and the USA/CFA or acoustic analysis under predicted with its peak registering at approximately 1.4 ms.

The response predictions (Fig. 5) produced by the USA only analysis are of a more regular and larger peaked oscillatory form than those of the acoustic analysis. One contributory factor to this may be the lack of damping in the USA only analysis compared with the fluid elements in the acoustic treatment.

The differing timescales for the two plots make it difficult to compare the measured and predicted performances given in Figures 4 and 5 respectively, but it is evident that the USA/CFA acoustic analysis comes closer to the measured with an underprediction of the maximum peak strain by some 30%. The measured strain response of Figure 4 appears to have a more regular cyclic pattern than that of the acoustic pattern in Figure 5.

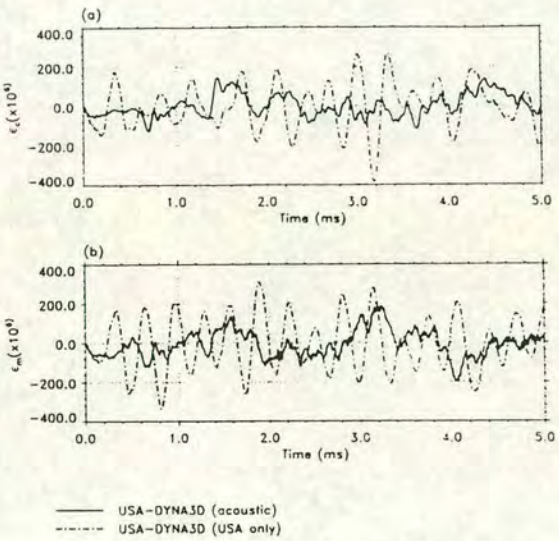

Fig. 5 Response at closest approach to explosive charge (θ=0°, ϕ=90°): (a) circumferential strain ε_c, (b) meridional strain ε_m

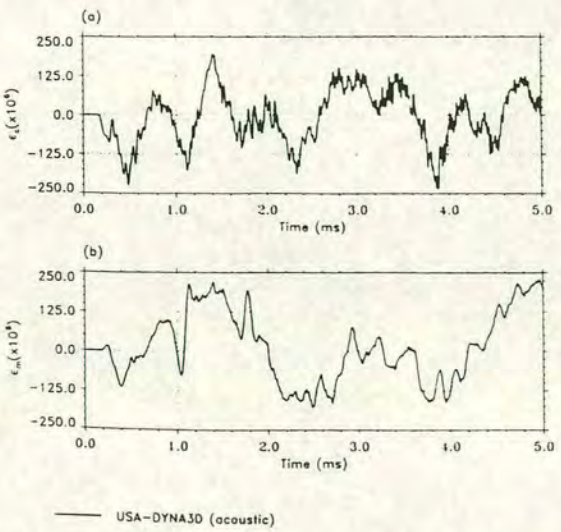

Fig. 6 Response at (θ=180°, ϕ=150°)
(a) circumferential strain ε_c, (b) meridional strain ε_m

For the charge size used (1g) there was no evidence to suggest dimpling in the shell wall. Interestingly the acoustic analysis predicted higher peak strains near the base on the meridian in the shadow side of the structure (θ=180°,ϕ=150°) suggesting that buckling might eventually occur first in that region (see Fig. 6). The plots in Figures 5 and 6 were composed from one data point every microsecond.

6.2 *Buckling*

Evidence of buckling in these symmetric analyses and tests was absent although the sensitive regions were being highlighted (ie at maximum diameter on the meridian nearest to the charge, and near the base on the meridian most remote from the charge).

Any buckling under the fast transient dynamic loadings investigated here would fall automatically into the dynamic category. It has been suggested (Royles 1994) that dynamic buckling could be examined non-destructively by means of a modal method using impact testing and concentrating on the response during the application of the force pulse. However, a more direct approach would be to extend response predictions for an echinodome subjected to increasing magnitudes of explosive load and utilise a Southwell plot technique to establish the buckling load (Southwell 1932, Royles & El-Deeb 1993). Such work would require validating experimentally.

6.3 *Future strategy*

The improvement of the computer modelling of fluid-structure interaction during explosive loading is clearly necessary beyond the capabilities of the USA/CFA type of numerical analysis. The modelling of the fluid and explosive charge using Eulerian elements capable of representing solid, liquid and gas along with Lagrangian elements for the structure is being adopted in this work programme. The timescales for running such problems on scalar or vector machines are large and the advent of software capable of operating on massively parallel processing (MPP) machines is awaited eagerly.

7 CONCLUSIONS

The USA/CFA type of simulation with LS-DYNA3D produced responses of the right order

compared with validation tests and superior to the USA only type of analysis. However, comparison between analysis and experiment was by no means exact.

8 ACKNOWLEDGMENTS

The authors are grateful for the support of the M.o.D. DERA, OASYS Ltd, EPSRC, and the University of Edinburgh.

REFERENCES

Akkas, N., & J.E. Jackson 1984. Structure and stability in fluid structure systems under hydrodynamic shock loading. *J. Sound & Vibration.* 97,20: 247-259.

Belytscho, T., Kennedy, J.M. & D.F. Schoeberle 1978. Quasi Eulerian finite element formulation and fluid-structure interaction. *Proc. ASME/CSME Pressure Vessel Conf., Montreal; June 1978:* 78-PVP-60. New York: ASME.

Boyd, A.R. & R. Royles 1997. Modelling free field UNDEX using LS-DYNA3D. *Proc. First European LS-DYNA Conf., Stratford upon Avon, 20-21 Mar 1997.* 18: S2.1-S2.11. London: OASYS.

Chisum, J.E. & Y.S. Shin 1995. Multimaterial Eulerian and coupled Lagrangian-Eulerian finite element analysis of underwater shock problems. *Report NPS ME-95-001.* Monterey, CA: Naval Postgraduate School.

Cole, R.H., 1984. *Underwater Explosions.* Princeton, NJ: Princeton U.P.

Deruntz, J.A., 1989. The underwater shock analysis code and its applications. *Proc. 60th Shock and Vibration Symposium, DTRC Bethesda, MD, Nov 1989.* 1: 89-107. Arlington, VA: SAVIAC.

Donea, J., Fasoli-Stella, P., Giuliani, S., Halleux, J.P. & A.V. Jones, 1979. An arbitrary Lagrangian-Eulerian finite element procedure for transient dynamic fluid-structure interaction problems. *Proc. 5th Int. Conf. on Structural Mechanics in Reactor Technology, Berlin, Aug 1979.* B1/3. Berlin: SMIRT-V.

El-Deeb, K.M.M. & R. Royles 1993. Dynamic and static buckling assessment of an echinodome. *Computers and Structures.* 46,5: 899-904.

El-Deeb, K.M.M. & R. Royles 1998. Response of an echinodome to explosive loading. *J. Shock and Vibration.* In press.

Geers, T.L. 1978. Doubly asymptotic approximations for transient motions of submerged structures. *J. Acoustical Soc. of America.* 64,5: 1500-1508.

Gourinat, Y. & F. Benyahia 1997. Splashdown and landing of spacecrafts computation and tests. *Proc. First European LS-DYNA Conf. Stratford upon Avon, 20-21 Mar 1997.* 8: 6.1-6.6. London: OASYS.

Hamdan, F.H. & R.E. Hobbs 1997. Shock induced fluid-structure interaction: the Lagrangian fluid formulation revisited: implications and modelling assumptions. *Proc. Marine Structures III Conf., Dunfermline, 20-23 May 1997.* London: M.o.D. DERA.

Haxton, R.S., 1990. Predicting the shock response of submarine platforms. *Proc. Undersea Defence Conf., London 7-9 Feb 1990.* 337-345. Tunbridge Wells: Microwave.

Haxton, R.S., El-Deeb, K.M.M., Royles, R. & I. Hunter 1995. Further assessment of numerical procedures for the study of fluid-structure interaction. *Strain.* 31,3: 107-112.

Hirt, C.W., Amsden, A.A. & J.L. Cook 1974. An arbitrary Lagrangian-Eulerian computing method for all flow speeds. *J. Computational Physics.* 14: 227-253.

Lenselink, H. & E. de Vries 1994. Analysis of the loading of an aluminium cylinder by an underwater explosion. *Proc. MSC World Users' Conf., 20-24 June 1994.*

LSTC 1997. *LS-DYNA3D manuals, version 7 (LS940).* Livermore Software Technology Corporation/OASYS.

Mair, H.U. 1996. Preliminary compilation of underwater explosion benchmarks. *Proc. 67th Shock and Vibration Symposium, Monterey, CA, Nov 1996.* 1: 361-379. Arlington, VA: SAVIAC.

McKeown, R.M., Grande, R. & J.M. Mentges 1994. Simulation of underwater explosions against submerged structures using the Dysmas/ELC code - Part B:analysis of an unstiffened cylinder. *Proc. 65th Shock and Vibration Symposium 1994.* 2: 253-261. Arlington, VA: SAVIAC.

Miller, R.D. 1994. On the fluid-structure coupling features of DYNA/DAA using a reduced fluid mesh (RFM). *Proc. 65th Shock and Vibration Symposium 1994.* 1: 207-216. Arlington, VA: SAVIAC.

Royles, R., Sofoluwe, A.B., Currie, A.J. & M.M. Baig 1980. Behaviour of an underwater structure of optimum strength. *Strain.* 16,1: 12-20.

Royles, R., & J.M. Llambias 1984. Storage aspects of liquid gases underwater and the structural implications. *Proc. Symposium on Storage and Transport of LPG and LNG, Antwerp.* 2: 55-72. Antwerp: KVITI (Kommissie Metaalbouw).

Royles, R. & K.M.M. El-Deeb 1993. Static buckling appraisal of an echinodome. *Experimental Mechanics.* 33,4: 263-269.

Royles, R. 1994. Non-destructive buckling examination of an echinodome. *Proc. 10th Int. Conf. on Experimental Mechanics, Lisbon, 18-22 July 1994.* 599-605. Rotterdam: Balkema.

Royles, R. & A.R. Boyd 1996. Influences of high performance computing on analysis and design of underwater structures. *Proc. 25th AIAS & Int. Conf. on Material Engineering, Gallipoli/Lecce 4-7 Sept 1996.* 1: 583-590. Lecce: AIAS.

Southwell, R.V. 1932. On the analysis of experimental observations in problems of elastic stability. *Proc. Roy. Soc. London.* 135A: 601-616.

UKELG 1989. Rapid phase transitions. *Proc. Meeting of UK Explosion Liaison Group, Shell UK, Thornton Research Centre, Chester.*